Springer Theses
Recognizing Outstanding Ph.D. Research

Jeffrey Michael McMahon

Topics in Theoretical and Computational Nanoscience

From Controlling Light at the Nanoscale to Calculating Quantum Effects with Classical Electrodynamics

Springer

Springer Theses

Recognizing Outstanding Ph.D. Research

For further volumes:
http://www.springer.com/series/8790

Aims and Scope

The series "Springer Theses" brings together a selection of the very best Ph.D. theses from around the world and across the physical sciences. Nominated and endorsed by two recognized specialists, each published volume has been selected for its scientific excellence and the high impact of its contents for the pertinent field of research. For greater accessibility to non-specialists, the published versions include an extended introduction, as well as a foreword by the student's supervisor explaining the special relevance of the work for the field. As a whole, the series will provide a valuable resource both for newcomers to the research fields described, and for other scientists seeking detailed background information on special questions. Finally, it provides an accredited documentation of the valuable contributions made by today's younger generation of scientists.

Theses are accepted into the series by invited nomination only and must fulfill all of the following criteria

- They must be written in good English.
- The topic of should fall within the confines of Chemistry, Physics and related interdisciplinary fields such as Materials, Nanoscience, Chemical Engineering, Complex Systems and Biophysics.
- The work reported in the thesis must represent a significant scientific advance.
- This entire work contains previously published material. I think that a complete list of all published papers that this work is based on is given in the references of Chap. 9
- If the thesis includes previously published material, permission to reproduce this must be gained from the respective copyright holder.
- They must have been examined and passed during the 12 months prior to nomination.
- Each thesis should include a foreword by the supervisor outlining the significance of its content.
- The theses should have a clearly defined structure including an introduction accessible to scientists not expert in that particular field.

Jeffrey Michael McMahon

Topics in Theoretical and Computational Nanoscience

From Controlling Light at the Nanoscale to Calculating Quantum Effects with Classical Electrodynamics

Doctoral Thesis accepted by
Northwestern University, Evanston, IL, USA

Springer

Author
Dr. Jeffrey Michael McMahon
Northwestern University
Evanston, IL 60208
USA
e-mail: mcmahonj@illinois.edu

Supervisor
Dr. George C. Schatz
Department of Chemistry
Northwestern University
Evanston, IL 60208
USA

ISSN 2190-5053 e-ISSN 2190-5061

ISBN 978-1-4419-8248-3 e-ISBN 978-1-4419-8249-0

DOI 10.1007/978-1-4419-8249-0

Springer New York Dordrecht Heidelberg London

Cover design: eStudio Calamar, Berlin/Figueres

Printed on acid-free paper

Springer is part of Springer Science+Business Media (www.springer.com)

Preface

Interest in structures with nanometer-length features has significantly increased as experimental techniques for their fabrication have become possible. The study of phenomena in this area is termed nanoscience, and is a research focus of chemists, pure and applied physicists, electrical engineers, and others. The reason for such focus is the wide range of novel effects that exist at this scale, both of fundamental and practical interest, which often arise from the interaction between metallic nanostructures and light, and range from large electromagnetic field enhancements to extraordinary optical transmission of light through arrays of subwavelength holes.

For the theoretician and computational scientist, this area has been, and continues to be rich with interesting problems to explore and phenomena to explain. For the most part, the phenomena can be explained using classical electrodynamics. However, recent experimental techniques allow individual nanostructures to be studied, questioning the accuracy of such methods at this most detailed level. Moreover, for structures with dimensions of just a few nanometers, the applicability of such methods at all needs to be questioned. Even if a system contains many hundreds of atoms or more so that a continuum level of description is adequate, the optical (and other) properties can be difficult to correctly calculate due to the importance of quantum effects. Thus, the theoretician is in trouble, and accurate descriptions of such structures remain largely unknown.

This dissertation is aimed at addressing some of the most fundamental and outstanding questions in nanoscience from a theoretical and computational perspective, specifically: (i) At the single nanoparticle level, how well do experiment and classical electrodynamics agree? (ii) What is the detailed relationship between optical response and nanoparticle morphology, composition, and environment? (iii) Does an optimal nanostructure exist for generating large electromagnetic field enhancements, and is there a fundamental limit to this? (iv) Can nanostructures be used to control light, such as confining it or causing fundamentally different scattering phenomena to interact, such as electromagnetic surface modes and diffraction effects? (v) Is it possible to calculate quantum effects using classical electrodynamics, and if so, how do they affect optical properties?

Evanston, IL, May 2011 Jeffrey Michael McMahon

Acknowledgments

Writing this dissertation turned out to be much harder than expected, and seemed, in some respects, to be as much work as the research projects themselves. However, it was well worth it, as I was able to view in perspective importance of the work that I have done over the past four years. I came to realize how, as a whole, it fits into the advancement of science. This work would not have been possible without the help from and support of numerous people, and I wish to acknowledge them here.

First off, I thank my advisor at Northwestern University, George C. Schatz. My success as a graduate student would not have been possible without him; from getting me interested in a number of different subjects, to the insight he had to offer, to having thoughtful discussions with me about topics of my own interest. I don't think I have ever met anyone like him, who seems to know something about almost everything. For example, at one point I became interested in quaternions (complexified complex numbers). Everyone I talked to, including a mathematician, had little or no knowledge of such objects, yet Schatz, to my surprise, did.

I also thank Stephen K. Gray, my advisor at Argonne National Laboratory. His availability and willingness to discuss science with me was very beneficial for my success. I am fortunate to have had such a resource.

I also thank my parents, Judy and Michael McMahon, for their love, support, and encouragement. My interest in science can probably be attributed to that of my father. Moreover, I would not be where I am today without their financial support during my undergraduate studies.

Lastly, but definitely not least, I thank my wife, Melanie McMahon. Neither this, nor many other things in my life, would have been possible without her. In respect to science, she was helpful in a number of instances, such as teaching me about experimental inductively coupled plasma measurements. Outside of science she has also been helpful, from making dinner almost every night to bringing me water and Gatorade during my weekend long runs in the summer, when I trained for marathons. But most of all, it is her love, support, and encouragement that is special, and for which I am most thankful.

There are many others who I am thankful to. However, I wish not to compose a lengthy list of names here, for fear that I will leave some people off. Thus, I chose to only name those that impacted me the most. For everyone else, I hope that you understand, and do know that I am grateful.

Evanston, IL May 2011 Jeffrey Michael McMahon

Contents

Abbreviations and Symbols

Units of Measure

μm Micrometer ($1 \cdot 10^{-6}$ m)
nm Nanometer ($1 \cdot 10^{-9}$ m)
fs Femtosecond ($1 \cdot 10^{-15}$ s)

Mathematical Symbols

$\hat{\boldsymbol{n}}$ Unit vector normal to a surface
$\hat{\mathbf{x}}$ Unit vector in the x-direction in a Cartesian coordinate system
$\hat{\mathbf{y}}$ Unit vector in the y-direction in a Cartesian coordinate system
$\hat{\mathbf{z}}$ Unit vector in the z-direction in a Cartesian coordinate system
f^* Complex conjugate of the function f

Physical Constants

$\boldsymbol{c}$ Speed of light in a vacuum ($2.99792458 \cdot 10^8$ m/s)
$\hbar$ Planck's constant ($\sim 1.055 \cdot 10^{-34}$ J · s $\approx 6.582 \cdot 10^{-16}$ eV · s)
$\boldsymbol{e}$ Charge of an electron ($\sim -1.602 \cdot 10^{-19}$ C)
$\boldsymbol{m_e}$ Mass of an electron ($\sim 9.109 \cdot 10^{-31}$ kg)
μ_0 Vacuum permeability, or permeability of free space ($4\pi \cdot 10^{-7}$ N/A^2)
ε_0 Vacuum permittivity, or permittivity of free space ($1/\mu_0 c^2 \approx 8.854 \cdot 10^{-12}$ F/m)

Physical Symbols

x Position vector (not to be confused with the x-direction in a Cartesian coordinate system)
p Momentum vector
E Electric field
D Electric displacement field

$\mathbf{H}$	Auxiliary magnetic field (or just magnetic field)
$\mathbf{B}$	Magnetic field
$\|\mathbf{E}\|^2$	Electric field intensity
$\|\mathbf{E}\|^4$	Square of the electric field intensity (often in the context of a maximum enhancement)
$<\|\mathbf{E}(\omega)\|^4>$	Average square of the electric field intensity (often over the surface of a structure)
$\|\mathbf{D}\|^2$	Electric displacement field intensity
$\|\mathbf{H}\|^2$	Auxiliary magnetic field intensity (or just magnetic field intensity)
$\mathbf{J}$	Electric current density
$\mathbf{S}$	Poynting vector
$\boldsymbol{\mu}$	Permeability
$\boldsymbol{\varepsilon}$	Permittivity
$\boldsymbol{n}$	Refractive index ($n^2 = \varepsilon$)
$\boldsymbol{\omega}$	Angular frequency (or just frequency)
$\mathbf{k}$	Wavevector (often in a dielectric medium)
$\mathbf{k}_0$	Wavevector of incident (or free-space) light
$\boldsymbol{k}$	Wavevector magnitude (often in a dielectric medium)
$\boldsymbol{k}_0$	Wavevector magnitude of incident (or free-space) light
$\boldsymbol{\lambda}$	Wavelength (often in a dielectric medium)
$\boldsymbol{\lambda}_0$	Wavelength of incident (or free-space) light
$\boldsymbol{\lambda}_\mathrm{L}$	Wavelength of a longitudinal plasmon

Chemical Symbols and Refractive Indices

Al_2O_3	Aluminum oxide; $n = 1.77$
C	Carbon (ω dependent)
Carbon disulfide	$n = 1.64$
Chloroform	$n = 1.445$
Formvar	$n = 1.5$
Glass	$n = 1.5$ or $n = 1.523$
Au	Gold (ω dependent)
Hexane	$n = 1.375$
ITO	Indium tin oxide; $n = 2.0$
Pd	Palladium (ω dependent)
SiO_2	Silicon dioxide; $n = 1.5$
Si_3N_4	Silicon nitride; $n = 2.0$
Ag	Silver (ω dependent)
Toluene	$n = 1.496$
Water	$n = 1.33$

Abbreviations

ABC	Additional boundary condition (a material-interface boundary condition in relation to nonlocal dielectric effects)

ADE	Auxiliary differential equation
CPML	Convolutional perfectly matched layers
D2L	Drude plus two Lorentz pole dielectric function
DFT	Density-functional theory
EM	Electromagnetic
EF	Enhancement factor
EOT	Extraordinary optical transmission
FDTD	Finite-difference time-domain method
FWHM	Full width at half maximum
HRTEM	High-resolution transmission electron microscopy
LH	Lynch and Hunter (dielectric data)
LSPR	Localized surface plasmon resonance
JC	Johnson and Christy (dielectric data)
NSOM	Near-field scanning optical microscope (or microscopy)
PEC	Perfect electric conductor
PML	Perfectly matched layers
pRK	Partitioned Runge–Kutta method
RA	Rayleigh anomaly
RA–SPP	Rayleigh anomaly—surface plasmon polariton
RCWA	Rigorous coupled-wave analysis
RI	Refractive index
RIU	Refractive index unit
RPA	Random phase approximation
SEM	Scanning electron microscope
SERS	Surface-enhanced Raman scattering (or spectroscopy)
SI	Symplectic integrator
SMSERS	Single molecule surface-enhanced Raman scattering (or spectroscopy)
SP	Surface plasmon
SPP	Surface plasmon polariton
SPP–BW	Surface plasmon polariton Bloch-wave
TD-FEM	Time-domain finite-element method
TE_z	Transverse electric to z
TEM	Transmission electron microscopy
TF–SF	Total-field—scattered-field technique
TM_z	Transverse magnetic to z

Chapter 1
Introduction

The ultimate goal of theoretical science is to explain phenomena that occur in nature. At the current time, (it is believed that) many of the fundamental laws of nature have been elucidated, and now, most of the phenomena of interest are those that arise from collective effects. Consider, for example, the branch of chemistry. In principle, nearly all of chemistry can be described using the fundamental theory of quantum mechanics (the mechanics of small particles). For the most basic systems, such as a hydrogen-like atoms (i.e., those with a single electron), analytical (theoretical) solutions to the relevant equations exist (using simplifying approximations), and have been known for some time. However, for larger, and more complex systems, such descriptions are not possible. Thus, at this level, theoretical and computational science has merged (terms which will be used interchangeably throughout this dissertation), where the latter approach is used to numerically obtain approximate solutions to the equations of the former.

For systems slightly larger than a hydrogen-like atom (e.g., a molecule), theorists solve the fundamental (or "ab initio") equations of quantum mechanics on a computer, termed electronic structure calculations. One such method, and the only one that will be referred to in this work (albeit, in a limited number of cases), is the density-functional theory (DFT). This method highlights the aforementioned "collective effects", where the important quantity is the electron density, which effectively contains information on the collective behavior of all electrons [1]. However, such techniques are only applicable to relatively small systems, such as a few hundred atoms, which is due to an incredibly poor scaling of required computational effort with system size. Even with increases in supercomputing power, current methods and technology will never be able to simulate arbitrarily large systems ab initio. (Although, other forms of computing, such as quantum computing, may someday make this a reality.)

For systems much larger than a hydrogen-like atom (e.g., those that can be resolved by eye), quantum effects are often not important. Thus, such systems can be described in classical terms, and complicated systems can be simulated using classical methods. For example, the interaction of light with with a system can be

J. M. McMahon, *Topics in Theoretical and Computational Nanoscience*,
Springer Theses, DOI: 10.1007/978-1-4419-8249-0_1,

described by Maxwell's equations, and in a geometric optics picture. In this limit, the wavelength is essentially zero with respect to the size of the system, and quantities are constant functions of the wavelength, such as refractive indices (RIs).

Recent advances in experimental fabrication and synthesis techniques [2, 3] have allowed exploration to occur between these two size extremes, from a few nanometers to a few micrometers (structures which contain many hundreds to millions of atoms, or more). Such area is (loosely) termed nanoscience, because the systems of interest contain features at the nanometer length scale. This area has not only been the subject of intense interest by chemists, but also pure and applied physicists, electrical engineers, and others. In reality though, this area can be viewed as the natural progression of chemistry to large scales, where, for example, such systems are (essentially) realizations of Feynman's idea of forming systems atom-by-atom [4]. For large enough system sizes (relatively speaking), modifications of classical quantities, such as the RI to account for a frequency dependence, are often good enough approximations to make, such that Maxwell's equations can continue to be applied. Although, one question becomes: at this length scale, just how well can computational science, with such approximations, be used to describe systems for which detailed experimental data exists (e.g., that of a single nanoparticle)? The answer to this question [5, 6] will be addressed in Chap. 4. Even more pressing questions are: at a small enough scale (yet one which is too large to treat using quantum mechanics), do these classical approximations break down due to quantum effects, and if so, then what does one do? The answer to the former is yes, due to "nonlocal dielectric effects", and the answer to the latter [7, 8] will be addressed in Chap. 8.

The reason for such intense focus by such a diverse group of scientists is that many novel effects exist at this scale, often due to the interaction of such systems with light, and which do not fit the paradigms of either quantum mechanics or geometric optics. Such effects are the driving force behind the topics in this dissertation, some of which are briefly described here, and then more in-depth in Sect. 1.1. From a practical standpoint, the novel effects that arise from nanoscale structures offer the possibility to control and manipulate light with unprecedented ability. For example, the optical responses of nanostructures (e.g., nanoparticles) show striking properties, such as large, frequency-dependent scattering, which can be controlled by the size, shape, and local dielectric environment of the structure [9].

Although, detailed relationships between optical responses and the parameters of such systems are not yet fully elucidated (particularly the interaction of a nanostructure with the local environment), mainly due to lack of detailed experiments to compare to (e.g., correlated measurements [5]). This topic will be addressed in Chaps. 4 and 5. Moreover, due to the breakdown of classical approximations, and the inability to apply computational quantum mechanics, the optical responses of very small nanostructures are largely unknown (at all), which is the topic of Chap. 8.

Another novel property of nanostructures is that those with junctions have the ability to concentrate electromagnetic (EM) fields stronger than a regular antenna [10, 11]. However, the limit of such enhancement, and the best structure(s) for achieving this, remains elusive, which is the subject of Chaps. 5 and 8.

Besides isolated nanostructures, artificially structured materials with periodic order (at the nanometer scale) also offer novel approaches to manipulate light. For systems made from the noble metals, such systems can be classified as plasmonic crystals, where the overall properties are controlled by the particular material and periodic lattice arrangement. For example, periodic arrays of subwavelength diameter holes have been found to transmit a large amount of light relative to the prediction of geometric optics [12]. Although, while many novel and unexpected effects have been elucidated for such systems, new effects continue to be found [13–17], and some of these will be discussed in Chap. 6.

While many other examples exist [18, 19], the final ones that will be of interest in this work are optical corrals [20, 21], which provide ways to confine light on dielectric surfaces. Such structures will be discussed in Chap. 7.

This chapter is divided into two sections. The first gives a more thorough introduction to the topics that will be addressed in this dissertation (i.e., those mentioned above), including nanostructures, nanostructured metal films, optical corrals, and nonlocal dielectric effects. The second section succinctly emphasizes the important questions that will be answered in this work, and gives a brief, yet in-depth overview of the format of this dissertation.

1.1 Topics in Nanoscience

1.1.1 Isolated Nanostructures

The optical response of a nanostructure is highly dependent on the details of the system. The most prominent example (which also displays general characteristics of other nanosystems) is the interaction of a noble metal nanoparticle (isolated nanostructure), such as gold (Au) or silver (Ag), with light. This interaction leads to a frequency dependent optical response, such as scattering, and has been understood since the time of Faraday [22] (the specific details of this are not important at this point, but examples for spherical nanoparticles can be found in Sect. 8.5.1). Such behavior arises from the excitation of the *sp*-band (conduction band) electrons on the surface of the nanoparticle, which can form a coherent oscillation called a localized surface plasmon resonance (LSPR), as is shown schematically in Fig. 1.1. The particular resonance shown in Fig. 1.1 is called a dipolar LSPR, due to the oscillation symmetry. Although, it also is possible to create other distributions of surface charge, called multipolar (higher-order) LSPRs.

It was not until recently that such structures became the subject of intense focus. This is primarily due to the fact that only recent advances in experimental fabrication (and synthesis) techniques [2] have led to the practical realization of their potential uses as components in a diverse range of technologies, such as waveguides [23–25], photonic circuits [26, 27], molecular rulers [28], and

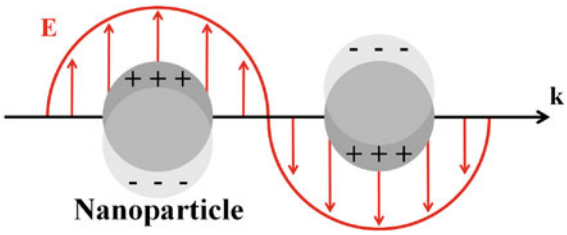

Fig. 1.1 The interaction of a light wave (shown as an electric field **E** with propagation vector **k**) with a nanoparticle. The conduction electrons coherently oscillate in resonance with **E**

chemical and biological sensors [29–34]. This versatility stems from the fact that LSPR frequencies are extremely sensitive to the nanoparticle composition [35], size [36], shape [9, 37, 38], dielectric environment [39–41], and proximity to other nanoparticles [42–46]. However, not all dependencies are completely understood, particularly the detailed relationship between the optical response and structural properties of single nanoparticles in relation to the local dielectric environment, primarily due to the lack of single nanoparticle measurements [5, 6, 47]. This topic will be explored further in Chap. 4.

Another particularly important aspect of LSPRs, with special relevance to chemistry, is that their excitation leads to enhanced EM fields on, or near the nanoparticle surfaces [10, 48–51]. Such enhancements are fundamentally interesting, but are also important for both the technological applications mentioned above, as well as surface-enhanced Raman scattering (or spectroscopy) (SERS) [52–54]. In SERS, Raman scattering is greatly enhanced by adsorbing molecules on a rough metal surface, typically Ag, but also Au or copper, which is one of the most sensitive methods for obtaining the vibrational spectra of molecules (vide infra).

For the case of a nonresonant, weakly-interacting adsorbate, it is believed that the EM enhancements that result from LSPR excitations will dominate the SERS signal [55–59] (although, this point will be revisited in Chap. 8, where it is demonstrated that this may not always be the case). In brief, excitation of LSPRs leads to an electric field (**E**) enhancement of the incident light at frequency ω, $|\mathbf{E}(\omega)|^2$, as well as light emitted by the oscillating dipole induced in the molecule at (the Stokes shifted) frequency ω', $|\mathbf{E}(\omega')|^2$. Kerker et al. [60] demonstrated that the overall EM enhancement is proportional to $|\mathbf{E}(\omega)|^2|\mathbf{E}(\omega')|^2$, which is approximately $|\mathbf{E}(\omega)|^4$, if the width of the LSPR resonance is large compared to the difference in ω and ω' (as is often the case). EM enhancements of greater than 10^8 for single nanoparticles [49] and 10^{10} for coupled nanoparticles [10, 11, 48, 51, 61] have been predicted based on calculations. SERS enhancements can be so high that even single molecule detection is possible [62, 63] (often though, in these cases, resonant Raman scattering and chemical effects also contribute to the enhancement [58, 64]). Owing to these remarkable effects, considerable effort has been devoted to the development of chemical and biological sensors based on SERS [65, 66].

However, many open questions remain, such as: (i) What are the maximum enhancements that one can expect to achieve [10]? (ii) What structure gives the

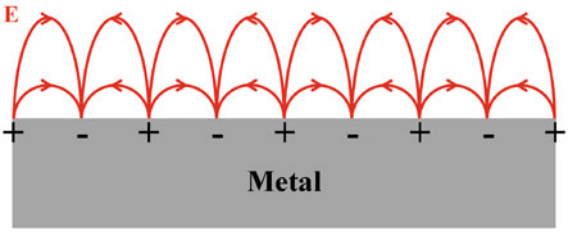

Fig. 1.2 Illustration of the charge oscillation at a metal–dielectric interface, which light can couple into to form a SPP

highest enhancement [11]? and (iii) For a given structure, how many molecules contribute to the SERS signal [10, 67]? These questions will be addressed in Chap. 5. The first question will also be revisited in Chap. 8, where a fundamental (and practical) limitation is believed to have been found [68].

1.1.2 Nanostructured Metal Films

Periodically nanostructured metal films have been the subject of much research since approximately 1998 with the discovery that periodic arrays of subwavelength diameter holes can transmit a large amount of light relative to the prediction of geometric optics, a phenomenon known as extraordinary optical transmission (EOT) [12]. The primary mechanism of this is due to the coupling of light into surface electrons at a metal–dielectric interface (on the incident side), creating a propagating charge oscillation along the surface, called a surface plasmon polariton (SPP). (Note that a SPP is similar to a LSPR, except that it is propagating.) A schematic diagram of such a charge oscillation is shown in Fig. 1.2. Tunneling of the SPP through the metal film, which can rescatter into light, is the mechanism responsible for EOT [69].

What is particularly interesting about such structures is, that in addition to SPPs, a number of distinct mechanisms for the interaction of light with them are possible, including LSPRs (as discussed above), Rayleigh anomalies (RAs) [70], which are light waves diffracted parallel to the surface, and waveguide modes, which (in this context) is the guiding of EM waves. Often it is possible to vary these interactions independently, or to couple them [13–15, 17], leading to a variety of complex optical properties and offering many novel approaches to control light. Such topics form the basis for Chap. 6.

The popularity of these systems has been fueled by the fact that they can be fabricated by a variety of techniques, such as electron beam lithography [12, 71], nanosphere lithography [72], and soft lithography [3, 73], allowing precise control over the important dimensions of the problem.

These systems have found many applications, as has recently been reviewed [74], including sensing based on spectral features that are sensitive to the refractive index (RI) of the materials interfacing with the metal [13, 15, 72, 75–77] and substrates for SERS [78, 79] or enhanced fluorescence [80].

Nanostructured metal films have attracted extensive interest among theorists, as computational methods for solving Maxwell's equations have progressed to the point where it is possible to provide accurate solutions for many of the important experiments that have been done (see Chap. 3 for descriptions of such methods). Thus, there have been extensive simulations of the transmission of light by hole arrays and related structures, including isolated apertures and particle arrays in metal films [13–15, 17, 21, 76, 81–85]. There have even been simulations of near-field scanning optical microscope (NSOM) measurements of hole arrays, characterizing the details of the EM fields associated with SPPs [84]. These types of simulations are discussed in Chap. 6, where elucidation of new phenomena relevant from both fundamental perspectives and to applications are discussed.

1.1.3 Optical Corrals

Metallic structures that can confine and manipulate light on surfaces are of interest for emerging applications in optoelectronics [86], photonics [12, 26, 86], and chemical and biological sensing [2, 87]. One type of structure that has been used to confine light on a dielectric surface is an optical corral [88], a microscale ($1-10\,\mu m$) analogue of the nanoscale quantum corral [89]. For example, calculations performed on an optical corral made from dielectric pads arranged in a $3\,\mu m$ diameter circle have shown that confined EM waves can generate patterns that resemble those of their electronic counterparts [88]. Near-field scanning optical microscopy (NSOM) has also been used to observe confined photonic states within structures composed of 100 nm diameter Au posts (also 100 nm high) arranged in a $3.6\,\mu m$ diameter circle (and also in a $4 \times 2\,\mu m$ structure) on an indium tin oxide (ITO) substrate [90].

Such structures allow new fundamental studies of control over light in confined geometries on surfaces. Optical corrals are thoroughly discussed in Chap. 7, from isolated slits [21] (a simple, 1D optical corral) to circular and elliptical structures [20].

1.1.4 Nonlocal Dielectric Effects

Recently, interest in metallic structures with small features (even relative to sizes at the nanoscale), on the order of 10 nm or less, has significantly increased as experimental techniques for their fabrication have become possible [2]. Even if the features involve many hundreds of atoms or more so that a continuum level of description is adequate (i.e., not depending on the actual atomic positions), their optical responses can be difficult to correctly describe because continuum classical methods break down due to quantum effects. Such behavior can lead unusual optical properties relative to predictions based on classical electrodynamics [91].

For example, in isolated spherical nanoparticles, LSPRs are found to be shifted to higher energies (blueshifted) relative to classical predictions [92]. Additionally, in thin metal films, anomalous absorption is observed [93, 94].

A full quantum mechanical treatment would of course be best, but this is not practical for these sizes. However, it is possible to incorporate some of the most important quantum effects within classical electrodynamics: electron scattering, electron spill-out, and spatial nonlocality of the material polarization. (It should be noted that some quantum mechanical effects are already included when the ω dependence of the bulk dielectric constant is considered, such as interband electron transitions.) The first is related to increased electron scattering at the nanostructure surfaces due to a short electron mean free path. Fortunately, this effect can be (essentially) described by a size-dependent correction to the material properties [95]; see Chap. 8. The second effect (which, at the most fundamental level is related to the first [96, 97]) is that, in reality, metallic surface boundaries are not infinitely sharp (due to the electron density varying smoothly), and thus the boundary properties of a nanostructure are different than in the interior. This effect is either from surface interactions with the environment, or extension of the surface (quantum mechanical) wavefunctions "spilling out" into the surrounding medium. Such an effect can be partially accounted for by a dielectric layer model [98], which is also discussed in Chap. 8. The third quantum effect is that the polarization of the material at one point in space depends not only on the local $\mathbf{E}$, but also on the $\mathbf{E}$ in its neighborhood [99], hence the description as a "nonlocal" effect. Such a statement is justified in Chap. 8, which also forms the basis of discussion therein.

Nonlocal effects can be (roughly) understood by considering the effect of momentum in small structures. When light interacts with a structure of size d (which could correspond to a nanoparticle size, junction gap distance, etc.), wavevector components $\mathbf{k}$ (related to the momentum $\mathbf{p}$ by $\mathbf{p} = \hbar\mathbf{k}$, where $\hbar$ is Planck's constant) are generated with magnitude $k = 2\pi/d$. This in turn imparts an energy of $E = (\hbar\mathbf{k})^2/2m_e$, where m_e is the mass of an electron, to (relatively) free electrons in the metal. For small d, these energies can correspond to the optical range (considered in this work to be 1–6 eV). This analysis suggests that $\mathbf{k}$-dependent effects should come into play for d less than approximately 2 nm. In metals, however, somewhat larger d values also exhibit these effects because electrons in motion at the Fermi velocity can be excited by the same energy with a smaller momentum increase due to dispersion effects [100]. Thus, at optical energies, the optical response of a structure is not only frequency dependent, as described above, but also $\mathbf{k}$ dependent. Since $\mathbf{k}$ and $\mathbf{x}$ (the position vector) are Fourier transform pairs (see Appendix A), the optical response at one position depends on all others. Such $\mathbf{k}$ dependence also contains quantum mechanical effects; see Appendix D.

Since the first formulation of nonlocal electromagnetics [99], complications introduced by such effects have made direct incorporation of them into classical electrodynamics difficult [7, 8]. This has caused applications to remain limited to simple systems, such as spherical structures [101, 102], or aggregates thereof [103–106], and planar surfaces [107], and most within the electrostatic limit.

Therefore, the optical properties of very small structures remain largely unknown. Chapter 8 addresses these issues.

1.2 Format of this Dissertation

To succinctly summarize, this dissertation is aimed at addressing the following questions:

- (i) What are the main theoretical and computational tools needed to study systems at the nanometer length scale? (ii) How can Maxwell's equations be solved to arbitrarily high precision while preserving dynamical invariants of the problem (e.g., the energy density)? (Chap. 3)
- (i) At the single nanoparticle level, how well do experiment and classical electrodynamics agree? (ii) What is the detailed relationship between optical response and nanoparticle morphology, composition, and environment? (Chaps. 4 and 5)
- (i) Does an optimal nanostructure exist for generating large electromagnetic field enhancements? (ii) Is there a fundamental limit to this? (Chaps. 5 and 8)
- Can nanostructures be used to control light, such as confining it, or causing fundamentally different scattering phenomena to interact, such as electromagnetic surface modes and diffraction effects? (Chaps. 6 and 7)
- Is it possible to calculate quantum effects using classical electrodynamics, and if so, how do they affect optical properties? (Chap. 8)

The approach herein is to address the above questions from the perspective of classical electrodynamics. The basic electrodynamic theory that will be needed to understand this work, Maxwell's equations, is presented in Chap. 2. In Chap. 3, the theoretical and computational methods that are used to solve Maxwell's equations of electromagnetics are reviewed. Particular focus will be on the finite-difference time-domain (FDTD) method and the finite-element method (FEM). However, the rigorous coupled-wave analysis (RCWA) and the modal expansion methods are also discussed. In addition, a method to propagate Maxwell's equations in time to an arbitrarily high order of accuracy is presented. In Chap. 4, the detailed relationship between the optical response of a cubic nanoparticle and the morphology, composition, and local environment of it is discussed in relation to single-nanoparticle experimental data. In Chap. 5, junction containing structures are studied for their ability to generate large EM enhancements, with particular focus on the application to SERS. Chapter 6 discusses nanostructured metal films, focusing mainly on periodic arrays of subwavelength holes. Specific emphasis will be placed on novel interactions, such as diffractive effects with resonances. In Chap. 7, optical corrals and isolated slits are studied as possible systems to confine and control light on dielectric surfaces. Chapter 8 discusses a method to incorporate quantum effects within the framework classical electrodynamics. Additionally, the optical properties

of small structures are presented (calculated using the developed method). Chapter 9 concludes by readdressing the questions posed above in light of the work presented.

Chapters 4–8 contain relatively stand-alone topics, and could, in principle, be read without reference to the others. However, the collective importance of this work will not be as well appreciated this way. In addition, symbols, abbreviations, and terminology that are used in later chapters are often defined in earlier ones. Although, a complete compilation of these can be found at the beginning of this dissertation.

References

1. Hohenberg P, Kohn W (1964) Inhomogeneous electron gas. Phys Rev 136:B864–B871
2. Willets KA, Van Duyne RP (2007) Localized surface plasmon resonance spectroscopy and sensing. Annu Rev Phys Chem 58:267–297
3. Henzie J, Lee MH, Odom TW (2007) Multiscale patterning of plasmonic metamaterials. Nat Nanotechnol 2:549–554
4. Feynman RP (1960) There's plenty of room at the bottom. Eng Sci 23:22–36
5. McMahon JM, Wang Y, Sherry LJ, Van Duyne RP, Marks LD, Gray SK, Schatz GC (2009) Correlating the structure, optical spectra, and electrodynamics of single silver nanocubes. J Phys Chem C 113:2731–2735
6. Ringe E, McMahon JM, Sohn K, Cobley C, Xia Y, Huang J, Schatz GC, Marks LD, Van Duyne RP (2010) Unraveling the effects of size, composition, and substrate on the localized surface plasmon resonance frequencies of gold and silver nanocubes: a systematic single-particle approach. J Phys Rev C 114:12511–12516
7. McMahon JM, Gray SK, Schatz GC (2009) Nonlocal optical response of metal nanostructures with arbitrary shape. Phys Rev Lett 103:097403
8. McMahon JM, Gray SK, Schatz GC (2010) Calculating nonlocal optical properties of structures with arbitrary shape. Phys Rev B 82:035423
9. Kelly KL, Coronado E, Zhao LL, Schatz GC (2003) The optical properties of metal nanoparticles: the influence of size, shape, and dielectric environment. J Phys Chem B 107:668–677
10. McMahon JM, Henry A-I, Wustholz KL, Natan MJ, Freeman RG, Van Duyne RP, Schatz GC (2009) Gold nanoparticle dimer plasmonics: finite element method calculations of the electromagnetic enhancement to surface-enhanced Raman spectroscopy. Anal Bioanal Chem 394:1819–1825
11. Wustholz KL, Henry A-I, McMahon JM, Freeman RG, Valley N, Piotti ME, Natan MJ, Schatz GC, Van Duyne RP (2010) Structure-activity relationships in gold nanoparticle dimers and timers for surface-enhanced raman spectroscopy. J Am Chem Soc 132:10903–10910
12. Ebbesen TW, Lezec HJ, Ghaemi HF, Thio T, Wolff PA (1998) Extraordinary optical transmission through subwavelength hole arrays. Nature 391:667–669
13. McMahon JM, Henzie J, Odom TW, Schatz GC, Gray SK (2007) Tailoring the sensing capabilities of nanohole arrays in gold films with Rayleigh anomaly-surface plasmon polaritons. Opt Express 15:18119–18129
14. McMahon JM, Gray SK, Schatz GC (2011) Surface nanophotonics theory. In: G. Wiederrecht (ed) Comprehensive nanoscience and technology. Elsevier, Amsterdam
15. Gao H, McMahon JM, Lee MH, Henzie J, Gray SK, Schatz GC, Odom TW (2009) Rayleigh anomaly-surface plasmon polariton resonances in palladium and gold subwavelength hole arrays. Opt Express 17:2334–2340
16. Odom TW, Gao H, McMahon JM, Henzie J, Schatz GC (2009) Plasmonic superlattices: hierarchical subwavelength hole arrays. Chem Phys Lett 483:187–192

17. Schatz GC, McMahon JM, Gray SK (2007) Tailoring the parameters of nanohole arrays in gold films for sensing applications. In: Mark I Stockman (ed) Plasmonics: metallic nanostructures and their optical properties V, pp 664103(1–8)
18. Joannopoulos JD, Johnson SG, Winn JN, Meade RD (2008) Photonic crystals: molding the flow of light, 2nd edn. Princeton University Press, Princeton
19. Shalaev VM (2006) Optical negative-index metamaterials. Nat Photonics 1:41–48
20. Babayan Y, McMahon JM, Li S, Gray SK, Schatz GC, Odom TW (2009) Confining standing waves in optical corrals. ACS Nano 3:615–620
21. McMahon JM, Gray SK, Schatz GC (2008) Dephasing of electromagnetic fields in scattering from an isolated slit in a gold film. In: Kawata S (ed) Plasmonics: nanoimaging, nanofabrication, and their applications IV. pp 703311/1–6
22. Faraday M (1857) The Bakerian lecture: experimental relations of gold (and other metals) to light. Philos T R Soc Lond 147:145–181
23. Atwater HA (2007) The promise of plasmonics. Sci Am 296:56–63
24. Dionne JA, Lezec HJ, Atwater HA (2006) Highly confined photon transport in subwavelength metallic slot waveguides. Nano Lett 6:1928–1932
25. Dionne JA, Sweatlock LA, Atwater HA, Polman A (2006) Plasmon slot waveguides: towards chip-scale propagation with subwavelength-scale localization. Phys Rev B 73:035407
26. Ozbay E (2006) Plasmonics: merging photonics and electronics at nanoscale dimensions. Science 311:189–193
27. Ebbesen TW, Genet C, Bozhevolnyi SI (2008) Surface plasmon circuitry. Phys Today 61:44–50
28. Reinhard BM, Siu M, Agarwal H, Alivisatos AP, Liphardt J (2005) Calibration of dynamic molecular rulers based on plasmon coupling between gold nanoparticles. Nano Lett 5:2246–2252
29. Stewart ME, Anderton CR, Thompson LB, Maria J, Gray SK, Rogers JA, Nuzzo RG (2008) Nanostructured plasmonic sensors. Chem Rev 108:494–521
30. Anker JN, Hall WP, Lyandres O, Shah NC, Zhao J, Van Duyne RP (2008) Biosensors. Nat Mater 7:442–453
31. Haes AJ, Chang L, Klein LW, Van Duyne RP (2005) Detection of a biomarker for Alzheimer's disease from synthetic and clinical samples using a nanoscale optical biosensor. J Am Chem Soc 127:2264–2271
32. McFarland AD, Van Duyne RP (2003) Single silver nanoparticles as real-time optical sensors with zeptomole sensitivity. Nano Lett 3:1057–1062
33. Haes AJ, Van Duyne RP (2002) A nanoscale optical biosensor: selectivity of an approach based on the localized surface plasmon resonance spectroscopy of triangular silver nanoparticles. J Am Chem Soc 124:10596–10604
34. Elghanian R, Storhoff JJ, Mucic RC, Letsinger RL, Mirkin CA (1997) Selective colorimetric detection of polynucleotides based on the distance-dependent optical properties of gold nanoparticles. Science 277:1078–1081
35. Link S, Wang ZL, El-Sayed MA (1999) Alloy formation of gold–silver nanoparticles and the dependence of the plasmon absorption on their composition. J Phys Chem B 103:3529–3533
36. Haynes CL, Van Duyne RP (2001) Nanosphere Lithography: a versatile nanofabrication tool for studies of size-dependent nanoparticle optics. J Phys Chem B 105:5599–5611
37. Jensen TR, Malinsky MD, Haynes CL, Van Duyne RP (2000) Nanosphere lithography: tunable localized surface plasmon resonance spectra of silver nanoparticles. J Phys Chem B 104:10549–10556
38. Jin R, Cao YC, Hao E, Metraux GS, Schatz GC, Mirkin CA (2003) Controlling anisotropic nanoparticle growth through plasmon excitation. Nature 425:487–490
39. Sherry LJ, Chang S-H, Schatz GC, Van Duyne RP, Wiley BJ, Xia Y (2005) Localized surface plasmon resonance spectroscopy of single silver nanocubes. Nano Lett 5:2034–2038

40. Xu G, Chen Y, Tazawa M, Jin P (2006) Surface plasmon resonance of silver nanoparticles on vanadium dioxide. J Phys Chem B 110:2051–2056
41. Pinchuk A, Hilger A, von Plessen G, Kreibig U (2004) Substrate effect on the optical response of silver nanoparticles. Nanotechnology 15:1890–1896
42. Malinsky MD, Kelly KL, Schatz GC, Van Duyne RP (2001) Chain length dependence and sensing capabilities of the localized surface plasmon resonance of silver nanoparticles chemically modified with alkanethiol self-assembled monolayers. J Am Chem Soc 123:1471–1482
43. Haynes CL, McFarland AD, Zhao L, Van Duyne RP, Schatz GC, Gunnarsson L, Prikulis J, Kasemo B, Käll M (2003) Nanoparticle optics: the importance of radiative dipole coupling in two-dimensional nanoparticle arrays. J Phys Chem B 107:7337–7342
44. Zhao L, Kelly KL, Schatz GC (2003) The extinction spectra of silver nanoparticle arrays: influence of array structure on plasmon resonance wavelength and width. J Phys Chem 107:7343–7350
45. Huang W, Qian W, El-Sayed MA (2005) The optically detected coherent lattice oscillations in silver and gold monolayer periodic nanoprism arrays: the effect of interparticle coupling. J Phys Chem B 109:18881–18888
46. Gunnarsson L, Rindzevicius T, Prikulis J, Kasemo B, Käll M, Zou S, Schatz GC (2005) Confined plasmons in nanofabricated single silver particle pairs: experimental observations of strong interparticle interactions. J Phys Chem B 109:1079–1087
47. Wang Y, Eswaramoorthy SK, Sherry LJ, Dieringer JA, Camden JP, Schatz GC, Van Duyne RP, Marks LD (2009) A method to correlate optical properties and structures of metallic nanoparticles. Ultramicroscopy 109:1110–1113
48. Hao E, Schatz GC (2004) Electromagnetic fields around silver nanoparticles and dimers. J Chem Phys 120:357–366
49. Kottmann JP, Martin OJF, Smith DR, Schultz S (2000) Spectral response of plasmon resonant nanoparticles with a non-regular shape. Opt Express 6:213–219
50. Kottmann JP, Martin OJF (2001) Plasmon resonant coupling in metallic nanowires. Opt Express 8:655–663
51. Xu H (2004) Theoretical study of coated spherical metallic nanoparticles for single-molecule surface enhanced spectroscopy. Appl Phys Lett 85:5980–5982
52. Albrecht MG, Creighton JA (1977) Anomalously intense Raman spectra of pyridine at a silver electrode. J Am Chem Soc 99:5215–5217
53. Jeanmaire DL, Van Duyne RP (1977) Surface Raman spectroelectrochemistry: Part I. Heterocyclic, aromatic, and aliphatic amines adsorbed on the anodized silver electrode. J Electroanal Chem 84:1–20
54. Fleischman M, Hendra PJ, McQuillan AJ (1974) Raman spectra of pyridine adsorbed at a silver electrode. Chem Phys Lett 26:163–166
55. Gersten J, Nitzan A (1980) Electromagnetic theory of enhanced Raman scattering by molecules adsorbed on rough surfaces. J Chem Phys 73:3023
56. Schatz GC (1984) Theoretical studies of surface enhanced Raman scattering. Acc Chem Res 17:370–376
57. Metiu H, Das P (1984) The electromagnetic theory of surface enhanced spectroscopy. Annu Rev Phys Chem 35:507–536
58. Xu H, Aizpurua J, Käll M, Apell P (2000) Electromagnetic contributions to single-molecule sensitivity in surface-enhanced Raman scattering. Phys Rev E 62:4318–4324
59. Schatz GC, Van Duyne RP (2002) Electromagnetic mechanism of surface-enhanced spectroscopy. In: Chalmers JM, Griffiths PR (eds) Handbook of vibrational spectroscopy. Wiley, New York
60. Kerker M, Wang DS, Chew H (1980) Surface enhanced Raman scattering (SERS) by molecules adsorbed at spherical particles. Appl Optics 19:3373–3388
61. Zou S, Schatz GC (2005) Silver nanoparticle array structures that produce giant enhancements in electromagnetic fields. Chem Phys Lett 403:62–67

62. Nie S, Emory SR (1997) Probing single molecules and single nanoparticles by surface-enhanced Raman scattering. Science 275:1102–1106
63. Kneipp K, Wang Y, Kneipp H, Perelman LT, Itzkan I, Dasari RR, Feld MS (1997) Single molecule detection using surface-enhanced Raman scattering (SERS). Phys Rev Lett 78:1667–1670
64. Dieringer JA, Wustholz KL, Masiello DJ, Camden JP, Kleinman SL, Schatz GC, Van Duyne RP (2009) Surface-enhanced Raman excitation spectroscopy of a single Rhodamine 6G molecule. J Am Chem Soc 131:849–854
65. Camden JP, Dieringer JA, Zhao J, Van Duyne RP (2008) Controlled plasmonic nanostructures for surface-enhanced spectroscopy and sensing. Acc Chem Res 41:1653–1661
66. Stiles PL, Dieringer JA, Shah NC, Van Duyne RP (2008) Surface-enhanced Raman spectroscopy. Annu Rev Anal Chem 1:601–626
67. Zeman EJ, Carron KT, Schatz GC, Van Duyne RP (1987) A surface enhanced resonance Raman study of cobalt phthalocyanine on rough Ag films: theory and experiment. J Chem Phys 87:4189
68. McMahon JM, Gray SK, Schatz GC (2011) Fundamental behavior of electric field enhancements in the gaps between closely spaced nanostructures. Phys Rev B 83:115428
69. Barnes WL, Murray AW, Dintinger J, Devaux E, Lezec HJ, Ebbesen TW (2004) Surface plasmon polaritons and their role in the enhanced transmission of light through periodic arrays of sub-wavelength holes in a metal film. Phys Rev Lett 92:107401
70. Hessel A, Oliner AA (1965) A new theory of Wood's anomalies on optical gratings. Appl Opt 4:1275–1297
71. Ghaemi HF, Thio T, Grupp DE, Ebbesen TW, Lezec HJ (1998) Surface plasmons enhance optical transmission through subwavelength holes. Phys Rev B 58:6779–6782
72. Hicks EM, Zhang X, Zou S, Lyandres O, Spears KG, Schatz GC, Van Duyne RP (2005) Plasmonic properties of film over nanowell surfaces fabricated by nanosphere lithography. J Phys Chem B 109:22351–22358
73. Lee MH, Gao H, Henzie J, Odom TW (2007) Microscale arrays of nanoscale holes. Small 3:2029–2033
74. Gordon R, Sinton D, Kavanagh KL, Brolo AG (2008) A new generation of sensors based on extraordinary optical transmission. Acc Chem Res 41:1049–1057
75. Lee MH, Gao H, Odom TW (2009) Refractive index sensing using quasi one-dimensional nanoslit arrays. Nano Lett 9:2584–2588
76. Stewart ME, Mack NH, Malyarchuck V, Soares JANT, Lee T-W, Gray SK, Nuzzo RG, Rogers JA (2006) Quantitative multispectral biosensing and 1D imaging using quasi-3D plasmonic crystals. Proc Natl Acad Sci USA 103:17143–17148
77. Brolo AG, Gordon R, Leathem B, Kavanagh KL (2004) Surface plasmon sensor based on the enhanced light transmission through arrays of nanoholes in gold films. Langmuir 20:4813–4815
78. Reilly TH, Chang S-H, Corbman JD, Schatz GC, Rowlen KL (2007) Quantitative evaluation of plasmon enhanced Raman scattering from nanoaperture arrays. J Phys Chem C 111:1689–1694
79. Brolo AG, Arctander E, Gordon R, Leathem B, Kavanagh KL (2004) Nanohole-enhanced Raman scattering. Nano Lett 4:2015–2018
80. Brolo AG, Kwok SC, Moffitt MG, Gordon R, Riordon J, Kavanagh KL (2005) Enhanced fluorescence from arrays of nanoholes in a gold film. J Am Chem Soc 127:14936–14941
81. Porto JA, García-Vidal FJ, Pendry JB (1999) Transmission resonances on metallic gratings with very narrow slits. Phys Rev Lett 83:2845–2848
82. Bravo-Abad J, Martín-Moreno L, García-Vidal FJ (2004) Transmission properties of a single metallic slit: from the subwavelength regime to the geometrical-optics limit. Phys Rev E 69:026601
83. Chang S-H, Gray SK, Schatz GC (2005) Surface plasmon generation and light transmission by isolated nanoholes and arrays of nanoholes in thin metal films. Opt Express 13:3150–3165

84. Yin L, Vlasko-Vlasov VK, Rydh A, Pearson J, Welp U, Chang S-H, Gray SK, Schatz GC, Brown DB, Kimball CW (2004) Surface plasmons at single nanoholes in Au films. Appl Phys Lett 85:467–469
85. Atkinson AL, McMahon JM, Schatz GC (2009) FDTD studies of metallic nanoparticle systems. In: Self organization of molecular systems, from molecules and clusters to nanotubes and proteins, NATO science for peace and security series A, chemistry and biology. Springer, Netherlands
86. Barnes WL, Dereux A, Ebbesen TW (2003) Surface plasmon subwavelength optics. Nature 424:824–830
87. Haes AJ, Haynes CL, McFarland AD, Schatz GC, Van Duyne RP, Zou S (2005) Plasmonic materials for surface-enhanced sensing and spectroscopy. MRS Bull 30:368–375
88. Colas des Francs G, Girard C, Weeber J-C, Chicane C, David T, Dereux A, Peyrade D (2001) Optical analogy to electronic quantum corrals. Phys Rev Lett 86:4950–4953
89. Crommie MF, Lutz CP, Eigler DM (1993) Confinement of electrons to quantum corrals on a metal surface. Science 262:218–220
90. Chicanne C, David T, Quidant R, Weeber JC, Lacroute Y, Bourillot E, Dereux A, Colas des Francs G, Girard C (2002) Imaging the local density of states of optical corrals. Phys Rev Lett 88:097402
91. Kreibig U, Vollmer M (1995) Optical properties of metal clusters. Springer, Berlin
92. Palomba S, Novotny L, Palmer RE (2008) Blue-shifted plasmon resonance of individual size-selected gold nanoparticles. Opt Commun 281:480–483
93. Anderegg M, Feuerbacher B, Fitton B (1971) Optically excited longitudinal plasmons in potassium. Phys Rev Lett 27:1565–1568
94. Lindau I, Nilsson PO (1970) Experimental evidence for excitation of longitudinal plasmons by photons. Phys Lett A 31:352–353
95. Coronado EA, Schatz GC (2003) Surface plasmon broadening for arbitrary shape nanoparticles: a geometrical probability approach. J Chem Phys 119:3926–3934
96. Ruppin R (1976) Optical properties of a metal sphere with a diffuse surface. J Opt Soc Am 66:449–453
97. Apell P, Penn DR (1983) Optical properties of small metal spheres: surface effects. Phys Rev Lett 50:1316–1319
98. Peng S, McMahon JM, Schatz GC, Gray SK, Sun Y (2010) Reversing the size-dependence of surface plasmon resonances in colloidal nanoparticles (Submitted)
99. Agarwal GS, Pattanayak DN, Wolf E (1974) Electromagnetic fields in spatially dispersive media. Phys Rev B 10:1447–1475
100. Raether H (1988) Surface plasmons on smooth and rough surfaces and on gratings. Springer, Berlin
101. Dasgupta BB, Fuchs R (1981) Polarizability of a small sphere including nonlocal effects. Phys Rev B 24:554–561
102. Chang R, Leung PT (2006) Nonlocal effects on optical and molecular interactions with metallic nanoshells. Phys Rev B 73:125438
103. García de Abajo FJ (2008) Nonlocal effects in the plasmons of strongly interacting nanoparticles, dimers, and waveguides. J Phys Chem C 112:17983–17987
104. Tserkezis C, Gantzounis G, Stefanou N (2008) Collective plasmonic modes in ordered assemblies of metallic nanoshells. J Phys Condens Matter 20:075232
105. Pack A, Hietschold M, Wannemacher R (2001) Failure of local Mie theory: optical spectra of colloidal aggregates. Opt Commun 194:277–287
106. Yannopapas V (2008) Non-local optical response of two-dimensional arrays of metallic nanoparticles. J Phys Condens Matter 20:325211
107. Jones WE, Kliewer KL, Fuchs R (1969) Nonlocal theory of the optical properties of thin metallic films. Phys Rev 178:1201–1203

Chapter 2
Basic Electromagnetic Theory

In this chapter, an introduction to the basic electromagnetic concepts that are needed to understand this dissertation are discussed. A full overview of electromagnetics is beyond the scope of this work, and so only the most relevant concepts are reviewed. The reader interested in a more in-depth analysis is referred to Refs. [1, 2].

2.1 Maxwell's Equations

The interaction of light with matter in the classical continuum limit (many hundreds of atoms or more) is described by Maxwell's equations,

$$\frac{\partial}{\partial t}\mathbf{D}(\mathbf{x},t) + \mathbf{J}(\mathbf{x},t) = \nabla \times \mathbf{H}(\mathbf{x},t) \tag{2.1}$$

$$\frac{\partial}{\partial t}\mathbf{B}(\mathbf{x},t) = -\nabla \times \mathbf{E}(\mathbf{x},t) \tag{2.2}$$

$$\nabla \cdot \mathbf{D}(\mathbf{x},t) = \rho \tag{2.3}$$

$$\nabla \cdot \mathbf{B}(\mathbf{x},t) = 0 \tag{2.4}$$

where $\mathbf{E}(\mathbf{x}, t)$ is the electric field, $\mathbf{D}(\mathbf{x}, t)$ is the electric displacement field, $\mathbf{B}(\mathbf{x}, t)$ is the magnetic field, $\mathbf{H}(\mathbf{x}, t)$ is the auxiliary magnetic field (sometimes referred to as just the magnetic field), and $\mathbf{J}(\mathbf{x}, t)$ and ρ are the external current and charge densities, respectively. (In this work, both $\mathbf{B}(\mathbf{x}, t)$ and $\mathbf{H}(\mathbf{x}, t)$ will be referred to as the magnetic field, with the reference clear from the context. Although, it is worth emphasizing that the former is the fundamental quantity, and the latter is a derived one [2]. While collectively known as Maxwell's equations, Eqs. 2.1–2.4 are individually known as the Maxwell–Ampére law, Faraday's law, Gauss' law, and Gauss' law for magnetism, respectively. Before these equations can be solved,

J. M. McMahon, *Topics in Theoretical and Computational Nanoscience*, Springer Theses, DOI: 10.1007/978-1-4419-8249-0_2,

relationships between both $\mathbf{D}(\mathbf{x}, t)$ and $\mathbf{E}(\mathbf{x}, t)$ as well as $\mathbf{B}(\mathbf{x}, t)$ and $\mathbf{H}(\mathbf{x}, t)$ are needed. In this work, a linear constitutive relationship between $\mathbf{B}(\mathbf{x}, t)$ and $\mathbf{H}(\mathbf{x}, t)$ is assumed, $\mathbf{B}(\mathbf{x}, t) = \mu \mathbf{H}(\mathbf{x}, t)$, where μ is the permeability of the medium. Furthermore, in applications only nonmagnetic materials will be considered ($\mu = \mu_0$, where μ_0 is the vacuum permeability). In this case, the interaction of light with matter is completely described by the relationship between $\mathbf{D}(\mathbf{x}, t)$ and $\mathbf{E}(\mathbf{x}, t)$, which is further discussed below, and then again in Chap. 8.

Another fundamental equation, which is not technically one of Maxwell's, but can derived from Eqs. 2.1 and 2.3, is that of continuity

$$\nabla \cdot \mathbf{J}(\mathbf{x}, t) = -\frac{\partial}{\partial t}\rho, \tag{2.5}$$

which is the mathematical form of the law of conservation of charge.

As written, the quantities in Eqs. 2.1–2.4 are functions of $\mathbf{x}$ and t. However, Maxwell's equations can be written in a variety of other forms, which are often useful for solving particular problems. The additional form of most relevance herein corresponds to when the field quantities have a time-harmonic oscillation, $e^{-i\omega t}$, where ω is the angular frequency (often referred to as simply the frequency). The reason for this is that most materials have an electromagnetic response that depends on ω, such as Au or Ag [3, 4] (which are the focus of this work); see Sect. 2.3. In this case, by Fourier transforming Eqs. 2.1–2.4 (see Appendix A.1), Maxwell's equations become

$$-i\omega \mathbf{D}(\mathbf{x}, \omega) + \mathbf{J}(\mathbf{x}, \omega) = \nabla \times \mathbf{H}(\mathbf{x}, \omega) \tag{2.6}$$

$$-i\omega \mathbf{B}(\mathbf{x}, \omega) = -\nabla \times \mathbf{E}(\mathbf{x}, \omega) \tag{2.7}$$

$$\nabla \cdot \mathbf{D}(\mathbf{x}, \omega) = \rho \tag{2.8}$$

$$\nabla \cdot \mathbf{B}(\mathbf{x}, \omega) = 0, \tag{2.9}$$

where the quantities are defined similar to before, but are now functions of ω rather than t. It should be understood herein that any time that time-domain quantities are discussed that the frequency-domain solutions may be obtained by Fourier transformation, and vice-versa; Appendix A.1. In passing, it is noted that electrostatics is the limiting case of Eqs. 2.6–2.9 as $\omega \to 0$.

In some cases, it can be beneficial to work with a single equation in terms of $\mathbf{B}$ and $\mathbf{H}$ or $\mathbf{D}$ and $\mathbf{E}$ alone. For example, working in the frequency domain, simple manipulations of Eqs. 2.6 and 2.7 gives

$$\nabla \times \left[\frac{1}{\mu}\nabla \times \mathbf{E}(\mathbf{x}, \omega)\right] - \omega^2 \mathbf{D}(\mathbf{x}, \omega) = i\omega \mathbf{J}(\mathbf{x}, \omega) \tag{2.10}$$

$$\nabla \times \left[\frac{1}{\varepsilon}\nabla \times \mathbf{H}(\mathbf{x}, \omega)\right] - \omega^2 \mathbf{B}(\mathbf{x}, \omega) = \nabla \times \left[\frac{1}{\varepsilon}\mathbf{J}(\mathbf{x}, \omega)\right], \tag{2.11}$$

where ε is the permittivity of the medium (where no specific functional dependence is yet attached to this quantity). [Technically, Eq. 2.11 can only be obtained by assuming a linear constitutive relationship between $\mathbf{D}$ and $\mathbf{E}$, i.e., $\mathbf{D}(\mathbf{x},\omega) = \varepsilon\mathbf{E}(\mathbf{x},\omega)$.] Equations 2.10 and 2.11 are known as the (inhomogeneous) vector wave equations, and they automatically satisfy Eqs. 2.8 and 2.9.

If the system is invariant along an axis, which herein will be taken to be the z-axis, Eqs. 2.10 and 2.11 can be simplified to (inhomogeneous) scalar wave equations,

$$\left[\frac{\partial}{\partial x}\left(\frac{1}{\mu}\frac{\partial}{\partial x}\right)+\frac{\partial}{\partial y}\left(\frac{1}{\mu}\frac{\partial}{\partial y}\right)\right]E_z(\mathbf{x},\omega)+\omega^2 D_z(\mathbf{x},\omega)=i\omega J_z(\mathbf{x},\omega) \tag{2.12}$$

$$\begin{aligned}&\left[\frac{\partial}{\partial x}\left(\frac{1}{\varepsilon}\frac{\partial}{\partial x}\right)+\frac{\partial}{\partial y}\left(\frac{1}{\varepsilon}\frac{\partial}{\partial y}\right)\right]H_z(\mathbf{x},\omega)+\omega^2 B_z(\mathbf{x},\omega)\\ &\qquad=-\frac{\partial}{\partial x}\left[\frac{1}{\varepsilon}J_y(\mathbf{x},\omega)\right]+\frac{\partial}{\partial y}\left[\frac{1}{\varepsilon}J_x(\mathbf{x},\omega)\right],\end{aligned} \tag{2.13}$$

where the electromagnetic field is completely defined by the z-component. Equations 2.12 and 2.13 correspond to two distinct sets of polarization, one where the x and y-components of $\mathbf{E}(\mathbf{x},\omega)$ and $\mathbf{D}(\mathbf{x},\omega)$ are transverse to the z-axis, called TE_z polarization (Transverse Electric to z), Eq. 2.12, and one where the x and y-components of $\mathbf{H}(\mathbf{x},\omega)$ and $\mathbf{B}(\mathbf{x},\omega)$ are transverse to the z-axis, called TM_z polarization (Transverse Magnetic to z), Eq. 2.13.

2.2 Boundary Conditions

Many functions satisfy Maxwell's equations. However, the physical solution also satisfies boundary conditions. For example, at the interface between two media, the electromagnetic fields must satisfy four field continuity conditions,

$$\hat{n}\times(\mathbf{E}_1-\mathbf{E}_2)=0 \tag{2.14}$$

$$\hat{n}\cdot(\mathbf{D}_1-\mathbf{D}_2)=\rho_S \tag{2.15}$$

$$\hat{n}\times(\mathbf{H}_1-\mathbf{H}_2)=\mathbf{J}_S \tag{2.16}$$

$$\hat{n}\cdot(\mathbf{B}_1-\mathbf{B}_2)=0 \tag{2.17}$$

where the subscripts 1 and 2 denote different mediums, $\hat{n}$ is a unit vector normal to the interface pointing from medium 2 into 1, and ρ_S and $\mathbf{J}_S$ are the surface charge and electric current densities, respectively. The boundary conditions are greatly simplified when one of the mediums cannot sustain internal fields, known as a perfect electric conductor (PEC),

$$\hat{n}\times\mathbf{E}=0 \tag{2.18}$$

$$\hat{n} \cdot \mathbf{B} = 0 \tag{2.19}$$

where $\mathbf{E}$ and $\mathbf{B}$ are the exterior fields, and $\hat{n}$ points away from the surface. Note that, in this case, the boundary can always support surface charge and current densities,

$$\hat{n} \cdot \mathbf{D} = \rho_S \tag{2.20}$$

$$\hat{n} \times \mathbf{H} = \mathbf{J}_S. \tag{2.21}$$

2.3 The Dielectric Function

As mentioned in Sect. 2.1, before Maxwell's equations (in any form) can be solved, relationships between $\mathbf{B}$ and $\mathbf{H}$ as well as $\mathbf{D}$ and $\mathbf{E}$ are needed. The former was already given, and thus (herein) the latter describes completely how a system responds to light. In the most general case

$$\mathbf{D}(\mathbf{x}, \omega) = \varepsilon_0 \int d\mathbf{x}' \varepsilon(\mathbf{x}, \mathbf{x}', \omega) \mathbf{E}(\mathbf{x}', \omega), \tag{2.22}$$

where $\varepsilon(\mathbf{x}, \mathbf{x}', \omega)$ is a spatially dependent and frequency dispersive relative dielectric function and ε_0 is the vacuum permittivity. Thus, the optical response of a material is described through $\varepsilon(\mathbf{x}, \mathbf{x}', \omega)$, and $\mathbf{D}(\mathbf{x}, \omega)$ can be considered a generalized $\mathbf{E}(\mathbf{x}, \omega)$ that contains information on both the incident $\mathbf{E}(\mathbf{x}, \omega)$ and that due to polarization of the material.

The approximation $\varepsilon(\mathbf{x}, \mathbf{x}', \omega) \approx \varepsilon(\omega)\delta(\mathbf{x} - \mathbf{x}')$ corresponds to local electrodynamics, where only ω is variable. Such an approximation is valid for large structures (those with features greater than ~ 10 nm), and is made for the first portion of this dissertation. The more rigorous case is the subject of Chap. 8.

For a lot of materials at the nanoscale, the dielectric function depends on ω (i.e., with respect to ω, the material is dispersive). For metals like Au and Ag, $\varepsilon(\omega)$ is well described in the classical continuum limit (i.e., many hundreds of atoms or more) by three separate components,

$$\varepsilon(\omega) = \varepsilon_\infty + \varepsilon_{\text{inter}}(\omega) + \varepsilon_{\text{intra}}(\omega) \tag{2.23}$$

the value as $\omega \to \infty$, ε_∞, the interband contribution from *d*-band to *sp*-band (conduction band) electron transitions, $\varepsilon_{\text{inter}}(\omega)$, and a contribution due to excitations of the *sp*-band electrons, $\varepsilon_{\text{intra}}(\omega)$.

$\varepsilon_{\text{inter}}(\omega)$ can be physically described using a multipole Lorentz oscillator model [5],

$$\varepsilon_{\text{inter}}(\omega) = \sum_n \frac{\omega_{\text{L}n}^2 \Delta\varepsilon_{\text{L}n}}{\omega(\omega + i2\delta_{\text{L}n}) - \omega_{\text{L}n}^2} \tag{2.24}$$

where n is an index labeling the individual d-band to sp-band electron transitions occurring at ω_{Ln}, $\Delta\varepsilon_{Ln}$ is the shift in relative permittivity at the transition, and δ_{Ln} is the electron dephasing rate. Because the primary focus in this work is on Ag and Au, n is taken to be two, since there are two interband transitions in Au at optical frequencies (near 3 and 4 eV [3]), and only one in Ag (near 3.8 eV, which both poles thus describe).

$\varepsilon_{\text{intra}}(\omega)$ is responsible for the plasmonic optical response of metals, and can be described by the Drude model [5],

$$\varepsilon_{\text{intra}}(\omega) = -\frac{\omega_{\text{D}}^2}{\omega(\omega + i\gamma)} \tag{2.25}$$

where ω_{D} is the plasma frequency and γ is the collision frequency.

Combined, Eqs. 2.23–2.25 correspond to a Drude plus two Lorentz pole oscillator (D2L) dielectric model. The common method to use the D2L model is to fit it to experimentally determined bulk dielectric data (using simulated annealing, for example). For Ag and Au, two of the most common experimental data sets, and which will be used in this work, are those of Johnson and Christry (JC) [3] and Lynch and Hunter (LH) [4]. The D2L model often describes the empirical data well, with only negligible differences.

The use of models for ε is advantageous for a number of reasons. First of all, it allows separation of the different effects in the optical response of a material. For example, physical insight can be obtained into the conduction band electron motion separate from that of the interband transitions. (This issue will be revisited in Chap. 8.) Furthermore, such models are common with time-domain computational methods, such as FDTD (see Sect. 3.2), since the frequency-domain data cannot be used directly. For frequency-domain methods, however, the empirically determined dielectric data can be used directly. Although, in this work, even these methods rely on the D2L model, primarily to create a cohesiveness throughout the work, but also because of the other advantages discussed.

Throughout this work, various D2L fits are used for Ag and Au (for one reason or another), as well as other materials. The D2L parameters used for all calculations have been tabulated in Appendix B.

References

1. Jackson JD (1998) Classical electrodynamics, 3rd edn. Wiley, New York
2. Schwartz M (1987) Principles of electrodynamics, 1st edn. Dover, New York
3. Johnson PB, Christy RW (1972) Optical constants of the noble metals. Phys Rev B 6: 4370–4379
4. Lynch DW, Hunter WR (1985) Comments on the optical constants of metals and an introduction to the data for several metals. In: Palik ED (ed) Handbook of optical constants of solids. Academic Press, Orlando, pp 275–368
5. Bohren CF, Huffman DR (1983) Absorption and scattering of light by small particles. Wiley, New York

Chapter 3
Theoretical and Computational Methods

Preface

The content that appears in this chapter has been largely adapted from the following publications:

Zhao J, Pinchuk AO, McMahon JM, Li S, Ausman LK, Atkinson AL, Schatz GC (2008) Methods for describing the electromagnetic properties of silver and gold nanoparticles. Acc Chem Res 41:1710–1720. doi:10.1021/ar800028j

Atkinson AL, McMahon JM, Schatz GC (2009) FDTD studies of metallic nanoparticle systems. In: Self organization of molecular systems, from molecules and clusters to nanotubes and proteins. NATO science for peace and security series A: chemistry and biology. Springer, Netherlands. doi:10.1007/978-90-481-2590-6

McMahon JM, Gray SK, Schatz GC (2009) A discrete action principle for electrodynamics and the construction of explicit symplectic integrators for linear, non-dispersive media. J Comp Phys 228:3421–3432. doi:10.1016/j.jcp.2009.01.019

McMahon JM, Gray SK, Schatz GC (2011) Surface nanophotonics theory. In: Wiederrecht G (ed) Comprehensive nanoscience and technology. Elsevier, Amsterdam

In this chapter, only the 3D variants of FDTD and FEM are presented. It is straightforward to adapt these formulations to 2D (or even 1D). The interested reader (either in these lower dimensional formulations, or on the methods in general) is referred to Refs. [1–6].

Most codes that are outlined here, and used throughout this dissertation, are freely available on the author's personal website: http://www.thecomputationalphysicist.com.

J. M. McMahon, *Topics in Theoretical and Computational Nanoscience*, Springer Theses, DOI: 10.1007/978-1-4419-8249-0_3,

3.1 Introduction

Analytical solutions to Maxwell's equations (Chap. 2) only exist for the most basic systems. For example, Mie theory [7] can be used to analytically describe the relationship between the optical response, dielectric environment, and size (and shape) of spherical (or spheroidal) particles [8], including multilayer ones [9]. Analytical solutions also exist also for planar surfaces and multilayer films [10]. However, for more complex shapes, analytical descriptions or simplifying approximations to these equations do not exist, and even predicting their solution(s) can be challenging. In these cases, numerical methods must be used.

Two of the most popular, and generally applicable methods to solve Maxwell's equations (which are heavily used in this dissertation) will be discussed in this chapter, FDTD [5] and FEM [6]. While useful because they are entirely general (i.e, not specific to a particular problem), both of them can be computationally demanding (especially the former). Fortunately, more efficient methods are available for some specific problems. For example, for periodically modulated films, the rigorous coupled-wave analysis (RCWA) can be used, and for an isolated slit in a metal film, an electrodynamic mode (modal) expansion is possible. These methods are also used throughout this dissertation, and will be briefly outlined in this chapter as well.

All computational methods have drawbacks, such as the efficiency that was discussed above. For example, in all time-domain methods (even those outside of electrodynamics), one of the most important issues is the technique used to approximate the time derivatives in Eqs. 2.1 and 2.2. This approximation is responsible for the accuracy of the numerical solution as it evolves in time. Developing high-accuracy approximations to these derivatives is challenging, because mathematically better approximations often end up degrading the physical solution (even dynamical invariants), such as dissipating the energy density of an electromagnetic wave in free space. A general method to approximate the time derivatives in Eqs. 2.1 and 2.2 to arbitrary accuracy, while also preserving the dynamical invariants of the problem (e.g., the energy density), is presented in Sect. 3.3. This topic is relatively stand-alone in this dissertation (and in the grand context of this work), and not a lot will be lost if it is skipped (e.g., a chemist may find little interest in this). However, the interested reader (most likely an electrical engineer, or someone interested in the theory of numerical analysis) is encouraged to read it.

3.2 The Finite-Difference Time-Domain Method

The most popular general purpose method is the Finite-Difference Time-Domain (FDTD) method [5, 11]. FDTD explicitly solves the time-domain Maxwell–Ampère law and Faraday's law in differential forms, Eqs. 2.1 and 2.2. Because it

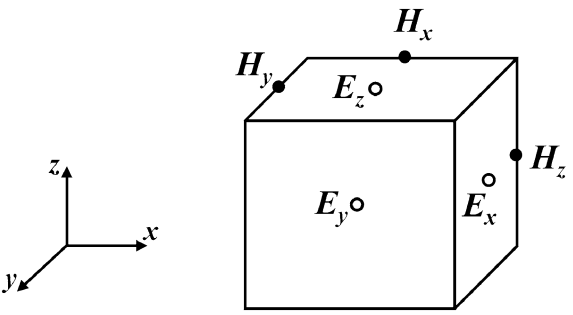

Fig. 3.1 Yee spatial-lattice used in the FDTD method

solves these equations directly [as well as Eqs. 2.3 and 2.4 implicitely—vide infra], FDTD is considered nominally exact. In the most popular version of this method [5], the computational domain is discretized using a grid (often Cartesian, with spacings of Δx, Δy, and Δz), and the partial derivatives are approximated using central finite-difference expressions derived from Taylor expansions (which are second-order accurate—i.e., the truncation errors are of higher order than two). See Appendix A.2 for a brief introduction to finite-differences.

Even though only Eqs. 2.1 and 2.2 are explicitly solved, special care must be taken in order to satisfy Gauss' laws, Eqs. 2.3 and 2.4. One way to do this, suggested by Yee in his seminal paper [11], is (using a Cartesian grid) to shift all of the field components by half of a grid spacing relative to each other, known as the Yee spatial-lattice; see Fig. 3.1. For a proof of this result, see Ref. [5].

To obtain second-order accuracy in the temporal derivatives of Eqs. 2.1 and 2.2, $\mathbf{E}(\mathbf{x}, t)$ and $\mathbf{H}(\mathbf{x}, t)$ [note that in the common formulation of FDTD, $\mathbf{H}(\mathbf{x}, t)$ is worked with directly, instead of $\mathbf{B}(\mathbf{x}, t)$] are defined on time grids shifted by Δt. In Eq. 2.1, for example, the time derivative of $\mathbf{E}(\mathbf{x}, t)$ therefore "leaps over" the spatial derivatives of $\mathbf{H}(\mathbf{x}, t)$, known as a leap-frog algorithm (vide infra).

Using the Yee spatial-lattice (Fig. 3.1) and second-order accurate central finite-differences (in both the time and spatial derivatives), approximations to Eqs. 2.1 and 2.2 become

$$\varepsilon_{i+1/2,j,k}\frac{\mathrm{E}^{n+1/2}_{x\,i+1/2,j,k}-\mathrm{E}^{n-1/2}_{x\,i+1/2,j,k}}{\Delta t}+\mathrm{J}^{n}_{x\,i+1/2,j,k}$$
$$=\frac{\mathrm{H}^{n}_{z\,i+1/2,j+1/2,k}-\mathrm{H}^{n}_{z\,i+1/2,j-1/2,k}}{\Delta y}-\frac{\mathrm{H}^{n}_{y\,i+1/2,j,k+1/2}-\mathrm{H}^{n}_{y\,i+1/2,j,k-1/2}}{\Delta z} \tag{3.1}$$

$$\varepsilon_{i,j+1/2,k}\frac{\mathrm{E}^{n+1/2}_{y\,i,j+1/2,k}-\mathrm{E}^{n-1/2}_{y\,i,j+1/2,k}}{\Delta t}+\mathrm{J}^{n}_{y\,i,j+1/2,k}$$
$$=\frac{\mathrm{H}^{n}_{x\,i,j+1/2,k+1/2}-\mathrm{H}^{n}_{x\,i,j+1/2,k-1/2}}{\Delta z}-\frac{\mathrm{H}^{n}_{z\,i+1/2,j+1/2,k}-\mathrm{H}^{n}_{z\,i-1/2,j+1/2,k}}{\Delta x} \tag{3.2}$$

$$\varepsilon_{i,j,k+1/2}\frac{\mathrm{E}^{n+1/2}_{z\,i,j,k+1/2}-\mathrm{E}^{n-1/2}_{z\,i,j,k+1/2}}{\Delta t}+\mathrm{J}^{n}_{z\,i,j,k+1/2}$$
$$=\frac{\mathrm{H}^{n}_{y\,i+1/2,j,k+1/2}-\mathrm{H}^{n}_{y\,i-1/2,j,k+1/2}}{\Delta x}-\frac{\mathrm{H}^{n}_{x\,i,j+1/2,k+1/2}-\mathrm{H}^{n}_{x\,i,j-1/2,k+1/2}}{\Delta y} \tag{3.3}$$

$$\mu_{i,j+1/2,k+1/2}\frac{\mathrm{H}^{n+1}_{x\,i,j+1/2,k+1/2}-\mathrm{H}^{n}_{x\,i,j+1/2,k+1/2}}{\Delta t}$$
$$=\frac{\mathrm{E}^{n+1/2}_{y\,i,j+1/2,k+1}-\mathrm{E}^{n+1/2}_{y\,i,j+1/2,k}}{\Delta z}-\frac{\mathrm{E}^{n+1/2}_{z\,i,j+1,k+1/2}-\mathrm{E}^{n+1/2}_{z\,i,j,k+1/2}}{\Delta y} \tag{3.4}$$

$$\mu_{i+1/2,j,k+1/2}\frac{\mathrm{H}^{n+1}_{y\,i+1/2,j,k+1/2}-\mathrm{H}^{n}_{y\,i+1/2,j,k+1/2}}{\Delta t}$$
$$=\frac{\mathrm{E}^{n+1/2}_{z\,i+1,j,k+1/2}-\mathrm{E}^{n+1/2}_{z\,i,j,k+1/2}}{\Delta x}-\frac{\mathrm{E}^{n+1/2}_{x\,i+1/2,j,k+1}-\mathrm{E}^{n+1/2}_{x\,i+1/2,j,k}}{\Delta z} \tag{3.5}$$

$$\mu_{i+1/2,j+1/2,k}\frac{\mathrm{H}^{n+1}_{z\,i+1/2,j+1/2,k}-\mathrm{H}^{n}_{z\,i+1/2,j+1/2,k}}{\Delta t}$$
$$=\frac{\mathrm{E}^{n+1/2}_{x\,i+1/2,j+1,k}-\mathrm{E}^{n+1/2}_{x\,i+1/2,j,k}}{\Delta y}-\frac{\mathrm{E}^{n+1/2}_{y\,i+1,j+1/2,k}-\mathrm{E}^{n+1/2}_{y\,i,j+1/2,k}}{\Delta x}. \tag{3.6}$$

Equations 3.1–3.6 can be solved by discretizing a domain, specifying ε and μ at the discrete grid points, and sequentially solving Eqs. 3.1–3.3 and then (3.4–3.6). Note that 2D equations can be derived from Eqs. 3.1–3.6 by dropping all derivatives with respect to the invariant z-axis (which split into independent TE_z and TM_z modes).

3.2.1 Practical Issues

Before FDTD can be used in practice, (exterior) boundary conditions must be applied and initial waves of arbitrary form must be introduced into the system. Additionally, to model dispersive materials, the equations must be modified. These issues are discussed in this subsection.

Boundary Conditions

FDTD can be used to study periodic systems by modeling only a single unit cell and truncating the domain using periodic boundary conditions. Even when simulating infinite domains, the computational domain must be truncated. However, many techniques have been developed to mimic open regions of space. One of the most successful techniques is to truncate the domain with artificial materials that

absorb nearly all incident waves, called perfectly matched layers (PML) [12]. An efficient and accurate way of implementing PML with the Yee spatial-lattice is to use convolutional PML (CPML) [13]. The implementation of CPML involves stretching the spatial derivatives and superimposing time-dependent two-component functions onto them. A brief introduction to the implementation of CPML is provided in Sect. 3.3.5 and Ref. [14], and a more complete discussion of PML, including CPML, can be found in Ref. [15]. These techniques were used for all of the FDTD calculations in this dissertation, unless otherwise specified.

Initial Conditions

Given suitable initial conditions defined everywhere in the computational domain, Eqs. 3.1–3.6 will properly evolve the fields according to Eqs. 2.1–2.4. However, defining computational domains for initial conditions with a large spatial extent is often inefficient and unnecessary. A more efficient technique to introduce fields into the computational domain, particularly with the Yee spatial-lattice, is to use the total-field–scattered-field (TF–SF) technique [15–17]. The implementation of this involves splitting the domain into two regions, an interior total-field region and an exterior scattered-field region. The FDTD method is applied directly in each region without modification. However, near the boundaries, where the spatial derivatives extend into both regions, the fields are modified using the (known) incident field so that all equations are consistent.

The TF–SF technique was used for all of the FDTD calculations in this dissertation, unless otherwise specified. Additionally, in order to obtain accurate Fourier-transformed fields necessary for field (intensity) profiles and optical responses (see Sect. 2), incident Gaussian-damped sinusoidal pulses containing frequency content over the range(s) of interest were used, and simulations were carried out to at least 100 fs.

Dispersive Materials

Equations 3.1–3.6 only apply to regions of non-dispersive materials. Dispersive materials, such as Au and Ag, can be modeled using a modified set of FDTD equations, where the frequency-dependent response is modeled in the time-domain using equivalent current densities that are updated self consistently with the normal FDTD equations. This is known as the auxiliary differential equation (ADE) method [5, 18, 19]. In this approach, a model for the dispersive material is chosen (e.g., the D2L model), inserted into the Maxwell–Ampère law in the frequency-domain (Eq. 2.6), and the resulting equation is Fourier-transformed to the time-domain to obtain a modified equation that can be used in FDTD. An example of such a procedure (albeit with a slightly more complicated dielectric function that depends on both ω and $\mathbf{k}$), is given in Chap. 8 and Appendix E.

For the D2L model in Eqs. 2.23–2.25, the modified Maxwell–Ampère law in time-discretized form is

$$C_1\mathbf{E}(\mathbf{x})^{n+1/2} = C_2\mathbf{E}(\mathbf{x})^{n-1/2} + C_3\mathbf{E}(\mathbf{x})^{n-3/2} + \nabla\times\mathbf{H}(\mathbf{x})^n - \frac{1}{2}\Bigg\{(1+\kappa_\mathrm{D})\mathbf{J}(\mathbf{x})_\mathrm{D}^{n-1/2} + \sum_{m=1}^{2}\left[(1+\alpha_{\mathrm{L}m})\mathbf{J}(\mathbf{x})_{\mathrm{L}m}^{n-1/2} + \zeta_{\mathrm{L}m}\mathbf{J}(\mathbf{x})_{\mathrm{L}m}^{n-3/2}\right]\Bigg\}, \tag{3.7}$$

where

$$C_1 = \frac{\varepsilon_0\varepsilon_\infty}{\Delta t} + \frac{1}{2}\beta_\mathrm{D} + \frac{1}{4\Delta t}\sum_{m=1}^{2}\gamma_{\mathrm{L}m} \tag{3.8}$$

$$C_2 = \frac{\varepsilon_0\varepsilon_\infty}{\Delta t} - \frac{1}{2}\beta_\mathrm{D} \tag{3.9}$$

$$C_3 = \frac{1}{4\Delta t}\sum_{m=1}^{2}\gamma_{\mathrm{L}m} \tag{3.10}$$

$$\kappa_\mathrm{D} = \frac{1-\gamma_\mathrm{D}\Delta t/2}{1+\gamma_\mathrm{D}\Delta t/2} \tag{3.11}$$

$$\beta_\mathrm{D} = \frac{\omega_D^2\varepsilon_0\Delta t/2}{1+\gamma_\mathrm{D}\Delta t/2} \tag{3.12}$$

$$\alpha_{\mathrm{L}m} = \frac{2-\omega_{\mathrm{L}m}^2\Delta t^2}{1+\delta_{\mathrm{L}m}\Delta t} \tag{3.13}$$

$$\zeta_{\mathrm{L}m} = \frac{\delta_{\mathrm{L}m}\Delta t - 1}{\delta_{\mathrm{L}m}\Delta t + 1} \tag{3.14}$$

$$\gamma_{\mathrm{L}m} = \frac{\varepsilon_0\Delta\varepsilon_{\mathrm{L}m}\omega_{\mathrm{L}m}^2\Delta t^2}{1+\delta_{\mathrm{L}m}\Delta t}, \tag{3.15}$$

and the summations over the Lorentz poles use the index m rather than n (as in other chapters) to avoid confusion with the time-step superscript. Equation 3.7 is updated analogously to Eqs. 3.1–3.6, and the equivalent current densities, $\mathbf{J}(\mathbf{x})_\mathrm{D}$ and $\mathbf{J}(\mathbf{x})_{\mathrm{L}m}$, are updated using the ADEs

$$\mathbf{J}(\mathbf{x})_\mathrm{D}^{n+1/2} = \kappa_\mathrm{D}\mathbf{J}(\mathbf{x})_\mathrm{D}^{n-1/2} + \beta_\mathrm{D}\left[\mathbf{E}(\mathbf{x})^{n+1/2} + \mathbf{E}(\mathbf{x})^{n-1/2}\right] \tag{3.16}$$

$$\mathbf{J}(\mathbf{x})_{\mathrm{L}m}^{n+1/2} = \alpha_{\mathrm{L}m}\mathbf{J}(\mathbf{x})_{\mathrm{L}m}^{n-1/2} + \zeta_{\mathrm{L}m}\mathbf{J}(\mathbf{x})_{\mathrm{L}m}^{n-3/2} + \gamma_{\mathrm{L}m}\left(\frac{\mathbf{E}(\mathbf{x})^{n+1/2} - \mathbf{E}(\mathbf{x})^{n-3/2}}{2\Delta t}\right). \tag{3.17}$$

3.2.2 Optical Responses

The optical properties of most of the nanostructures in this work were determined from intensity profiles of the electromagnetic fields (often at a particular ω), or from their optical cross sections [8] (i.e., the amount of power absorbed and/or scattered relative to the incident light). The former can be calculated by straightforward Fourier transform (by using a discrete version of that given in Appendix A.1), and the latter can be calculated by integrating the outward power flow over a closed perimeter or surface encompassing the structure (the flux) [8, 20], as outlined below.

The absorption cross section σ_{abs} is defined as

$$\sigma_{\text{abs}} = \frac{P_{\text{abs}}(\omega)}{I_{\text{inc}}(\omega)}, \tag{3.18}$$

where $P_{\text{abs}}(\omega)$ is the absorbed power per unit area and $I_{\text{inc}}(\omega)$ is the magnitude of the incident power. $P_{\text{abs}}(\omega)$ can be defined in terms of the time-averaged Poynting vector associated with the total fields, $\mathbf{S}(\mathbf{x}, \omega)$,

$$P_{\text{abs}}(\omega) = \oint_S dS\, \mathbf{S}(\mathbf{x}, \omega) \cdot \hat{\mathbf{n}} \tag{3.19}$$

$$\mathbf{S}(\mathbf{x}, \omega) = \frac{1}{2}\Re[\mathbf{E}(\mathbf{x}, \omega) \times \mathbf{H}(\mathbf{x}, \omega)^*] \tag{3.20}$$

where the closed surface integral encompasses the structure and * denotes complex conjugation. The scattering cross section σ_{sc} can be calculated analogously by using the scattered fields, and the extinction cross section is the sum of the two, $\sigma_{\text{ext}} = \sigma_{\text{abs}} + \sigma_{\text{sc}}$.

3.2.3 Advantages and Disadvantages

There are many advantages to FDTD. One is the simple and straightforward formulation, as outlined in Eqs. 3.1–3.6. Perhaps the biggest advantage though is its applicability to a wide range of problems. Any structure can be modeled by simply specifying ε and μ (possibly dispersive, using the ADE technique) over a computational domain (periodic or nonperiodic), and arbitrary incident fields (or other excitation sources) can be easily inserted into the simulations (using the TF–SF technique). Because of these advantages, FDTD has been used to model a number of systems in nanoscience (and other areas), from small to large nanostructures [20–23] and to periodic systems [24–29].

However, there are disadvantages. First of all, the computational domain must be discretized using a grid, which leads to geometrical modeling errors, termed "staircasing errors" (the grid causes geometries to look like a staircase). This can, if one is not careful, render the fields close to the surface of a structure inaccurate.

Moreover, FDTD is computationally inefficient. For example, in order to model fine details, small grid spacings have to be used. However, this means that small grid spacings must be used throughout the entire computational domain (in general), which can be very computationally demanding.

3.3 A Discrete Action Principle for Electrodynamics and the Construction of Explicit Symplectic Integrators

Before beginning this section, it should be mentioned that most of the theoretical background for this work is outside the scope of this dissertation. Such topics include the potential form of Maxwell's equations and gauge invariance, the principle of least action, and Lagrangian mechanics. These topics will not be discussed in detail, and the interested reader is instead referred to Refs. [30, 31]. Additionally, the relevant concepts, and work herein, may not be of interest to most chemists (these topics are most likely of interest to a physicist, electrical engineer, or numerical analyst), and skipping this section will not deter one from the rest of the work in this dissertation. Nonetheless, it does represent a thought-provoking exercise as to the appropriate way to integrate Maxwell's equations in time, and also discusses fundamental issues that are encountered in most numerical methods. Therefore, the author encourages the reader to explore this section.

In this section, a discrete action principle for electrodynamics is derived that can be used to construct explicit symplectic integrators for Maxwell's equations. Different integrators are constructed depending on the choice of discrete Lagrangian used to approximate the action. By combining discrete Lagrangians in an explicit symplectic partitioned Runge–Kutta method, an integrator capable of achieving any order of accuracy is obtained. Using the von Neumann stability analysis, it is shown that the integrators greatly increase the numerical stability and reduce the numerical dispersion compared to other methods. For practical purposes, it is demonstrated how to implement the integrators using many techniques used in FDTD. However, this approach is also applicable to other spatial discretizations, such as those used in finite element methods. Using this implementation, numerical examples are presented that demonstrate the ability of the integrators to efficiently reduce and maintain a minimal amount of numerical dispersion, particularly when the time-step is less than the stability limit. The integrators are therefore advantageous for modeling large, inhomogeneous computational domains.

3.3.1 Introduction

Many numerical methods have been developed to simulate the dynamics of electromagnetic fields, such as the FDTD method (discussed in Sect. 3.2) [5, 11] and time-domain FEM (TD-FEM) (the analogous frequency-domain formulation is

discussed in Sect. 3.4) [6]. Typically these methods integrate Maxwell's equations by approximating the time derivatives with second-order accurate Taylor expansions. These integration methods, along with the spatial discretization, can lead to a significant amount of numerical dispersion [5, 6], where waves propagate with a wavelength-dependent velocity through the computational domain. This causes phase errors, pulse broadening, as well as other problems. In order to reduce the numerical dispersion, higher-order approximations to the derivatives are often used. In the context of FDTD, these methods are typically applied to the spatial derivatives [32]. However, they can also be applied to the time derivatives [33], as long as care is taken so that the dynamical invariants of the problem (e.g. the energy density) are preserved. One type of time-integrator that preserves dynamical invariants up to a desired order of accuracy is a symplectic integrator (SI) [34–47]. SIs for Maxwell's equations have appeared before [48–50] in the context of Hamiltonian mechanics. Some of these schemes have been derived using a "helicity" Hamiltonian [51], which is not the physical energy density, but nonetheless is equivalent to Maxwell's equations. However, it is of interest to develop numerical approaches based on physical premises so they can be easily extended to more complex situations, such as the coupling of electromagnetics with quantum mechanics [52]. Another scheme [49] was derived using a physical Hamiltonian. However, the SIs developed have limited applicability due to the constraints imposed on the Hamiltonian.

In this section, a different approach is taken, and Lagrangian mechanics is used to derive a discrete action principle for electrodynamics that can be used to construct a variety of SIs. This approach is based on the discrete variational integration ideas developed by Marsden and West [53], which have recently been applied by Qin and Guan to describe charged particle motion in magnetic fields [54]. Their ideas are extended from particle Lagrangian mechanics to a field theory in terms of a Lagrangian density [35]. The physically correct Lagrangian density is then used to develop SIs for a larger class of problems in electrodynamics than possible using previous approaches. Even though the Lagrangian density is in terms of potentials, it is shown that the integrators, after construction, can easily be expressed and implemented entirely in terms of fields.

The structure of this section is as follows. In Sect. 3.2.2, Maxwell's equations are reviewed in terms of potentials, and the discrete action principle is extended to a field theory. In Sect. 3.3.3, SIs for Maxwells equations are constructed, including an integrator capable of achieving any order of accuracy. The numerical stability and dispersion of the SIs are analyzed in Sect. 3.3.4. Practical implementation of the SIs using FDTD techniques is discussed in Sect. 3.3.5. In Sect. 3.3.6, numerical examples are presented. A summary and outlook are given in Sect. 3.3.7.

3.3.2 The Discrete Action Principle for Electrodynamics

The dynamics of electromagnetic fields are described by Maxwell's equations, which, in the time domain, are given by Eqs. 2.1–2.4. Lagrangian mechanics can

also be used to describe the dynamics, by using the vector $[\mathbf{A}(\mathbf{x},t)]$ and scalar $[\phi(\mathbf{x},t)]$ potentials, which are related to $\mathbf{E}(\mathbf{x},t)$ and $\mathbf{B}(\mathbf{x},t)$ by

$$\mathbf{B}(\mathbf{x},t) = \nabla \times \mathbf{A}(\mathbf{x},t) \tag{3.21}$$

$$\mathbf{E}(\mathbf{x},t) = -\frac{\partial}{\partial t}\mathbf{A}(\mathbf{x},t) - \nabla\phi(\mathbf{x},t). \tag{3.22}$$

In the remainder of this section, the $\mathbf{x}$ and t dependencies (or discrete analogues) are assumed in all quantities, and are not shown explicitely for clarity. The Lagrangian density, $\mathcal{L}$, for the electromagnetic field can be expressed as

$$\mathcal{L} = \frac{\varepsilon}{2}\mathbf{E}\cdot\mathbf{E} - \frac{1}{2\mu}\mathbf{B}\cdot\mathbf{B} + \mathbf{J}\cdot\mathbf{A} - \rho\phi \tag{3.23}$$

or

$$\mathcal{L} = \frac{\varepsilon}{2}\left|-\frac{\partial}{\partial t}\mathbf{A} - \nabla\phi\right|^2 - \frac{1}{2\mu}|\nabla\times\mathbf{A}|^2 + \mathbf{J}\cdot\mathbf{A} - \rho\phi, \tag{3.24}$$

where $\mathcal{L}$ is a function of $\mathbf{A}$, $\partial\mathbf{A}/\partial t$, and ϕ. It is important to note that $\mathcal{L}$, as written, does not contain a conjugate momentum to ϕ, $\partial\phi/\partial t$, which arises by fixing the gauge (for certain choices) [31], and would be necessary in order to develop an integrator in terms of potentials. However, the desired integrators are in terms of gauge-invariant fields, and therefore this step is unnecessary (see Sect. 3.3.3). Equations 2.1 and 2.2 arise from requiring that the action be stationary,

$$\delta \int dt \int d\mathbf{x}\, \mathcal{L} = 0 \tag{3.25}$$

where x, y, z, and t are independent variables, and variations are taken with respect to ϕ (and $\partial\phi/\partial t$ for certain gauge choices), each component of $\mathbf{A}$ and $\partial\mathbf{A}/\partial t$, and the spatial derivatives that enter into $\nabla\phi$ and $\nabla\times\mathbf{A}$.

Marsden and West showed that, given a suitable Lagrangian, it is possible to form a symplectic integration scheme based on a discrete form of the action principle [53]. Their development was in terms of particle Lagrangian mechanics, but it is straightforwardly generalized to a field theory using a Lagrangian density as follows. Equation 3.25 is first approximated as

$$\delta \sum_n \int d\mathbf{x}\, \mathcal{L}_d(n, n+1) = 0, \tag{3.26}$$

where $L_d(n, n+1)$ is an approximation to the time integral of Eq. 3.24 over a small time interval, h, from time $t = t_n$ to $t_n + h$,

$$\mathcal{L}_d(n, n+1) \approx \int_{t_n}^{t_n+h} dt\, \mathcal{L}. \tag{3.27}$$

Within each interval, the functions to be varied are ϕ and the components of $\mathbf{A}$ at times t_n and $t_n + h$, which can be denoted by ϕ^n, ϕ^{n+1}, $\mathbf{A}^n$, and $\mathbf{A}^{n+1}$, as well as the spatial derivatives that enter into $\nabla\phi^n$, $\nabla\phi^{n+1}$, $\nabla \times \mathbf{A}^n$, and $\nabla \times \mathbf{A}^{n+1}$. All variations are treated in the standard manner of variational calculus. The components $\mathbf{A}^n$ and $\mathbf{A}^{n+1}$ allow $\partial\mathbf{A}/\partial t$ to be approximated by relating each of the components of $\delta\mathbf{A}^{n+1}$ to $\delta\mathbf{A}^n$ (and similarly for ϕ for certain gauge choices). Requiring that the variation with respect to A_α be zero, where $\alpha = x$, y, or z, leads to

$$\frac{\delta}{\delta A_\alpha^n}\mathcal{L}_d(n, n+1) + \frac{\delta}{\delta A_\alpha^n}\mathcal{L}_d(n-1, n) = 0, \tag{3.28}$$

where variational derivatives are involved,

$$\frac{\delta}{\delta A_\alpha^n}\mathcal{L}_d(n, n+1) = \frac{\partial}{\partial A_\alpha^n}\mathcal{L}_d(n, n+1) - \sum_\beta \frac{\partial}{\partial \beta}\frac{\partial}{\left(\partial A_\alpha^n/\partial\beta\right)}\mathcal{L}_d(n, n+1) \tag{3.29}$$

where $\beta = x$, y, or z. It is not hard to show that Eq. 3.28 remains satisfied in the course of time iterations $n = 0, 1, \ldots$ if the variables

$$P_\alpha^n = -\frac{\delta}{\delta A_\alpha^n}\mathcal{L}_d(n, n+1) \tag{3.30}$$

and

$$P_\alpha^{n+1} = \frac{\delta}{\delta A_\alpha^{n+1}}\mathcal{L}_d(n, n+1) \tag{3.31}$$

are the discrete momenta canonically conjugate to A_α. Equations 3.30 and 3.31 can be used to generate SIs, and are analogous to the equations developed by Marsden and West [53], except that they include functional derivatives.

3.3.3 Symplectic Integrators

SIs can be constructed in many ways using the ideas presented in Sect. 3.3.2. One method is to choose a form for the discrete Lagrangian, the simplest of which for Eq. 3.24 is

$$\mathcal{L}_d(n, n+1) = h\left(\frac{\varepsilon}{2}\left|\frac{\mathbf{A}^{n+1} - \mathbf{A}^n}{h} + \nabla\phi^{n+1}\right|^2 - \frac{1}{2\mu}\left|\nabla \times \mathbf{A}^{n+1}\right|^2 + \mathbf{J}\cdot\mathbf{A}^{n+1} - \rho\phi^{n+1}\right). \tag{3.32}$$

The discrete momenta, Eqs. 3.30 and 3.31, of $\mathbf{A}$ are then

$$\mathbf{P}^n = \varepsilon\left(\frac{\mathbf{A}^{n+1} - \mathbf{A}^n}{h} + \nabla\phi^{n+1}\right) \tag{3.33}$$

$$\mathbf{P}^{n+1} = \varepsilon\left(\frac{\mathbf{A}^{n+1} - \mathbf{A}^n}{h} + \nabla\phi^{n+1}\right) - h\left(\frac{1}{\mu}\nabla \times \nabla \times \mathbf{A}^{n+1} - \mathbf{J}\right), \tag{3.34}$$

which can be re-arranged to give the update $(\mathbf{P}^n, \mathbf{A}^n) \rightarrow (\mathbf{P}^{n+1}, \mathbf{A}^{n+1})$,

$$\mathbf{A}^{n+1} = \mathbf{A}^n + h\left(\frac{1}{\varepsilon}\mathbf{P}^n - \nabla\phi^{n+1}\right) \tag{3.35}$$

$$\mathbf{P}^{n+1} = \mathbf{P}^n - h\left(\frac{1}{\mu}\nabla \times \nabla \times \mathbf{A}^{n+1} - \mathbf{J}\right). \tag{3.36}$$

As was noted previously, without gauge fixing [31] an update equation for ϕ cannot be derived from Eq. 3.32, and thus the SI in Eqs. 3.35 and 3.36 is incomplete. However, in terms of gauge-invariant fields, a complete SI can be obtained by taking the curl of both sides of Eq. 3.35 and noting that Eqs. 3.22 and 3.33 imply that $\mathbf{P} = -\varepsilon\mathbf{E}$,

$$\mathbf{B}^{n+1} = \mathbf{B}^n - h(\nabla \times \mathbf{E}^n) \tag{3.37}$$

$$\mathbf{E}^{n+1} = \mathbf{E}^n + \frac{h}{\varepsilon}\left(\frac{1}{\mu}\nabla \times \mathbf{B}^{n+1} - \mathbf{J}\right). \tag{3.38}$$

It is important to note that, despite the appearance and context of Eqs. 3.37 and 3.38, $\mathbf{E}$ and $\mathbf{B}$ are not canonically conjugate variables.

Equations 3.37 and 3.38 represent a simple, first-order accurate in time propagation scheme for Maxwell's equations derived from a discrete Lagrangian approximation to the physically correct Lagrangian density. These equations are similar to the leapfrog method, which is symplectic, often used in FDTD (see Sect. 3.2) and TD-FEM, except that the fields are not staggered in time. Higher-order integration schemes can be constructed using more complex discrete Lagrangians, although they are often implicit.

Discrete Lagrangians can also be combined to give a new discrete Lagrangian of higher order or some other desired property [54, 55], from which an explicit SI can be derived. A simple way to do this is to use an explicit symplectic partitioned Runge–Kutta (pRK) method [38, 41, 42], which below is generalized to describe field theory problems. In this approach, a given time-step is broken up into r stages, and the canonical variables A and P, which include, but are not limited to the vector potential and conjugate momentum, are updated as

$$A^{j+1} = A^j + hb_j\left(\frac{\partial}{\partial t}A\right)^j \tag{3.39}$$

Method	Order	Coefficients	Comments
SI.1	1	$b_1 = 1,\ \tilde{b}_1 = 1$	Symplectic Euler
SI.2	2	$b_1 = 0,\ b_2 = 1,\ \tilde{b}_1 = \tilde{b}_2 = 1/2$	Ruth's symplectic leapfrog[a]
SI.3	3	$b_j = \tilde{b}_{4-j}$ $\tilde{b}_1 = 0.9196615230173999$ $\tilde{b}_2 = 0.25/\tilde{b}_1 - \tilde{b}_1/2,\ \tilde{b}_3 = 1 - \tilde{b}_1 - \tilde{b}_2$	McLachlan and Atela's optimal third-order method[b]
SI.4	4	$b_{7-j} = \tilde{b}_j \quad j = 1,\ldots,6$ $\tilde{b}_1 = 0.2167979108466032$ $\tilde{b}_2 = -0.0283101143283301$ $\tilde{b}_3 = 0.3901418904713324$ $\tilde{b}_4 = -0.2414087476423302$ $\tilde{b}_5 = 0.5908564573813148$ $\tilde{b}_6 = 0.0719226032714098$	Gray and Manolopoulos' fourth-order method[c]

Fig. 3.2 Select coefficients for the explicit pRK method, Eqs. 3.39 and 3.40. Note that the superscripts a, b, and c refer to Refs. [36], [40], and [47], respectively

$$P^{j+1} = P^j + h\tilde{b}_j\left(\frac{\partial}{\partial t}P\right)^{j+1} \tag{3.40}$$

for $j = 1\ldots r$, where

$$\left(\frac{\partial}{\partial t}P\right)^j = \frac{\delta}{\delta A^j}\mathcal{L} \tag{3.41}$$

$$P^j = \frac{\delta}{\delta(\partial A/\partial t)^j}\mathcal{L} \tag{3.42}$$

and the coefficients b_j and $\tilde{b}_j$ must satisfy certain conditions in order for the pRK method to be symplectic and explicit [41, 42]. Note that the time derivative $(\partial A/\partial t)^j$ appearing in Eq. 3.39 is obtained by solving (the implicit) Eq. 3.42. The SI in Eqs. 3.39 and 3.40 updates the initial values (P^1, A^1) at time t_n to their final values (P^{r+1}, A^{r+1}) at time $t_n + h$. The coefficients b_j and $\tilde{b}_j$ exist for any order of accuracy, and have been derived by numerous authors [34–47]. The table in Fig. 3.2 shows a small selection of these coefficients.

For the Lagrangian density in Eq. 3.24, the explicit pRK method is

$$\mathbf{A}^{j+1} = \mathbf{A}^j + b_j h\left(\frac{1}{\varepsilon}\mathbf{P}^j - \nabla\phi^{j+1}\right) \tag{3.43}$$

$$\mathbf{P}^{j+1} = \mathbf{P}^j - \tilde{b}_j h\left(\frac{1}{\mu}\nabla\times\nabla\times\mathbf{A}^{j+1} - \mathbf{J}\right), \tag{3.44}$$

from which a discrete Lagrangian for each step can be identified as

$$\mathcal{L}_d(j, j+1) = h\left[\frac{1}{b_j}\frac{\varepsilon}{2}\left|\frac{\mathbf{A}^{j+1} - \mathbf{A}^j}{h} + \nabla\phi^{j+1}\right|^2 + \tilde{b}_j\left(-\frac{1}{2\mu}\left|\nabla\times\mathbf{A}^{j+1}\right|^2 + \mathbf{J}\cdot\mathbf{A}^{j+1} - \rho\phi^{j+1}\right)\right]. \tag{3.45}$$

If $r = 1$, Eqs. 3.43–3.45 are equivalent to Eqs. 3.32, 3.35, and 3.36, the symplectic Euler method (SI.1); see the table in Fig. 3.2. For $r \neq 1$, Eqs. 3.43–3.45 are equivalent to a composition of symplectic Euler steps (SI.1) scaled by b_j and $\tilde{b}_j$, a general result for every explicit symplectic pRK method [41, 56]. Again, without gauge fixing [31], an update equation for ϕ cannot be derived from Eqs. 3.43 and 3.44, but a complete SI in terms of $\mathbf{B}$ and $\mathbf{E}$ can be obtained by taking the curl of both sides of Eq. 3.43 and using the relation $\mathbf{P} = -\varepsilon\mathbf{E}$,

$$\mathbf{B}^{j+1} = \mathbf{B}^{j} - hb_j\left(\nabla \times \mathbf{E}_j\right) \tag{3.46}$$

$$\mathbf{E}^{j+1} = \mathbf{E}^{j} + h\tilde{b}_j\frac{1}{\varepsilon}\left(\frac{1}{\mu}\nabla \times \mathbf{B}^{j+1} - \mathbf{J}\right). \tag{3.47}$$

It is interesting to note that Eqs. 3.46 and 3.47 could have been derived by treating $\mathbf{E}$ and $\mathbf{B}$ as canonically conjugate variables, and applying the pRK method directly to Eqs. 2.1 and 2.2 using a "helicity" Hamiltonian [51], similar to Ref. [48]. However, as noted before, it is very important to realize that $\mathbf{E}$ and $\mathbf{B}$ are not canonically conjugate variables with respect to a Hamiltonian that corresponds to the physical energy density. A SI derived on the basis of a "helicity" Hamiltonian is only guaranteed to preserve "helicity" up to a desired order of accuracy, and not the physical dynamical invariants. Only by arriving at Eqs. 3.46 and 3.47 using the physically correct Lagrangian density for the electromagnetic field and true canonical variables, $\mathbf{A}$ and $\partial\mathbf{A}/\partial t$, is it possible to show that the physical dynamical invariants are preserved. In addition, the approach of developing SIs using the physically correct Lagrangian density allows the extension of these principles to other problems, such as the coupling of quantum mechanics and electrodynamics [52], which typically occurs through a Lagrangian density for the combined system.

3.3.4 *Numerical Stability and Dispersion*

A fundamental source of error in numerical methods is that waves propagate with a wavelength-dependent velocity, known as numerical dispersion. For spatially discretized domains, the dispersion also depends on the propagation direction with respect to the discretization [5, 57]. In addition, explicit methods are limited to a maximum stable time-step, $h_{\max}$ [58]. Both of these issues can be analyzed using the von Neumann stability analysis [33], which below is applied to the SIs developed. For simplicity, considering a source free region ($\mathbf{J} = 0$), Eqs. 3.46 and 3.47 can be rewritten in matrix form,

$$\begin{bmatrix}\mathbf{B}^{n+1}\\ \mathbf{E}^{n+1}\end{bmatrix} = \left\{\prod_{j=r}^{1}\begin{bmatrix}\mathbf{I} & \mathbf{0}\\ (h\tilde{b}_j/\varepsilon\mu)\mathbf{C} & \mathbf{I}\end{bmatrix}\begin{bmatrix}\mathbf{I} & (-hb_j)\mathbf{C}\\ \mathbf{0} & \mathbf{I}\end{bmatrix}\right\}\begin{bmatrix}\mathbf{B}^{n}\\ \mathbf{E}^{n}\end{bmatrix} \tag{3.48}$$

where the field vector contains all Cartesian components,

$$\begin{bmatrix} \mathbf{B}^n \\ \mathbf{E}^n \end{bmatrix} = \begin{bmatrix} B_x^n & B_y^n & B_z^n & E_x^n & E_y^n & E_z^n \end{bmatrix}^T, \tag{3.49}$$

$\mathbf{I}$ is the 3×3 identity matrix, and $\mathbf{C}$ is a matrix containing the spatial operations from the curl operator,

$$\mathbf{C} = \begin{bmatrix} 0 & -\partial/\partial z & \partial/\partial y \\ \partial/\partial z & 0 & -\partial/\partial x \\ -\partial/\partial y & \partial/\partial x & 0 \end{bmatrix}. \tag{3.50}$$

It is important to note the order of matrix multiplication in Eq. 3.48. Eigenmodes of the continuous Eqs. 2.1 and 2.2 are assumed to be of the form

$$\begin{bmatrix} \mathbf{B}^n \\ \mathbf{E}^n \end{bmatrix} = \zeta^n e^{i(\mathbf{k}\cdot\mathbf{x})} \begin{bmatrix} \mathbf{B}^0 \\ \mathbf{E}^0 \end{bmatrix}, \tag{3.51}$$

where the time dependence of the mode is contained in the phase factor ζ, which analytically is $e^{-i\omega h}$ (where ω is the angular frequency of the mode), and gives information on both the numerical stability and dispersion. Inserting Eq. 3.51 into Eq. 3.48 and rearranging gives

$$\zeta \begin{bmatrix} \mathbf{B}^0 \\ \mathbf{E}^0 \end{bmatrix} = \left\{ \prod_{j=r}^{1} \begin{bmatrix} \mathbf{I} & \mathbf{0} \\ (h\tilde{b}_j/\varepsilon\mu)\tilde{\mathbf{C}} & \mathbf{I} \end{bmatrix} \begin{bmatrix} \mathbf{I} & (-hb_j)\tilde{\mathbf{C}} \\ \mathbf{0} & \mathbf{I} \end{bmatrix} \right\} \begin{bmatrix} \mathbf{B}^0 \\ \mathbf{E}^0 \end{bmatrix}, \tag{3.52}$$

where

$$\tilde{\mathbf{C}} = \begin{bmatrix} 0 & -f_z & f_y \\ f_z & 0 & -f_x \\ -f_y & f_x & 0 \end{bmatrix} \tag{3.53}$$

with f_α (with $\alpha = x$, y, or z) being the result of applying the operations in Eq. 3.50 on Eq. 3.51, which depends on the spatial discretization. For example, for grid-based central discretizations

$$f_\alpha = i2\frac{\sin(k_\alpha \Delta\alpha/2)}{\Delta\alpha}, \tag{3.54}$$

where k_α is the α-component of $\mathbf{k}$. Equation 3.52 is an eigenvalue equation with eigenvalues ζ, and while it is possible to solve by hand for low stage numbers r, the analysis can become quite extensive as r increases, and Maplesoft Maple 9.5 was used below to obtain expressions for ζ when $r > 2$.

Method	Stability coefficient (C)	Number of full steps	Efficiency
FDTD	2.000000000	1.0	1.000
SI.1	2.000000000	1.0	1.000
SI.2	2.000000000	1.0	1.000
SI.3	4.520089519	3.0	0.753
SI.4	8.240410106	6.0	0.687

Fig. 3.3 Stability coefficients for Eq. 3.55, and the efficiency in comparison to SI.1. The FDTD method is included in this table, as discussed in the text

Numerical Stability

If $|\zeta| > 1$, then the eigenmode (Eq. 3.51) increases in powers of n, and the method is unstable. Therefore, to find the stability limit, Eq. 3.52 is solved for h with the condition $|\zeta| \leq 1$. Numerically, by rearranging the expressions so-obtained for h, it is found, for all SIs discussed, that

$$h \leq iC\left(\frac{\varepsilon\mu}{f_x^2 + f_y^2 + f_z^2}\right)^{1/2}, \tag{3.55}$$

where C is a stability coefficient that depends on the integrator. It is important to note that Eq. 3.55 appears to be imaginary, but the spatial discretization functions, f_α, are also imaginary, which makes the expression real. For example, using the SI.2 coefficients and Eq. 3.54, $C = 2$ and Eq. 3.55 gives the stability limit of the FDTD method [5]. Stability coefficients for the SIs from the table in Fig. 3.2 are shown in the table in Fig. 3.3. The high-order integrators are seen to greatly increase the stability limit, allowing much larger time steps, with SI.4 giving an increase of $\sim$4.12 times SI.1 and SI.2. However, this increase in stability comes at the expense of increased computational effort (multiple steps), and the efficiencies, in comparison to the single-step methods and FDTD, are also shown in the table in Fig. 3.3. Even though there is a slight decrease in efficiency, the following section shows there is a great reduction in numerical dispersion.

Numerical Dispersion

After one time-step ($n \rightarrow n + 1$), Eq. 3.51 shows that the phase of the eigenmodes, ζ, will be rotated in the complex plane by an angle determined by ωh. The amount of rotation using numerical methods will differ from the analytical form, with a difference that depends on ω (for a fixed h), leading to numerical dispersion. It is numerically found, for all of the SIs with r-stages that are considered here, that

$$\Re(\zeta) = 1 - g\sum_{j=1}^{r} c_j, \tag{3.56}$$

where c_j are the numerically determined coefficients that depend on the integrator, and

Method	Coefficients (c_j)	Max. error (%)	Average error (%)
SI.1	$c_1 = -0.5$	293.47939	32.53317
SI.2	$c_1 = -0.5$	293.47939	32.53317
SI.3	$c_1 = -0.5$ $c_2 = 0.0416$ $c_3 = -0.001076073122$	8.93847	0.96005
SI.4	$c_1 = -0.5$ $c_2 = 0.0416$ $c_3 = -0.001365305423$ $c_4 = 0.000021335663 12$ $c_5 = -0.0000001495359056$ $c_6 = 0.0000000003017236690$	0.00393	0.02687

Fig. 3.4 Coefficients for Eq. 3.56, and the maximum and average errors associated with the SIs rotation of the real part of the eigenmode phase compared to the analytical form, $\cos(\omega h)$, over the range $0 \geq \omega h < \pi$

$$g = -\left(\frac{h^2}{\varepsilon\mu}\right)\left(f_x^2 + f_y^2 + f_z^2\right). \tag{3.57}$$

Values of the coefficients for the SIs in the table in Fig. 3.2 are shown in the table in Fig. 3.4. Considering an exact spatial discretization, so the dispersion due to the SIs alone can be studied, Eq. 3.57 becomes

$$g = \left(\frac{h^2}{\varepsilon\mu}\right)\left(k_x^2 + k_y^2 + k_z^2\right) = \left(\frac{h^2}{\varepsilon\mu}\right)\mathbf{k}^2 = (\omega h)^2. \tag{3.58}$$

From Eq. 3.58, it is seen that Eq. 3.56 is essentially a truncated Taylor expansion for $\cos(\omega h)$, which is the analytical form of $\Re(\zeta)$ in Eq. 3.51. Figure 3.5 shows Eq. 3.56 and $\cos(\omega h)$ plotted over the range $0 \geq \omega h < \pi$ for the SIs in the table in Fig. 3.2. High numerical dispersion is seen to occur using the low-order SIs, SI.1 and SI.2, especially for high ω, which significantly decreases by using the high-order ones. Calculated values of the maximum and average errors of each SI are shown in the table in Fig. 3.4, where, for example, it is seen that the average error using SI.4 is only 0.027% compared to 32.533% by using SI.1 or SI.2. It is important to also note that significant additional dispersion arises from the spatial discretization, which can be independent from the time-integration method, such as intrinsic velocity anisotropy in FDTD [57].

3.3.5 *Practical Implementation Using FDTD Techniques*

Just as with FDTD outlined in Sect. 3.2, for the SIs to be practically useful, the spatial domain must be discretized, boundary conditions must be applied, and initial waves of arbitrary form must be easily introduced into the domain. These are extremely important issues that are often not considered when new numerical approaches for solving Maxwell's equations are developed. The modern forms of the FDTD method effectively deal with these issues (as outlined in Sect. 3.2) [5], thus accounting for its continued popularity. In this section, it is described how such techniques can be used for the implementation of these integrators.

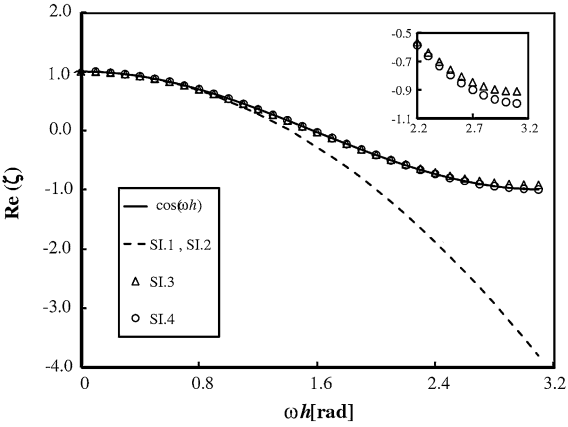

Fig. 3.5 SI rotation of the real part of the eigenmode phase after a single time-step in comparison to the analytical form, $\cos(\omega h)$, over the range $0 \geq \omega h < \pi$. The inset shows an expanded view of the high ωh region

Spatial Discretization

As mentioned previously, for a numerically accurate solution it is crucial that the spatial discretization allows **E** and **B** to satisfy Eqs. 2.3 and 2.4, as well as the appropriate boundary conditions across material interfaces. One suitable discretization is with the Yee spatial-lattice [11] (see Fig. 3.1), where **E** and **B** circulate each other on a Cartesian grid, and the spatial derivatives are approximated using Taylor expansions.

Boundary Conditions

Also mentioned previously, even when simulating infinite domains, the computational domain must be truncated. The focus here will be on one of the most successful techniques to truncate a domain, CPML [13], which absorbs nearly all incident waves and simulates an infinite extent along the truncation direction. Neglecting reflection errors from the CPML, the interior numerical solution (i.e. not inside the CPML) is unaffected [5].

The implementation of CPML involves stretching the spatial derivatives in the curl operators and superimposing time-dependent functions, Φ and Ψ, onto them. In a region of CPML, Eqs. 3.46 and 3.47 become

$$\mathbf{B}^{j+1} = \mathbf{B}^{j} - hb_j\left(\nabla_S \times \mathbf{E}^{j} + \Phi^{j}\right) \tag{3.59}$$

$$\mathbf{E}^{j+1} = \mathbf{E}^{j} + h\tilde{b_j}\frac{1}{\varepsilon}\left(\frac{1}{\mu}\nabla_S \times \mathbf{B}^{j+1} + \Psi^{j+1} - \mathbf{J}\right), \tag{3.60}$$

where $\nabla_S\times$ is a curl operator with stretched spatial derivatives,

$$\nabla_S \times \mathbf{F} = \hat{\mathbf{x}}\left(\frac{1}{\kappa_y}\frac{\partial F_z}{\partial y} - \frac{1}{\kappa_z}\frac{\partial F_y}{\partial z}\right) + \hat{\mathbf{y}}\left(\frac{1}{\kappa_z}\frac{\partial F_x}{\partial z} - \frac{1}{\kappa_x}\frac{\partial F_z}{\partial x}\right) + \hat{\mathbf{z}}\left(\frac{1}{\kappa_x}\frac{\partial F_y}{\partial x} - \frac{1}{\kappa_y}\frac{\partial F_x}{\partial y}\right) \tag{3.61}$$

where κ_α ($\alpha = x$, y, or z) is a scaling factor that increases from 1 at $\alpha = 0$ to $\kappa_{\alpha,\max}$ at $\alpha = d_\alpha$, where d_α is the depth of the CPML in the α-direction. Various formulas exist for κ_α [5], one of the most successful being polynomial grading with CPML depth [59],

$$\kappa_\alpha = 1 + (\kappa_{\alpha,\max} - 1)\left(\frac{\alpha}{d_\alpha}\right)^m \tag{3.62}$$

where m is the polynomial order. The functions Φ and Ψ are given by

$$\Phi = \hat{\mathbf{x}}(\Phi_{x,y,z} - \Phi_{x,z,y}) + \hat{\mathbf{y}}(\Phi_{y,z,x} - \Phi_{y,x,z}) + \hat{\mathbf{z}}(\Phi_{z,x,y} - \Phi_{z,y,x}) \tag{3.63}$$

$$\Psi = \hat{\mathbf{x}}(\Psi_{x,y,z} - \Psi_{x,z,y}) + \hat{\mathbf{y}}(\Psi_{y,z,x} - \Psi_{y,x,z}) + \hat{\mathbf{z}}(\Psi_{z,x,y} - \Psi_{z,y,x}), \tag{3.64}$$

and are updated by the equations

$$\Phi^{j+1}_{\alpha,\beta,\gamma} = w_{1,\alpha}\Phi^{j}_{\alpha,\beta,\gamma} + w_{2,\alpha}\frac{\partial E^{j+1}_\gamma}{\partial \beta} \tag{3.65}$$

$$\Psi^{j+1}_{\alpha,\beta,\gamma} = w_{1,\alpha}\Psi^{j}_{\alpha,\beta,\gamma} + w_{2,\alpha}\frac{1}{\mu}\frac{\partial B^{j+1}_\gamma}{\partial \beta}, \tag{3.66}$$

where $\alpha, \beta, \gamma = x, y$, or z, and

$$w_{1,\alpha} = e^{-\left(\frac{\sigma_\alpha}{\varepsilon_0\kappa_\alpha} + \frac{a_\alpha}{\varepsilon_0}\right)\Delta h} \tag{3.67}$$

$$w_{2,\alpha} = \frac{\sigma_\alpha}{\sigma_\alpha\kappa_\alpha + \kappa_\alpha^2 a_\alpha}(w_{1,\alpha} - 1), \tag{3.68}$$

where $\Delta h = h\tilde{b}^j$ and $\Delta h = hb^j$ for the coefficients in Eqs. 3.65 and 3.66, respectively. Polynomial gradings for σ_α and a_α are given by

$$\sigma_\alpha = \sigma_{\alpha,\max}\left(\frac{\alpha}{d_\alpha}\right)^m \tag{3.69}$$

$$a_\alpha = a_{\alpha,\max}\left(1 - \frac{\alpha}{d_\alpha}\right)^{m_a}, \tag{3.70}$$

where the polynomial order m_a is independent from m. Equations 3.69 and 3.70 show that σ_α increases from 0 at $\alpha = 0$ to $\sigma_{\alpha,\max}$ at $\alpha = d_\alpha$, and a_α decreases from $a_{\alpha,\max}$ at $\alpha = 0$ to 0 at $\alpha = d_\alpha$. Optimum parameters for $d_\alpha, m, m_a, \kappa_\alpha, \sigma_\alpha$, and a_α are simulation dependent, but for general FDTD simulations, effective parameters

have been found to be $d_\alpha \approx 10\Delta\alpha$, $m = 3$ or 4, $m_a = 1$, $7 < \kappa_{\alpha,\max} < 20$, $0.15 < a_{\alpha,\max} < 0.3$, and $0.8\sigma_{\alpha,\text{opt}} < \sigma_{\alpha,\max} < 1.4\sigma_{\alpha,\text{opt}}$ [60, 61], where

$$\sigma_{\alpha,\text{opt}} \approx \frac{0.8(m+1)}{\Delta\alpha}\left(\frac{\varepsilon_0}{\varepsilon_{r,\text{eff}}\mu_{r,\text{opt}}\mu_0}\right)^{1/2}, \tag{3.71}$$

with $\Delta\alpha$ being the grid spacing in the α-direction, and $\varepsilon_{r,\text{eff}}$ and $\mu_{r,\text{eff}}$ are the effective relative permittivity and permeability, respectively, of the CPML (chosen to be the materials at infinity). For a complete discussion of CPML, including derivations of Eqs. 3.59–3.71 (for FDTD), see Refs. [5, 13].

Initial Conditions

Given suitable initial conditions defined everywhere in the computational domain, the SIs will properly evolve the fields according to Eqs. 2.1 and 2.2. The most efficient technique to introduce fields into the computational domain, particularly with the Yee spatial-lattice, is to use the TF–SF technique [15–17], as discussed in Sect. 3.2.1. The SIs can be used directly in each region without modification. However, near the boundaries, where the spatial derivatives extend into both regions, the spatial derivatives must be modified using the (known) incident field so that all equations are consistent (as with regular FDTD).

3.3.6 *Numerical examples*

In this section, numerical examples are presented that demonstrate the validity of the FDTD implementation techniques, and that the high-order SIs do efficiently reduce the numerical dispersion. The first example considers a calculation of the scattering cross section of a 100 nm radius infinite cylinder in the xy-plane with a RI of $n = 3.0$ illuminated with TE_z-polarized light. For this calculation, a 2D computational domain 300×300 nm was discretized using the Yee spatial-lattice with grid spacings of $\Delta x = \Delta y = 1$ nm, and terminated with 20 layers of CPML. Spatial derivatives were approximated using second-order accurate Taylor expansions. A Gaussian-damped sinusoidal pulse traveling in the $+x$-direction,

$$e^{-\frac{[t-(x-x_0)/c]^2}{2\sigma^2}}\sin(\omega_0 t) \tag{3.72}$$

where σ is the width of the damping, x_0 is the center position of the pulse at $t = 0$, and ω_0 is the center angular frequency, was introduced into the computational domain using the TF–SF technique. The parameters in Eq. 3.72 were chosen such that the pulse had wavelength content over the range of interest ($\lambda = 350$–$1,000$ nm): $\sigma = 0.11$ fs and $\omega_0 = 600$ nm. The scattering cross section was calculated by

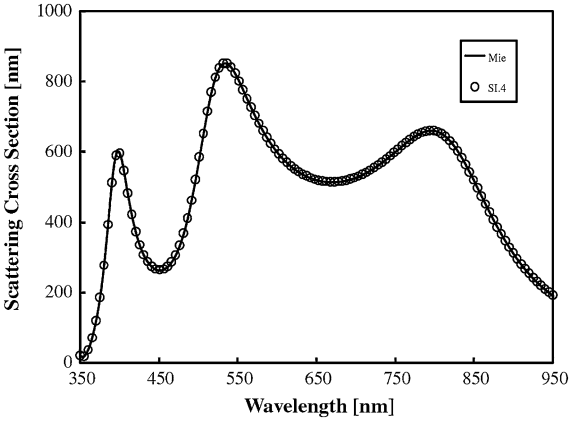

Fig. 3.6 Scattering cross section of a 100 nm radius infinite cylinder with RI of $n = 3.0$ calculated with SI.4 and implemented using FDTD techniques. The results are in comparison to the analytical Mie theory result

integrating the normal component of the Poynting vector around a closed surface encompassing the cylinder using the frequency-domain scattered fields, which were obtained by Fourier transforming the time-domain fields for 100 fs, as outlined in Sect. 3.2.1. The result calculated using SI.4 with $h = 0.99h_{\max}$ is shown in Fig. 3.6, where very accurate results can be seen. Figure 3.6 is not meant to imply that the other SIs give significantly less accurate results (see below for a detailed comparison), but rather that the FDTD implementation techniques work.

In order to appreciate the ability of the high-order SIs to efficiently reduce numerical dispersion, the analytical propagation of a narrow Gaussian pulse can be compared to the numerical result over a long distance. A 400 μm 1D computational domain was discretized using the Yee spatial-lattice with grid spacings of $\Delta x = 5$ nm. Spatial derivatives were again approximated using second-order accurate Taylor expansions. A Gaussian pulse traveling in the $+x$ direction,

$$E_y(t,x) = e^{-\frac{[t-(x-x_0)/c]^2}{2\sigma^2}} \tag{3.73}$$

$$B_z(t,x) = \frac{1}{c} e^{-\frac{[t-(x-x_0)/c]^2}{2\sigma^2}}, \tag{3.74}$$

was inserted into the computational domain by specifying initial values of E_y and B_z, Eqs. 3.73 and 3.74, everywhere with $t = 0, x_0 = 200\mu\text{m}$, and $\sigma = 0.025$ fs, chosen such that the pulse contained wavelength content down to approximately 60 nm, where extremely high numerical dispersion was expected to occur. The simulation was stopped after 500 fs, upon which time the pulse had only propagated approximately 150 μm, and therefore no boundary truncation (e.g. CPML) was necessary.

For all t, E_y and B_z are theoretically specified everywhere in the computational domain by Eqs. 3.73 and 3.74. However, because of numerical dispersion, not all frequency components of the pulse will propagate at the same speed, and thus over time its structure will deform. In order to measure this deformation, the energy of the error between the analytical and numeric pulses can be looked at,

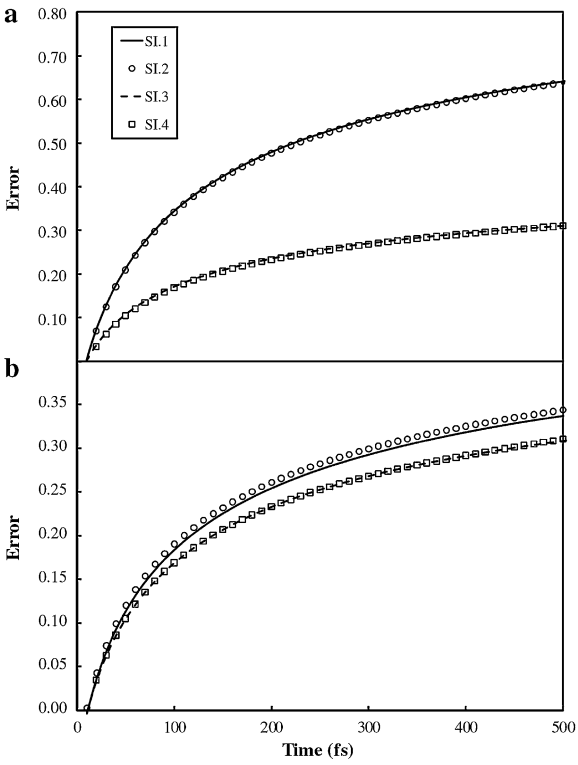

Fig. 3.7 Energy of the error relative to the incident energy as a function of time in the propagation of a 1D Gaussian pulse for SIs.1–4 with **a** $h = 0.95h_{\max}$ and **b** $h = 0.5h_{\max}$

$$\int \frac{1}{2}\left\{\varepsilon\left[E_y^n(x) - E_y(nh,x)\right]^2 + \frac{1}{\mu}\left[B_z^n(x) - B_z(nh,x)\right]^2\right\}dx. \tag{3.75}$$

For the discretization under consideration, Eq. 3.75 becomes

$$\Delta x \sum_{l=1}^{L} \frac{1}{2}\left\{\varepsilon\left[E_y^n(l\Delta x) - E_y(nh,l\Delta x)\right]^2 + \frac{1}{\mu}\left[B_z^n(l\Delta x) - B_z(nh,l\Delta x)\right]^2\right\}, \tag{3.76}$$

where L is the number of grid points. Absolute errors normalized by the incident energy with $h = 0.95h_{\max}$ for all of the SIs discussed are shown in Fig. 3.7a. It should be noted that measurements began after the pulse had propagated 10 fs to avoid numerical errors associated the initial conditions (e.g., evanescent and $-x$-directed wave components). For all SIs, the error is seen to increase over time, as expected, and those associated with SI.3 and SI.4 are less than half of that of SI.1 and SI.2.

It is interesting to observe what happens when $h \ll h_{\max}$. This may correspond to a simulation with an inhomogeneous computational domain, where $h_{\max}$ differs by region. Figure 3.7b shows the same situation as Fig. 3.7a, except with $h = 0.5h_{\max}$.The errors associated with SI.1 and SI.2 are seen to dramatically

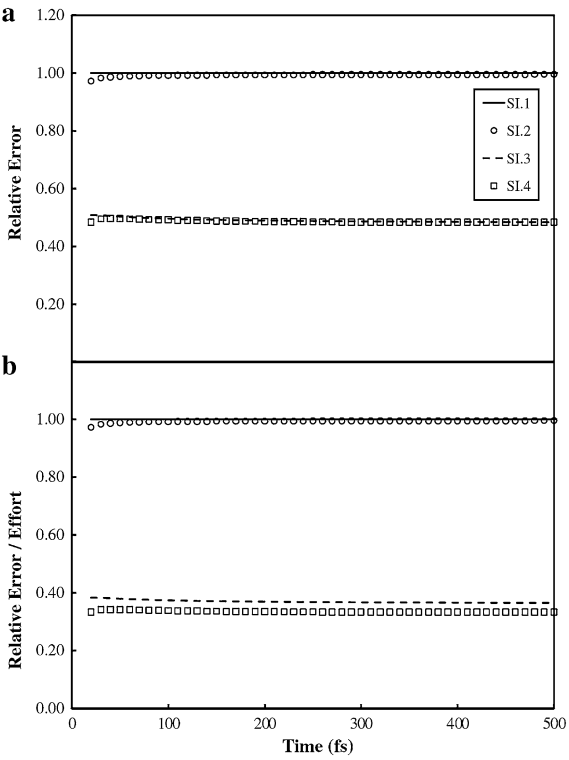

Fig. 3.8 **a** Energy of the error as a function of time in the propagation of a 1D Gaussian pulse for SIs.1–4 relative to SI.1 and with $h = 0.95h_{\max}$. **b** Error per computational effort

decrease, whereas those of SI.3 and SI.4 remain relatively the same (and still below SI.1 and SI.2). The high-order integrators are therefore particularly well-suited for maintaining a minimal amount numerical dispersion in inhomogeneous computational domains. In order to directly compare the SIs, the errors relative to the single step method (SI.1) can be calculated, Fig. 3.8a. As expected from Fig. 3.7, the error of SI.2 is almost identical to SI.1, while SI.3 and SI.4 have significantly less. In addition, although hard to discern from Fig. 3.8, the relative errors of SI.3 and SI.4 decrease over time. Multiplying the results in Fig. 3.8a by the efficiency in Fig. 3.3 gives an idea of the error per computational effort. The result is shown in Fig. 3.8b, and demonstrates that the high-order SIs efficiently minimize numerical dispersion.

3.3.7 Summary and Outlook

A discrete action principle for electrodynamics was derived, which was then used to construct explicit SIs for Maxwell's equations. The physically correct electrodynamics Lagrangian density, involving the vector and scalar potentials, was used

for this formulation, but it was demonstrated that the integrators could all be expressed entirely in terms of the electric and magnetic fields. By combining discrete Lagrangians in an explicit symplectic pRK method, an integrator capable of achieving any order of accuracy was obtained. The numerical stability was shown to be greatly increased and the numerical dispersion greatly decreased, compared to other methods, by using the high-order integrators. Numerical examples were presented that demonstrated this, especially as the time-step was decreased from the maximum stable one. These integrators are therefore particularly well-suited for modeling the propagation of electromagnetic waves in large, inhomogeneous computational domains. It was demonstrated that the integrators can be used along with a lot of the standard embellishments of FDTD, which were used for the numerical examples. However, the integrators are not limited to a finite-difference method, and can also be implemented using other approaches.

The integrators presented in this section do not explicitly allow for dispersive materials, which would involve additional current or polarization terms that would be coupled to **E**. However, such behavior can be incorporated with the integrators using a split-operator approach as used in Ref. [62], and is, at the time of this writing, under investigation, as well as other approaches for modeling these materials.

Before ending this section, it is worth mentioning that the ideas presented here can be used to construct SIs for other approaches in physics that are based on Lagrangian mechanics, such as the Car–Parrinello molecular dynamics method [63] and time-domain DFT [64].

3.4 The Finite-Element Method (FEM)

A method which does not suffer the geometric modeling limitations and have (as much) computational inefficiency of FDTD is the Finite-Element Method (FEM). Finite-element methods are particularly useful for solving a partial differential equation constrained by boundary conditions. In this dissertation, FEM is used to solve Eqs. 2.10 and 2.13. The method outlined below is specifically for the 3D variant (Eq. 2.10), from which the corresponding 2D version (Eq. 2.13) can be inferred (technically, the surface integral portions of 3D FEM correspond to 2D FEM). Further details of the 2D method can be found in Refs. [2, 6].

Inserting $\mathbf{D}(\mathbf{x},\omega) = \varepsilon_0\varepsilon(\omega)\mathbf{E}(\mathbf{x},\omega)$ into Eq. 2.10 gives an equation in terms of only one unknown field, $\mathbf{E}(\mathbf{x},\omega)$,

$$\nabla \times \left[\frac{1}{\mu_r}\nabla \times \mathbf{E}(\mathbf{x},\omega)\right] - k_0^2\varepsilon(\omega)\mathbf{E}(\mathbf{x},\omega) = ik_0Z_0\mathbf{J}(\mathbf{x},\omega), \tag{3.77}$$

where $k_0 = \omega/c$, where c is the speed of light in a vacuum, $\mu_r = \mu/\mu_0$ and $\varepsilon(\omega)$ are relative permeability and permittivity values, respectively, and $Z_0 = (\mu_0/\varepsilon_0)^{1/2}$ is the impedance of free space.

Before Eq. 3.77 can be solved, boundary conditions must be applied. A major focus herein is on open-region scattering problems, and infinitely far from scattering object(s) embedded in a uniform (background) dielectric medium with RI n_b (and $\mu_r = 1$) and illuminated by a plane wave (see Sect. 3.4.1), the form of the scattered fields, $\mathbf{E}^{\text{sc}}(\mathbf{x}, t)$, are outward propagating plane waves,

$$\lim_{r\to\infty} r[\nabla \times \mathbf{E}^{\text{sc}}(\mathbf{x}, t) - ik_0 n_b \hat{r} \times \mathbf{E}^{\text{sc}}(\mathbf{x}, t)] = 0 \tag{3.78}$$

where $\hat{r}$ is the outward pointing unit vector associated with $r = (x^2 + y^2 + z^2)^{1/2}$. Equation 3.78 is known as the Sommerfeld radiation condition, which for open-region scattering problems is a necessary boundary condition on the exterior of a computational domain. (Note that for a scattering object at the origin, Eq. 3.78 is exact as $r \to \infty$.)

3.4.1 Open-Region Scattering Functional

From the calculus of variations, $\mathbf{E}(\mathbf{x}, \omega)$, incorporating Eqs. 3.77 and 3.78 in a domain V truncated by a spherical surface ∂V (this requirement is not necessary, however a more sophisticated boundary condition than Eq. 3.78 should be used in this case [6]) is determined from the functional

$$\begin{aligned} F[\mathbf{E}(\mathbf{x}, \omega)] = \frac{1}{2}\int_V \Big\{ & \frac{1}{\mu_r}[\nabla \times \mathbf{E}(\mathbf{x}, \omega)] \cdot [\nabla \times \mathbf{E}(\mathbf{x}, \omega)] \\ & - k_0^2 \varepsilon(\omega)\mathbf{E}(\mathbf{x}, \omega) \cdot \mathbf{E}(\mathbf{x}, \omega) \Big\} dV - \frac{1}{2}\int_{\partial V} \Big\{ \frac{ik_0 n_b}{\mu_r}[\hat{r} \times \mathbf{E}(\mathbf{x}, \omega)] \cdot [\hat{r} \times \mathbf{E}(\mathbf{x}, \omega)] \\ & - \frac{1}{\mu_r}\mathbf{E}(\mathbf{x}, \omega) \cdot \mathbf{U}^{\text{inc}}(\mathbf{x}, \omega) \Big\} d(\partial V) - ik_0 Z_0 \int_V [\mathbf{E}(\mathbf{x}, \omega) \cdot \mathbf{J}(\mathbf{x}, \omega)] dV, \end{aligned} \tag{3.79}$$

where

$$\mathbf{U}^{\text{inc}}(\mathbf{x}, \omega) = \hat{r} \times \nabla \times \mathbf{E}^{\text{inc}}(\mathbf{x}, \omega) - ik_0 n_b \hat{r} \times \hat{r} \times \mathbf{E}^{\text{inc}}(\mathbf{x}, \omega), \tag{3.80}$$

where $\mathbf{E}^{\text{inc}}$ is the incident field. It is important to note that, in practice, $\hat{r}$ should be interpreted as $\hat{n}$, the outward pointing unit vector normal to the surface. See Appendix C for a derivation of Eq. 3.79. It is easily verified that the stationary point of $F[\mathbf{E}(\mathbf{x}, \omega)]$, $\delta F[\mathbf{E}(\mathbf{x}, \omega)] = 0$, gives Eq. 3.77 in V with Eq. 3.78 on ∂V. For the work herein, $\mathbf{E}^{\text{inc}}(\mathbf{x}, \omega)$ is assumed to be plane wave with amplitude E_0 in the medium n_b,

$$\mathbf{E}^{\text{inc}}(\mathbf{x}, \omega) = \mathrm{E}_0 \Big[\cos(\alpha)\hat{\boldsymbol{\theta}} + \sin(\alpha)\hat{\boldsymbol{\phi}}\Big] e^{i\mathbf{k}^{\text{inc}} \cdot \mathbf{x}} \tag{3.81}$$

where α is the polarization angle and $\mathbf{k}^{\text{inc}}$ is given by

$$\mathbf{k}^{\text{inc}} = n_b k_0[\sin(\theta)\cos(\phi)\hat{\mathbf{x}} + \sin(\theta)\sin(\phi)\hat{\mathbf{y}} + \cos(\theta)\hat{\mathbf{z}}], \tag{3.82}$$

where θ and ϕ are the polar and azimuthal angles, respectively, and $\hat{\boldsymbol{\theta}}$ and $\hat{\boldsymbol{\phi}}$ are the corresponding unit vectors.

To find the stationary point of $F[\mathbf{E}(\mathbf{x},\omega)]$, the computational domain is discretized using a number of elements (which can be tetrahedral, cubic, etc.), and the unknown field $\mathbf{E}(\mathbf{x},\omega)$ is approximated over each one. Information about the computational domains that were used for the calculations in this dissertation are discussed in the context of specific applications (e.g., see Chap. 5). The functional in Eq. 3.79 can then be written as

$$F[\mathbf{E}(\mathbf{x},\omega)] = \sum_e F[\mathbf{E}(\mathbf{x},\omega)^e]^e, \tag{3.83}$$

where $\mathbf{E}(\mathbf{x},\omega)^e$ is the field defined only over the element e, and is determined from the functional $F[\mathbf{E}(\mathbf{x},\omega)^e]^e$.

3.4.2 Basis Functions Approximation

To approximate $\mathbf{E}(\mathbf{x},\omega)^e$, a basis function expansion is used. Basis functions in V and on ∂V are both needed, which also must be compatable—i.e., the basis functions on the faces of V must reduce to those on ∂V on the corresponding face of V. (Below, the basis functions for V are specifically described, from which those on ∂V can be inferred.) The form of this expansion depends on the type of element used for discretization, which below is taken to be tetrahedral in V (which implies a triangular discretization on ∂V). It is important to note that, regardless of the element shape, the basis functions should also be chosen such that Eqs. 2.8 and 2.9 are satisfied over each element, as well as the boundary condition that requires the tangential component of $\mathbf{E}(\mathbf{x},\omega)$ to be continuous across elements with different permittivities, Eq. 2.14.

In this dissertation, basis functions constructed from Whitney edge elements (vector-form basis functions) [65] are used,

$$\boldsymbol{\Omega}^{\gamma\beta}(\mathbf{x}) = \xi_\gamma \nabla\xi_\beta - \xi_\beta \nabla\xi_\gamma \tag{3.84}$$

where γ and β are two nodes of a given element which share the edge $\gamma\beta$, and ξ_γ and ξ_β are the corresponding simplex coordinates. Equation 3.84 satisfies all of the aforementioned necessary conditions of basis functions, and implies that there are six such functions per tetrahedral volume and three per triangular facet (six even permutations of γ and $\beta = 1, 2, 3,$ or 4 with $\gamma < \beta$). The basis functions in Eq. 3.84 point from node γ to β and have a constant tangential component along edge $\gamma\beta$, which goes to zero along all other edges [65]. While the basis functions in Eq. 3.84

can be used directly, the field described by such a function is represented as a polynomial of first-order, $p_f = 1$, and the curl of this field is represented by a polynomial of one less order, $p_c = p_f - 1 = 0$ (in electrodynamics, both the field and its curl are important). In order to obtain a more accurate representation of $\mathbf{E}(\mathbf{x}, \omega)$, basis functions constructed from Eq. 3.84 that have a curl complete to a higher order can be used [66]. For a given order p_c, the field is interpolated at $(p_c + 1)(p_c + 3)(p_c + 4)/2$ points: $6(p_c + 1)$ points along the edges, $4p_c(p_c + 1)$ on the faces, and $p_c(p_c - 1)(p_c + 1)/2$ in the interior. Each interpolation point is related to a given edge $\gamma\beta$, and is described by four indices i, j, k, and l, which range from 1 to $p_c + 1$ with the constraint $i + j + k + l = p_c + 2$. This indexed point corresponds to the location

$$\xi = \left(\frac{i}{p_c + 2}, \frac{j}{p_c + 2}, \frac{k}{p_c + 2}, \frac{l}{p_c + 2}\right), \tag{3.85}$$

where $\xi = (\xi_1, \xi_2, \xi_3, \xi_4)$.

The approximation to $\mathbf{E}(\mathbf{x}, \omega)$ within each element is then

$$\mathbf{E}^e(\mathbf{x}, \omega) \approx \sum_{\gamma\beta} \sum_{i,j,k,l} \mathbf{\Omega}^{\gamma\beta}_{i,j,k,l}(\mathbf{x}) \phi^{\gamma\beta}_{i,j,k,l}(\omega), \tag{3.86}$$

where $\phi^{\gamma\beta}_{i,j,k,l}(\omega)$ is the (unknown) value of $\mathbf{E}(\mathbf{x}, \omega)$ at ξ and $\mathbf{\Omega}^{\gamma\beta}_{i,j,k,l}(\mathbf{x})$ is the p_c^{th}-order basis function given by

$$\mathbf{\Omega}^{\gamma\beta}_{i,j,k,l}(\mathbf{x}) = N^{\gamma\beta}_{i,j,k,l} \frac{(p_c + 2)^2 \xi_\gamma \xi_\beta \hat{\alpha}_{i,j,k,l}(\xi)}{i_\gamma i_\beta} \mathbf{\Omega}^{\gamma\beta}(\mathbf{x}), \tag{3.87}$$

where i_γ and i_β are the values of i, j, k, or l for γ and $\beta = 1, 2, 3$, or 4 respectively, $N^{\gamma\beta}_{i,j,k,l}$ is a normalization factor,

$$N^{\gamma\beta}_{i,j,k,l} = \frac{p_c + 2}{p_c + 2 - i_\gamma - i_\beta} l^{\gamma\beta} \tag{3.88}$$

where $l^{\gamma\beta}$ is the length of edge $\gamma\beta$ (at the point ξ), and $\hat{\alpha}_{i,j,k,l}$ is a Silvester–Lagrange interpolating polynomial,

$$\hat{\alpha}_{i,j,k,l}(\xi) = \hat{R}_i(p_c + 2, \xi_1) \hat{R}_j(p_c + 2, \xi_2) \hat{R}_k(p_c + 2, \xi_3) \hat{R}_l(p_c + 2, \xi_4) \tag{3.89}$$

where $\hat{R}_i(p, \xi)$ (or analogously for j, k, or l) is a shifted Silvester polynomial given by

$$\hat{R}_i(p, \xi) = \begin{cases} \frac{1}{(i-1)!} \prod_{m=1}^{i-1} (p\xi - m) & \text{if} \quad 2 \le i \le p + 1 \\ 1 & \text{if} \quad i = 1 \end{cases}. \tag{3.90}$$

It is found that taking $p_c = 1$ is sufficient to adequately converge far-field properties (e.g., cross sections), while $p_c \ge 2$ is necessary to converge those in the

near-field (e.g., the electromagnetic fields near the surface of a structure). Therefore, in this dissertation, p_c values were taken to be 1 and 2, respectively.

3.4.3 Determination of the Unknown Field

Inserting Eq. 3.86 into Eqs. 3.83 and 3.79 and finding the stationary point with respect to each $\phi_j(\omega)$ gives a set of linear equations for the unknown values $\phi_i(\omega)$ (where i and j now refer to global index numbers for the unknowns, and should not be confused with any aforementioned indices),

$$([\mathrm{K}_V] + [\mathrm{K}_{\partial V}])\{\phi\} = \{b\} \tag{3.91}$$

where $\{\phi\}$ is a column vector containing $\phi_i(\omega)$, and $\{b\}$, $[\mathrm{K}_V]$, and $[\mathrm{K}_{\partial V}]$ are a known column vector and known matrices given by

$$[\mathrm{K}_V]_{ij} = \int_V \left\{ \frac{1}{\mu_r} [\nabla \times \boldsymbol{\Omega}_i(\mathbf{x})] \cdot \left[\nabla \times \boldsymbol{\Omega}_j(\mathbf{x})\right] - k_0^2 \varepsilon(\omega) \boldsymbol{\Omega}_i(\mathbf{x}) \cdot \boldsymbol{\Omega}_j(\mathbf{x}) \right\} dV \tag{3.92}$$

$$[\mathrm{K}_{\partial V}]_{ij} = -\int_{\partial V} \frac{ik_0 n_b}{\mu_r} [\hat{r} \times \boldsymbol{\Omega}_i(\mathbf{x})] \cdot \left[\hat{r} \times \boldsymbol{\Omega}_j(\mathbf{x})\right] d(\partial V) \tag{3.93}$$

$$\{b\}_i = -\frac{1}{2} \int_{\partial V} \frac{1}{\mu_r} \boldsymbol{\Omega}_i(\mathbf{x}) \cdot \mathbf{U}^{\mathrm{inc}}(\mathbf{x}, \omega) d(\partial V) + ik_0 Z_0 \int_V [\boldsymbol{\Omega}_i(\mathbf{x}) \cdot \mathbf{J}(\mathbf{x}, \omega)] dV. \tag{3.94}$$

The integrals in Eqs. 3.92–3.94 can either be evaluated numerically [67, 68] or analytically, after which the (highly sparse and complex-symmetric) matrix equation (Eq. 3.91) can be solved directly (for very small systems) or by using iterative methods. For the calculations in this dissertation, $[\mathrm{K}_V]$ and $[\mathrm{K}_{\partial V}]$ were evaluated analytically, while $\{b\}$ was evaluated numerically using Gauss–Legendre quadrature (7 points per triangular face). The resulting matrix equation was solved using a sparse LU decomposition.

3.4.4 Optical Responses

After solving for the unknown field $\mathbf{E}(\mathbf{x}, \omega)$, optical responses (cross sections) can be calculated using volume integral equations [69],

$$\sigma_{\mathrm{abs}} = \frac{k_0}{|\mathrm{E}_0|^2} \int_V \mathrm{Im}[\varepsilon(\omega)] \mathbf{E}(\mathbf{x}, \omega) \cdot \mathbf{E}(\mathbf{x}, \omega)^* dV \tag{3.95}$$

$$\sigma_{\text{ext}} = \frac{k_0}{|\mathrm{E}_0|^2}\text{Im}\left\{\int_V [\varepsilon(\omega) - 1]\mathbf{E}(\mathbf{x},\omega)\cdot\mathbf{E}^{\text{inc}}(\mathbf{x},\omega)^* dV\right\} \tag{3.96}$$

$$\sigma_{\text{sc}} = \sigma_{\text{ext}} - \sigma_{\text{abs}}. \tag{3.97}$$

3.4.5 Advantages and Disadvantages

Just like any computational method (e.g., FDTD), FEM has advantages and disadvantages. The biggest disadvantage is its complicated formulation, as outlined above. Another disadvantage is that FEM is not particularly well-suited for modeling periodic systems. For example, the method outlined in this section was for open-region scattering problems. A completely different formulation exists for periodic systems due to different boundary conditions than that in Eq. 3.78. Thus, the method is not as generally applicable as FDTD, for example.

However, the advantages outweigh the disadvantages in a number of situations. The biggest advantage of FEM is that it does not suffer from geometric modeling errors, and, in principle, can model any structure exactly [6]. This allows the determination of near-fields around structures arbitrarily close to their surfaces, a property particularly important for a number of effects, such as SERS enhancements; see Chap. 5. In addition, FEM is often more computationally efficient than FDTD. For example, in order to model fine details in a large computational domain, all one has to do is use small elements in the necessary region(s), or places where the fields are expected to rapidly vary, and large elements elsewhere. In one study comparing FDTD to FEM, it was found that to accurately calculate the near-fields of a 50 nm diameter cubic Ag nanoparticle, FDTD took 8 h to complete on 256 2.6 GHz dual-core processors, while FEM only took 4 h on a single 3.4 GHz processor [3].

3.5 Specialized Methods

As mentioned in Sect. 3.1, both FDTD and FEM can be computationally demanding. Therefore, for some specific applications, specialized methods that are more computationally efficient have been developed. Two methods that are of relevance to the work in this dissertation are RCWA and the modal expansion method, both described below.

3.5.1 The Rigorous Coupled-Wave Analysis

A computationally efficient approach to study periodically structured films is RCWA [70, 71]. An additional benefit of RCWA is that specific diffraction orders can be independently studied.

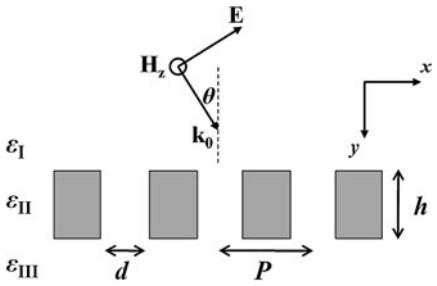

Fig. 3.9 Schematic diagram of a 1D metallic grating illuminated with TE_z polarized light. The parameters in the figure are defined in the text

A schematic diagram of the 2D system under consideration with RCWA is shown in Fig. 3.9 for TE_z polarization. The system consists of a 1D metallic grating, with slits of diameter d, permittivity ε_s, and periodicity P in a metal film with thickness h and permittivity $\varepsilon_{\mathrm{II}}$, all of which is surrounded by dielectric media with permittivities ε_{I} and $\varepsilon_{\mathrm{III}}$. The grating is illuminated from above with TE_z polarized light incident at an angle θ with respect to the film normal.

Inside the grating region, the permittivity can be expanded using a Fourier series,

$$\varepsilon_{\mathrm{II}}(x) = \sum_n \varepsilon_n e^{ingx} \tag{3.98}$$

where n is an integer and $g = 2\pi/P$ is the period of the reciprocal lattice. The Fourier components of Eq. 3.98 are

$$\varepsilon_n = (\varepsilon_s - \varepsilon_{\mathrm{M}})\frac{\sin(n\pi f)}{n\pi} \tag{3.99}$$

for $n \neq 0$ and

$$\varepsilon_0 = f\varepsilon_s + (1-f)\varepsilon_{\mathrm{M}} \tag{3.100}$$

for $n = 0$, where $f = d/P$ is the filling factor. In Eq. 3.100, ε_0 corresponds to the average value of the dielectric function of the grating region, and should not be confused with the vacuum permittivity.

For TE_z polarization, the incident magnetic field, H_z^{inc}, is

$$H_z^{\mathrm{inc}} = e^{-i(k_{\mathrm{I}x}x + k_{\mathrm{I}y}y)}, \tag{3.101}$$

where $k_{\mathrm{I}}x = k_{\mathrm{I}}\sin\theta$ and $k_{\mathrm{I}}y = k_{\mathrm{I}}\cos\theta$, with $k_{\mathrm{I,III}} = k_0\varepsilon_{\mathrm{I,III}}^{1/2}$. Diffraction by the grating gives rise to a set of diffraction orders, where the in-plane wavevector magnitude of the nth diffracted wave is $k_{y_n} = k_{\mathrm{I}}x + ng$. In terms of these diffraction orders, Rayleigh expansions can be used to express the reflected and transmitted magnetic fields in regions I and III as

$$H_z^{\mathrm{I}} = H_z^{\mathrm{inc}} + \sum_n r_n e^{-i(k_{x_n}x - k_{\mathrm{I}y_n}y)} \tag{3.102}$$

$$H_z^{\mathrm{III}} = \sum_n t_n e^{-i[k_{x_n} x + k_{\mathrm{III}y_n}(y-h)]}, \tag{3.103}$$

where $k^2_{\mathrm{I,III}\,y_n} = k^2_{\mathrm{I,III}} - k^2_{x_n}$, and the coefficients r_n and t_n correspond to the amplitudes of the nth reflected and transmitted waves, respectively. Inside region II, Bloch's theorem can be used to express H_z and E_x using Fourier expansions,

$$H_z^{\mathrm{II}} = \sum_n \mathrm{H}_{\mathrm{II}_n}(y) e^{-ik_{x_n} x} \tag{3.104}$$

$$E_x^{\mathrm{II}} = i\frac{\mu}{\varepsilon} \sum_n \mathrm{E}_{\mathrm{II}_n}(y) e^{-ik_{x_n} x} \tag{3.105}$$

where $\mathrm{H}_{\mathrm{II}_n}$ and $\mathrm{E}_{\mathrm{II}_n}$ are the normalized amplitudes of the spatial harmonics. It can be shown that $\mathrm{H}_{\mathrm{II}_n}$ and $\mathrm{E}_{\mathrm{II}_n}$ are related by a set of coupled equations, and by projecting them onto a set of plane waves and matching H_z and E_x at the film interfaces (Eqs. 2.14 and 2.16), they can be used to solve for the coefficients r_n and t_n [72].

Once r_n and t_n are determined, the diffraction efficiencies can be calculated from

$$R_n = |r_n|^2 \Re\left[\frac{k_{\mathrm{I}y_n}}{k_0 \varepsilon_{\mathrm{I}}^{1/2} \cos\theta}\right] \tag{3.106}$$

$$T_n = |t_n|^2 \Re\left[\frac{\varepsilon_{\mathrm{I}}^{1/2} k_{\mathrm{III}_{y_n}}}{k_0 \varepsilon_{\mathrm{III}} \cos\theta}\right]. \tag{3.107}$$

In practice, RCWA is often less rigorous than FDTD because of the approximation of the dielectric function of the grating region (Eq. 3.98) by a finite number of terms. In addition, convergence issues exist for RCWA for TE_z polarization due to material discontinuities inside the grating. However, with care they are possible to avoid [73].

For the RCWA results presented herein, the model of Ref. [72] was used, which provides analytical expressions for the diffraction efficiencies for normal incident light and only retaining the first two diffraction orders and Fourier components in the grating region. In addition, this 2D method was applied to 3D problems, but such an approximation has been demonstrated previously to capture (most of) the important features [24, 25].

3.5.2 *The Modal Expansion Method*

To describe the transmission through an isolated slit, a modal expansion of the electromagnetic fields in the presence of the slit can be used [72]. A schematic

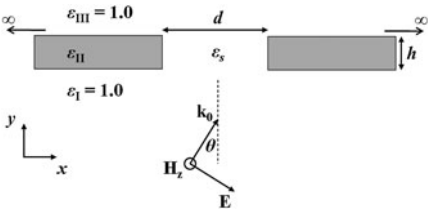

Fig. 3.10 Schematic diagram of an isolated slit in a metal film in air illuminated using TE_z polarized light. The parameters in the figure are defined in the text

diagram of the system under consideration is shown in Fig. 3.10. The system consists of an isolated slit with diameter d and relative permittivity ε_s in a PEC film with thickness h in air. Even though the method is applied to a PEC film, it has previously been demonstrated that the obtainable results accurately describe many aspects of a real metal [73]. The slit is illuminated from below with TE_z polarized light at an angle θ with respect to the film normal.

For TE_z polarization, H_z is expressed in regions I and III as a superposition of propagating and evanescent plane waves,

$$H_z^{\mathrm{I}} = H_z^{\mathrm{inc}} + \int_{-\infty}^{\infty} dk \rho(k) e^{i(kx - k_y y)} \tag{3.108}$$

$$H_z^{\mathrm{III}} = \int_{-\infty}^{\infty} dk \tau(k) e^{i(kx + k_y y)} \tag{3.109}$$

where $\rho(k)$ and $\tau(k)$ are the reflection and transmission amplitudes, respectively, $k_y = (k_0^2 - k^2)^{1/2}$, and the incident magnetic field, H_z^{inc}, is given by

$$H_z^{\mathrm{inc}} = e^{i(k_{0x}x + k_{0y}y)}, \tag{3.110}$$

where k_{0x} and k_{0y} are projections of the incident wavevector magnitude along the x and y-axes, respectively. In region II, H_z is expanded in terms of the eigenmodes of a waveguide,

$$H_z^{\mathrm{II}} = \sum_{m=0}^{\infty} \left[A_m e^{i\beta_m y} + B_m e^{-i\beta_m y} \right] \phi_m(x) \tag{3.111}$$

where m is the order of the waveguide mode, $\beta_m = \left[k_0^2 \varepsilon_s - (m\pi/d)^2 \right]^{1/2}$ and $\phi_m(x) = (2/d^{1/2}) \cos[m\pi(x + d/2)/d]$ is the solution to Eq. 2.13 within the slit subject to PEC boundary conditions at $x = \pm d/2$, Eq. 2.21. By matching H_z and E_x at the film interfaces (Eqs. 2.18 and 2.21) and projecting the resulting equations onto plane waves, the modal amplitudes A_m and B_m can be determined via the numerical solution of a set of linear equations [72].

References

1. McMahon JM, Gray SK, Schatz GC (2011) Surface nanophotonics theory. In: Wiederrecht G (ed) Comprehensive nanoscience and technology. Elsevier, Amsterdam
2. McMahon JM, Henry AI, Wustholz KL, Natan MJ, Freeman RG, Van Duyne RP, Schatz GC (2009) Gold nanoparticle dimer plasmonics: finite element method calculations of the electromagnetic enhancement to surface-enhanced Raman spectroscopy. Anal Bioanal Chem 394:1825–1825
3. Zhao J, Pinchuk AO, McMahon JM, Li S, Ausman LK, Atkinson AL, Schatz GC (2008) Methods for describing the electromagnetic properties of silver and gold nanoparticles. Acc Chem Res 41:1720–1720
4. Atkinson AL, McMahon JM, Schatz GC (2009) FDTD studies of metallic nanoparticle systems. In: Self organization of molecular systems, from molecules and clusters to nanotubes and proteins, NATO science for peace and security series A, chemistry and biology. Springer, Netherlands
5. Taflove A, Hagness S (2005) Computational electrodynamics: the finite-difference time-domain method, 3rd edn. Artech House, Boston
6. Jin J (2002) The finite element method in electromagnetics. Wiley, New York
7. Mie G (1908) Beiträge zur Optik trüber Medien, speziell kolloidaler Metallösungen. Ann Phys 25:377–445
8. Bohren CF, Huffman DR (1983) Absorption and scattering of light by small particles. Wiley, New York
9. Peña O, Pal U (2009) Scattering of electromagnetic radiation by a multilayered sphere. Comput Phys Commun 180:2348–2354
10. Yeh P (1988) Optical waves in layered media, 1st edn. Wiley, New York
11. Yee SK (1966) Numerical solution of initial boundary value problems involving Maxwell's equations in isotropic media. IEEE Trans Antennas Propagat 14:302–307
12. Berenger JP (1994) A perfectly matched layer for the absorption of electromagnetic waves. J Comp Phys 114:185–200
13. Roden JA, Gedney SD (2000) Convolutional PML (CPML): an efficient FDTD implementation of the CFS-PML for arbitrary media. Microw Opt Techn Let 27:334–339
14. McMahon JM, Gray SK, Schatz GC (2009) A discrete action principle for electrodynamics and the construction of explicit symplectic integrators for linear, non-dispersive media. J Comp Phys 228:3421–3432
15. Umashankar KR, Taflove A (1982) A novel method to analyze electromagnetic scattering of complex objects. IEEE T Electromagn Compat 24:397–405
16. Mur G (1981) Absorbing boundary conditions for the finite difference approximation of the time-domain electromagnetic field equations. IEEE T Electromagn C 23:377–382
17. Merewether DE, Fisher R, Smith FW (1980) On implementing a numeric Huygen's source scheme in a finite difference program to illuminate scattering bodies. IEEE T Nucl Sci 27:1829–1833
18. Kashiwa T, Fukai I (1990) A treatment by FDTD method of dispersive characteristics associated with electronic polarization. Microw Opt Techn Lett 3:203–205
19. Joseph RM , Hagness SC, Taflove A (1991) Direct time integration of Maxwell's equations in linear dispersive media with absorption for scattering and propagation of femtosecond electromagnetic pulses. Opt Lett 16:1412–1414
20. Gray SK, Kupka T (2003) Propagation of light in metallic nanowire arrays: finite-difference time-domain studies of silver cylinders. Phys Rev B 68:045415
21. McMahon JM, Wang Y, Sherry LJ, Van Duyne RP, Marks LD, Gray SK, Schatz GC (2009) Correlating the structure, optical spectra, and electrodynamics of single silver nanocubes. J Phys Chem 113:2731–2735
22. Babayan Y, McMahon JM , Li S, Gray SK, Schatz GC, Odom TW (2009) Confining standing waves in optical corrals. ACS Nano 3:615–620

23. Ringe E, McMahon JM, Sohn K, Cobley C, Xia Y, Huang J, Schatz GC, Marks LD, Van Duyne RP (2010) Unraveling the effects of size, composition, and substrate on the localized surface plasmon resonance frequencies of gold and silver nanocubes: a systematic single particle approach. J Phys Chem C 114:12511–12516
24. McMahon JM, Henzie J, Odom TW, Schatz GC, Gray SK (2007) Tailoring the sensing capabilities of nanohole arrays in gold films with Rayleigh anomaly-surface plasmon polaritons. Opt Express 15:18119–18129
25. Schatz GC, McMahon JM, Gray SK (2007) Tailoring the parameters of nanohole arrays in gold films for sensing applications. In: Mark I Stockman (ed) Plasmonics: metallic nanostructures and their optical properties V, pp 664103(1–8)
26. Gao H, McMahon JM, Lee MH, Henzie J, Gray SK, Schatz GC, Odom TW (2009) Rayleigh anomaly-surface plasmon polariton resonances in palladium and gold subwavelength hole arrays. Opt. Express 17:2334–2340
27. Odom TW, Gao H, McMahon JM, Henzie J, Schatz GC (2009) Plasmonic superlattices: hierarchical subwavelength hole arrays. Chem Phys Lett 483:187–192
28. Stewart ME, Mack NH, Malyarchuck V, Soares JANT, Lee TW, Gray SK, Nuzzo RG, Rogers JA (2006) Quantitative multispectral biosensing and 1D imaging using quasi-3D plasmonic crystals. Proc Natl Acad Sci USA, 103:17143–17148
29. Chang SH, Gray SK, Schatz GC (2005) Surface plasmon generation and light transmission by isolated nanoholes and arrays of nanoholes in thin metal films. Opt Express 13:3150–3165
30. Schwartz M (1987) Principles of electrodynamics, 1st edn. Dover Publications, New York
31. Jackson JD (1998) Classical electrodynamics, 3rd edn. Wiley, New York
32. Manry CW, Broschat SL, Schneider JB (1995) Higher-order FDTD methods for large problems. J Appl Comput Electromagnet Soc 10:17–29
33. Press WH, Flannery BP, Teukolsky SA, Vetterling WT (1988) Numerical recipes in C: the art of scientific computing, 1st edn. Cambridge University Press, Cambridge
34. Verlet L (1967) Computer "experiments" on classical fluids. I. Thermodynamical properties of Lennard–Jones molecules. Phys Rev 159:98–103
35. Goldstein H (1980) Classical mechanics, 2nd edn. Addison-Wesley, MA
36. Ruth RD (1983) A canonical integration technique. IEEE Trans Nucl Sci NS-30:2669–2671
37. Yoshida H (1990) Construction of higher order symplectic integrators. 150:262–268
38. Suris YB (1990) Hamiltonian methods of Runge–Kutta type and their variational interpretation. Math Mod 2:78–87
39. Candy J, Rozmus W (1991) A symplectic integration algorithm for separable Hamiltonian functions. J Comp Phys 92:230–256
40. McLachlan RI, Atela P (1992) The accuracy of symplectic integrators. Nonlinearity 5:541–562
41. Okunbor DI, Skeel RD (1992) Explicit canonical methods for Hamiltonian systems. Math Comput 59:439–455
42. Sanz-Serna JM (1992) The numerical integration of Hamiltonian systems. In: Cash JR, Gladwell I (eds) Computational ordinary differential equations. Clarendon Press, Oxford
43. Tuckerman M, Berne BJ, Martyna GJ (1992) Reversible multiple time scale molecular dynamics. J Chem Phys 97:1990–2001
44. Calvo MP, Sanz-Serna JM (1993) The development of variable-step symplectic integrators with applications to the two-body problem. Siam J Sci Comput 14:936–952
45. Sanz-Serna JM, Calvo MP (1993) Numerical Hamiltonian problems, 1st edn. Chapman and Hall, London
46. Gray SK, Noid DW, Sumpter BG (1994) Symplectic integrators for large scale molecular dynamics simulations: a comparison of several explicit methods. J Chem Phys 101:4062–4072
47. Gray SK, Manolopoulos DE (1996) Symplectic integrators tailored to the time-dependent Schrödinger equation. J Chem Phys 104:7099–7112
48. Saitoh I, Suzuki Y, Takahashi N (2001) The symplectic finite difference time domain method. IEEE T Magn 37:3251–3254

49. Huang Z, Wu X (2005) Symplectic partitioned Runge–Kutta scheme for Maxwell's equations. Int J Quant Chem 106:839–842
50. Sha W, Huang Z, Wu X , Chen M (2007) Application of the symplectic finite-difference time-domain scheme to electromagnetic simulation. J Comp Phys 225:33–50
51. Anderson N, Arthurs AM (1978) A variational principle for Maxwell's equations. Int J Electron 45:333–334
52. Masiello D, Deumens E, Öhrn Y (2005) Dynamics of an atomic electron and its electromagnetic field in a cavity. Phys Rev A 71:032108
53. Marsden JE, West M (2001) Discrete mechanics and variational integrators. Acta Numer 10:357–514
54. Qin H, Guan X (2008) Variational symplectic integrator for long-time simulations of the guiding-center motion of charged particles in general magnetic fields. Phys Rev Lett 100:035006
55. McLachlan RI, Gray SK (1997) Optimal stability polynomials for splitting methods, with application to the time-dependent Schrödinger equation. Appl Numer Math 25:275–286
56. Hairer E, Lubich C, Wanner G (2002) Geometric numerical integration: structure-preserving algorithms for ordinary differential equations, 1st edn. Springer, Berlin
57. Liu Y (1996) Fourier analysis of numerical algorithms for the Maxwell equations. J Comp Phys 124:396–416
58. Hoffman J (1992) Numerical methods for engineers and scientists, 1st edn. McGraw-Hill, New York
59. Berenger JP (1996) Perfectly matched layer for the FDTD solution of wave-structure interaction problems. IEEE Trans Antennas Propagat 51:110–117
60. Willets KA, Van Duyne RP (2007) Localized surface plasmon resonance spectroscopy and sensing. Annu Rev Phys Chem 58:267–297
61. Elghanian R, Storhoff JJ, Mucic RC, Letsinger RL, Mirkin CA (1997) Selective colorimetric detection of polynucleotides based on the distance-dependent optical properties of gold nanoparticles. Science 277:1078–1081
62. Borisov AG, Shabanov SV (2005) Lanczos pseudospectral method for initial-value problems in electrodynamics and its applications to ionic crystal gratings. J Comp Phys 209:643–664
63. Car R, Parrinello M (1985) Unified approach for molecular dynamics and density-functional theory. Phys Rev Lett 55:2471–2474
64. Runge E, Gross EKU (1984) Density-functional theory for time-dependent systems. Phys Rev Lett 52:997
65. Nedelec JC (1980) Mixed finite elements in $\mathbf{R}^3$. Numer Meth 35:315–341
66. Graglia RD, Wilton DR, Peterson AF (1997) Higher order interpolatory vector bases for computational electromagnetics. IEEE Trans Antennas Propagat AP-45:329–342
67. Dunvant DA (1985) High degree efficient symmetrical Gaussian quadrature rules for the triangle. Int J Numer Meth Eng 29:1129–1148
68. Keast P (1986) Moderate degree tetrahedral quadrature formulas. Comput Meth Appl Mech Eng 55:339–348
69. Saxon DS (1955) Lecture on the scattering of light. UCLA Department meteorological science report 9
70. Moharam MG, Grann EB, Pommet DA, Gayrold TK (1995) Formulation for stable and efficient implementation of the rigorous coupled-wave analysis of binary gratings. J Opt Soc Am A 12:1068–1076
71. Lalanne P, Morris GM (1996) Highly improved convergence of the coupled-wave method for TM polarization. J Opt Soc Am A 13:779–784
72. Benabbas A, Halte V, Bigot JY (2005) Analytical model of the optical response of periodically structured metallic films. Opt Express 13:8730–8745
73. McMahon JM, Gray SK, Schatz GC (2008) Dephasing of electromagnetic fields in scattering from an isolated slit in a gold film. In: Kawata S (ed) Plasmonics: nanoimaging, nanofabrication, and their applications IV, pp 703311/1–6

Chapter 4
Correlated Single-Nanoparticle Calculations and Measurements

Preface

The content that appears in this chapter has been largely adapted from the following publications:

McMahon JM, Wang Y, Sherry LJ, Van Duyne RP, Marks LD, Gray SK, Schatz GC (2009) Correlating the Structure, Optical Spectra, and Electrodynamics of Single Silver Nanocubes. J Phys Chem C 113:273–2735. doi:10.1021/jp8098736

Ringe E, McMahon JM, Sohn K, Cobley C, Xia Y, Huang J, Schatz GC, Marks LD, Van Duyne RP (2010) Unraveling the Effects of Size, Composition, and Substrate on the Localized Surface Plasmon Resonance Frequencies of Gold and Silver Nanocubes: A Systematic Single-Particle Approach. J Phys Chem C 114: 12511–12516

The experimental work that appears in this chapter was done by Wang Y, Sherry LJ, Ringe E, Sohn K, Cobley C, Xia Y, Huang J, Marks LD, and Van Duyne RP. Although, the experimental aspects are not discussed heavily, and the reader interested in such details is referred to Refs. [1–3].

4.1 Introduction

In Chap. 1, it was stated that the purpose of science is to describe the phenomena of nature. In this chapter, the question of how well can one correlate computational modeling with experiments at the nanoscale is addressed. In order to do this, experimental single-nanoparticle data (both optical responses and structural information) must be available [3–5], and a completely correlated computation and measurement must be made. This can be done by using structural information from experimental high-resolution transmission electron microscopy (HRTEM) measurements (which can resolve subnanometer features and has $\sim$10,000 times higher magnification capabilities than optical microscopy) in an FDTD simulation,

J. M. McMahon, *Topics in Theoretical and Computational Nanoscience*, Springer Theses, DOI: 10.1007/978-1-4419-8249-0_4,

which can then be compared with experimental LSPR spectroscopy measurements of the same nanoparticle. (In addition, three-dimensional and internal crystallographic structural information can be obtained by using HRTEM via various techniques, such as electron energy loss spectroscopy and diffraction.)

This chapter describes fully correlated computations and measurements of Ag nanocubes (Au nanocubes are briefly discussed as well), which are used to determine how well classical EM applies at the nanoscale. This chapter also explores the relationship between particle morphology, substrate composition, and LSPR spectral position(s) for these systems. The relative merits of the JC [6] and LH [7] Ag dielectric data for describing perfect crystalline nanoparticles are also addressed.

4.2 Computational Considerations

The calculations in this section were performed using FDTD as outlined in Sect. 3.2. Computational domains were discretized using grid spacings of 1.0 nm in all directions for the Ag nanocubes and 0.5 nm for the Au nanocubes, and terminated with CPML. The dielectric functions of Ag, Au, and carbon (C) were approximated using the D2L model fit to empirically determined dielectric data [6–8] over wavelengths important to this study ($\lambda = 300-800\,\text{nm}$); Appendix B. Plots of these fits, which will be relevant later, are shown in Fig. 4.1. Formvar and glass were both modeled using a constant RI of $n = 1.5$.

4.3 Correlation of Computation and Experiment

Colloidal Ag nanocubes were synthesized, and a correlated LSPR spectrum and HRTEM image of a single nanocube was obtained [3]; Fig. 4.2. From the HRTEM image, the face-to-face widths are found to be 85.6(5) and 80.9(5) nm along both in-plane directions, with two of the corners rounded to 11.0(5) nm radii of curvature and the other two rounded to 12.0(5) nm. The structural information available from this image is limited by the HRTEM resolution and the top-down perspective. However, a cube height of 83(1) nm can be assumed by taking the average of the in-plane face-to-face widths, and the radii of curvature of the bottom edges and corners can be inferred from the corresponding top corners.

Two main peaks are observed in the LSPR spectrum, a narrow peak at 399 nm and a broad peak at 461 nm. The assignment of these peaks has been analyzed in detail previously [9], where it was demonstrated that they are resonances associated with the tips of the nanocube, where the EM fields are the most intense. Two peaks result from the two dielectric environments present, and have adiabatic correlations with the dipole and quadrupole resonances of the cube in a homogeneous environment. By analogy to the corresponding resonances for spherical or

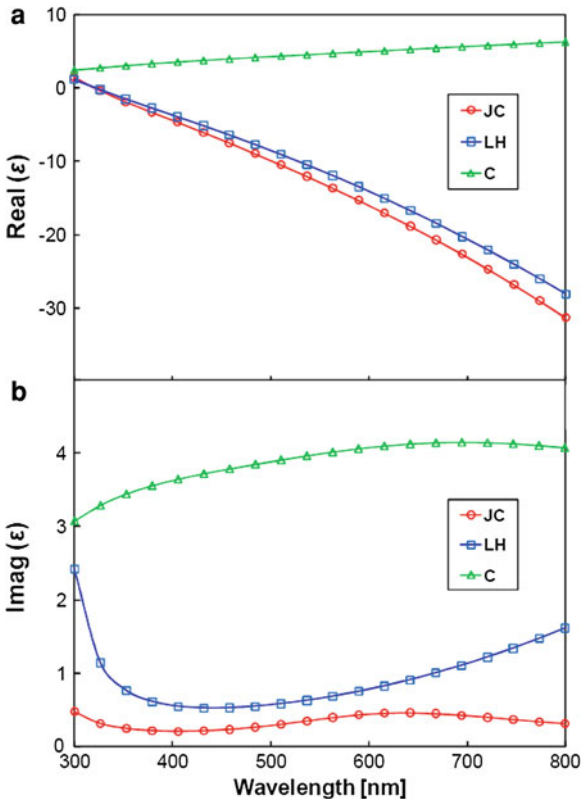

Fig. 4.1 **a** Real and **b** imaginary parts of the Ag (JC and LH) and C dielectric constants, evaluated using Eq. 2.23 with parameters from Appendix B

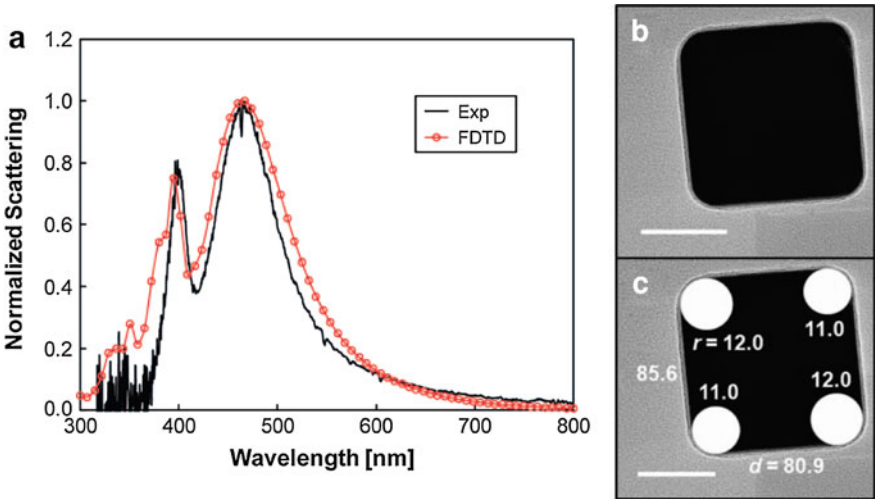

Fig. 4.2 Correlated LSPR–HRTEM measurement of a single Ag nanocube: **a** LSPR spectrum, **b** HRTEM image, and **c** same as **b** with overlaid structural parameters (in nm). The *inset white scale bars* in **b** and **c** represent 40 nm; the FDTD calculated scattering cross section is also shown in **a** with open *red circles*

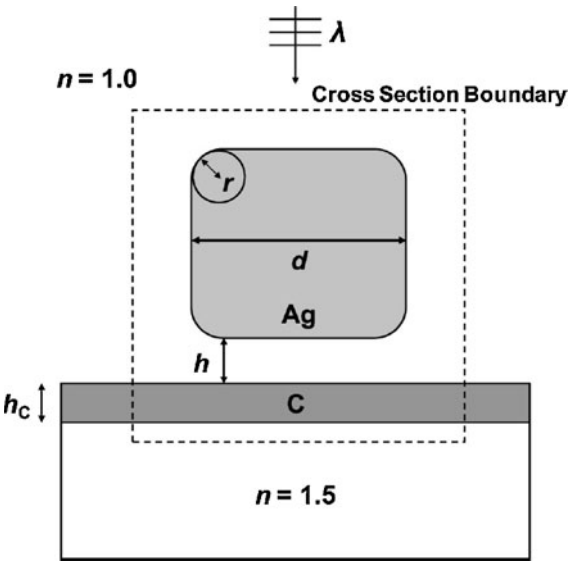

Fig. 4.3 Two-dimensional schematic diagram of the nanocube system modeled with FDTD. The parameters in the figure are defined in the text

spheroid-shaped particles, the dipole resonance is expected to be broader than the latter due to important radiative damping effects [10]. Figure 4.2a shows that this analogy holds for the cube resonances, with the linewidth of the higher wavelength peak being 2.03 times that of the lower wavelength one (experimental). Of course, other effects can also contribute to the linewidths, such as charge transfer processes between the particle and its surrounding medium (so-called "chemical interface damping" effects [11]). However, in the present application, the widths of the peaks seem to be well accounted for by electrodynamics calculations in which the particle and surrounding media are described using bulk dielectric constants; see Sect. 4.4.4.

For the FDTD calculations, the Ag nanocube was defined by its dielectric constant (JC or LH), face-to-face width (d), and radii of curvature of the corners and sides (r). Even though in the experiment each face-to-face width and radius of curvature of a corner or side is slightly different, for simplicity they were assumed identical for the calculations (which should not affect any of the presented results). The nanocube was spaced by a distance h from a C layer with thickness h_C. The C layer was placed on an infinite $n = 1.5$ substrate, and the surrounding medium was air $(n = 1.0)$. Figure 4.3 shows a two-dimensional schematic diagram of the described system. Scattering cross sections using normal incident illumination were calculated for comparison with the experimental LSPR spectrum. Even though in the experiment the cube is illuminated at an angle, and light is only collected for a range of angles around the forward direction [1], past studies of these effects indicate that calculations and experiment should nonetheless have similar LSPR spectra.

The scattering cross section of a nanocube with a face-to-face width of $d = 83\,\text{nm}$ and $r = 13\,\text{nm}$ of rounding, spaced $h = 2\,\text{nm}$ above an $h_C = 2\,\text{nm}$ thick C

layer, and modeled with JC dielectric data is shown in Fig. 4.2a, where excellent agreement with experiment is seen. The nanocube in this calculation was positioned at $h = 2$ nm above the C layer to simulate the effect that it may not be resting directly on the substrate. This spacing could arise from physisorbed or weakly chemisorbed water, carbon dioxide, and hydrocarbons on the substrate, as well as citrate, oxygen, and possibly hydroxyls on the nanocube surface. Depending on the thickness and dielectric constant of adsorbed molecules, the LSPR positions and linewidths will be affected, so other choices of h are considered below. Unfortunately, there is no way to estimate the dielectric constant(s) of this, so in the rest of this chapter it is taken to be 1.0.

4.4 System Parameters

To determine the effects that the nanocube parameters and local dielectric environment have on the optical response, as well as to determine if such parameters can be considered "free" to use to fit calculations to experiment, further FDTD calculations were carried out.

4.4.1 Face-to-Face Width

Scattering cross sections calculated for nanocubes modeled using the LH dielectric data with face-to-face widths of $d = 80$ and 90 nm and no corner rounding are compared to experiment in Fig. 4.4a. These parameters were chosen to elucidate only the effect due to the face-to-face width, and are at the extremes of the actual parameters seen in the HRTEM image (Fig. 4.2c). The $d = 80$ nm nanocube is seen to agree better with experiment, with the higher and lower wavelength peaks 21 and 10 nm closer to the experimental values, respectively. The difference in shifts is related to the smaller dielectric sensitivity of the lower wavelength (more quadrupolar) mode compared to the higher wavelength (more dipolar) mode, as found previously for other particle shapes [12]. This effect arises from the shorter range of the near-field decay of the lower wavelength mode. However, even for the $d = 80$ nm nanocube, the calculated lower and higher wavelength peak positions are 35 and 44 nm redshifted from the experimental values, respectively. Such discrepancy arises from the choice of parameters other than the face-to-face width, which also have a large effect on the positions of both peaks and their relative amplitudes (see the other sections below).

4.4.2 Corner Rounding

Scattering cross sections calculated for a $d = 80$ nm nanocube with corners and sides rounded to various radii of curvature and compared to experiment are shown in Fig. 4.4b. In addition, to increase the dielectric substrate sensitivity, the

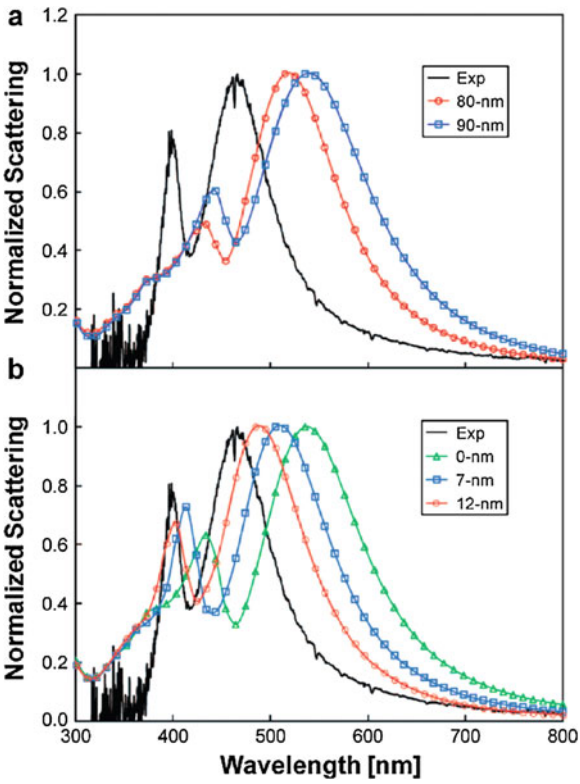

Fig. 4.4 FDTD calculated scattering cross sections of a Ag nanocube in response to **a** the variation in the face-to-face width, with no corner rounding and placed $h =$ 2 nm above the C layer, and **b** the variation in the radii of curvature of the corners and sides of a $d = 80$ nm nanocube placed $h = 1$ nm above the C layer. In both cases, the nanocube was modeled with the LH dielectric data, and the C layer was $h_C = 2$ nm thick

nanocube was moved to $h = 1$ nm above the C layer. The FDTD calculations show that the higher wavelength peak shifts by 41 nm as the radii increase from $r = 0$ to 12 nm, whereas the lower wavelength peak only shifts by 29.5 nm. These results are again related to the dielectric sensitivity of the quadrupolar mode versus the dipolar one, and they highlight the importance of the near-field contact area in determining the dielectric response of the nanocube, as has been found previously for other particle shapes [13].

4.4.3 Substrate Effect

Additional insight concerning the effect of the C layer is provided by scattering cross sections calculated with the nanocube placed directly on the substrate, with and without C present; Fig. 4.5. For these calculations, the contact area was made large by using a $d = 90$ nm nanocube with only $r = 7$ nm rounding, and the effect of C was heightened by making the layer $h_c = 3$ nm thick. The results show that the C layer has little effect on the lower wavelength peak, but redshifts and significantly damps the higher wavelength one. This is again related to the fact that

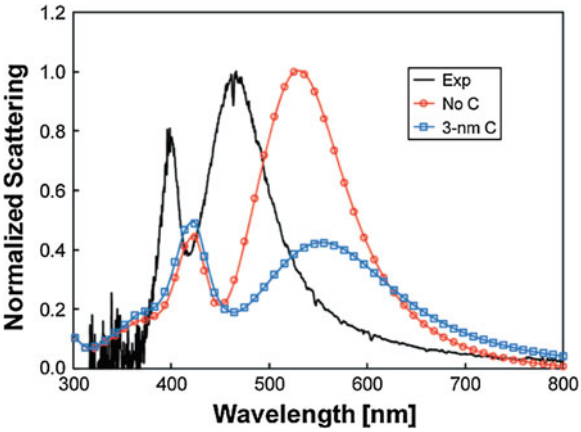

Fig. 4.5 FDTD calculated effect of the C layer on a $d = 90$ nm Ag nanocube. The nanocube was modeled with the LH dielectric data, has corners and sides rounded to $r = 7$ nm radii of curvature, and was placed directly on the substrate (with or without the C layer)

the near-field decay of the lower wavelength mode is much shorter than the higher wavelength one, and is therefore relatively unaffected by the substrate. These findings demonstrate the exquisite sensitivity of LSPR properties to substrate position and dielectric response, a result previously demonstrated by using gold nanorings [14]. Additionally, this demonstrates that the optimal parameters that were chosen to compare to experiment (Sect. 4.3) are unique.

4.4.4 Empirical Dielectric Data Sets

To assess the relative merits of the JC and LH Ag dielectric data when used to model perfect crystalline nanoparticles (such as the nanocubes in this chapter), scattering cross sections of a $d = 90$ nm nanocube with $r = 7$ nm rounding were calculated to compare to experiment for both sets of data; Fig. 4.6. For these calculations, there was no C layer, and the nanocube was placed directly on the $n = 1.5$ substrate. It is seen that the JC data gives results that agree much better with experiment, with the lower and higher wavelength peaks 10 and 21 nm closer to the experimental values, respectively. In addition, the JC dielectric data more accurately describes the width and relative amplitude of the lower wavelength peak.

Both the JC and LH dielectric data sets are inferred from thin films that are presumably polycrystalline or somewhat amorphous in character. It is therefore not a priori obvious why the JC dielectric data best describes the perfect crystalline nanocubes discussed here. However, it has been found that for crystalline Ag nanowires, the LH dielectric data provides a too lossy of description, and effectively reducing the loss (more consistent with the JC dielectric data) improves agreement with experiment [15]. Similar conclusions were also obtained in studies of Ag nanostrips made using electron-beam methods [16].

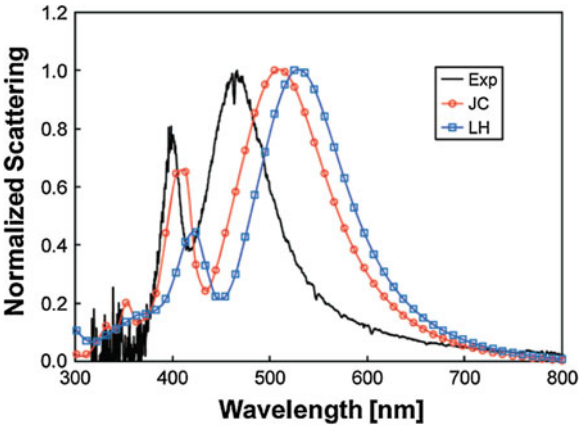

Fig. 4.6 Comparison of the JC to LH Ag dielectric data for modeling perfect crystalline nanoparticles, using a $d = 90$ nm nanocube as the example. The nanocube has corners and sides rounded to $r = 7$ nm radii of curvature and was placed directly on a $n = 1.5$ RI substrate with no C layer

4.5 Summary and Outlook

The discussion in this chapter shows that by carefully correlating computations and experimental measurements, near perfect agreement can be obtained. Additionally, for large nanostructures (i.e., those composed of many hundreds of thousands of atoms, or more), classical electrodynamics applied with bulk dielectric data is sufficient to describe the novel phenomena that arise. However, care must be taken in selection of the empirical dielectric data set to use, as it was demonstrated that the JC Ag dielectric data is more accurate for describing perfect crystalline nanoparticles compared to that of LH.

By varying structural parameters, the FDTD calculations showed strong sensitivity between the nanocube optical response and the face-to-face width, corner and side rounding, and the substrate. These results impose strict requirements on determination of such parameters (~ 1 nm resolution) if calculation and experiment are to match, and demonstrate that there are no "free parameters" (at least, geometric) that can be used in the simulations. These results are also beneficial for understanding of the relationship between optical response, structure, and dielectric environment of single nanoparticles. For example, the near-field contact area between a nanoparticle and its substrate was demonstrated to be particularly influential on the optical response.

Before ending this chapter, it should be noted that the results presented are not particular to the studied system (a Ag nanocube), nor should the following results be indicative that these results are particular only to nanocubes. Recently, similar correlated computations and measurements of Au nanocubes on Formvar and silicon nitride (Si_3N_4, a semiconductor) substrates were made that support the presented claims [2]. (Note that the Formvar substrate was similar to the one used in this chapter, except that the C layer was placed down, such that the nanocube was not in near-field contact with it. Additionally, for the calculations, Si_3N_4 was taken to have a constant RI of $n = 2.0$.)

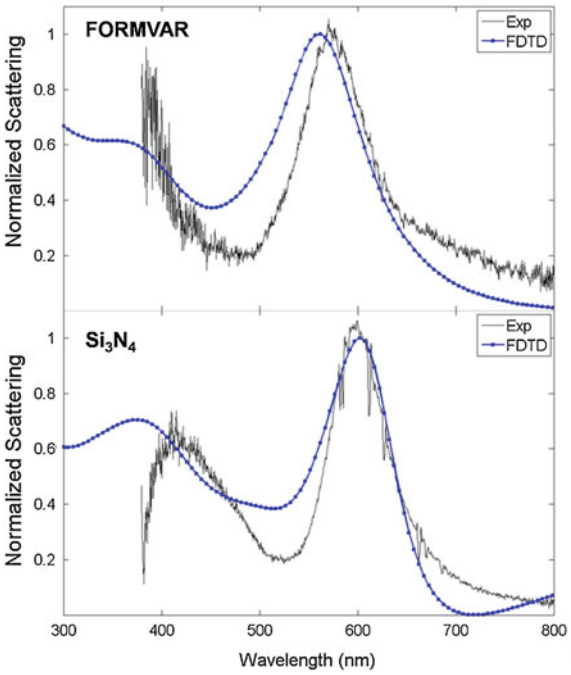

Fig. 4.7 Comparison of FDTD calculated *blue line with symbols* and experimental *solid black line* scattering from isolated Au nanocubes on *top* Formvar and *bottom* Si_3N_4. Structural information from HRTEM measurements was used in the FDTD calculations; the experimental spectra were obtained using correlated HRTEM–LSPR measurements

Using HRTEM, experimental nanocube parameters were obtained: for the Formvar substrate, $d = 84.0\,\text{nm}$ and $r = 15.2\,\text{nm}$, and for the Si_3N_4 one, $d = 74.2\,\text{nm}$ and $r = 12.7\,\text{nm}$. By using these parameters in FDTD calculations, excellent agreement with the experiments were again obtained; Fig. 4.7. However, for the nanocube on Formvar, the calculated dipolar LSPR appears 10 nm to the blue of the experimental one. This can be attributed to the fact that the FDTD calculations assume that there are no contaminants on the surface of the nanocube, which could possibly create a higher local dielectric environment, leading to a redshift in the experimental result. This would not have as significant of an effect on the Si_3N_4 results, where the substrate RI is already high (much like the small C layer in the Ag nanocube results).

References

1. McMahon JM, Wang Y, Sherry LJ, Van Duyne RP, Marks LD, Gray SK, Schatz GC (2009) Correlating the structure, optical spectra, and electrodynamics of single silver nanocubes.J Phys Chem C 113:2731–2735
2. Ringe E, McMahon JM, Sohn K, Cobley C, Xia Y, Huang J, Schatz GC, Marks LD, Van Duyne RP (2010) Unraveling the effects of size, composition, and substrate on the localized surface plasmon resonance frequencies of gold and silver nanocubes: a systematic single-particle approach. J Phys Chem C 114:12511–12516

3. Wang Y, Eswaramoorthy SK, Sherry LJ, Dieringer JA, Camden JP, Schatz GC, Van Duyne RP, Marks LD (2009) A method to correlate optical properties and structures of metallic nanoparticles. Ultramicroscopy 109:1110–1113
4. Scherer NF, Pelton M, Jin R, Jureller JE, Liu M, Kim HY, Park S, Guyot-Sionnest P (2006) Optical nonlinearities of metal nanoparticles: Single-particle measurements and correlation to structure. P Spie 6323:632309/1–632309/6
5. Mock JJ, Barbic M, Smith DR, Schultz DA, Schultz S (2002) Shape effects in plasmon resonance of individual colloidal silver nanoparticles. J Chem Phys 116:6755–6759
6. Johnson PB, Christy RW (1972) Optical constants of the noble metals. Phys Rev B 6:4370–4379
7. Lynch DW, Hunter WR (1985) Comments on the optical constants of metals and an introduction to the data for several metals. In: Palik ED (ed) Handbook of optical constants of solids, Academic Press, Orlando, pp 275–368
8. Arakawa ET, Dolfini SM, Ashley JC, Williams MW (1985) Arc-evaporated carbon films: optical properties and electron mean free paths. Phys Rev B 31:8097–8101
9. Sherry LJ, Chang SH, Schatz GC, Van Duyne RP, Wiley BJ, Xia Y (2005) Localized surface plasmon resonance spectroscopy of single silver nanocubes. Nano Lett 5:2034–2038
10. Kelly KL, Coronado E, Zhao LL, Schatz GC (2003) The optical properties of metal nanoparticles: the influence of size, shape, and dielectric environment. J Phys Chem B 107:668–677
11. Hovel H, Fritz S, Hilger A, Kreibig U, Vollmer M (1993) Width of cluster plasmon resonances: bulk dielectric functions and chemical interface damping. Phys Rev B 48:18178–18188
12. Sherry LJ, Jin R, Mirkin CA, Schatz GC, Van Duyne RP (2006) Localized surface plasmon resonance spectroscopy of single silver triangular nanoprisms. Nano Lett 6:2060–2065
13. Malinsky MD, Kelly KL, Schatz GC, Van Duyne RP (2001) Nanosphere lithography: effect of substrate on the localized surface plasmon resonance spectrum of silver nanoparticles. J Phys Chem B 105:2343–2350
14. Larsson EM, Alegret J, Käll M, Sutherland DS (2006) Sensing characteristics of NIR localized surface plasmon resonances in gold nanorings for application as ultrasensitive biosensors. Nano Lett 7:1256–1263
15. Laroche T, Vial A, Roussey M (2007) Crystalline structure's influence on the near-field optical properties of single plasmonic nanowires. Appl Phys Lett 91:123101
16. Drachev VP, Chettiar UK, Kildishev AV, Yuan HK, Cai W, Shalaev VM (2008)The Ag dielectric function in plasmonic metamaterials. Opt Express 16:1186–1195

Chapter 5
Optimal SERS Nanostructures

Preface

The content that appears in this chapter has been largely adapted from the following publications:

McMahon JM, Henry A-I, Wustholz KL, Natan MJ, Freeman RG, Van Duyne RP, Schatz GC (2009) Gold nanoparticle dimer plasmonics: finite element method calculations of the electromagnetic enhancement to surface-enhanced Raman spectroscopy. Anal Bioanal Chem 394:1819–1825. DOI: 10.1007/s00216-009-2738-4

Wustholz KL, Henry A-I, McMahon JM, Freeman RG, Valley N, Piotti ME, Natan MJ, Schatz GC, Van Duyne RP (2010) Structure-activity relationships in gold nanoparticle dimers and trimers for surface-enhanced raman spectroscopy. J Am Chem Soc 132:10903–10910

The experimental work that appears in this chapter was done by Wustholz KL, Henry A-I, Freeman RG, Natan MJ, and Van Duyne RP. Although, the experimental aspects are not discussed heavily, and the reader interested in such details is referred to Refs. [1, 2].

5.1 Introduction

Understanding the relationship between nanoparticle structure and activity represents a significant challenge, particularly for the field of SERS. However, the relationship between SERS enhancement factors (EFs) and the structural and optical properties of "hot spot" (a position of significant EM enhancement) containing systems remain elusive. For example, the role of LSPRs in SERS enhancements of nanoparticle aggregates, especially those containing hot spots, has only briefly been studied in detail [2]. Such determination of the structure–activity relationship (the latter meaning optical response and EM enhancement)

J. M. McMahon, *Topics in Theoretical and Computational Nanoscience*,
Springer Theses, DOI: 10.1007/978-1-4419-8249-0_5,

has been (experimentally) problematic for a number of reasons. First of all, the vast majority of SERS measurements are performed in bulk, using thousands to millions of nanoparticles, and a lot of information is lost in the averaging over an ensemble. Secondly, SMSERS substrates are polydisperse Ag nanoparticles that are randomly aggregated using salt; the heterogeneity and irreproducibility of these nanostructures makes it difficult to perform systematic investigations. Finally, previous studies showed no observable correlation between SMSERS intensity and the extinction properties of the aggregates [3], though these investigations were complicated by the fact that the location of the molecule on the substrate was not known.

It is desirable to address several outstanding questions about the nature of enhancement in structures containing hot spots, so that a better understand of SERS (the EM enhancement, at least) and possible design rules for optimal structures can be elucidated. (Such questions are also important from a fundamental perspective.) For example, what structural and optical features lead to large maximum and average enhancements? The first quantity is important for SMSERS, whereas the latter is important for regular SERS (the general detection of many molecules). Also, does a hot spot dominate the optical properties of a structure?

In the first half of this chapter, a fully correlated measurement, such as that described in Chap. 4, is used to determine the extent that classical electromagnetics correlates to SERS experiments at the single nanoparticle level (in regards to optical responses and EM enhancements). The relationship between structure and activity is then studied. The findings motivate the second half of this chapter, where the focus is on a system consisting of two cylindrical dimers, which are also modeled after a related experimental system. Such a system represents possibly the most simple (and maybe also the most efficient) setup that can generate large enhancements, a single junction. EM enhancements for a variety of nanoparticle separations, including the possibility of touching or coalesced nanoparticles, are then studied. From these results, it is possible to determine the conditions for SMSERS, and when many molecules are present, the fraction that contribute to (a specific percentage of) the SERS signal for various molecular diameters and nanoparticle separations. The work in the latter half of this chapter expands on previous theoretical studies of strongly coupled nanowires and spheres [4–8].

5.2 Computational Considerations

For the 3D calculations in Sect. 5.3, the structure was placed at the origin, and the computational domain was extended to 400 nm, sufficiently far so that Eq. 3.78 is (approximately) satisfied. Tetrahedral elements of the nanostructures were limited to $40\,\mathrm{nm}^3$, except for junction regions, which were limited to $10\,\mathrm{nm}^3$, and the outer regions to $90\,\mathrm{nm}^3$. The dielectric function of Au was modeled after the empirical data of JC [9] using the D2L model with parameters in Appendix B. Silicon dioxide (SiO_2) was taken to have a constant RI of $n = 1.5$.

For the 2D FEM calculations in Sect. 5.4, circular-shaped computational domains with a 300 nm radius were used with the cylinder dimer placed at the origin. Domains were discretized using triangular elements, with much smaller criteria than used for the 3D calculations. Within each element, the unknown field was approximated using linear nodal basis functions. The dielectric function of Au was modeled using the D2L model fit to the LH empirical data [10] over wavelengths important to this study ($\lambda = 300 - -800\,\text{nm}$); Appendix B. (The 2D FEM calculations that are briefly discussed in Sect. 5.3 were modeled similarly, except that the JC dielectric data was used.)

5.3 Structure–Activity in Nanostructures

In this section, a correlated TEM, dark-field Rayleigh scattering microscopy (hereon just scattering microscopy), SERS, and FEM study of aggregated Au nanoparticles encapsulated by a SiO_2 shell is discussed, which addresses the questions posed in Sect. 5.1 as well as determines the viability of using classical EM to reliably calculate SERS EFs. Such encapsulated Au nanoparticles are interesting and advantageous from both theoretical and experimental perspectives. Theoretically, the structure of such systems are simple. Experimentally, such systems can be used for the detection of biomolecules using Ag or Au nanoparticles as SERS "nanotags" [11], by functionalizing the surface to bind to a target analyte.

5.3.1 Correlated Computation and Experiment

A TEM image of a trimer structure containing three Au cores in an "L" shape is shown in Fig. 5.1a. Two junctions (presumed hot spots) are present, where Au cores in the vertically-oriented dimer appear to be separated by a gap-size (d_{gap}) of less than 1 nm, and the horizontally-oriented one seems to be coalesced ($d_{gap} < 0$). In order to measure the optical properties of this structure, a correlated TEM–LSPR measurement was used [12–15] (see also Chap. 4). The resulting scattering spectrum, Fig. 5.1b, contains three peaks, corresponding to dipolar and multipolar LSPRs [1].

Using a uniform coating of molecules that give a strong SERS signal (the details of which are not relevant to this discussion), the experimental EF can be determined by computing the ratio of SERS to normal Raman scattering, normalized for laser powers, acquisition times, and number of molecules [2]. [Note that a uniform coating is important, because below the experimental SERS signal is compared to calculated average $|\mathbf{E}(\omega)|^4$ enhancements, $\langle|\mathbf{E}(\omega)|^4\rangle$.] For the vibrational mode with the highest signal to noise ratio, the EF is found to be 1.8×10^8.

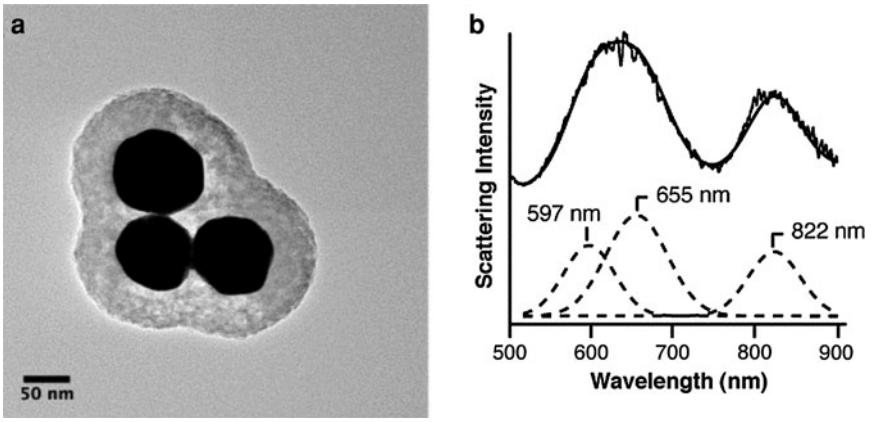

Fig. 5.1 Correlated experimental structural and optical characterization of an individual SERS nanostructure. **a** TEM image of a trimer in an L-shape, which is composed of three Au cores encapsulated in a SiO_2 shell. **b** Corresponding LSPR spectrum obtained by scattering microscopy (*solid line*), which is fit to a sum of three Gaussian functions (*dashed lines*)

The geometric parameters of the L-shaped nanostructure obtained from the TEM measurement were used for the FEM computations (much like the correlated measurements in Chap. 4); Fig. 5.2a. Accordingly, the diameters of the Au cores (d_{Au}) and SiO_2 shells (d_{shell}) were taken to be 100 nm and 50 nm, respectively. (For simplicity, all Au cores and shells were considered to be spherical.) By varying gap-sizes from -2 to 2 nm, it was found that in order to best reproduce the experimental LSPR spectrum, d_{gap} should equal to -0.35 nm, which is consistent with the TEM image in Fig. 5.1a (and also within the strict tolerances set in Chap. 4).

The resulting scattering cross section exhibits maxima at 578, 636, and 813 nm; Fig. 5.2b. Consistent with this, the experimental spectrum can be fit to three Gaussian functions centered at 597, 655, and 822 nm, as shown in Fig. 5.1b.

The corresponding structure-averaged EM enhancement $[\langle|\mathbf{E}(\omega)|^4\rangle]$ as a function of excitation wavelength evaluated 0.1 nm from the nanostructure surface is shown in Fig. 5.2b. Similar to computational studies of Au dimers [1] (see Sect. 5.4.2), $\langle|\mathbf{E}(\omega)|^4\rangle$ is relatively constant between 600 and 900 nm, varying by less than an order of magnitude in this region. An intensity profile of the EM enhancement at 633 nm, $|\mathbf{E}(633\,\text{nm})|^4$, is presented in Fig. 5.2c. It is seen that the trimer concentrates the field at the junctions between the Au cores, giving two hot spots, with a maximum EF of 3.2×10^9 and an average EF of 1.1×10^6. This latter value underestimates the experimentally obtained one by about two orders of magnitude, which is not surprising considering that surface roughness and chemical enhancements, both not accounted for in the calculations, will increase the overall enhancement [16, 17]. Thus, classical EM is found to do a decent job in describing SERS enhancements at the single nanoparticle level.

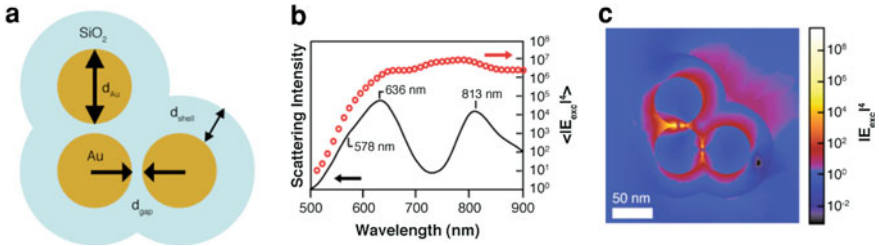

Fig. 5.2 FEM calculations of the L-shaped nanostructure. **a** d_{Au} and d_{shell} were set to 100 nm and 50 nm, respectively, consistent with the TEM measurement. **b** The best fit to the experimental scattering spectrum (*solid line*) was obtained using a value for d_{gap} of − 0.35 nm. $\langle|\mathbf{E}(\omega)|^4\rangle$ as a function of excitation wavelength is also shown, using *open red circles*. **c** $|\mathbf{E}(633\,\text{nm})|^4$ for the L-shaped structure reveals two hot spots, and the overall structure gives maximum and average EFs of 3.2×10^9 and 1.1×10^6, respectively

5.3.2 *Effects of Structure on Enhancement Factor*

The correlated structural, optical, and computational study of the L-shaped nanostructure discussed in Sect. 5.3.1 demonstrates that EM enhancements are localized in hot spots, and that the EF is relatively wavelength independent. This latter observation suggests that the LSPR need not match the excitation wavelength in order to achieve high enhancements. What, then, is the most important physical or optical property for establishing high EFs?

Number of Junctions

An immediate suggestion is that the optimal nanostructure is the one that contains the most junctions. However, a calculation of $\langle|\mathbf{E}(\omega)|^4\rangle$ for an analogous (2D) dimer (single junction) shows that systems with one junction give similar enhancements to those with two; Fig. 5.3. The dimers exhibit significantly different LSPR spectra than trimers (not shown—but a representative set can be found in Sect. 5.4 and also Ref. [1]), yet the EFs are within an order of magnitude; Figs. 5.2 and 5.3. These results strongly suggest that the number of junctions has relatively little impact on the overall EF. However, to determine if this is the case in general, it is necessary to study many structures, and also take other factors into account. Based on an in-depth experimental study utilizing a statistical analysis of 30 nanostructures (dimers, trimers of various configurations, etc.) [2], it is found that the above statements are valid. For example, a diverse set of LSPRs are seen, but the EF always varies by less than two orders of magnitude. Thus, the addition of more hot spots does not result in significant additional enhancements, but does, however, affect the LSPR spectra.

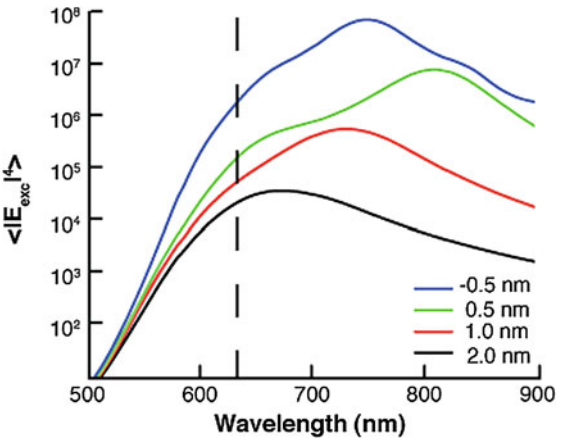

Fig. 5.3 Calculated $\langle|\mathbf{E}(\omega)|^4\rangle$ for a dimer, showing how the average enhancement is highly dependent on d_{gap}. The *dotted line* indicates 633 nm

Figure 5.3 also demonstrates that the average enhancement depends heavily on d_{gap} [a subject which will be revisited in Sect. 5.4 for $|\mathbf{E}(\omega)|^4$]. For example, by changing d_{gap} from -0.5 to 2 nm, the average EF at 633 nm (often, experiments are concerned with a fixed laser wavelength, 633 nm being one of them) is decreased by roughly two orders of magnitude. This result is also consistent with the aforementioned experimental statistical study of EFs [2].

Effect of d_{gap} in a Multi-gap Nanostructure

The fact that adding more hot spots to a nanostructure does not increase EF suggests that one hot spot dominates the overall enhancement. In order to study this more systematically, the enhancements for a trimer (or higher aggregate) system with one gap fixed and the other variable can be studied. $\langle|\mathbf{E}(\omega)|^4\rangle$ enhancements for (2D) L-shaped trimers with one gap fixed (along the vertical direction in the analogous Fig. 5.2) at either 2 or 0.5 nm, and the other (along the horizontal direction) variable from 2 to -0.5 nm, are shown in Figs. 5.4 and 5.5, respectively. A number of observations can be made from these results. First of all, the cross sections are quite different in all cases. Consistent with other studies [1], these results indicate that the optical response is a quantity highly dependent on the structure of the system (such as the number of nanoparticles, if a nanoparticle system), the value of d_{gap} (if the structure contains a junction), and the polarization of the incident light with respect to the structure (a topic which will not be discussed here).

By comparing the $\langle|\mathbf{E}(\omega)|^4\rangle$ enhancements to the cross sections, it can be seen that there is relatively little correlation between the two further supporting the claims in the previous section and experimental results [2] (not shown). Perhaps the most important observation from Figs. 5.4 and 5.5 is made by comparing the $\langle|\mathbf{E}(\omega)|^4\rangle$ results, where it is seen that the smallest gap always dominates them.

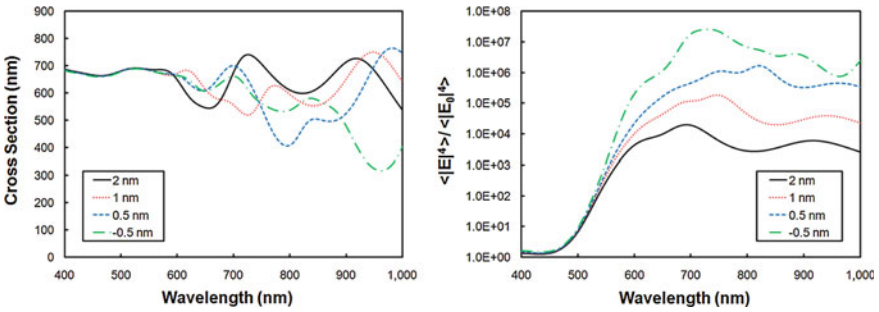

Fig. 5.4 Calculated $\langle|\mathbf{E}(\omega)|^4\rangle$ for a L-shaped trimer with one gap fixed at 2 nm and the other variable from 2 to −0.5 nm

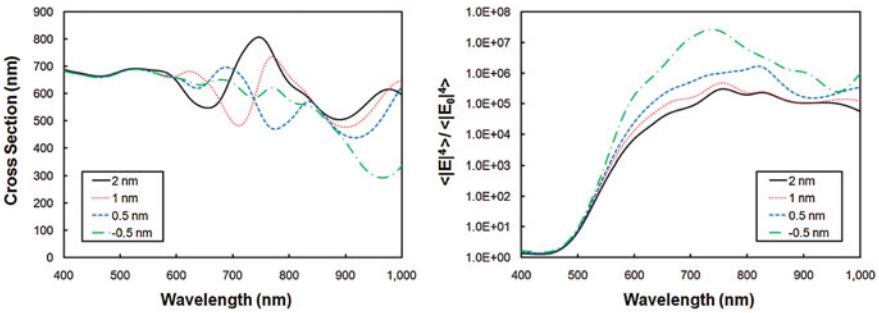

Fig. 5.5 Calculated $\langle|\mathbf{E}(\omega)|^4\rangle$ for a L-shaped trimer with one gap fixed at 0.5 nm and the other variable from 2 to −0.5 nm

For example, regardless of the fixed gap, it is seen that the maximum $\langle|\mathbf{E}(\omega)|^4\rangle$ occurs for a −0.5 nm variable gap-separation, which in both cases is the smallest gap. Additionally, for the 2-nm fixed gap, the $\langle|\mathbf{E}(\omega)|^4\rangle$ enhancements drastically increase with decreasing variable gap (2 nm → 1 nm → 0.5 nm → −0.5 nm). Considering that, in this case, the variable gap is always smaller than the fixed gap, it can be concluded that the smallest one has the most influence on $\langle|\mathbf{E}(\omega)|^4\rangle$. Additionally, for the 0.5-nm fixed gap, there is relatively little increase in $\langle|\mathbf{E}(\omega)|^4\rangle$ until the variable gap becomes −0.5 nm, even further supporting the idea that the smallest gap dominates the results.

5.4 Electromagnetic Contribution to SERS

Considering that only one junction dominates EM enhancements (see Sect. 5.3), dimer structures offer the ideal platform for studying them. In this section, FEM calculations are carried out to determine extinction spectra and the EM

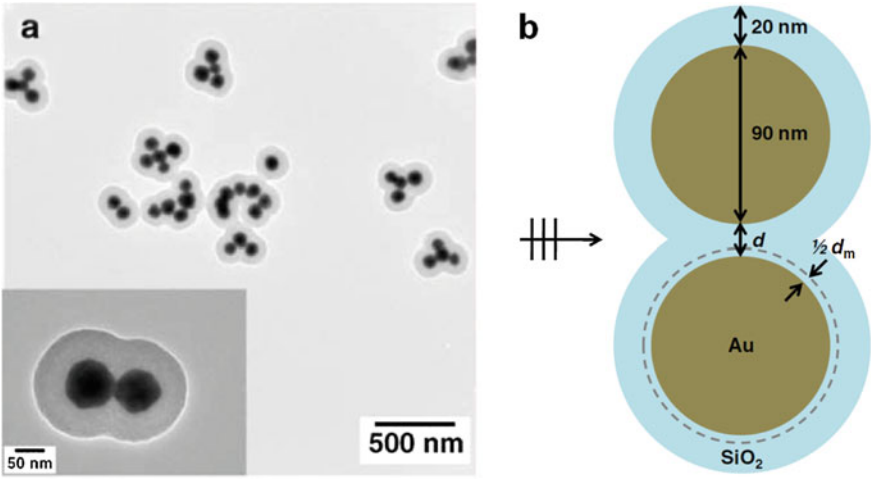

Fig. 5.6 **a** TEM image of SiO_2-coated Au nanoparticles, showing the sample is predominately aggregates; *inset* fused nanoparticle dimer. **b** Schematic diagram of the system modeled using FEM. The *dotted line* indicates the region where probability distributions, $P\left[|\mathbf{E}(\omega)|^4\right]$, were calculated

contribution to SERS, focusing on dimers comprised of 90 nm diameter Au cylindrical nanoparticles, which are assumed to be coated with SERS active molecules, and each with a 20-nm SiO_2 protective shell. These structures are modeled after experiment, and are very similar to those in Sect. 5.3. Note that the focus in this section is on maximum $|\mathbf{E}(\omega)|^4$ enhancements, rather than on average values.

5.4.1 Correlation of Computations with Experiment

TEM images of nanostructures can again be used to obtain realistic structure parameters for the calculations. Figure 5.6a demonstrates that a typical sample consists of aggregated particles containing approximately 2–5 nanoparticles, each with an average diameter of 90 nm and protective SiO_2 shell with width of 50 nm. For the FEM calculations, the focus is on a simple dimer structure with the nanoparticles arranged head-to-head; inset of Fig. 5.6a. The structure can be simplified by treating it as a 2D (nanowire) system, which should not strongly influence the LSPR spectra (although, slight blueshifts may occur because 2D resonances are often blueshifted relative to those in 3D).

A schematic diagram of the system under consideration is shown in Fig. 5.6b: two 90-nm diameter infinite Au cylinders, each with a 20 nm thick SiO_2 shell (used to reduce computational cost, but which behaves similarly to a 50-nm shell), are separated by a distance d and illuminated using light polarized along the dimer axis.

5.4.2 Optical Properties

Extinction Spectra

Figure 5.7 presents extinction spectra for spacings of $d = 5$ to -10 nm (again, negative distances correspond to fused nanoparticles). The $d = 5$ nm spectrum is fairly close to what is found for a Au monomer, a single strong resonance near 600 nm, corresponding to the dipolar LSPR [18]. When d is reduced to 1 nm, the dipole resonance redshifts to around 700 nm, and high-order multipole resonances begin to appear near 600 nm, related to different distributions of polarization charge (see Sect. 1.1.1). These results are consistent with those found by Kottman and Martin for coupled Ag nanowires [5]. The redshifting increases as d decreases; and curiously, the fused structure with $d = -1$ nm is quite similar to that with $d = 0.25$ nm. For d values below -1 nm, the dipole resonance blueshifts, eventually falling below 700 nm for $d = -10$ nm, consistent with the structure becoming less prolate.

Maximum EM Enhancements

Figure 5.8 shows the maximum EM enhancements $[|\mathbf{E}(\omega)|^4]$, regardless of the position (although, below it is shown that this always occurs at the same spot), for the d values under consideration. Broader peaks are seen than in Fig. 5.7, along with a sharp rise as d is decreased. In particular, significant changes are observed as d is decreased from 1 to 0.5 to 0.25 nm, where the maximum EM enhancement increases by three orders of magnitude, from approximately 10^8 to 10^9 to 10^{10}, respectively. Notice that a separation of $d = 0.5$ nm is needed to get EM enhancements above 10^8, a value considered necessary for SMSERS.

For all separations, the EM enhancement peaks near (but not necessarily at) the LSPR positions in the extinction spectra; Fig. 5.7. However, based on the analysis in Sect. 5.3, it should be understood that this is probably due to the simplicity of the dimer structure, and is not a result that will hold in general. In addition, the dipolar resonance (most red) is seen to always be the most intense, consistent with results previously demonstrated by Hao and Schatz [19]. Furthermore, regardless of the wavelength, the maximum EM enhancement is always located at the junction (along the dipolar axis). Considering that higher-order LSPRs are not oriented along this axis, it is surprising that even in these cases this is where the maximum EM enhancements are found (often LSPR symmetries are associated with high enhancements, but in these situations it is possible that hybrid high-order multipole–dipole resonances can occur [20]). Although, this effect is understandable when the viewpoint is taken that the nanoparticle dimer acts as an antenna, concentrating EM fields at the junction. Figure 5.9a shows $|\mathbf{E}(\omega)|^4$ at $\lambda = 785$ nm for $d = 0.25$ nm, demonstrating the extent of this localization, which is approximately 4×0.25 nm.

As soon as the nanoparticles fuse ($d < 0$ nm), an extremely large increase in EM enhancements (over four orders of magnitude compared to $d = 0.25$ nm) to

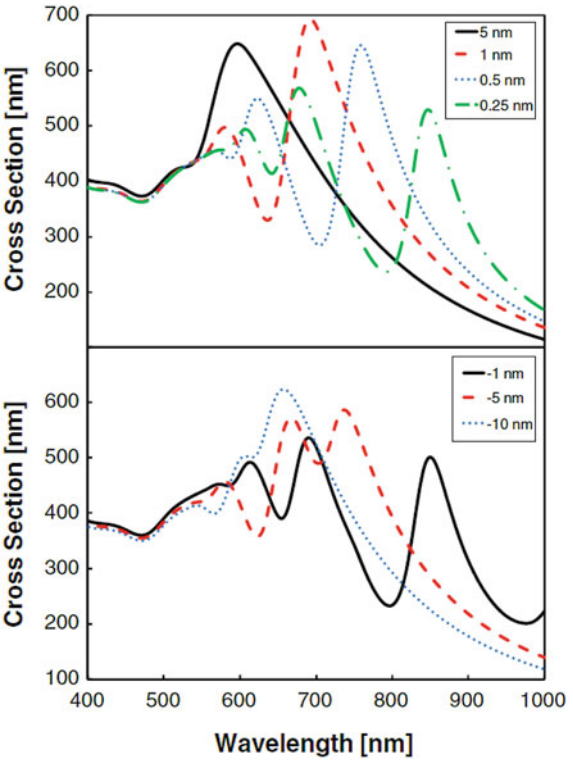

Fig. 5.7 Extinction cross sections for nanoparticle separations of $d = 5$ to -10 nm, for *top* positive and *bottom* negative separations

greater than 10^{14} as well as an extreme redshift of the dipolar LSPR to the red of 1,000 nm is observed. These EM enhancements are significantly larger than has been reported in most of the past EM studies of fused structures [5, 21, 22], and in fact they suggest that in these systems non-resonant SMSERS should be possible. The reason for this exotic behavior is that the crevice formed by the dimer overlap is incredibly sharp, yet it is not severe enough to exclude the positions where strong localization of the EM enhancement occurs. Figure 5.9b shows $|\mathbf{E}(\omega)|^4$ at $\lambda = 785$ nm for $d = -1$ nm, where it is seen that the large EM enhancements come at the expense of the field being further localized to an area less than 0.1×0.1 nm, consistent with that previously found for arrays of fused cylinder structures [22]. As the dimer overlap is further increased, the EM enhancements rapidly decrease.

5.4.3 Molecular Effects

To correlate the EM enhancements with a SERS signal, it is first necessary to assume that molecules with a diameter d_m form a close packed monolayer around both nanoparticles (as long as they can fit, which is similar to the actual

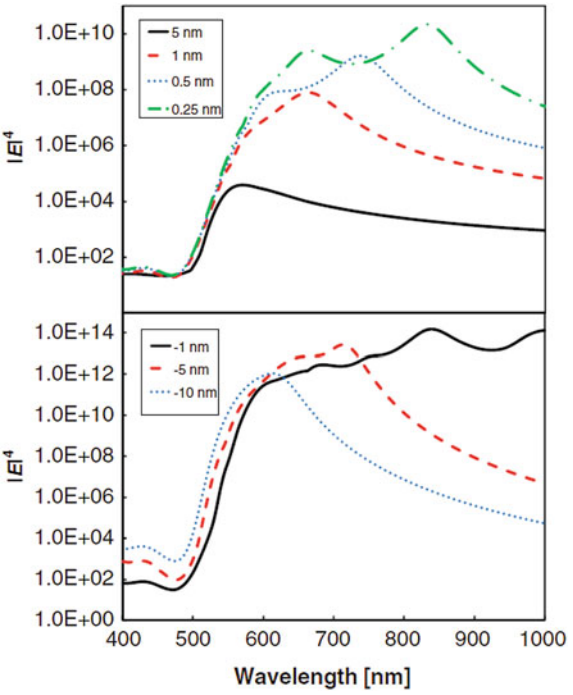

Fig. 5.8 Maximum EM enhancements for nanoparticle separations of $d = 5$ to -10 nm, for *top* positive and *bottom* negative separations

experimental system outlined in Sect. 5.3). Probabilities of finding $|\mathbf{E}(\omega)|^4$ at 1/2 of d_m from the nanoparticle surface, $P\left[|\mathbf{E}(\omega)|^4\right]$ (shown as a dotted line in Fig. 5.6b), are shown in Fig. 5.10 for $\lambda = 785$ nm (another common experimental wavelength). The purpose of this is twofold: (1) to take into account that even though some structures give orders of magnitude greater EM enhancements than others (e.g., $d = -1$ nm), they are often highly confined (see Fig. 5.9); and (2) to take into consideration that large molecules will not be able to fit into too small crevices and junctions where the EM enhancements are the most intense

Three molecular diameters were considered, $d_m = 0.25, 1.0,$ and 2.0 nm, for two nanoparticle separations, $d = 0.25$ and -1 nm. Separations of $d = 5$ to -20 nm (which are not of direct relevance for this discussion) can be found in the Supporting Information of Ref. [1]. For all cases, almost 100% of $P\left[|\mathbf{E}(\omega)|^4\right]$ is for $|\mathbf{E}(\omega)|^4$ indicating that over the majority of the structure there is essentially no EM enhancement, which is confirmed by comparison with Fig. 5.9. A gradual decline in $P\left[|\mathbf{E}(\omega)|^4\right]$ with increasing $|\mathbf{E}(\omega)|^4$ is observed, indicating that higher EM enhancements are more strongly localized. However, it should be pointed out that for $d_m = 0.25$ nm there is a strong drop in $P\left[|\mathbf{E}(\omega)|^4\right]$ near $|\mathbf{E}(\omega)|^4 = 10^8$, which then increases with $|\mathbf{E}(\omega)|^4$. By comparison with Fig. 5.9, this is seen to

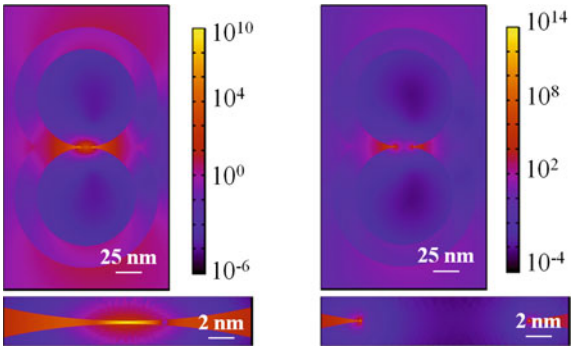

Fig. 5.9 $|\mathbf{E}(\omega)|^4$ at $\lambda =$ 785 nm for nanoparticle separations of *left* $d =$ 0.25 nm and *right* $d = -1$ nm.

occur because $|\mathbf{E}(\omega)|^4$ decays significantly to the right of the junction region, a "shadowing" effect arising from the close nanoparticle spacing. The molecular size effects are apparent in Fig. 5.10, where it is seen that the larger the molecule, the lower the maximum value of $|\mathbf{E}(\omega)|^4$. In addition, for all cases, except when $d_m = 0.25$ nm and $d = 0.25$ nm, a sharp drop is seen in $P\left[|\mathbf{E}(\omega)|^4\right]$ for the highest $|\mathbf{E}(\omega)|^4$values, indicating that the molecules cannot sample the entire maximum $|\mathbf{E}(\omega)|^4$ region.

Two ways of correlating the EM enhancements with a SERS signal can be used. First, $P\left[|\mathbf{E}(\omega)|^4\right]$ can be multiplied by $|\mathbf{E}(\omega)|^4$, giving an expected signal distribution as a function of $|\mathbf{E}(\omega)|^4$; Fig. 5.10. For $d = 0.25$ nm, the highest values of $|\mathbf{E}(\omega)|^4$ are dominant. This is understandable, considering that for positive separations, all of the molecules can sample locations with the highest EM enhancements. For $d = -1$ nm, the next to highest values are seen to be dominant. This result is also understandable, as the sharp crevices exclude molecules of any size from the maximum $|\mathbf{E}(\omega)|^4$ region.

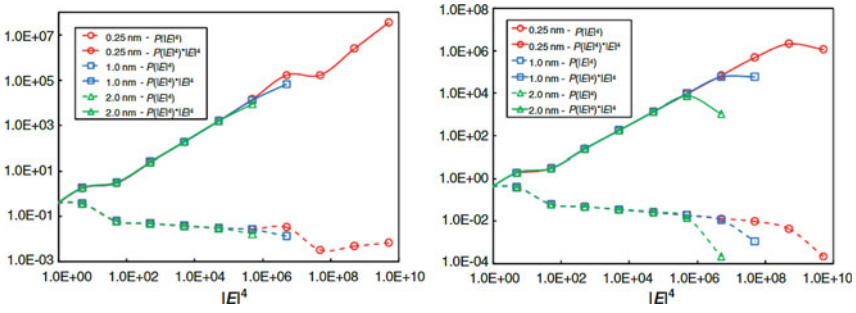

Fig. 5.10 Probability distributions of $|\mathbf{E}(\omega)|^4$,$P\left[|\mathbf{E}(\omega)|^4\right]$, for nanoparticle separations of *left* $d = 0.25$ nm and *right* $d = -1$ nm.

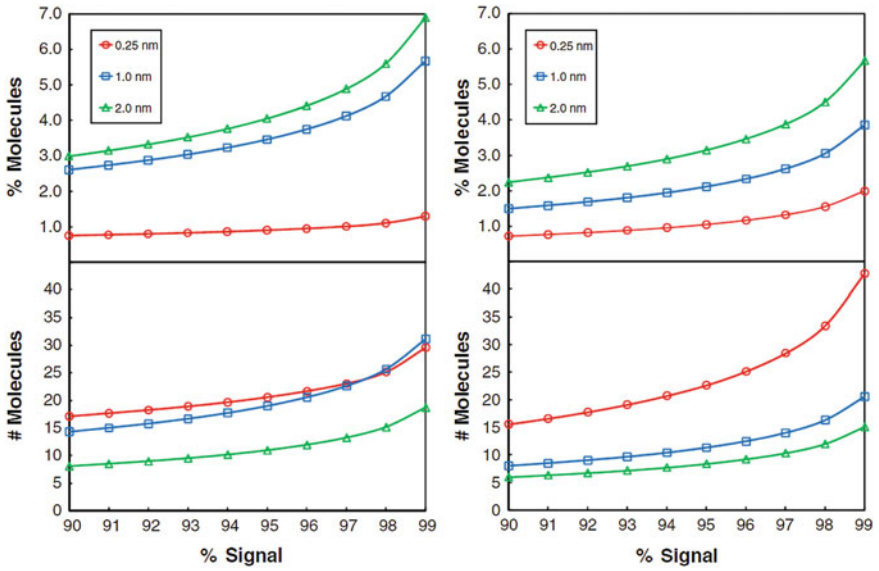

Fig. 5.11 *Top* percent and *bottom* corresponding number of molecules that contribute to the SERS signal for nanoparticle separations of *left* $d = 0.25$ nm and *right* $d = -1$ nm.

Another way of correlating the EM enhancements with a SERS signal is to first add up $|\mathbf{E}(\omega)|^4$ at each position to get an average signal. By then sorting the $|\mathbf{E}(\omega)|^4$ values, the percentage (and number) of molecules that contribute to a certain percentage of the signal can be determined; Fig. 5.11. For example, for $d = -1$ nm, less molecules (percentage wise) are predicted to contribute to more of the signal compared to $d = 0.25$ nm. Interestingly, for all d and d_m, 3% less than of the molecules (a total of approximately 5–15) contribute to greater than 90% of the signal.

5.5 Summary and Outlook

In this chapter, correlated TEM, LSPR, SERS, and FEM studies of dimer and trimer nanostructures were discussed. Classical electrodynamics was demonstrated to be accurate for calculating SERS enhancements, based on a comparison of the experimental SERS signal with FEM calculations of $\langle|\mathbf{E}(\omega)|^4\rangle$. FEM calculations also showed that that EFs do not correlate with aggregation state [14], meaning that a single hot spot between two particles is sufficient, and the extra ones do not not contribute significantly to the signal. However, the EFs were found to depend significantly on the gap size, d_{gap}, especially for spacings of less than 1 nm, where enhancements as high as 10^{14} were seen in the crevices of fused structures.

Additionally, for structures with more than one hot spot, the one with the smallest d_{gap} was seen to dominate the overall enhancement. For small enough gaps, the EM contribution to SERS in junction structures was found to completely dominate the signal, which in favorable cases could enable the possibility of SMSERS.

Related to these findings is that, in contrast to what has been observed for isolated nanoparticles [23], the LSPR has little bearing on SERS EFs, consistent with previous investigations of nanoparticle aggregates [3]. Although, both the LSPRs and SERS EFs are highly dependent on d_{gap}, just not necessarily each other. The 329 interested reader is referred to Ref. [2] for additional experimental and theoretical details.

The ramifications of these findings for the design of SERS-active nanoparticle structures are significant. Molecular recognition approaches that bring nanoparticles within close but not intimate $(d_{gap} < 1\,nm)$ proximity will not lead to structures with high EFs. Technically, a gap is not required at all. It is the creation of hot spots, where two particles are in subnanometer proximity or have coalesced to form crevices $(d_{gap} < 0\,nm)$, that is paramount to achieving the maximum possible SERS enhancement.

Additionally in this chapter, by assuming a uniform coating of SERS molecules around both nanoparticles of a dimer, it was systematically determined (by intensity probability distribution information for molecules of various sizes) that smaller molecules can, in some cases, exhibit larger EFs due to the high localization of EM enhancements. Additionally, for small separations, less than 3% of molecules always contribute to greater than 90% of a SERS signal, which, regardless of the separation, the highest (or next to highest) EM enhancements always dominate. These results demonstrate some of the challenges associated with observing SMSERS. For moderate concentrations, a few molecules will always give the majority of the signal, and for low concentrations, single molecules must find (and be able to fit in) highly localized positions of EM enhancement.

Before ending this chapter, it should be emphasized that the importance of nonlocal dielectric effects was not included in the calculations. Analogous systems (in regards to EM enhancements) will be further addressed in Chap. 8 with such effects included.

References

1. McMahon JM, Henry A-I, Wustholz KL, Natan MJ, Freeman RG, Van Duyne RP, Schatz GC (2009) Gold nanoparticle dimer plasmonics: finite element method calculations of the electromagnetic enhancement to surface-enhanced Raman spectroscopy. Anal Bioanal Chem 394:1819–1825
2. Wustholz KL, Henry A-I, McMahon JM, Freeman RG, Valley N, Piotti ME, Natan MJ, Schatz GC, Van Duyne RP (2010) Structure-activity relationships in gold nanoparticle dimers and timers for surface-enhanced raman spectroscopy. J Am Chem Soc 132:10903–10910

3. Michaels AM, Nirmal M, Brus LE (1999) Surface enhanced Raman spectroscopy of individual Rhodamine 6G molecules on large Ag nanocrystals. J Am Chem Soc 121:9932
4. Xu H (2004) Theoretical study of coated spherical metallic nanoparticles for single-molecule surface enhanced spectroscopy. Appl Phys Lett 85:5980–5982
5. Kottmann JP, Martin OJF (2001) Plasmon resonant coupling in metallic nanowires. Opt Express 8:655–663
6. Aravind PK, Nitzan A, Metiu H (1981) The interaction between electromagnetic resonances and its role in spectroscopic studies of molecules adsorbed on colloidal particles or metal spheres. Surf Sci 110:189–204
7. Vanin AI (1995) Surface-amplified Raman scattering of light by molecules adsorbed on groups of spherical particles. J Appl Spect 62:32–36
8. Félidj N, Aubard J, Lévi G (1999) Discrete dipole approximation for ultraviolet–visible extinction spectra simulation of silver and gold colloids. J Chem Phys 111:1195
9. Johnson PB, Christy RW (1972) Optical constants of the noble metals. Phys Rev B 6:4370–4379
10. Lynch DW, Hunter WR (1985) Comments on the optical constants of metals and an introduction to the data for several metals. In: Palik ED (ed) Handbook of Optical Constants of Solids. Academic Press, Orlando, pp 275–368
11. Doering WE, Piotti ME, Natan MJ, Freeman RG (2007) SERS as a foundation for nanoscale, optically detected biological labels. Adv Mater 19:3100–3108
12. McMahon JM, Wang Y, Sherry LJ, Van Duyne RP, Marks LD, Gray SK, Schatz GC (2009) Correlating the structure, optical spectra, and electrodynamics of single silver nanocubes. J Phys Chem C 113:2731–2735
13. Ringe E, McMahon JM, Sohn K, Cobley C, Xia Y, Huang J, Schatz GC, Marks LD, Van Duyne RP (2010) Unraveling the effects of size, composition, and substrate on the localized surface plasmon resonance frequencies of gold and silver nanocubes: a systematic single-particle approach. J Phys Chem C 114:12511–12516
14. Camden JP, Dieringer JA, Wang Y, Masiello DJ, Marks LD, Schatz GC, Van Duyne RP (2008) Probing the structure of single-molecule surface-enhanced Raman scattering hot spots. J Am Chem Soc 130:12616–12617
15. Wang Y, Eswaramoorthy SK, Sherry LJ, Dieringer JA, Camden JP, Schatz GC, Van Duyne RP, Marks LD (2009) A method to correlate optical properties and structures of metallic nanoparticles. Ultramicroscopy 109:1110–1113
16. Aikens CM, Schatz GC (2006) TDDFT studies of absorption and SERS spectra of pyridine interacting with Au_{20}. J Phys Chem A 110:13317–13324
17. Laor U, Schatz GC (1981) The role of surface roughness in surface enhanced Raman spectroscopy (SERS): the importance of multiple plasmon resonances. Chem Phys Lett 82:566–570
18. Bohren CF, Huffman DR (1983) Absorption and Scattering of Light by Small Particles. Wiley, New York
19. Hao E, Schatz GC (2004) Electromagnetic fields around silver nanoparticles and dimers. J Chem Phys 120:357–366
20. Prodan E, Radloff C, Halas NJ, Nordlander P (2003) A hybridization model for the plasmon response of complex nanostructures. Science 302:419–422
21. Xu H, Aizpurua J, Käll M, Apell P (2000) Electromagnetic contributions to single-molecule sensitivity in surface-enhanced Raman scattering. Phys Rev E 62:4318–4324
22. García-Vidal FJ, Pendry JB (1996) Collective theory for surface enhanced Raman scattering. Phys Rev Lett 77:1163–1166
23. McFarland AD, Young MA, Dieringer JA, Van Duyne RP (2005) Wavelength-scanned surface-enhanced Raman excitation spectroscopy. J Phys Chem B 109:11279–11285

Chapter 6
Nanostructured Metal Films

Preface

The content that appears in this chapter has been largely adapted from the following publications:

Schatz GC, McMahon JM, Gray SK (2007) Tailoring the parameters of nanohole arrays in gold films for sensing applications. Proc SPIE 6641 664103/1–8 doi:10.1117/12.790647

McMahon JM, Henzie J, Odom TW, Schatz GC, Gray SK (2007) Tailoring the sensing capabilities of nanohole arrays in gold films with Rayleigh anomaly-surface plasmon polaritons. Opt Express 15:18119–18129. doi:10.1364/OE.15.018119

Gao H, McMahon JM, Lee MH, Henzie J, Gray SK, Schatz GC, Odom TW (2009) Rayleigh anomaly-surface plasmon polariton resonances in palladium and gold subwavelength hole arrays. Opt Express 17:2334–2340. doi:10.1364/OE.17.002334

Odom TW, Gao H, McMahon JM, Henzie J, Schatz GC (2009) Plasmonic superlattices: hierarchical subwavelength hole arrays. Chem Phys Lett 483: 187–192. doi:10.1016/j.cplett.2009.10.084

McMahon JM, Gray SK, Schatz GC (2011) Surface nanophotonics theory. In: Wiederrecht G (ed) Comprehensive nanoscience and technology. Elsevier, Amsterdam

The experimental work that appears in this chapter was done by Gao H, Henzie J, Lee MH, and Odom TW. Although, the experimental aspects are not discussed heavily, and the reader interested in such details is referred to Refs. [1–5].

Even though the discussion on isolated holes in Sect. 6.3 and other periodic systems in Sect. 6.7 was not work performed directly by the author, it does appear in his published work [1]. Additionally, these discussions are very short, and combined with the rest of this chapter and the work on isolated slits in Sect. 7.4 makes this chapter a thorough reference for nanostructured metal films, particularly subwavelength arrays of holes and other structures.

J. M. McMahon, *Topics in Theoretical and Computational Nanoscience*,
Springer Theses, DOI: 10.1007/978-1-4419-8249-0_6,

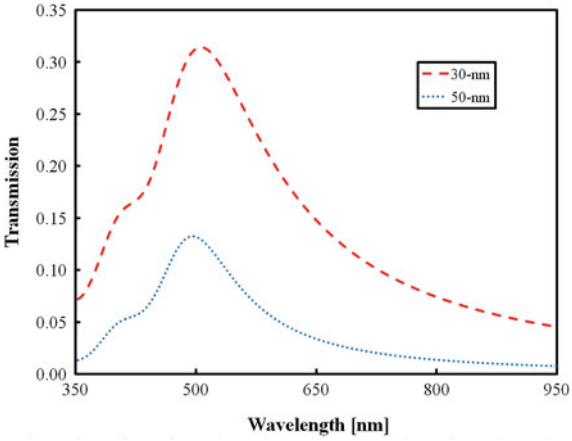

Fig. 6.1 Transmission through 30 and 50 nm thick Au films on a glass substrate in air

6.1 Introduction and Theoretical Background

Many mechanisms for the interaction of light with nanostructured metal films are possible. As briefly outlined in Chap. 1, such interactions lead to a variety of interesting phenomena, and allow for the possibility to control light at the nanoscale. One of these interactions is through surface plasmons (SPs), oscillations of electron density at a metal–dielectric interface. Under certain circumstances, light can be efficiently coupled into them, resulting in a SPP [6], which can lead to EOT relative to transmission through a metal film without SPPs [7]. For future reference, the transmission through 30 and 50 nm thick Au films (obtainable from a simple analytical formula [8]) on a glass substrate (RI of $n = 1.5$) in air are shown in Fig. 6.1.

The peak structure in Fig. 6.1 arises from the direct transmission of light through the Au film, which occurs when the real part of the relative permittivity is +1 (vide infra), leading to transparency in the absence of damping. On a flat metal film–dielectric interface, SPs propagate in the plane with a wavevector magnitude of [6]

$$k_{\mathrm{SP}} = \frac{\omega}{c}\left(\frac{\varepsilon_{\mathrm{M}}\varepsilon_r}{\varepsilon_{\mathrm{M}} + \varepsilon_r}\right)^{1/2}, \tag{6.1}$$

where $\varepsilon_{\mathrm{M}} = \varepsilon(\omega)$ is the relative permittivity of the metal, Fig. 6.2 shows ε_{M} for Au and Ag over the range $\lambda = 300$–800 nm calculated using the D2L model with parameters from Appendix B, consistent with the LH [9] and JC [10] empirically determined dielectric data, respectively.

Figure 6.2 shows that $\Re(\varepsilon_{\mathrm{M}})$ decreases over the range 300–800 nm, becoming negative and large in magnitude. This quantity corresponds to the ability of the metal to easily polarize against the incident field. In addition, for a planar metal film, this leads to an increase in reflection and decrease in transmission, as can be

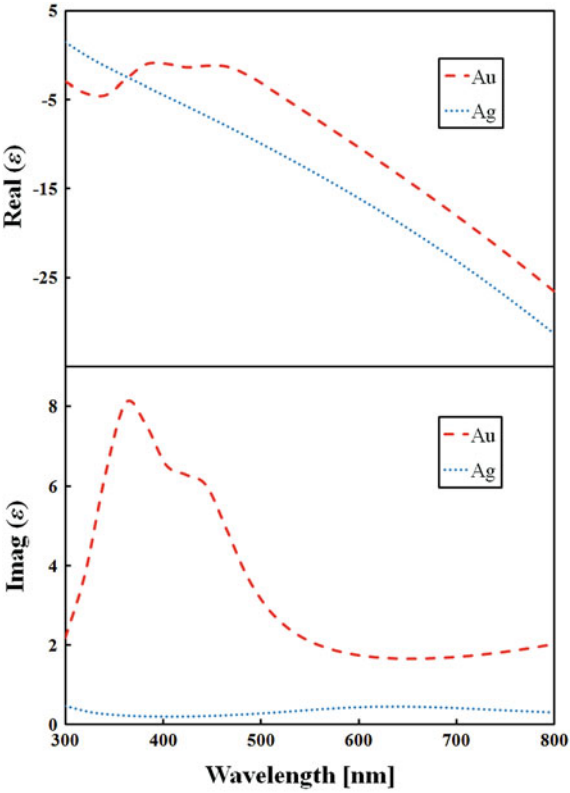

Fig. 6.2 Relative permittivities (ε_M) of Au and Ag calculated with the D2L model using parameters from Appendix B

seen by comparison with Fig. 6.1. Figure 6.2 also shows that both Au and Ag have a nonzero $\Im(\varepsilon_M)$, which corresponds to absorption in the metal. As a side note, the structure near 400 nm for Au arises from one of the aforementioned interband transitions, and is not directly responsible for any plasmonic effects.

Figure 6.3 shows the SP wavevector magnitude, Eq. 6.1, for Au and Ag metal film–air interfaces, as well as the free-space wavevector magnitude

$$k_0 = \frac{\omega}{c} = \frac{2\pi}{\lambda_0}, \tag{6.2}$$

where λ_0 the incident wavelength, as a function of ω (proportional to the energy), known as a dispersion diagram. Note that in a dielectric medium with permittivity (ε_r) the wavevector magnitude becomes

$$k = \frac{\omega}{c}\varepsilon_r^{1/2}. \tag{6.3}$$

For most ω, it is seen that $k_{SP} > k_0$, which is a result of $\varepsilon_M < 0$. In addition, near $\omega = 3.8 \times 10^{15}\text{s}^{-1}(\lambda = 496\,\text{nm})$ for Au and $\omega = 5.5 \times 10^{15}\text{s}^{-1}(\lambda = 342\,\text{nm})$ for Ag, a backbending of ck is seen. This is due to the complex nature of ε_M, which

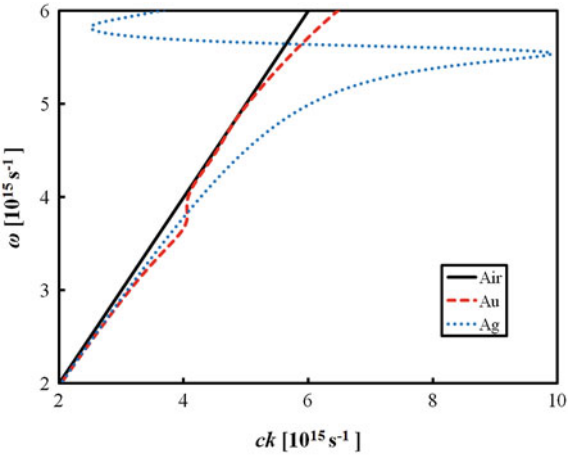

Fig. 6.3 Dispersion diagrams of light in air compared to SPs on Au and Ag metal film–air interfaces

causes $dk_{SP}/d\omega$ to change sign with $\Re(\varepsilon_M)$; see again Fig. 6.2. Because $k_{SP} > k_0$, it is not possible to excite SPPs on a metal film–dielectric interface without a source of additional momentum. Some common methods to provide this are prisms [11, 12], isolated holes [13, 14], and diffraction gratings. The focus in this work is on the latter, specifically hole arrays [2, 3, 7].

A diffraction grating generates x and y wavevector components with magnitudes

$$k_x = \frac{2\pi n_x}{P_x}, \tag{6.4}$$

$$k_y = \frac{2\pi n_y}{P_y}, \tag{6.5}$$

where n_x and n_y are diffraction orders and P_x and P_y are the corresponding periodicities in the x and y directions, respectively. For a square periodicity, $P = P_x = P_y$ and Eqs. 6.4 and 6.5 combine to give a total wavevector magnitude

$$k = \frac{2\pi}{P}\left(n_x^2 + n_y^2\right)^{1/2}. \tag{6.6}$$

Equating Eq. 6.6 with Eq. 6.1 shows that the wavelength of an SPP excited by a square 2D grating, λ_{SPP}, is given by

$$\lambda_{SPP} = \frac{P}{\left(s_x^2 + s_y^2\right)^{1/2}}\left(\frac{\varepsilon_M \varepsilon_r}{\varepsilon_M + \varepsilon_r}\right)^{1/2}, \tag{6.7}$$

where (s_x, s_y) is an integer pair that indicates the diffraction orders that excited the SPP (where the symbol s has replaced n in Eq. 6.6, in order to distinguish it from

diffraction orders that excite other effects; *vide infra*). Because of the system periodicity, the excited SPP is sometimes characterized as a SPP–Bloch wave (SPP–BW). Note that for oblique incidence, light couples with the grating according to the Bragg coupling condition [15], resulting in an in-plane wavevector magnitude of $k = \left[(k_0 \sin\theta_x + k_x)^2 + (k_0 \sin\theta_y + k_y)^2\right]^{1/2}$, where θ_x and θ_y are the incident angles with respect to the film normal in the x and y directions, respectively. Oblique incidence will not be thoroughly discussed in this work, but it should be noted that such a technique can be important for resolving degenerate modes and/or weak resonances.

Besides exciting SPPs, other mechanisms of light interaction with nanostructured metal films are possible. For example, by equating Eq. 6.6 with Eq. 6.3 one finds that

$$\lambda_{\mathrm{RA}} = \frac{P}{\left(w_x^2 + w_y^2\right)^{1/2}} \varepsilon_r^{1/2}, \tag{6.8}$$

where (w_x, w_y) is an integer pair again indicating the diffraction order. Equation6.8 corresponds to the light diffracted at an angle parallel to the grating, termed a Rayleigh anomaly (RA). A RA occurs at the threshold of a diffraction order (above which diffraction into that order is forbidden), and is sometimes also referred to as a Wood anomaly [13, 16]. However, it is important to keep in mind that, following the detailed analysis and classification of Wood anomalies by Hessel and Oliner [17], a RA is one of two types of Wood anomalies. The other type identified by them is a "resonant" anomaly, which could be a SPP, waveguide mode, or possibly a hybrid. Note that λ_{RA} is related to ε_r and the grating periodicity, but not the grating material (i.e., there is no dependence on ε_{M}).

It is important to note that the actual wavelengths associated with Eq. 6.7 are approximate, because coupling between resonances on the top and bottom film interfaces is ignored. Therefore, one expects this equation to be most accurate when the metal film is thick or the resonances occur significantly far from one another (e.g., when the dielectrics on the two sides of the metal film, ε_{I} and $\varepsilon_{\mathrm{III}}$, where I and III refer to the two sides, are significantly different). In thin metal films when ε_{I} and $\varepsilon_{\mathrm{III}}$ are similar (the difference being less than approximately 0.2), the actual positions of the SPP resonance features are red or blueshifted slightly relative to Eq. 6.7. This is due to SPP–SPP coupling, which leads to a set of hybridized SPPs, a high-energy (short-wavelength) antisymmetric combination and a low-energy (long-wavelength) symmetric one [18]. The low-energy mode is redshifted while the high-energy mode is blueshifted relative to their predicted positions. In addition, the amplitude of the symmetric mode increases, and that of the antisymmetric mode decreases.

Interactions between SPPs and RAs can also occur, leading to narrow spectral features that are particularly sensitive to the RI, a phenomenon known as the RA–SPP effect [2, 3] (see Sects. 6.4.1 and 6.4.2). RAs, however, are nonresonant

spectral features associated with a grating, so the RI sensitivity in this case is associated with the SPP, while the narrow linewidth is associated with the RA.

As briefly mentioned above, some of the most popular types of diffraction gratings in metal films are hole and slit arrays [2, 7, 19]. Besides generating additional momentum to couple into SPPs, the holes and slits themselves provide a waveguide mechanism for the transmission of light from the lower surface to the upper one [20, 21]. However, Bethe showed that the amount of transmission through a single aperture in an infinitely thin PEC film (which does not support SPPs) scales as $(d/2\lambda)^4$, where d is the aperture diameter [22]. Therefore, the transmission through subwavelength holes alone is very low, and other effects, mainly SPP excitations, are primarily responsible for the phenomena of EOT. However, the waveguide mechanism can result in other complex optical properties, such as the dephasing of an electromagnetic field [23, 24]; see Chap. 7.

6.2 Computational Considerations

Based on the discussion in Sect. 6.1, a lot of the interest in nanostructured metal films has to do with transmission, reflection, and absorption spectra. Often, but not always, the measured spectra are for "zero-order transmission"—i.e., the measurements are such that they do not include contributions from light scattered away from the incident direction. To obtain this result computationally, it is necessary to Fourier transform the time-domain $\mathbf{E}(\mathrm{x}, t)$ and $\mathbf{H}(\mathrm{x}, t)$ fields on xy-planes above or below the surfaces of the film. Since the wavevector for zero-order scattering is $\mathbf{k} = 0\hat{\mathbf{x}} + 0\hat{\mathbf{y}} + (\omega/c)\hat{\mathbf{z}}$, and z is fixed for a given xy-plane of interest, the relevant projections of the fields are simply proportional to integrating them over x and y [2]. If $\mathbf{E}_0(z_\mathrm{T}, \omega)$ and $\mathbf{H}_0(z_\mathrm{T}, \omega)$ denote these projections, then the zero-order transmission is given by $T(\omega) = P_\mathrm{T}(\omega)/P_\mathrm{inc}(\omega)$, where $P_\mathrm{T}(\omega) = \Re(\mathbf{E}_0 \times \mathbf{H}_0^*)_z/2$ and the quantity P_inc is the analogous incident flux.

For all of the FDTD calculations discussed in this chapter, grid spacings of $\Delta x = \Delta y = \Delta z = 4$ or 5 nm were used, and the computational domains were truncated with CPML. Test calculations using somewhat larger grid spacings indicated that the results are sufficiently converged. Also, for some calculations, absorbing boundary conditions rather than CPML were employed. For a discussion of this technique, see Ref. [2].

6.3 Isolated Holes

Besides waveguide effects associated with isolated apertures (a discussion of such effects is given in Sect. 7.4 in relation to slits), SPPs and LSPRs can be excited by, and in them, respectively [13, 14]. Consider a thin metal film with an isolated circular hole supported by a glass substrate in air, similar to Fig. 3.10. If the film is

illuminated from the glass side by incident light with a wavelength greater than the hole diameter, several interesting phenomena can occur. (A system of randomly distributed, but not too dense holes will exhibit similar behavior.)

First, even if the light is propagating normal to the film, it is possible to excite SPPs on the metal–air interface [25, 26]. This is because the hole itself acts as a scattering defect that can generate the additional momentum required for SPP generation (see Sect. 6.1). A combined FDTD and experimental study by Yin et al. [25] of 100 nm thick Au films with an isolated hole showed that SPPs tend to be launched from the holes in the direction of the incident polarization. The SPP near-fields were experimentally measured with a NSOM probe, and they showed periodic intensity variations, with peak-to-peak separations approximately equal to $\lambda_{SPP} = 2\pi/k_{SPP}$. It was at first surprising that there would be periodic oscillations in the intensity, since that of a pure SPP excitation should decay exponentially along the propagation direction [if $\Im(\varepsilon_M) > 0$]. However, theoretical analysis showed that the near-fields are composed of two interfering terms, the excited SPP and directly penetrating (or tunneling) light through the film. The resulting interference pattern is easily seen to have the observed oscillations. Subsequently carried out more detailed calculations and analysis Chang et al. [13], showing more explicitly that an isolated hole can act as a point source of SPPs.

When SPPs can be generated by an isolated hole, there can also be EOT [13, 26]. This was shown in a theoretical study by Wannemacher [26], who used a numerically rigorous multiple multipole approach [27]. In addition, while not emphasized in this dissertation, contributions to EOT can also arise from LSPR excitations, which are dipolar (and possibly higher order) charge oscillations associated with the holes themselves [13, 28, 29]. LSPR excitations associated with holes in metal films are analogous to those in metal nanoparticles, as shown by Käll and co-workers [28, 29] (see also Sect. 1.1.1). For example, light transmission through holes can mimic the corresponding optical scattering spectra of nanoparticles, displaying resonance features that redshift with hole size. It should be noted though that some interesting differences regarding elongated holes and particles have recently been pointed out [30]. It should again be mentioned that these effects are not completely isolated from one another (see Sect. 6.1), and in reality LSPRs and SPPs are inherently coupled.

6.4 Subwavelength Hole Arrays

The transmission of light through arrays of subwavelength diameter holes in metal films has been the focus of much research since the discovery by Ebbesen et al. of EOT [7]. A schematic diagram of a typical hole array in a Au film is shown in Fig. 6.4. The system consists of a square array of holes with diameter d and periodicity P in a Au film of thickness h, which is sandwiched between dielectric materials I and III with RIs of $n_I = \varepsilon_I^{1/2}$ and $n_{III} = \varepsilon_{III}^{1/2}$. Material I (bottom) is taken

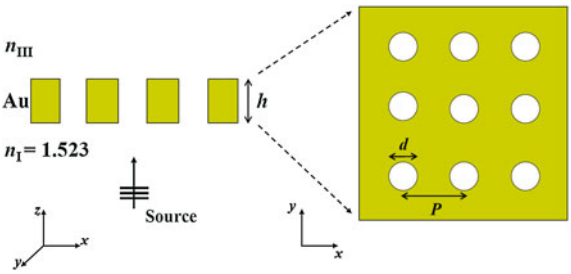

Fig. 6.4 Schematic diagram of a typical hole array in a Au film. The parameters in the figure are defined in the text

to be the substrate or supporting material for the film (e.g., glass), with a fixed RI, and material III (top) is a variable RI superstrate. Light is incident from region I, and the transmission spectrum is obtained in region III.

The mechanisms of EOT have been the subject of much discussion, and important contributions arise from SPPs, diffractive effects (including RAs), and localized waveguide modes [7, 13, 16, 31–34]. For example, all of these features play a role in the large RI sensitivity observed in Au films deposited on arrays of 500-nm wells molded in a polymer substrate [35]; see Sect. 6.7. It is worth mentioning once again that these effects are not isolated from one another, and can interact leading to additional effects; see Sect. 6.1 as well as Sects. 6.4.1 and 6.4.2.

The details of EOT vary significantly with parameters of the hole array structure, including size [36] and shape [37, 38] of the holes, metal thickness [39, 40], and periodicity. As an example of these concepts, Fig. 6.5 shows FDTD calculated zero-order transmission spectra for a hole array consisting of $d = 100\,\text{nm}$ holes separated by $P = 400\,\text{nm}$ in a Au film on a glass ($n_\text{I} = 1.523$) substrate and with a $n_\text{III} = 1.35$ superstrate as h is increased from 25 to 100 nm.

All of the spectra in Fig. 6.5 show a considerable amount of transmission (EOT) relative to the thin film transmission (Fig. 6.1). Initially, one may suspect that this is due to direct transmission of light through the holes. However, the geometric optics prediction for these parameters is less than 5%, and that predicted by Bethe's analysis [22] (see Sect. 6.1) is even less. The EOT can be primarily attributed to coupling of the incident light into SPPs.

A broad maximum near $\lambda = 490\,\text{nm}$ is observed in all spectra, with a peak transmission of about 15%. This peak is from direct transmission of light through the Au film, and is not related to any hole or array properties, as is confirmed by comparison with Fig. 6.1. The peak structure between $\lambda = 560$ and 580 nm can be attributed to a combination of a LSPR (see Sect. 6.3) in each hole and a $(1,1)n_\text{I}$ SPP–BW [i.e., the solution to Eq. 6.7 with $(s_x = 1, s_y = 1)$ and $\varepsilon_r = n_\text{I}^2$, associated with the metal–material I interface; see Sect. 6.1]. The minima in the spectra for $\lambda > 580\,\text{nm}$ can be assigned using the simple predictions of Eqs. 6.7 and 6.8. Note that a Fano resonance feature corresponds to a given SPP feature, and occurs as a minimum and an adjacent maximum, with the former often closer to the prediction of Eq. 6.7 [2, 13, 32, 34]. For example, the $(1,0)n_\text{III}$ SPP–BW is predicted to be at

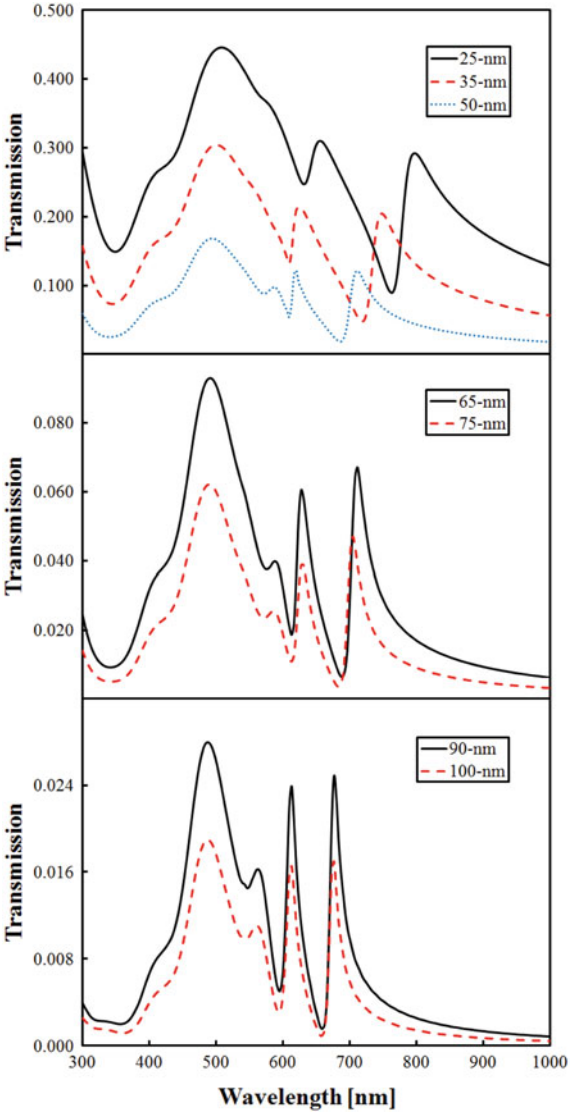

Fig. 6.5 FDTD calculated zero-order transmission through a hole array with $d =$ 100 nm holes separated by $P = 400$ nm in a Au film on a glass substrate and with a $n_{\mathrm{III}} = 1.35$ superstrate as h is increased from 25 to 100 nm

601 nm, and the $(1,0)n_{\mathrm{I}}$ SPP–BW at 662 nm. These positions are in relatively good agreement with the FDTD calculated minima. These occur at 610 and 683 nm, respectively, in the $h = 50$ nm results, for example; Fig. 6.5. It is important to note that as the film thickness is decreased for $h < 65$ nm, the peak positions shift considerably. This can be attributed to the aforementioned increase in coupling strength between SPP resonances on the top and bottom film surfaces (see Sect. 6.1).

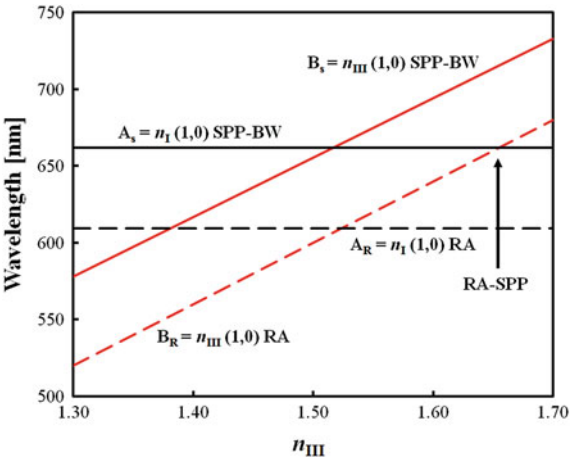

Fig. 6.6 Predicted positions of $(1,0)$ SPP–BWs and $(1,0)$ RAs (Eqs. 6.7 and 6.8, respectively) as a function of n_{III} for $n_I = 1.523$ and $P = 400\,\text{nm}$. The n_I SPP–BWs and RAs are denoted as A_S and A_R, and the n_{III} ones as B_S and B_R, respectively

6.4.1 RA–SPP Effect

Under certain circumstances, SPP–BWs and RAs on opposite sides of the film can strongly interact [2, 3, 5]. Figure 6.6 shows how the positions of SPP–BWs and RAs, predicted by Eqs. 6.7 and 6.8, respectively, evolve as n_{III} is varied while $n_I = 1.523$ and $P = 400\,\text{nm}$ remain fixed. Only the first-order cases $[(s_x = 1, s_y = 0)$ and $(w_x = 1, w_y = 0)]$ are shown in Fig. 6.6, since they are the strongest features in this wavelength range and for this P.

The crossing point labeled RA–SPP corresponds to where the (1, 0) n_{III} RA [i.e., the solution to Eq. 6.8 with $(w_x = 1, w_y = 0)$ and $\varepsilon_r = n_{III}^2$, associated with the material III region; see Sect. 6.1] and the $(1,0)n_I$ SPP–BW coexist, which can interact if the Au film is thin enough, leading to a strong variation in transmission amplitude for $h < 65\,\text{nm}$ [5]. The value of n_{III} at the RA–SPP crossing point for a general hole array can be found by equating Eq. 6.7 for n_I with Eq. 6.8 for n_{III} for the first diffraction orders,

$$n_{III} = \left[\frac{\varepsilon_M(\lambda_{RA-SPP})\varepsilon_I}{\varepsilon_M(\lambda_{RA-SPP}) + \varepsilon_I}\right]^{1/2}. \tag{6.9}$$

Equation 6.9, like Eq. 6.7, is an implicit relation for a wavelength. In this case, the wavelength λ_{RA-SPP} is that of the incident light where the $(1,0)n_I$ SPP–BW and $(1,0)n_{III}$ RA conditions are the same. The required P for the hole array at this crossing point can subsequently be found from

$$P = \frac{\lambda_{RA-SPP}}{n_{III}}, \tag{6.10}$$

To achieve the RA–SPP effect near some specific n_{III} value, Eq. 6.9 is first rewritten as a root equation, $f(\lambda_{RA-SPP}) = 0$, and solved using bisection for λ_{RA-SPP}. Then, Eq. 6.10 is used to determine the necessary P. For example, $n_I = 1.523$ corresponds to $n_{III} = 1.65$ and $\lambda_{RA-SPP} = 662\,\text{nm}$ with $P = 400\,\text{nm}$.

It turns out that RA–SPP solutions exist only for n_{III} values in a small range: $n_I < n_{III} < n_I + \Delta$, where Δ depends on the nature of the metal, n_I, and h (e.g., $\Delta \approx 0.35$ for a $h = 50\,\text{nm}$ thick Au film with $n_I = 1.523$). For example, to design a system sensitive to $n_{III} = 1.40$, it would therefore be necessary to use a supporting substrate with $n_I < 1.40$. In what follows, it is demonstrated that both FDTD calculations and experimental results confirm these expectations for a hole array in a $h = 50\,\text{nm}$ thick Au film with $d = 100\,\text{nm}$ and $P = 400\,\text{nm}$ on a glass ($n_I = 1.523$) substrate [2].

Figures 6.7 and 6.8 show the FDTD calculated and experimental zero-order transmission spectra for n_{III} ranging from 1.00 to 1.70. The level of agreement between experiment and the calculations is reasonable in terms of positions of the maxima and minima, and overall trends. However, there are some quantitative differences in the magnitudes of the largest transmission peaks, which are most likely due to small, but very sensitive deviations between the experimental hole array structure and the computational idealized configuration [35]. It is found, for example, that if the diameter of the holes is increased to 120 nm (vida infra), then the calculated transmission amplitude of the longest wavelength peak nearly doubles. Although the experimental holes have $d = 100\,\text{nm}$ on average, slight size differences can occur from the grain size of the evaporated Au films, or other relatively small imperfections. Additionally, to correlate with the experiments directly, the computed results should be scaled by $\hbar\omega$ (where $\hbar$ is Planck's constant) to convert between the calculated power per unit area and the measured energy per unit area (this is the major contributing reason for the discrepancies at high wavelengths; see Sect. 6.6).

Similar to Fig. 6.5, all of the spectra in Figs. 6.7 and 6.8 display a broad maximum near $\lambda = 490\,\text{nm}$ with a peak transmission of about 15%. This is due to direct transmission of light through the Au film. The peak structure between $\lambda = 560$ and 580 nm can be attributed to a combination of a LSPR in each hole and a $(1,1)n_I$ SPP–BW. The minima in the spectra for $\lambda > 580\,\text{nm}$ can be assigned using Fig. 6.6 (or equivalently, Eqs. 6.7 and 6.8). For example, when $n_{III} = 1.70$ (Fig. 6.8), the $B_S = (1,0)n_{III}$ SPP–BW is predicted to be at 733 nm, while the calculated and experimental wavelengths are seen to be 757 and 750 nm, respectively. In addition, the $A_S = (1,0)n_I$ SPP–BW is predicted to be at 662 nm, and the calculated and observed values are 669 and 660 nm. Finally, the $(1,1)n_{III}$ SPP–BW is predicted to be at 580 nm, while the calculated and observed values are 614 and 609 nm.

The result of coupling between SPPs on the top and bottom film interfaces can be seen as n_{III} is increased for $n_{III} < n_I$, where the hybridized $B_S = (1,0)n_{III}$ SPP–BW increases in wavelength from 574 to 620 nm and decreases in amplitude, while the hybridized $A_S = (1,0)n_I$ SPP–BW peak near 708 nm increases (Fig. 6.7).

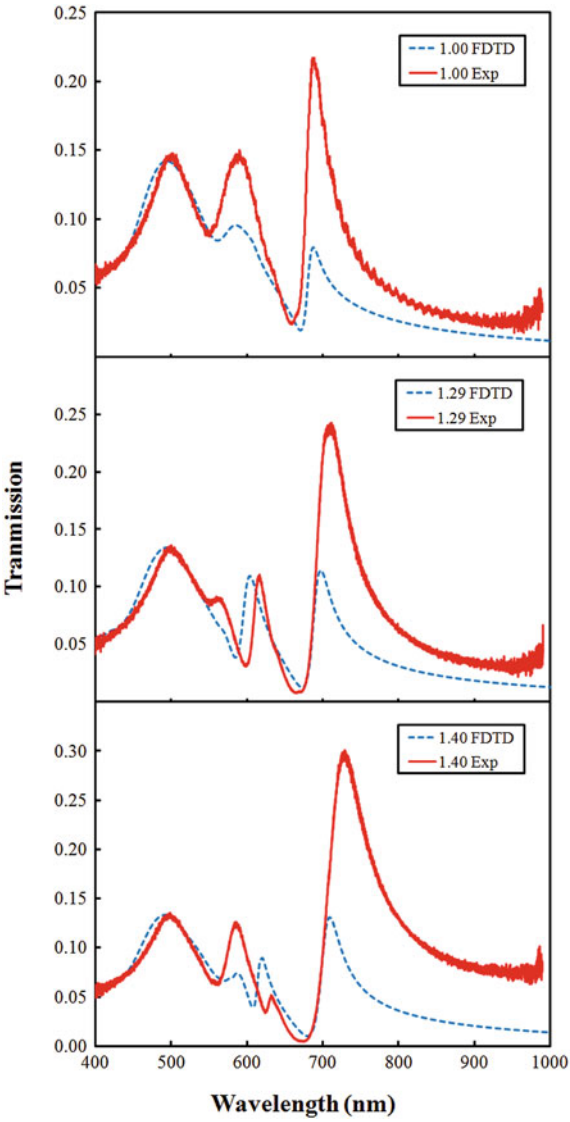

Fig. 6.7 FDTD calculated and experimental zero-order transmission spectra for a hole array in a $h = 50\,\text{nm}$ thick Au film with $d = 100\,\text{nm}$ and $P = 400\,\text{nm}$ for $n_{\text{III}} < n_{\text{I}}$, where $n_{\text{I}} = 1.523$

In this discussion so far, RAs have not appeared prominently in the calculated or measured transmission spectra, because they are generally narrow spectral features (or possibly just kinks) that can be overwhelmed by other processes. For $n_{\text{III}} > n_{\text{I}}$, the maximum to the immediate red of the minimum associated with the $\text{A}_{\text{S}} = (1,0)n_{\text{I}}$ SPP–BW shows a rapid rise and narrowing (Fig. 6.8). This rapid amplitude increase is a direct result of the RA–SPP effect, and the evolution of the peak associated with this is shown in Fig. 6.9 on a finer RI scale, calculated with both FDTD and RCWA (Sect. 3.5.1). Consistent with Fig. 6.6, the $\text{B}_{\text{R}} = (1,0)n_{\text{III}}$

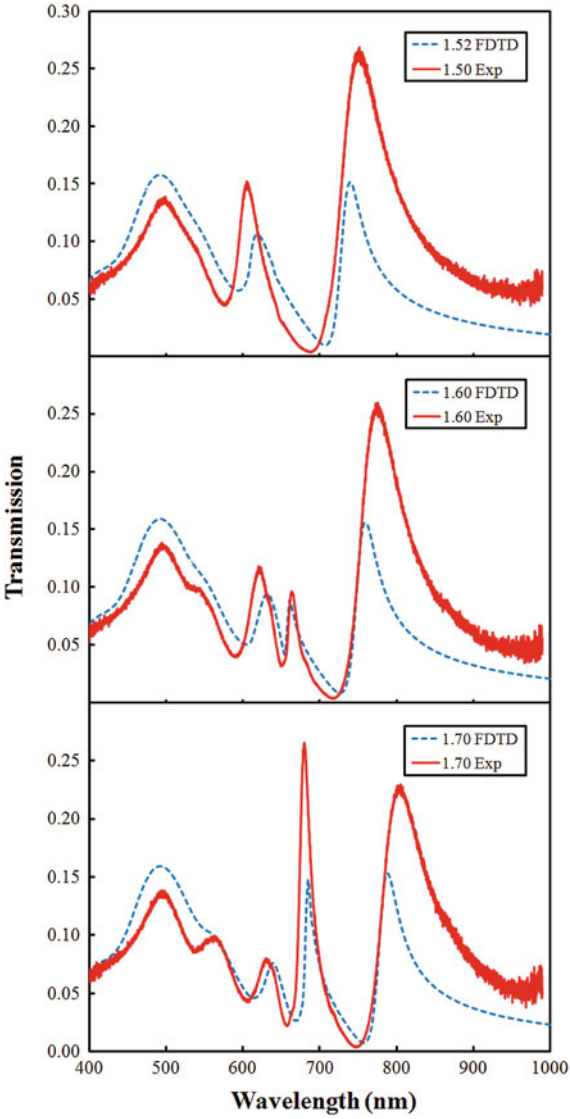

Fig. 6.8 FDTD calculated and experimental zero-order transmission spectra for a hole array in a $h = 50\,\text{nm}$ thick Au film with $d = 100\,\text{nm}$ and $P = 400\,\text{nm}$ for $n_{\text{III}} > n_{\text{I}}$, where $n_{\text{I}} = 1.523$

RA passes through the wavelength region of the $A_S = (1, 0)n_I$ SPP–BW, interacting with it to produce a narrow, n_{III}-sensitive spectral feature. Note that owing to partial RA character, the RA–SPP feature occurs close to the prediction of Eq. 6.9 (but still redshifted due to SPP–SPP coupling; see Sect. 6.1). The term "interacting" should be taken loosely, and in this case corresponds to the following. First-order diffraction is a virtual process, which means that SPP excitation associated with the bottom of the film can temporarily populate the virtual diffraction channel before ultimately scattering into the zero-order channel. This

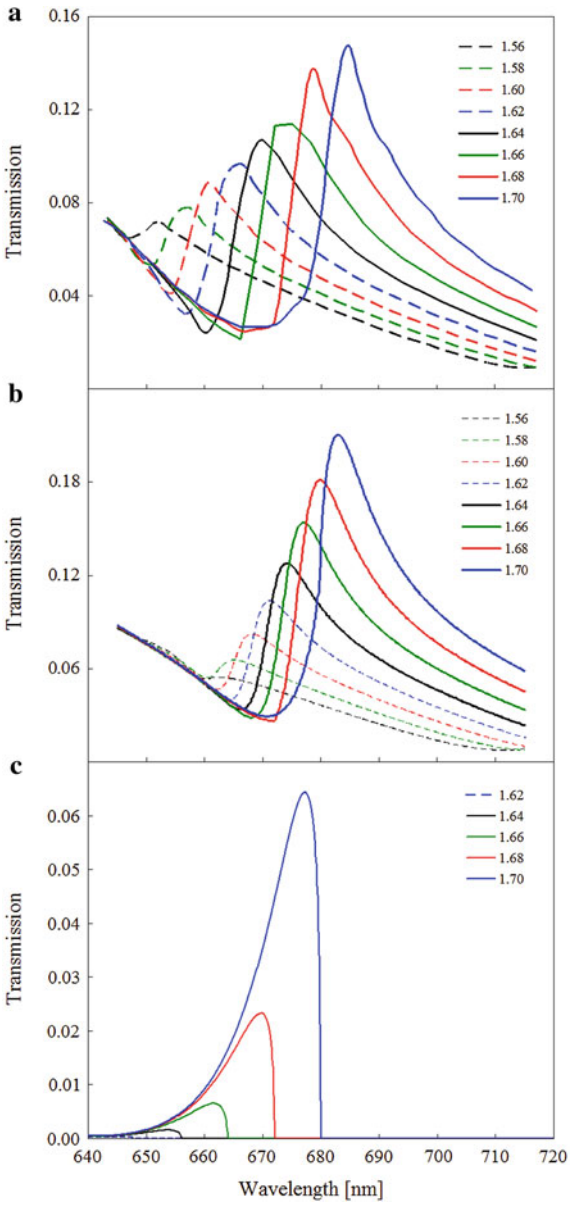

Fig. 6.9 **a** FDTD calculated zero-order transmission through a hole array in a $h = 50\,\text{nm}$ thick Au film with $d = 100\,\text{nm}$,$P = 400\,\text{nm}$, and $n_\text{I} = 1.523$. A rapid increase in amplitude of the peak associated with the RA–SPP effect is seen as n_III is varied. **b** RCWA calculated results consistent with **a**. **c** RCWA calculated first-order transmission as n_III is varied through the region of the RA–SPP effect

pathway operates in parallel with normal zero-order scattering to enhance transmission. When the wavelength is reduced further to allow first-order diffraction, scattering into the zero-order channel stops, leading to a sharp cutoff in the RA–SPP peak on the short wavelength side.

The FDTD calculated amplitude variation of the RA–SPP peak in the n_III range 1.55–1.70 is $\sim 65\%$ / RIU (RI unit) calculated and $\sim 150\%$ / RIU experimental [2]

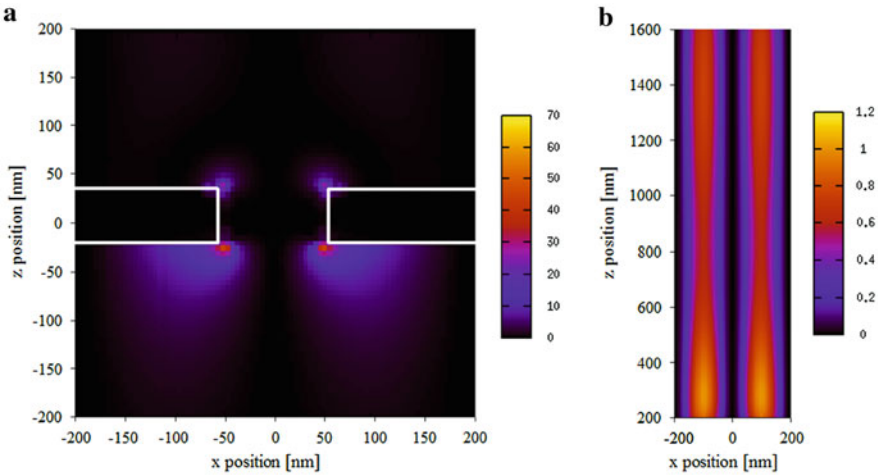

Fig. 6.10 FDTD calculated wavelength-resolved $|E_z|^2$ at $\lambda = 679\,\text{nm}$ for $n_{III} = 1.70$, showing **a** the region near the hole and **b** 200 nm above the Au film. The hole is centered at the origin, and the film boundaries are outlined in white

(differences that can again attributed to minor imperfections in the experimental systems); Fig. 6.9. The RCWA calculations reveal that first-order diffraction is also significantly enhanced by the RA–SPP effect; Fig. 6.9c. As expected, first-order diffraction, dominated by the $(1,0)n_{III}$ RA, exhibits a wavelength sensitivity equal to the theoretical upper limit, *P* / RIU.

FDTD-calculated electric field plots also verify coexistence and interaction between the $(1,0)n_I$ SPP–BW and $(1,0)n_{III}$ RA. Figure 6.10 shows the wavelength-resolved $|E_z|^2$ at $\lambda = 679\,\text{nm}$ for $n_{III} = 1.70$ (near the RA–SPP crossing point).. Figure 6.10a shows that the $(1,0)n_I$ SPP–BW has the greatest intensity on the n_I side, but also some noticeable intensity on the n_{III} side. The $(1,0)n_{III}$ RA is present in this plot, but is not visible since its intensity relative to the $(1,0)n_I$ SPP–BW is low. Figure 6.10b shows the field for $z > 200\,\text{nm}$ above the film surface, where characteristic RA features are visible—e.g., an extended propagating plane wave [41]. The high intensity of the $(1,0)n_{III}$ RA near the film interface, which decreases in strength as the distance from the film increases, suggests that the $(1,0)n_{III}$ RA is interacting with the $(1,0)n_I$ SPP–BW.

Further RCWA calculations (not shown) reveal that the RA–SPP effect persists strongly for film thicknesses up to $h = 65\,\text{nm}$ and for hole (or slit) diameters of $d > 80\,\text{nm}$ [5]. In addition, optimum values of $h = 45\,\text{nm}$ and $d = 175\,\text{nm}$ have been determined with respect to both RI sensitivity (defined as the change in amplitude per RIU, which is considered significant if greater than 1.0) and height-to-width ratio of the RA–SPP peak [defined as the maximum minus the minimum in the Fano-like profile, divided by the full width at half maximum (FWHM) of a single peak at the center of the RI range of the RA–SPP effect–or in other words, a measure of the sharpness of the RA–SPP feature] [5]. For example, using the

optimum hole diameter, the amplitude variation with RIU almost doubles. RCWA calculations carried out over a wide range of P and n_{I} values (also not shown) confirm that the rapid variations in transmission amplitude are always consistent with the predictions of Eqs. 6.9 and 6.10.

The other crossing points in Fig. 6.6 lead to couplings that are less relevant for obtaining narrow spectral features that are especially sensitive to variations of n_{III}. The coupling of the two SPP–BWs features near $n_{\mathrm{III}} = 1.523$ will lead to a broader peak than the RA–SPP one, since SPP–BWs are intrinsically broader than the RAs, due to their finite lifetimes. (The hybridization that results from this interaction, however, does play a role in the RA–SPP effect [2].) The crossing of the two RA features could produce narrow spectral features, but this effect is overwhelmed by SPP–BW coupling near the same wavelength. Finally, the n_{III} SPP–BW and n_{I} RA crossing near $n_{\mathrm{III}} = 1.35$ occurs in a wavelength region where high-order SPP–BWs, LSPRs, and direct transmission are all important.

6.4.2 RA–SPP Effect in Pd

The RA–SPP effect can be strong even in systems which are considered weakly plasmonic (i.e., ones that do not exhibit strong SPP features) [3, 42], often due to $\Im(\varepsilon_{\mathrm{M}})$ being large. For example, consider a hole array in a palladium (Pd) film (a weak plasmonic material) with $d = 160\,\mathrm{nm}$,$P = 400\,\mathrm{nm}$, and $h = 55\,\mathrm{nm}$.

Figure 6.11a shows that such a hole array on a glass substrate ($n_{\mathrm{I}} = 1.523$) in air ($n_{\mathrm{III}} = 1.00$) experimentally exhibits transmission intensities up to 18% near 665 nm. Such transmission should be compared to that through a 55-nm thick solid Pd film, which is very weak at most wavelengths, except for a broad peak around 900 nm with maximum intensity of $\sim$3%; Fig. 6.11a, dashed line. Considering that the geometric open area of the hole array is 12%, EOT is thus obtained even from this relatively weak plasmonic metal.

The EOT peaks are found to be closely related to the excitation of SPP–BW modes (just as for the Au films in Sect. 6.4.1. Specifically, the resonance features in the transmission spectra exhibit a Fano profile [34], with the minima close to the predictions of Eq. 6.7. Additionally, as predicted by Eq. 6.7, the maxima and minima in the transmission spectra are redshifted with increasing n_{III}.

Zero-order transmission spectra calculated using FDTD for n_{III} = 1.00 to 1.70 are shown in Fig. 6.11b. The calculations and experimental data show good agreement regarding the resonance positions. However, slight differences in the transmission amplitudes are present, which are (yet again) most likely because of minor, but unavoidable imperfections in the experimental samples.

As n_{III} increases past 1.55, the $(1,0)n_{\mathrm{III}}$ RA wavelength approaches the $(1,0)n_{\mathrm{I}}$ SPP–BW mode, and a distinct peak as narrow as 45 nm (FWHM) appears at 670 nm; Fig. 6.11, star. This can be attributed to the RA–SPP effect (see Sect. 6.4.1). The wavelength of this peak for $n_{\mathrm{III}} > 1.55$ occurs at a wavelength that is slightly

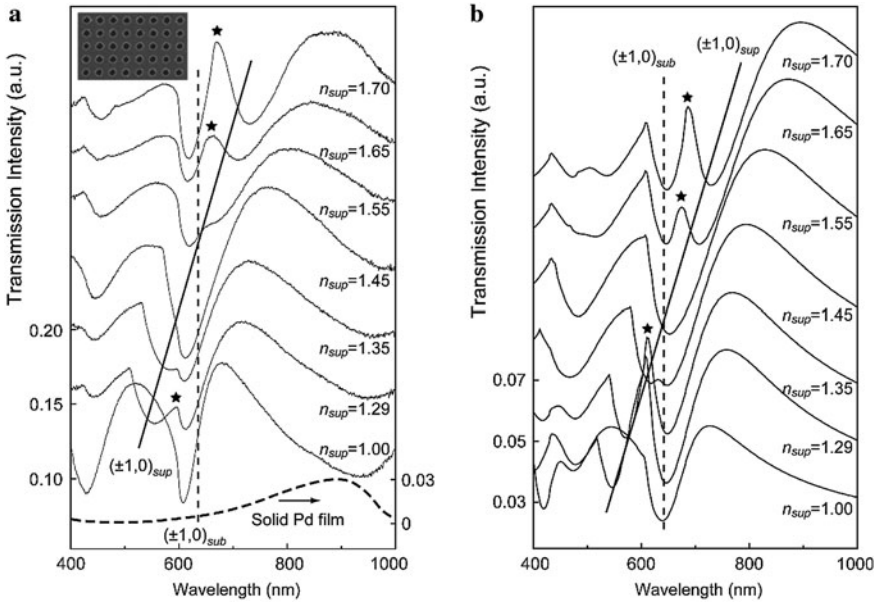

Fig. 6.11 Zero-order transmission spectra for Pd subwavelength hole arrays under normal incidence excitation. **a** Measured and **b** FDTD calculated spectra are in good agreement, and the positions of the SPP–BW minima are also in good agreement with Eq. 6.7 (*dashed* and *solid lines* for n_{I} and n_{III}, respectively). Transmission through a 55-nm solid Pd film is included as a reference in **a**; the RA–SPP features are indicated by *stars*; and the *inset* of **a** is a scanning electron microscope (SEM) image of an experimental system

longer than the RA condition in n_{III}, but shorter than the SPP–BW one at the Pd–n_{I} interface (analogous to the effect in Sect. 6.4.1). This can be seen in the FDTD calculations near 685 nm when $n_{\mathrm{III}} = 1.70$, for example; Fig. 6.11b, star. It is primarily because of the RA–SPP effect (in addition to normal EOT) that sharp features in the transmission spectra are observed in these systems at all, since Pd has a large $\Im(\varepsilon_{\mathrm{M}})$ at these wavelengths.

The RA–SPP effect is also observed when $n_{\mathrm{III}} < 1.55$, except that the roles of the n_{III} region and the Pd–n_{I} interface are reversed. (Recall that this effect was not observable in Au due to other effects that occurred in the same region; see Sect. 6.4.1). For example, strong variations in the transmission amplitude due to the RA–SPP effect are observable in the FDTD calculations near 606 nm when $n_{\mathrm{III}} = 1.293$. In this case, when n_{III} approaches 1.29, the RA–SPP feature occurs as the $(1,0)n_{\mathrm{III}}$ SPP–BW condition overlaps with that of the $(1,0)n_{\mathrm{I}}$ RA.

To (again) further verify coexistence and interaction between the $(1,0)n_{\mathrm{I}}$ SPP–BW and the $(1,0)n_{\mathrm{III}}$ RA, the wavelength-resolved $|\mathrm{E}_z|^2$ at $\lambda = 628\,\mathrm{nm}$ for $n_{\mathrm{III}} = 1.70$, near the minimum in the zero-order transmission spectrum associated with the ("normal") RA–SPP peak, can be looked at; Fig. 6.12. Figure 6.12a shows that the SPP–BW has the greatest intensity at the Pd–n_{I} interface, but also

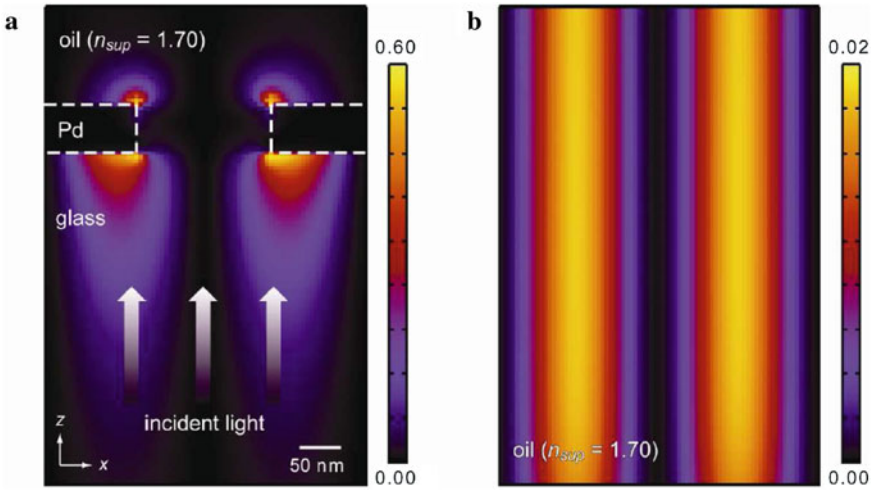

Fig. 6.12 FDTD calculated EM field distributions at $|E_z|^2$ at the RA–SPP minimum at $\lambda = 628$ nm for $n_I = 1.52$ (glass) and $n_{III} = 1.70$. **a** SPP intensity is visible on both sides of the Pd film. **b** Fields characteristic of a RA are evident at $z > 200$ nm above the film, where the SPP–BW intensity has significantly decayed

noticeable intensity on the n_{III} side. The RA is also present, but cannot be resolved because of its low intensity relative to the SPP–BW. Figure 6.12b shows the field at $z > 200$ nm above the film surface, a distance at which the SPP–BW fields have significantly decayed, and EM characteristics of a RA are evident [41].

Because Pd films attenuate the propagation of SPPs more strongly than Au at optical wavelengths, the RA–SPP peak near 670 nm is broader and less intense compared to the analogous peak in Au near 690 nm (in the latter case, FWHM = 34 nm; see Sect. 6.4.1). However, the spectral features in Pd are more well-defined and narrow compared to other Pd systems, where strong resonances have not been previously observed [43]. Thus, even in weakly plasmonic materials, the RA–SPP effect is a general phenomenon that that may be observed under the proper conditions. Furthermore, because $\Im(\varepsilon_M)$ becomes smaller with decreasing wavelength (a somewhat unusual feature) [44], Pd becomes more strongly plasmonic at short wavelengths. Thus, such plasmon resonances can be very distinct in the blue region of the visible spectrum, and could possibly be useful for applications (e.g., sensing) in regions where Au and Ag are impractical.

Since both SPPs and RAs are angle dependent, RA–SPP peaks also shift with the incident angle of light, θ. The required condition for the RA–SPP effect [overlap between the (1, 0) n_I SPP–BW and the (1, 0) n_{III} RA] in Pd should occur not only at normal incidence, but also out to large angles without changes in n_{III}. This is because SPP and RA features for Pd have similar slopes as function of θ [3]. Fig. 6.13a shows experimentally that the RA–SPP peak in Pd exhibits nearly the same amplitude and FWHM at angles all the way from 0 to 60°.

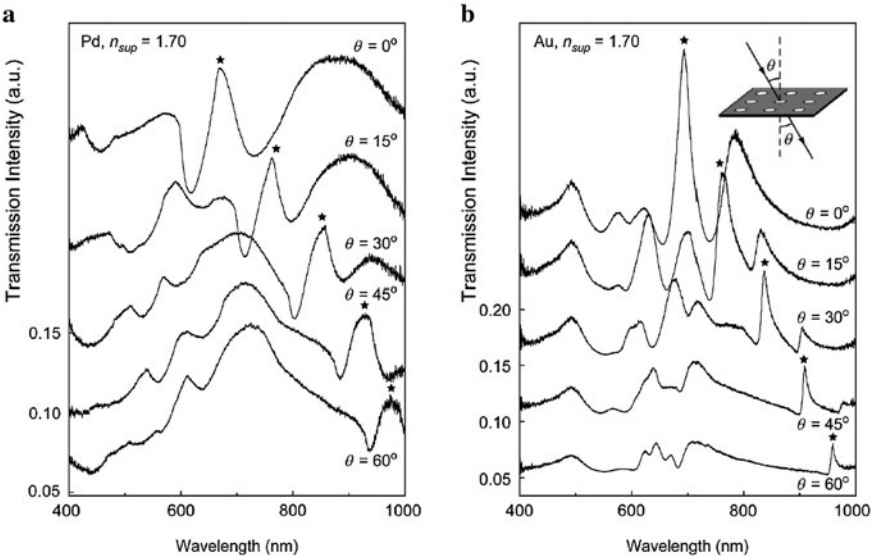

Fig. 6.13 Experimental angle-resolved transmission spectra for **a** Pd and **b** Au hole arrays with n_{III} = 1.70. The RA–SPP peak (*starred*) in Pd shifts with θ, but does not change much in amplitude and width, whereas the amplitude of that in Au dramatically decreases

In contrast, the amplitude of the RA–SPP peak in Au decreases dramatically with increasing θ when n_{III} = 1.70; Fig. 6.13b. The reason for this is that the (1, 0) n_I SPP–BW condition deviates significantly from the (1, 0) n_{III} RA one at large angles in Au [3]. Therefore, at least in Pd, changing the excitation angle presents another effective approach to tune RA–SPP features to desirable wavelengths, without compromising spectral quality.

6.5 Pillar Arrays

While counter-intuitive, the existence of holes in a metal film is not required to observe EOT [45]. All that is necessary is to couple into SPPs (or other effects) associated with the metal–dielectric interface, and for the metal film to be optically thick [16, 46]. As an example, consider a 400 nm periodic array of 60 nm high $\times$120 nm diameter Ag disks on top of a flat 30 nm thick Au film on a glass ($n_I = 1.523$) substrate with a variable index superstrate (n_{III}); Fig. 6.14.

FDTD calculated zero-order transmission spectra for superstrate indices of $n_{III} = 1.00$ to 1.65 are shown in Fig. 6.15. As can be seen, even without holes a large amount of transmission through this system occurs compared to a flat Au film (Fig. 6.1) This EOT arises because the Ag pillars act as a diffraction grating, which couples incident light into SPPs.

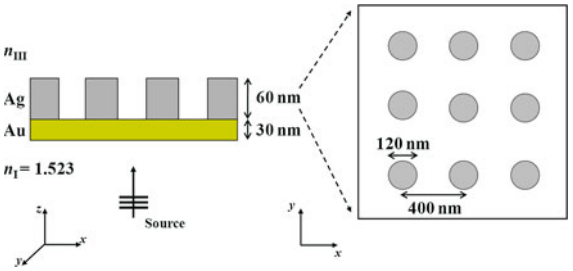

Fig. 6.14 Schematic diagram of a Ag pillar array on a Au film

As was the case for hole arrays (see Sects. 6.4.1 and 6.4.2), most peaks not due to direct transmission through the film can be explained using Eqs. 6.7 and 6.8. For example, for $n_{III} = 1.65$ the small minimum at 742 nm is close to the predicted $(1,0)n_{III}$ SPP–BW position of 712 nm. In addition, in all spectra a slight kink is seen near 603 nm, which can be attributed to a $(1,0)n_I$ RA, expected to occur at 609 nm. A large minimum is also observed in all of the spectra from the LSPR on the Ag disks (e.g., at 550 nm for $n_{III} = 1.35$, and 670 nm for $n_{III} = 1.65$), which is confirmed by plots of the wavelength-resolved $|E_z|^2$ at $\lambda = 666$ nm for $n_{III} = 1.65$; Fig. 6.16c, and calculations not involving the Au film (not shown).

Coupling between SPP–BWs on both sides of the film is strong when $n_I = 1.523$ and $n_{III} = 1.5$ are similar, as can be seen in the plot of $|E_z|^2$ at $\lambda = 619$ nm; Fig. 6.16a. RAs and SPP–BWs can also interact in these systems, giving the RA–SPP effect (see Sects. 6.4.1 and 6.4.2). For the system under consideration, this effect is seen in the spectra near 638 nm for $n_{III} = 1.65$ (Fig. 6.15), and is confirmed by the image of $|E_z|^2$ at $\lambda = 633$ nm (Fig. 6.16b), where a $(1,0)n_I$ SPP–BW and a $(1,0)n_{III}$ RA are seen to coexist.

The LSPR of the Ag disks provides an additional parameter that can be used to control EOT in such systems. For example, by using elliptical Ag disks the large minimum in the transmission spectra due to the LSPR can be redshifted by switching the polarization direction from the short to the long-axis. Figure 6.17 shows the transmission through a Ag pillar array with $n_{III} = 1.65$ for 120×240 nm pillars (1:2 aspect ratio), for both short (x) and long (y) axis polarizations. As can be seen, the (Ag pillar) LSPR is redshifted from 662 to 798 nm by switching the polarization direction. For circular polarization, both short and long-axis LSPR resonances are observed.

6.6 Superlattices

In addition to single-periodicity arrays, plasmonic superlattices also reveal novel interactions in nanostructured metal films. Such systems consist of a periodic array of finite sets (patches) of holes. These systems are novel because SPs can interact

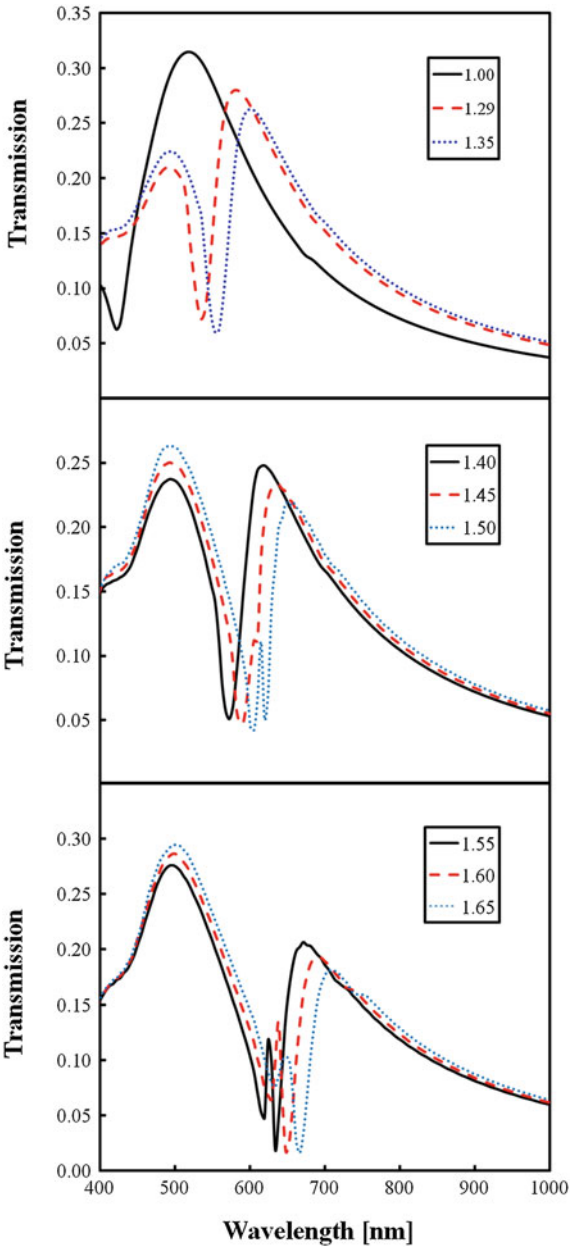

Fig. 6.15 FDTD calculated zero-order transmission spectra through periodic Ag pillars on a Au film with the parameters shown in Fig. 6.14, for various n_{III} values

over multiple length scales: tens of nanometers for LSPRs, hundreds of nanometers for intrapatch SPPs, and tens of micrometers for interpatch SPPs. The interplay between such interactions has not received much attention [4].

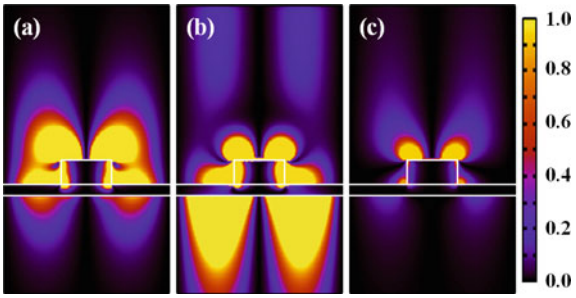

Fig. 6.16 FDTD calculated wavelength-resolved (and normalized) $|E_z|^2$ at **a** $\lambda = 619\,\text{nm}$ for $n_{III} = 1.5$, showing coupling of SPP–BWs on both sides of film, **b** $\lambda = 633\,\text{nm}$ for $n_{III} = 1.65$, showing the RA–SPP effect, and **c** $\lambda = 666\,\text{nm}$ for $n_{III} = 1.65$, showing the LSPR of a Ag pillar

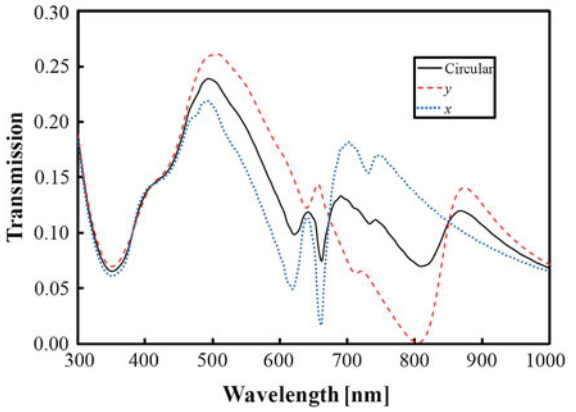

Fig. 6.17 FDTD calculated zero-order transmission for a $120 \times 240\,\text{nm}$ Ag pillar array, oriented along the *y*-axis, on a 30 nm thick Au film on a glass ($n_I = 1.5$) substrate with $n_{III} = 1.65$. Calculations for both linear and circular incident polarizations of light are shown

In this Section, 4 μm square patches of holes separated by 6 μm are considered. To simulate such systems with FDTD, a single unit cell $6 \times 6\,\mu\text{m}$ (in the plane of the film) containing one patch with periodic boundary conditions was modeled: 100 uniform holes with $d = 130\,\text{nm}$ separated by 400 nm, in accordance with experimental scanning electron microscope (SEM) images (not shown). Interestingly, calculations involving a distribution of hole diameters centered around $d = 130\,\text{nm}$ produced similar results. To compare with the experiments directly, the calculated transmission spectra were scaled by $E = \hbar\omega$, where E is the photon energy, in order to convert between the calculated power per unit area and the measured energy per unit area.

Figure 6.18 shows that the FDTD calculations agree well with experiment, and also reveal three classes of plasmon peaks: (1) interpatch coupling modes (I-1 and I-2); (2) a $(1, 1)n_{III}$ intrapatch SPP–BW; and (3) intrapatch coupling modes. The latter modes resemble the (1, 0) n_I and (1, 0) n_{III} SPP–BW modes; hence, they are labeled in Fig. 6.18b and will be referred to as such.

As indicated by how their resonance positions vary with RI, the $(1, 0)n_I$ and $(1, 0)n_{III}$ SPP–BW intrapatch modes are found to be strongly coupled, and most likely to each other. The $(1, 1)n_{III}$ intrapatch SPP–BW, however, has a resonance

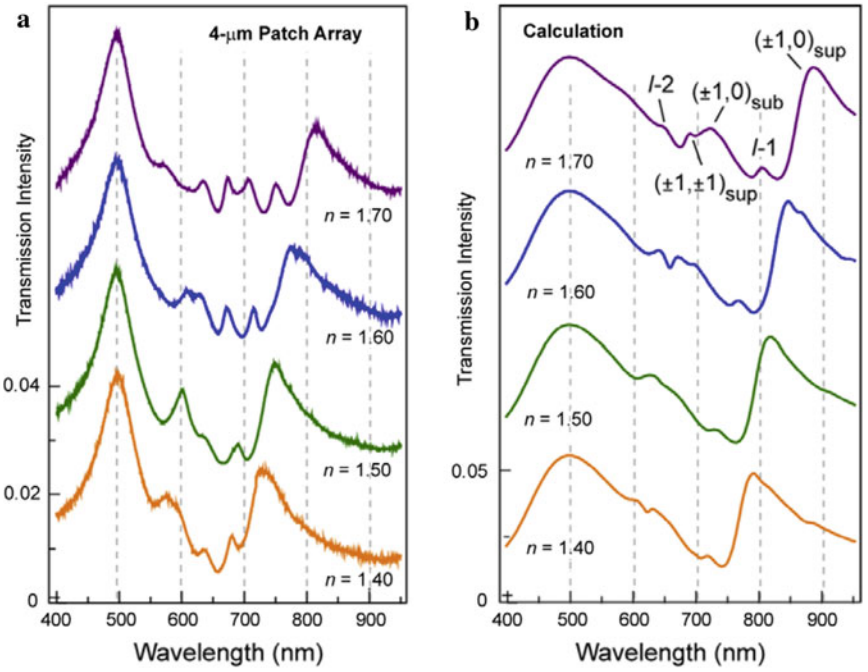

Fig. 6.18 **a** Experimental and **b** FDTD calculated zero-order transmission through a 4 μm patch array for various n_{III} values. The experimental results show many narrow peaks that shift nearly linearly in wavelength with increasing RI. Calculations identify five resonances, which are labeled in the $n = 1.70$ spectrum. The interpatch resonances are denoted as I-1 and I-2, and the intrapatch resonances, similar to the $(1,0)n_{\mathrm{III}}$ and $(1,0)n_{\mathrm{I}}$ SPP–BW modes, are labeled $(\pm 1, 0)_{\mathrm{sup}}$ and $(\pm 1, 0)_{\mathrm{sup}}$, respectively. A $(\pm 1, \pm 1)_{\mathrm{sup}}$ is also shown

position that varies nearly linearly with RI, indicating that it is not coupled to other effects.

For all intrapatch plasmon peaks, it is found that the small numbers of holes results in two main effects: (1) the peaks are redshifted by 100 nm from their predicted values (Eq. 6.7), and (2) RAs, which play a prominent role in transmission through infinite arrays (see Sects. 6.4.1 and 6.4.2), are absent.

The interpatch peaks I-1 and I-2 can be identified relative to the intrapatch peaks from calculations on isolated patches (not shown). For a superlattice periodicity of 6 μm, many closely spaced resonances are predicted from Eq. 6.7, and it is unexpected that only I-1 and I-2 appear so prominently. In addition, these peaks appear to follow the positions of the $(1,0)\,n_{\mathrm{I}}$ and $(1,0)\,n_{\mathrm{III}}$ SPP–BW intrapatch modes, indicating that the intrapatch and interpatch SPPs are not isolated from each other. In other words, SPPs can interact over multiple length scales, leading to a variety of unexpected effects, such as these. Furthermore, from the variations in their positions with RI, I-1 is a n_{I} resonance (an interpatch substrate mode) and

I-2 is a n_{III} resonance (an interpatch superstrate mode), which are either coupled to each other and/or to the (1, 0) n_I and (1, 0) n_{III} SPP–BW intrapatch resonances.

These multi-length scale interactions represent a promising avenue for future investigation. Further experimental support for the claims in this section, and a discussion of additional effects arising from such interactions, can be found in Ref. [4].

6.7 Other Periodic Systems

In addition to periodic arrays of holes and pillars in metal films, other periodic systems have been investigated. For example, Rogers and co-workers [35, 47, 48] have fabricated quasi-3D plasmonic crystals by depositing a Au film onto periodic arrays of finite-depth wells stamped in a polymer. Depending on the metal deposition technique, the resulting systems have either holes in the top film and Au disks in the bottom of the wells [35], or well structures conformally covered with a Au film [48] (i.e., the well side-wells are also coated). One advantage of these structures is that their greater complexity relative to simple hole arrays can be used to obtain extra sensitivity to RI. FDTD simulations have been used to identify the physical origins of the RI-sensitive transmission peaks, and in general they involve SPP–BWs, RAs, and LSPRs [35]. A related structure based on nanosphere lithography was studied by Hicks et al. [49], who looked at reflected, rather than transmitted, light.

Another interesting periodic system is an array of coaxial apertures in a metal film. Such systems are essentially hole arrays with metal pillars inside the holes [50–53], which can alternatively be viewed as dielectric (or possibly air) ring structures in a metal film, where the interior of the dielectric ring is the metal pillar and the exterior is the metal film. These systems are able to strongly support waveguide modes (see Sects. 3.5.2 and 7.4) that can travel up through the coaxial apertures, leading to a form of EOT. In addition, when the wavelengths are such that SPPs can be excited in the metal, FDTD calculations have shown that the waveguide modes can significantly redshift and exhibit unusual cutoff properties [50, 52]. Experimental results have been found to be in remarkably good accord with the computational predictions [51, 53], and Haftel and co-workers [52, 53] refer to these modes as cylindrical SPPs.

6.8 Summary and Outlook

The results in this chapter show the richness of phenomena associated with nanostructured metal films. Of particular focus was the discussed RA–SPP effect for light transmission through arrays of subwavelength holes in metal films, which leads to narrow transmission peaks that have strong RI sensitivities. A simple

model was presented that accurately predicts the system parameters, RIs, and wavelengths where RA–SPP effects occur. Both simulation and experiment confirmed the anticipated large amplitude changes on the basis of this model.

The RA–SPP effect could be useful for a variety of applications, particularly RI sensing. For example, the explicit variation of the transmission amplitude with n_{III} could be used directly to calibrate a system for superstrate sensing. The wavelength change of a spectral feature with RIU is also sometimes used as a sensing figure of merit. Since the SPP–BW component of the RA–SPP feature is essentially a $(1,0)n_{\mathrm{I}}$ SPP–BW, it is not expected that there would be a wavelength sensitivity with respect to n_{III}. However, from Fig. 6.9 it is found that the wavelength sensitivity is approximately 200 nm / RIU, which is probably related to hybridization effects between the $(1,0)n_{\mathrm{I}}$ SPP–BW and $(1,0)n_{\mathrm{III}}$ SPP–BW. Although smaller than values reported for predominantly n_{III} SPP–BWs and larger hole periodicities [35], this represents an additional feature that could be used in conjunction with the amplitude sensitivity.

The RA–SPP effect was shown to exist even in weakly plasmonic materials, such as Pd. This indicates that such features are a general effect that may be observed in all plasmonic materials, under the proper conditions. Hole arrays or related structures created from weak plasmonic materials offer new prospects for constructing plasmonic components, such as the design of SPP-based sensors and SERS substrates that require short wavelengths for efficient excitation.

Additional systems were also discussed, including isolated holes, pillar arrays, superlattices, and other periodic systems. All of these were shown to exhibit novel effects. For example, the superlattice results demonstrated that nanostructured metal films can cause plasmons to interact over multiple length scales. Specifically, it was shown that intrapatch SPPs (which act on the order of hundreds of nanometers) can interact with interpatch SPPs (which act on the order of tens of micrometers).

Before ending this chapter, it is worth mentioning that periodically structured metal films (such as hole arrays) or isolated apertures are not the only such nanostructured systems that exhibit novel effects. One particularly interesting example is that SPP propagation can be controlled analogous to classical optics. Considering that a SPP has momentum (Eq. 6.1), it is possible to derive a plasmonic Snell's law [54], $k_i \sin(\theta_i) = k_t \sin(\theta_t)$ where i and t correspond to the incident and transmitted (refracted) values, respectively.

Figure 6.19 shows FDTD calculations of a SPP excited and propagating along $+x$ at 2.5 eV on an aluminum (Al) film. Upon encountering a flat Ag interface at angle of $3\pi/4$ with respect to x, it refracts at an angle of $\theta_r \approx \pi/6.5$. Note that $\varepsilon_r = 6$ in this (and in the following example), which corresponds to diamond, and therefore $\Re(k_t)/\Re(k_i) \approx 1.52$ ($k_{\mathrm{Al}}c/\omega \approx 2.69 + i0.075$ and $k_{\mathrm{Ag}}c/\omega \approx 4.08 + i0.064$), which is analogous to an air–glass interface in classical optics.

As an additional example of this, consider a SPP propagating from Al into a Ag semi-cylindrical half-space (with a 400 nm diameter). Somewhat of a schematic diagram can be seen in the FDTD calculated $\mathbf{E}_z(t=0)$ in Fig. 6.20, where the Ag

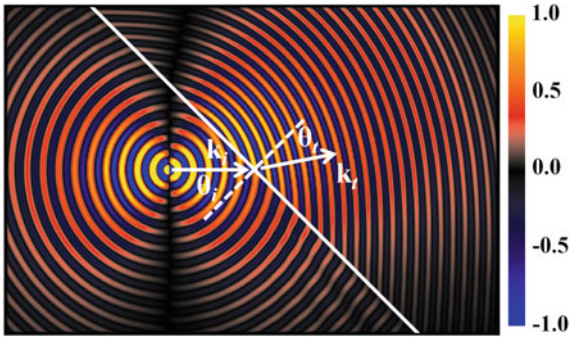

Fig. 6.19 FDTD calculations of $\mathbf{E_z}(\mathbf{t} = \mathbf{0})$ 10 nm above an Al/Ag metal film (on the left/right, respectively) at 2.5 eV, showing SPP refraction at the metal interface (shown as a *white line*)

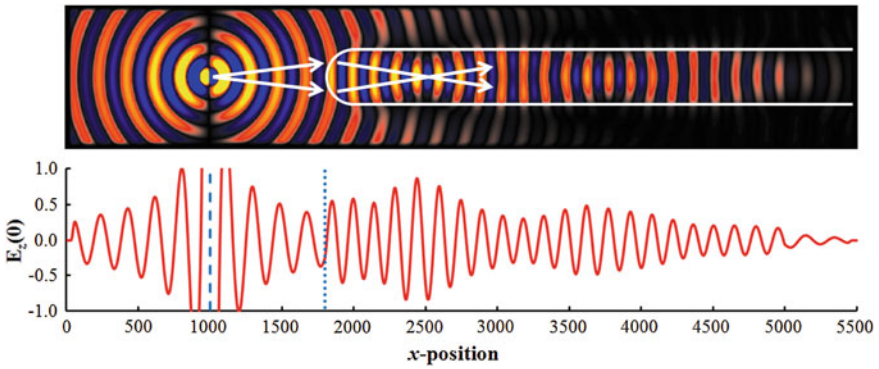

Fig. 6.20 FDTD calculations of SPP focusing by a Ag semi-cylindrical half-space at 2.5 eV. *Upper image* $\mathbf{E}_z(t = 0)$ 10 nm above the Al/Ag metal film. *Lower image* 2D slice through the center of the upper image (along the long direction). The Ag film is outlined in *white*; the *blue dashed line* indicates the SPP source position; and the *blue dotted line* indicates the front surface of the Ag film

film is outlined in white. White arrows are inserted into the intensity profile, which indicate the propagation directions of two SPP "rays". Two rays propagate outwards from the SPP source, refract at the Ag interface, and focus near $x \approx 2550$ nm. Considering the Ag cylindrical interface as a lens, this corresponds to a focal distance of approximately 750 nm, which is very close to analogous lensing in regular optics by a $n = 1.5$ lens in free space at 2.5 eV of 731 nm. The bottom plot in Fig. 6.20 shows $\mathbf{E}_z(t = 0)$ as a function of x, where the focusing can be clearly seen in the enhancement of the SPP magnitude. Since a SPP is attenuated as it propagates, this focusing leads to a significant increase in the propagation length.

Such systems, governed by a simple analog to Snell's law, could be useful for a wide range of optoelectronic devices, for example.

References

1. McMahon JM, Gray SK, Schatz GC (2011) Surface nanophotonics theory. Comprehensive Nanoscience and Technology. In: Wiederrech G (ed), Elsevier: Amsterdam
2. McMahon JM, Henzie J, Odom TW, Schatz GC, Gray SK (2007) Tailoring the sensing capabilities of nanohole arrays in gold films with Rayleigh anomaly–surface plasmon polaritons. Opt Express 15:18119–18129
3. Gao H, McMahon JM, Lee MH, Henzie J, Gray SK, Schatz GC, Odom TW (2009) Rayleigh anomaly–surface plasmon polariton resonances in palladium and gold subwavelength hole arrays. Opt Express, 17:2334–2340
4. Odom TW, Gao H, McMahon JM, Henzie J, Schatz GC (2009) Plasmonic superlattices: Hierarchical subwavelength hole arrays. Chem Phys Lett 483:187–192
5. Schatz GC, McMahon JM, Gray SK (2007) Tailoring the parameters of nanohole arrays in gold films for sensing applications. In: Mark I Stockman (ed), Plasmonics: Metallic Nanostructures and Their Optical Properties V. 664103:1–8
6. Raether H (1988) Surface Plasmons on Smooth and Rough Surfaces and on Gratings. Springer, Berlin
7. Ebbesen TW, Lezec HJ, Ghaemi HF, Thio T, Wolff PA (1998) Extraordinary optical transmission through subwavelength hole arrays. Nature 391:667–669
8. Yeh P (1988) Optical Waves in Layered Media. Wiley, New York
9. Lynch DW, Hunter WR (1985) Comments on the optical constants of metals and an introduction to the data for several metals. In: Palik ED (ed) Handbook of optical constants of solids. Orlando: FL 275–368
10. Johnson PB, Christy RW (1972) Optical constants of the noble metals. Phys Rev B 6:4370–4379
11. Kretschmann E (1971) The determination of the optical constants of metals by excitation of surface plasmons. Z Phys 241:313–324
12. Otto A (1968) Excitation of nonradiative surface plasma waves on silver by the method of frustrated total reflection. Z Phys 216:398–410
13. McMahon JM, Henzie J, Odom TW, Schatz GC, Gray SK (2007) Tailoring the sensing capabilities of nanohole arrays in gold films with Rayleigh anomaly–surface plasmon polaritons. Opt Express 15:18119–18129
14. Degiron A, Lezec HJ, Yamamoto N, Ebbesen TW (2004) Optical transmission properties of a single subwavelength aperture in a real metal. Opt Commun 239:61–66
15. Barnes WL, Murray AW, Dintinger J, Devaux E, Lezec HJ, Ebbesen TW (2004) Surface plasmon polaritons and their role in the enhanced transmission of light through periodic arrays of sub-wavelength holes in a metal film. Phys Rev Lett 92:107401
16. Ghaemi HF, Thio T, Grupp DE, Ebbesen TW, Lezec HJ (1998) Surface plasmons enhance optical transmission through subwavelength holes. Phys Rev B 58:6779–6782
17. Hessel A, Oliner AA (1965) A new theory of Wood's anomalies on optical gratings. Appl Optics 4:1275–1297
18. Darmanyan S, Nevière M, Zayats A (2004) Analytical theory of optical transmission through periodically structured metallic films via tunnel-coupled surface polariton modes. Phys Rev B 70:075103
19. Lee MH, Gao H, Odom TW (2009) Refractive index sensing using quasi one-dimensional nanoslit arrays. Nano Lett 9:2584–2588
20. Porto JA, García-Vidal FJ, Pendry JB (1999) Transmission resonances on metallic gratings with very narrow slits. Phys Rev Lett 83:2845–2848
21. Bravo-Abad J, Martín-Moreno L, García-Vidal FJ (2004) Transmission properties of a single metallic slit: From the subwavelength regime to the geometrical-optics limit. Phys Rev E 69:026601
22. Bethe HA (1944) Theory of diffraction by small holes. Phys Rev 66:163–182

23. Babayan Y, McMahon JM, Li S, Gray SK, Schatz GC, Odom TW (2009) Confining standing waves in optical corrals. ACS Nano 3:615–620
24. McMahon JM, Gray SK, Schatz GC (2008) Dephasing of electromagnetic fields in scattering from an isolated slit in a gold film. In: S. Kawata (ed) Plasmonics: Nanoimaging, Nanofabrication, and Their Applications IV, 703311:1–6
25. Yin L, Vlasko-Vlasov VK, Rydh A, Pearson J, Welp U, Chang S-H, Gray SK, Schatz GC, Brown DB, Kimball CW (2004) Surface plasmons at single nanoholes in Au films. Appl Phys Lett 85:467–469
26. Wannemacher R (2001) Plasmon-supported transmission of light through nanometric holes in metallic thin films. Opt Commun 195:107–118
27. Hafner C (1990) The Generalized Multipole Technique for Computational Electromagnetics. Artech House, Boston
28. Prikulis J, Hanarp P, Olofsson L, Sutherland D, Käll M (2004) Optical spectroscopy of nanometric holes in thin gold films. Nano Lett 4:1003–1007
29. Rindzevicius T, Alaverdyan Y, Sepulveda B, Pakizeh T, Käll M (2007) Nanohole plasmons in optically thin gold films. J Phys Chem C 111:1207–1212
30. Ringe E, McMahon JM, Sohn K, Cobley C, Xia Y, Huang J, Schatz GC, Marks LD, Van Duyne RP (2010) Unraveling the effects of size, composition, and substrate on the localized surface plasmon resonance frequencies of gold and silver nanocubes: A systematic single particle approach. J Phys Chem C 114:12511–12516
31. Treacy MMJ (2002) Dynamical diffraction explanation of the anomalous transmission of light through metallic gratings. Phys Rev B 66:195105
32. Jones WE, Kliewer KL, Fuchs R (1969) Nonlocal theory of the optical properties of thin metallic films. Phys Rev 178:1201–1203
33. Ruan Z, Qiu M (2006) Enhanced transmission through periodic arrays of subwavelength holes: The role of localized waveguide resonances. Phys Rev B 96:233901
34. Genet C, van Exter MP, Woerdman JP (2003) Fano-type interpretation of red shifts and red tails in hole array transmission spectra. Opt Commun 225:331–336
35. Stewart ME, Mack NH, Malyarchuck V, Soares JANT, Lee T-W, Gray SK, Nuzzo RG, Rogers JA (2006) Quantitative multispectral biosensing and 1D imaging using quasi-3D plasmonic crystals. P Natl Acad Sci USA 103:17143–17148
36. van der Molen KL, Segerink FB, van Hulst NF, Kuipers L (2004) Influence of hole size on the extraordinary transmission through subwavelength hole arrays. Appl Phys Lett 85:4316–4318
37. Klein Koerkamp KJ, Enoch S, Segerink FB, van Hulst NF, Kuipers L (2004) Strong influence of hole shape on extraordinary transmission through periodic arrays of subwavelength holes. Phys Rev Lett 92:183901
38. van der Molen KL, Klein Koerkamp KJ, Enoch S, Segerink FB, van Hulst NF, Kuipers L (2005) Role of shape and localized resonances in extraordinary transmission through periodic arrays of subwavelength holes: Experiment and theory. Phys Rev B 72:045421
39. Shou X, Agrawal A, Nahata A (2005) Role of metal film thickness on the enhanced transmission properties of a periodic array of subwavelength apertures. Opt Express 13:9834–9840
40. Kim JH, Moyer PJ (2006) Thickness effects on the optical transmission characteristics of small hole arrays on thin gold films. Opt Express 14:6595–6603
41. Steele J, Moran C, Aguirre A, Lee A, Halas NJ (2003) Metallodielectric gratings with subwavelength slots: Optical properties. Phys Rev B 68:205103
42. Gao H, Henzie J, Lee MH, Odom TW (2008) Screening plasmonic materials using pyramidal gratings. P Natl Acad Sci USA 105:20146–20151
43. Piciu OM, Docter MW, van der Krogt MC, Garini Y, Young IT, Sarro PM, Bossche A (2007) Fabrication and optical characterization of nano-hole arrays in gold and gold/palladium films on glass. Inst Mech Engin Part N: J Nanoengin Nanosyst 221:107–114
44. Johnson PB, Christy RW (1974) Optical constants of transition metals: Ti, V, Cr, Mn, Fe, Co, Ni, and Pd. Phys Rev B 9:5056–5070

45. Bonod N, Enoch S, Li L, Evgeny L, Nevière M (2003) Resonant optical transmission through thin metallic films with and without holes. Opt Express 11:482–490
46. Degiron A, Ebbesen TW (2004) Analysis of the transmission process through single apertures surrounded by periodic corrugations. Opt Express 12:3694–3700
47. Stewart ME, Anderton CR, Thompson LB, Maria J, Gray SK, Rogers JA, Nuzzo RG (2008) Nanostructured plasmonic sensors. Chem Rev 108:494–521
48. Yao JM, Stuart ME, Maria J, Lee T-W, Gray SK, Rogers JA, Nuzzo RG (2008) Seeing molecules by eye: Surface plasmon resonance imaging at visible wavelengths with high spatial resolution and submonolayer sensitivity. Angew Chem Int Ed 47:5013–5017
49. Hicks EM, Zhang X, Zou S, Lyandres O, Spears KG, Schatz GC, Van Duyne RP (2005) Plasmonic properties of film over nanowell surfaces fabricated by nanosphere lithography. J Phys Chem B 109:22351–22358
50. Baida FI, Belkhir A, Van Labeke D (2006) Subwavelength metallic coaxial waveguides in the optical range: Role of the plasmonic modes. Phys Rev B 74:205419
51. Poujet Y, Salvi J, Baida FI (2007) 90% Extraordinary optical transmission in the visible range through annular aperture metallic arrays. Opt Lett 32:2942–2944
52. Haftel MI, Schlockermann C, Blumberg G (2006) Enhanced transmission with coaxial nanoapertures: Role of cylindrical surface plasmons. Phys Rev B 74:235405
53. Orbons SM, Roberts A, Jamieson DN, Haftel MI, Schlockermann C, Freeman D, Luther-Davies B (2007) Extraordinary optical transmission with coaxial apertures. Appl Phys Lett 90:251107
54. McMahon JM, Gray SK, Schatz GC (2010) Geometric plasmonics. In preparation

Chapter 7
Optical Corrals

Preface

The content that appears in this chapter has been largely adapted from the following publications:

McMahon JM, Gray SK, Schatz GC (2008) Dephasing of electromagnetic fields in scattering from an isolated slit in a gold film. Proc. SPIE 7033: 703311/1-6. doi: 10.1117/12.790647

Babayan Y, McMahon JM, Li S, Gray SK, Schatz GC, Odom TW (2009) Confining standing waves in optical corrals. ACS Nano 3:615–620. doi: 10.1021/nn8008596

McMahon JM, Gray SK, Schatz GC (2011) Surface nanophotonics theory. In: Wiederrecht G (ed) Comprehensive Nanoscience and Technology. Elsevier, Amsterdam

The experimental work that appears in this chapter was done by Babayan Y and Odom TW. Although, the experimental aspects are not discussed heavily, and the reader interested in such details is referred to Refs. [1–3].

7.1 Introduction

In this chapter, FDTD modeling and near-field optical characterization of lithographically patterned arrays of micron-sized metallic circular rings are discussed, microscale (1−10 μm) analogues of the nanoscale quantum corral [4]. Such structures are of interest for confining and manipulating light on surfaces, which, for example, are of relevance for emerging applications in optoelectronics [5], photonics [5–7], and chemical and biological sensing [8, 9]. The wavelength dependence of such confinement will also be discussed. Additionally, elliptical corrals with three different eccentricities [$e = (1 - b^2/a^2)^{1/2}$, where a and b are the long and short axes, respectively] are discussed, which offer a novel platform

J. M. McMahon, *Topics in Theoretical and Computational Nanoscience*,
Springer Theses, DOI: 10.1007/978-1-4419-8249-0_7,

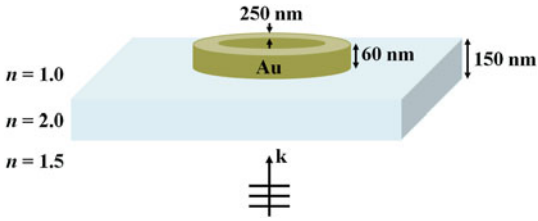

Fig. 7.1 Schematic diagram of an optical corral

for investigating polarization effects. Unlike in quantum corrals [4, 10, 11], such effects offer the potential to control the pattern of the standing waves. FDTD calculations of the intensities of the electric field $|E(x,\omega)|^2$ and magnetic field $|H(x,\omega)|^2$ are provided to support the experimental results. These calculations also reveal novel photonic effects, such as substrate effects and electromagnetic field dephasing, which are analyzed using a waveguide modal analysis. Such analysis is relevant for the aforementioned applications, but also enables a straightforward understanding of the relationship between NSOM measurements and the electric and magnetic fields that are typically used to interpret the corresponding near-field images.

7.2 Computational Considerations

Isolated corrals were modeled after the experiments as 60 nm high (larger than the skin depth of Au at optical wavelengths of $\sim$25 nm [12]) and 250 nm wide Au, Ag, or aluminum oxide (Al_2O_3) ring structures on top of a 150 nm thick $n = 2.0$ layer [similar to indium tin oxide (ITO)], and all on top of a glass ($n = 1.5$) substrate. A schematic diagram of the system under consideration is shown in Fig. 7.1. [2D FDTD calculations on analogous systems (not shown) indicate that isolated corrals produce results similar to those of a periodic array of them, such as the experimental ones in this chapter.] Computational domains were discretized using grid spacings of 5.0 nm in all directions. The dielectric functions of Au and Ag were modeled using the D2L model, accurately fit to empirically determined dielectric data over the relevant wavelengths (400–700 nm); Appendix B. Al_2O_3 was assumed to have a constant refractive index of $n = 1.77$. Field intensities were calculated 20 nm above the $n = 2.0$ layer by Fourier transforming the time-domain electric and magnetic fields.

7.3 Circular Corrals

Figure 7.2a shows a SEM image of a single circular corral made of Au with an inside diameter of 4.8 μm. When the structure is illuminated at normal incidence with circularly polarized 633 nm light and imaged by collection mode NSOM, two

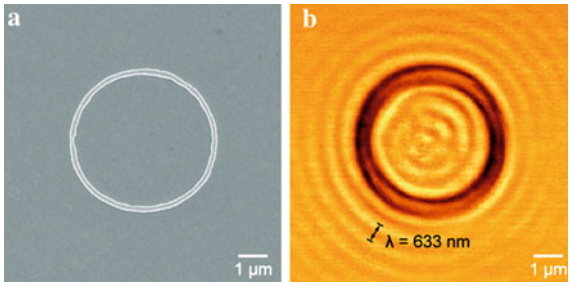

Fig. 7.2 A circular optical corral. **a** SEM image of a 4.8 μm diameter Au corral, **b** NSOM image of **a** illuminated using circularly polarized 633 nm incident light

specific features are found inside and around the corral: (1) evanescent waves with ~200–250 nm amplitude in the z-direction (normal to the surface), which can be quantified by single-point NSOM spectroscopy, and (2) standing wave patterns inside and outside of the structure with a wavelength close to that of the light used for imaging, as can be seen in Fig. 7.2b. The pattern inside the corral contains ripples, while that outside consists of concentric, circular fringes. In passing, it is interesting to note that the patterns formed within the optical corrals resemble the patterns of electronic standing waves in quantum corrals [4, 11, 10].

To investigate the effect of the corral size on the patterns, arrays of Au circular corrals with inner diameters of 2.23 and 5 μm center-to-center separations were fabricated; Fig. 7.3a. When these structures are imaged using circularly polarized 633 nm light, the number of internal ripples decrease (Fig. 7.3b, top), as expected, and the central spots become dark. These results are similar to those observed in NSOM images of the local density of states inside 2.7-μm circular Au discrete-wall corrals [13]. In addition, the standing wave pattern outside of the corrals becomes more well-defined. FDTD calculations of $|E(x,\omega)|^2$ for a 2.23-μm circular Au corral shows good agreement with the experimental patterns both inside and around the corral, including the peak-to-peak wavelength of the standing waves and the positions of the maxima and minima; Fig. 7.3c.

Changes in the intensity and pattern of the standing waves outside of the corrals can easily be explained as diffraction between opposite corral walls from both individual and neighboring corrals, where the longer wavelengths correspond to lower diffraction orders, and are thus more intense. However, the fields inside the corrals are found to only depend on the geometry and local dielectric environment of an individual corral. For example, calculations without the ITO substrate produces significantly different field patterns; Fig. 7.4. Without the substrate, the trends of the maxima and minima are reversed compared to its inclusion, and also resemble slit waveguide modes excited with TE_z polarized light [2]; see Sect. 7.4. These results demonstrate that the confined fields in the optical corrals can be tuned by the changing the substrate. The primary reason for this is that the effective incident wavelength in the corrals depends on the substrate, $\lambda_{\text{eff}} = \lambda_0/\varepsilon_{\text{sub}}^{1/2}$, where λ_{eff} is the effective incident wavelength and λ_0 is the actual incident wavelength inside the substrate with permittivity ε_{sub}. Presumably, the field

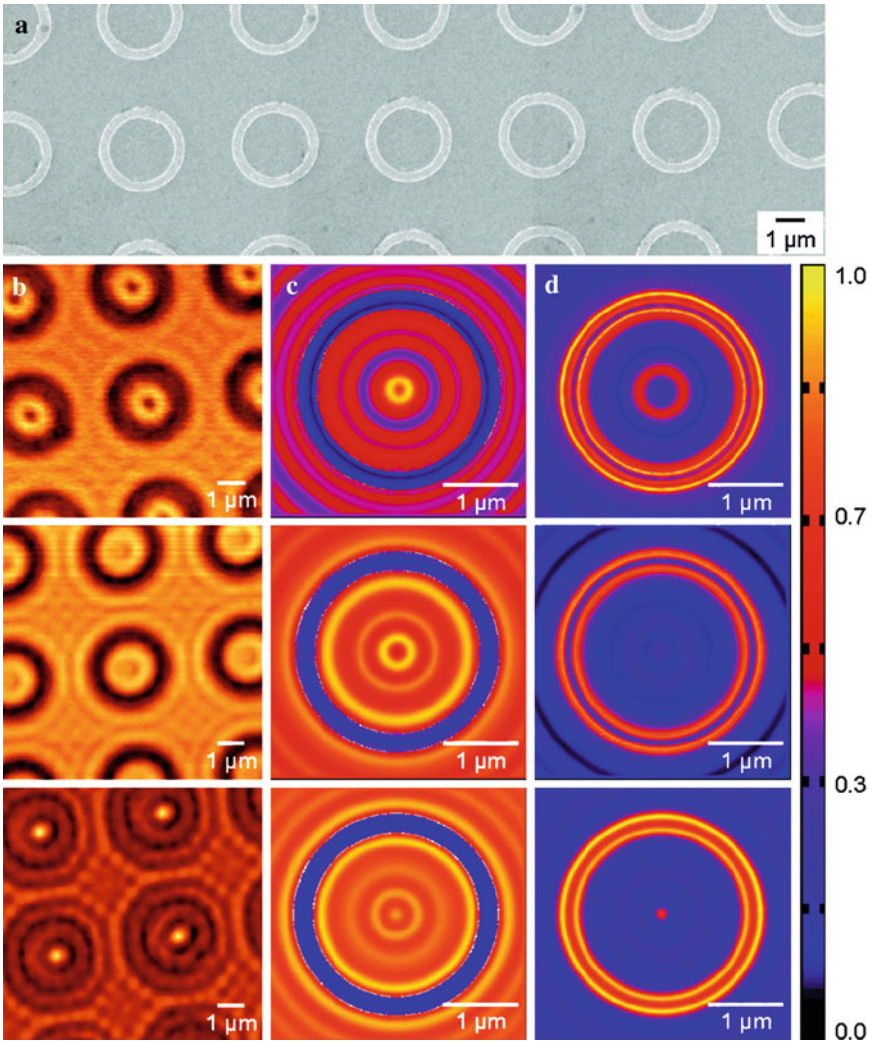

Fig. 7.3 Wavelength dependence of standing wave patterns in circular corrals. **a** SEM image of arrays of 2.23 μm diameter Au corrals, **b** Collection mode NSOM images of the corrals under *top* 633, *middle* 543, and *bottom* 457-nm light. FDTD calculations of **c** $|E(x,\omega)|^2$ and **d** $|H(x,\omega)|^2$ for the same conditions as in **b**

patterns will be completely reversed when $d\left(1-\varepsilon_{\text{sub}}^{1/2}\right)/\lambda_0 = n + 1/2$, where $n = 0, 1, 2,\ldots$ and d is the corral diameter.

Interestingly, $|E(x,\omega)|^2$ and $|H(x,\omega)|^2$ are found to be qualitatively backwards within the corrals; Figs. 7.3c, d and 7.4. This feature can be explained by performing calculations on a simplified system and using a waveguide modal analysis [2, 14]; see Sect. 7.4.

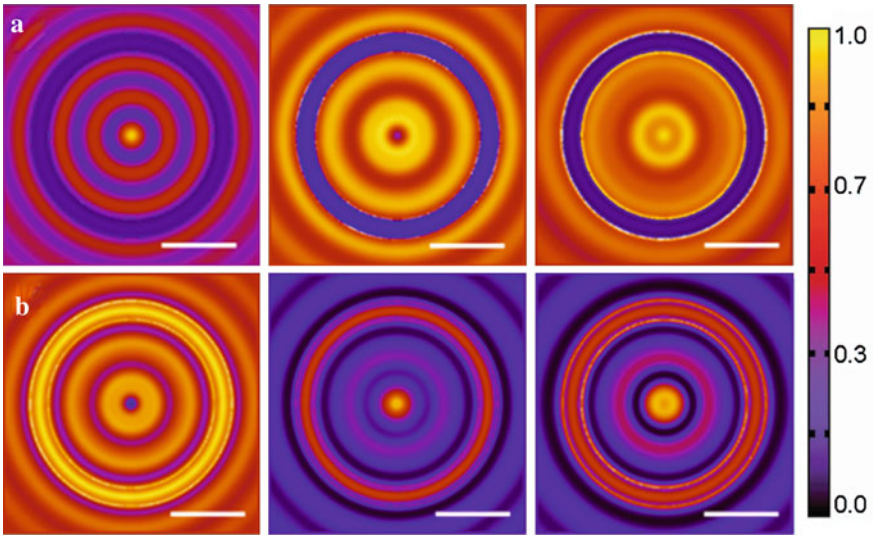

Fig. 7.4 FDTD calculated **a** $|E(x,\omega)|^2$ and **b** $|H(x,\omega)|^2$ inside a 2.23 μm inner diameter circular Au corral with no substrate for *left* 457, *middle* 543, and *right* 633 nm incident light. *Scale bars* represent 1 μm

Variations of the standing wave patterns in response to a change in the wavelength of the light are also observed. The 2.23-μm corrals illuminated and imaged using two additional wavelengths, 543 and 457 nm, are shown in Fig. 7.3b, c *middle* and *bottom*. When the 633-nm light is replaced with 543-nm, and then with 457-nm, the dark spot in the middle of the corral gradually switches to a bright one (Fig. 7.3b, *bottom*), which has an intensity $\sim$6 times higher than the lowest intensity spot. This observation suggests that only certain wavelengths of light are optimally sustained inside the corrals to produce a high intensity spot at the center.

To investigate the effect of the corral material on the patterns, circular corrals with Ag and Al_2O_3 (dielectric) walls with inner diameters of 2.35 μm were also fabricated; Fig. 7.5. When the corrals are excited with circularly polarized 633-nm light, identical patterns are produced inside both the metallic and dielectric structures, Fig. 7.5a, b, respectively. The dielectric corrals, however, are brighter than the metallic ones, which is expected because Al_2O_3 is transparent. Another variation between the images is in the contrast of the standing wave patterns, which indicates that the reflectivity of the corral material is important (a result not necessarily expected, a priori). Based on reflectivity values, the dielectric structures have the lowest contrast because that of Al_2O_3 is lower, compared to the metals, at 633 nm. Between the two metals, Ag has a slightly better contrast because it has $\sim$5% higher reflectivity at 633 nm than Au [15]. FDTD calculations of $|E(x,\omega)|^2$ for these corrals again support the experimentally observed results; Fig. 7.5, *right*.

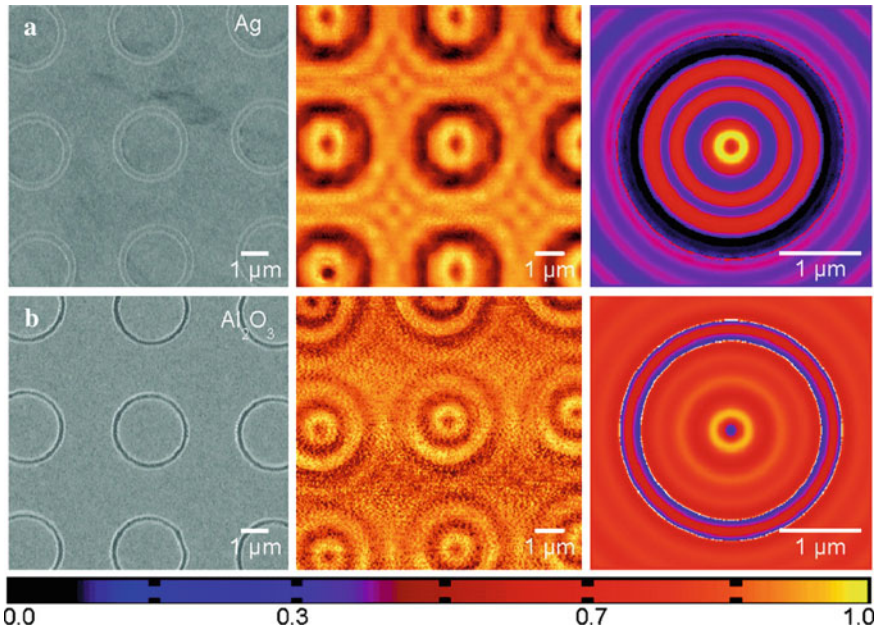

Fig. 7.5 Corral material dependence of standing wave patterns. *left* SEM, *middle* NSOM, and *right* FDTD calculations of $|E(x,\omega)|^2$ for **a** Ag and **b** Al_2O_3 corrals illuminated using 633-nm light

7.4 1D Corrals (Isolated Slits)

In order to understand the results in Sect. 7.3, it is helpful to focus on a simplified structure, a 1D slit with a width (d) of the same diameter as the corrals ($d = 2.23\,\mu$m) in a thin Au film (also with thickness of $h = 60$ nm) in air. In this way, the behavior of confined EM fields for 543-nm TE_z,TM_z, and circular (which contains both TE_z and TM_z polarizations, but out of phase) incident polarizations of light can be determined (polarizations which can all be important in the full structures). Figure 3.10 shows a schematic diagram of the system under consideration for TE_z polarization.

$|E(x,\omega)|^2$ and $|H(x,\omega)|^2$ inside the slit calculated with FDTD for TE_z polarization are shown in Fig. 7.6a. It is seen that the fields have oscillatory behavior within the slit, with a peak-to-peak separation of 515 and 545 nm for $|E(x,\omega)|^2$ and $|H(x,\omega)|^2$, respectively, which is very close to the free-space wavelength of 543 nm. In addition, it is seen that $|E(x,\omega)|^2$ and $|H(x,\omega)|^2$ are backwards. Both trends agree very well with the results in Sect. 7.3 for the full corral systems.

Assuming that Au can be treated as a PEC, the transverse component of the field inside the slit can be expanded as a superposition of the eigenmodes of a 1D parallel-plate waveguide, and a modal analysis can be used to gain physical insight into the problem [1, 2]; see Sect. 3.5.2. The field intensities calculated with this

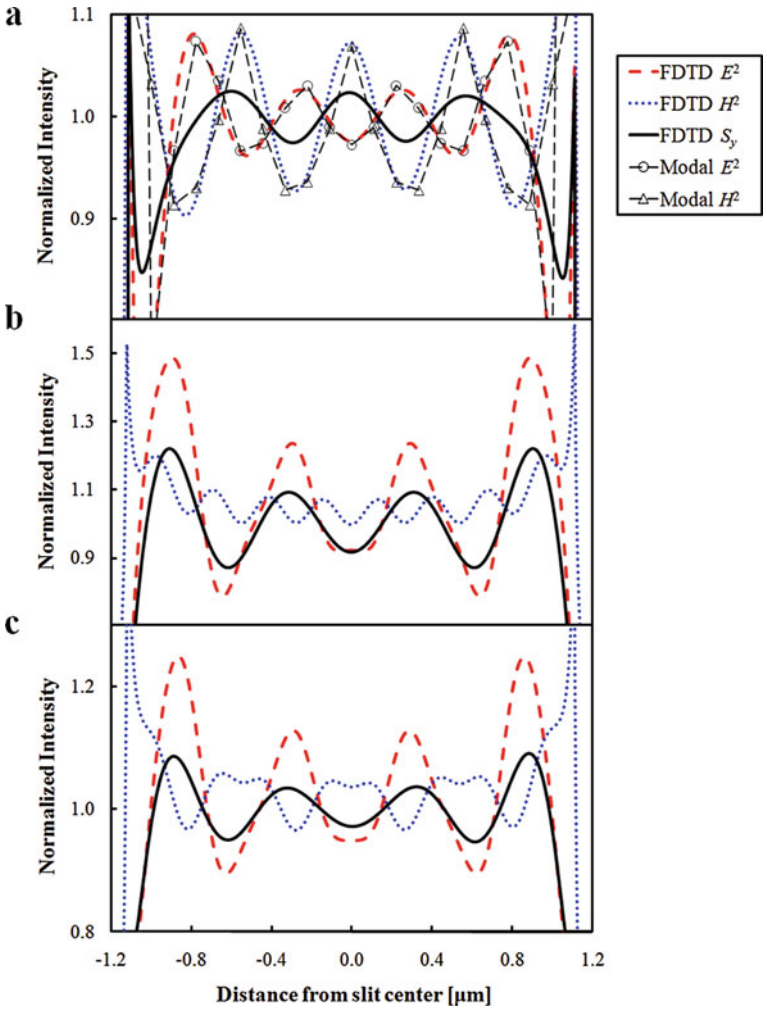

Fig. 7.6 FDTD calculated field intensities inside and power flow through a $d = 2.23\,\mu$m diameter slit in a $h = 60$ nm thick Au film for 543-nm incident light **a** TE_z, **b** TM_z, and **c** circularly polarized. Modal expansion method results are also shown for a PEC film for TE_z polarization

method are shown in Fig. 7.6a. The results agree very well with the FDTD calculations, confirming that the behavior of the fields inside a slit in a Au film and a PEC are similar.

The amplitudes of the waveguide modes, A_m and B_m in Eq. 3.111, obtained from the modal analysis are shown in Fig. 7.7. It is seen that coefficients are mainly composed of the $m = 0$ and $m = 8$ modes. The latter mode is entirely imaginary, which means that scattering by the slit (corral) induces a modal transition from propagating to evanescent. The transitional evanescent mode

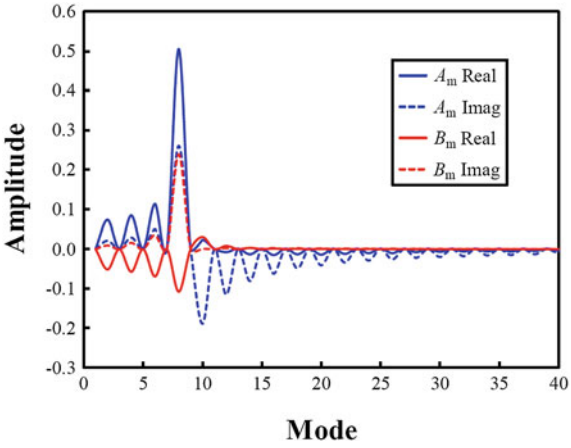

Fig. 7.7 Amplitudes of the waveguide modes inside a $d = 2.23$ μm diameter slit in a $h = 60$ nm thick PEC film for 543-nm TE_z polarized incident light. The $m = 0$ mode, which has amplitudes of $A_m = 0.658 - i0.846$ and $B_m = 0.601 + i0.858$, is not shown for clarity

corresponds to light that propagates parallel to the surface with a wavelength just slightly shorter than the incident light ($m\pi/d \approx k_0\varepsilon_s^{1/2}$). This analysis thus explains the similarity between this wavelength and the peak-to-peak separation of the standing waves, as well as their evanescent character. Furthermore, the superposition of the high-order evanescent modes onto the propagating ones explains the backwards behavior between $|E(x,\omega)|^2$ and $|H(x,\omega)|^2$. Lastly, this analysis explains the corral material dependence results, as $\phi_m(x)$ in the modal analysis (Sect. 3.5.2) (and the equivalent expression for TM_z polarization) is better satisfied as the reflectivity (or equivalently, the dielectric constant) goes to infinity. As this happens, the intensity of the confined waves should (and does) become stronger.

FDTD calculations of the normal component of the Poynting vector (a measure of the power flow), S_y, inside the slit are also shown in Fig. 7.6a. It is seen that power flow through the slit is governed by $|H(x,\omega)|^2$, except near the slit edges.

To completely describe all aspects of the full systems, other polarizations (e.g., TM_z polarization) need to be taken into account. The values of $|E(x,\omega)|^2$,$|H(x,\omega)|^2$, and S_y calculated using FDTD for TM_z polarization are shown in Fig. 7.6b. It is seen that the peak-to-peak separation of $|E(x,\omega)|^2$ is 590 nm, which again is very close to the free-space wavelength of 543 nm. However, the peak-to-peak separation of $|H(x,\omega)|^2$ is 270 nm, close to half of the free-space wavelength. This can be attributed to $H(x,\omega)$ components composed almost entirely of the $m = 8$ waveguide mode. This result is also seen for the y-component of $E(x,\omega)$ for TE_z polarization (not shown), except that it is overshadowed by the x-component, which contains both $m = 0$ and $m = 8$ modes. Additionally, for TM_z polarization, the power flow throughout the entire slit is governed by $E(x,\omega)$.

Finally, properties of $|E(x,\omega)|^2$,$|H(x,\omega)|^2$, and S_y calculated using FDTD for circular polarization are shown in Fig. 7.6c. The results are essentially a superposition of the TE_z and TM_z polarized results. However, the power flow throughout the entire slit is governed by $E(x,\omega)$, similar to the TM_z polarization results.

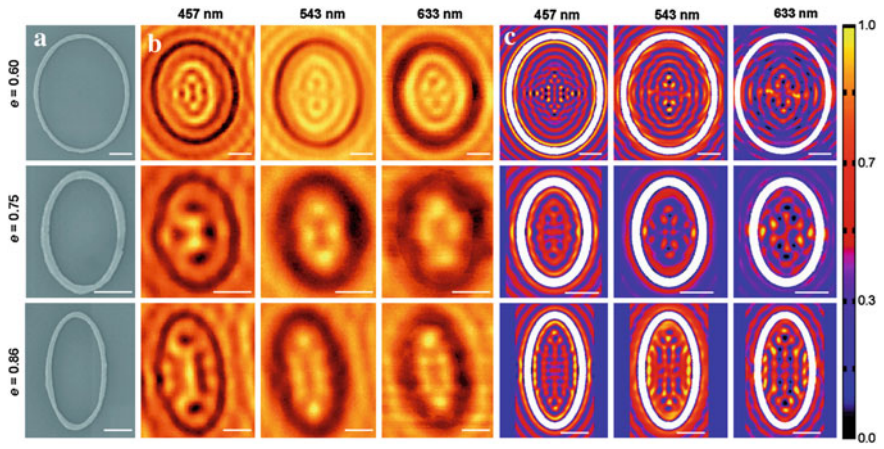

Fig. 7.8 Effect of the ellipse shape on the pattern of standing waves. **a** SEM images of ellipses with eccentricities of $e =$ *top* 0.60,*middle* 0.75, and *bottom* 0.86. **b** NSOM images for the corrals in **a** under circularly polarized light. **c** FDTD calculations of $|E(x,\omega)|^2$ for the corrals in **a**. All *scale bars* represent 1 μm

7.5 Elliptical Corrals

Although circular corrals provide a simple platform for studying the optical analogue of the quantum corral, more complex structures provide additional ways to manipulate light on dielectric surfaces. For example, structures with lower symmetries provide unique opportunities to study polarization effects on light confinement within the corral structures. Figure 7.8a shows ellipses with eccentricities of $e = 0.60$ ($a = 2.5\,\mu\text{m}$, $b = 2\,\mu\text{m}$), $e = 0.86$ ($a = 2\,\mu\text{m}$, $b = 1\,\mu\text{m}$), and $e = 0.75$ ($a = 1.5\,\mu\text{m}$, $b = 1\,\mu\text{m}$). Upon illumination of the ellipses with circularly polarized 457-nm light, complex patterns, which resemble those of quantum corrals with similar eccentricities [10], are formed inside the structures; Fig. 7.8b. Interestingly, ellipses with $e = 0.75$ and 0.86 suppress light at their focal points (dark spots are present), while the $e = 0.60$ ellipse does not. To investigate whether this phenomenon is related to the structure of the corral or to the wavelength of light used for imaging, ellipses imaged with 543 and 633-nm light are shown in Fig. 7.8b as well. For these wavelengths, the ellipses with larger eccentricities show bright spots at their focal points. These results demonstrate that the standing wave patterns can be controlled by changing either the shape of the corral or the excitation wavelength of light.

FDTD calculations were carried out for the elliptical corrals excited with circularly polarized light, and are shown in Fig. 7.8c. As with the circular corrals, $|E(x,\omega)|^2$ agrees well with experiment, and $|E(x,\omega)|^2$ and $|H(x,\omega)|^2$ are

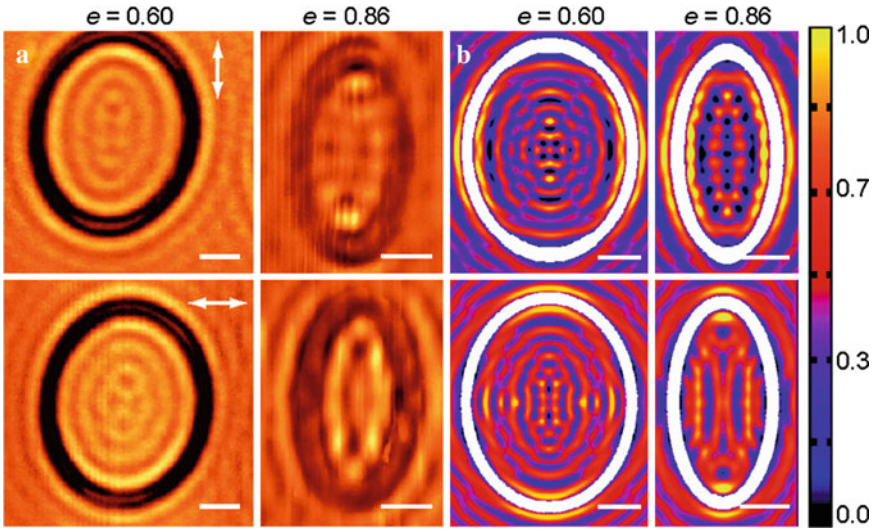

Fig. 7.9 Polarization effects on standing-wave patterns. **a** Ellipses with $e = 0.60$ and 0.86 imaged using 543-nm light with $E(x, \omega)$ linearly polarized along either the *top* long or *bottom* short axis. **b** FDTD calculations of $|E(x, \omega)|^2$. In **b**, the ellipses are outlined in white; all *scale bars* represent 1 μm

backwards (not shown). Based on the discussion in Sect. 7.4, all of these results can be understood as arising from interference between waveguide modes that are excited by the short and long axes of the corrals, which also dephases the fields.

Because of the low symmetries of the elliptical corrals, the fields confined within them are expected to exhibit a polarization dependence. The $e = 0.60$ and 0.86 ellipses imaged using linearly polarized (along either the short or long axis) 543-nm light are shown in Fig. 7.9a. FDTD calculations were also carried out for the elliptical corrals excited with linearly polarized light, and support the experimentally observed trends; Fig. 7.9b. These results confirm that standing wave patterns can be tailored by simply changing the polarization direction of the incident light, and once again can be explained using the same analysis given in Sect. 7.4. In the elliptical corrals, however, an asymmetric excitation of TE_z and TM_z polarized waveguide modes occurs, and the FDTD results show that the TM_z polarized waveguide mode is dominant.

7.6 Summary

A study of corral structures was presented. Such structures were shown to be useful to confine and manipulate light on dielectric surfaces, and can be considered optical analogues to quantum corrals. Circular corrals were used to elucidate the

basic effects in such structures, such as well-defined standing wave patterns. Such effects were shown to exhibit corral size, wavelength, material, and substrate dependencies. FDTD calculations supported the experimental results, and also revealed that $|E(x,\omega)|^2$ matches the measurements, while $|H(x,\omega)|^2$ is backwards.

In order to explain these effects, a simple waveguide model was used. These results helped determine that light scattering from the corrals produces evanescent waveguide modes at the dielectric interface with an effective wavelength similar to that of the incident light. Furthermore, when these modes are superimposed onto the propagating ones, a dephasing of $|E(x,\omega)|^2$ and $|H(x,\omega)|^2$ occurs. The results in Fig. 7.6 are particularly important to the interpretation of NSOM imaging measurements, as they show that the power flow (which is the property that is directly probed) provides a measurement of the local $E(x,\omega)$ in some cases and the local $H(x,\omega)$ in others. While this can complicate the use of NSOM to experimentally study interference effects, FDTD and the modal expansion method provide simple ways to model the results.

The aforementioned effects were further investigated in elliptical structures, which offer further tunability of the standing-wave patterns through both their eccentricity and the polarization of the incident light.

References

1. Babayan Y, McMahon JM, Li S, Gray SK, Schatz GC, Odom TW (2009) Confining standing waves in optical corrals. ACS Nano 3:615–620
2. McMahon JM, Gray SK, Schatz GC (2008) Dephasing of electromagnetic fields in scattering from an isolated slit in a gold film. In: Kawata S (ed), Plasmonics: Nanoimaging, Nanofabrication, and Their Applications IV 703311-1–6
3. McMahon JM, Gray SK, Schatz GC (2011) Surface nanophotonics theory. In: Wiederrecht G (ed) Comprehensive Nanoscience and Technology. Elsevier, Amsterdam
4. Crommie MF, Lutz CP, Eigler DM (1993) Confinement of electrons to quantum corrals on a metal surface. Science 262:218–220
5. Barnes WL, Dereux A, Ebbesen TW (2003) Surface plasmon subwavelength optics. Nature 424:824–830
6. Ebbesen TW, Lezec HJ, Ghaemi HF, Thio T, Wolff PA (1998) Extraordinary optical transmission through subwavelength hole arrays. Nature 391:667–669
7. Ozbay E (2006) Plasmonics: Merging photonics and electronics at nanoscale dimensions. Science 311:189–193
8. Haes AJ, Haynes CL, McFarland AD, Schatz GC, Van Duyne RP, Zou S (2005) Plasmonic materials for surface-enhanced sensing and spectroscopy. MRS Bull 30:368–375
9. Willets KA, Van Duyne RP (2007) Localized surface plasmon resonance spectroscopy and sensing. Annu Rev Phys Chem 58:267–297
10. Fiete GA, Heller EJ (2003) Colloquium: Theory of quantum corrals and quantum mirages. Rev Mod Phys 75:933–948
11. Manoharan HC, Lutz CP, Eigler DM (2000) Quantum mirages formed by coherent projection of electronic structure. Nature 403:512–515
12. Dawson P, Boyle MG (2006) Light emission from scanning tunneling microscope on polycrystalline Au films: What is happening at the single-grain level? J Opt A-Pure Appl Opt 8:S219–S226

13. Dereux A, Girard C, Chicanne C, Colasdes Francs G, David T, Bourillot E, Lacroute Y, Weeber JC (2003) Subwavelength mapping of surface photonic states. Nanotechnology 14:935–938
14. Bravo-Abad J, Martín-Moreno L, García-Vidal FJ (2004) Transmission properties of a single metallic slit: From the subwavelength regime to the geometrical-optics limit. Phys Rev E 69:026601
15. Johnson PB, Christy RW (1972) Optical constants of the noble metals. Phys Rev B 6:4370–4379

Chapter 8
Nonlocal Dielectric Effects

Preface

The content that appears in this chapter has been largely adapted from the following publications:

McMahon JM, Gray SK, Schatz GC (2009) Nonlocal optical response of metal nanostructures with arbitrary shape. Phys Rev Lett 103:097403. doi:10.1103/PhysRevLett.103.097403

McMahon JM, Gray SK, Schatz GC (2010) Calculating nonlocal optical properties of structures with arbitrary shape. Phys Rev B 82:035423. http://arxiv.org/abs/0912.4746

McMahon JM, Gray SK, Schatz GC (2010) Nonlocal dielectric effects in core–shell nanowires. J Phys Chem C 114:15903-15908. doi:10.1021/jp910899b

Peng S, McMahon JM, Schatz GC, Gray SK, Sun Y (2010) Reversing the size-dependence of surface plasmon resonances in colloidal nanoparticles. (submitted, 2010)

McMahon JM, Gray SK, Schatz GC (2011) Fundamental behavior of electric field enhancements in the gaps between closely spaced nanostructures. Phys Rev B 83:115428.

The experimental work that appears in this chapter was done by Peng S and Sun Y. Although, the experimental aspects are not discussed heavily, and the reader interested in such details is referred to Ref. [1].

8.1 Introduction

Interest in metallic structures with features on the order of 10 nm or less has significantly increased as experimental techniques for their fabrication have become possible [2]. As outlined in Chap. 1, even if the features involve many hundreds of atoms or more so that a continuum level of description is adequate,

J. M. McMahon, *Topics in Theoretical and Computational Nanoscience*, Springer Theses, DOI: 10.1007/978-1-4419-8249-0_8,

their optical response can be difficult to correctly model due to quantum mechanical effects, and thus such properties in this limit are largely unknown. Three important quantum effects were outlined in Chap. 1: electron–interface scattering, electron spill-out, and spatial nonlocality in the dielectric response. While all effects will be touched on in this chapter, the one of main interest is the latter.

In this chapter, an implementation of Maxwell's equations is presented that incorporates the spatially nonlocal dielectric response of arbitrarily shaped structures. Such a formulation allows the description of optical responses of structures that are too large to treat using quantum mechanics, yet too small for local continuum electrodynamics to be valid. Many applications of the method are also discussed. First, the optical properties of basic Au nanostructures in one, two, and three dimensions are determined, such as thin films, solid nanowires, and nanoparticles, respectively. Then, Au core–shell nanowires (nanoshells) are discussed in relation to hypothetical "experimental data". The focus there is on parameters of the nonlocal model, geometric parameters of the nanoshells, and the effect of the surrounding dielectric environment. Lastly, the effects of spatial nonlocality in the dielectric response on the near-field maximum and average $|\mathbf{E}(\mathbf{x},\omega)|^2$ enhancements will be discussed. These will first be discussed in relation to isolated Au nanowires, but then dimers of cylindrical and triangular Ag nanowires. The enhancements will be qualitatively compared to those obtained without nonlocal effects, such as those in Chap. 5, and it will be suggested that there is a fundamental and practical limit to them. Before ending the chapter, a brief discussion of effects related to electron spill-out, surface effects at the sub-nanometer-scale (yet still in the continuum picture), will be discussed.

8.2 Motivation

In Chap. 2, the interaction of a material with light was described (in the continuum limit) through a dielectric function ε that relates the electric displacement field $\mathbf{D}(\mathbf{x},\omega)$ (proportional to both the incident field and that due to material polarization) to the electric field $\mathbf{E}(\mathbf{x},\omega)$, Eq. 2.22. This relationship is repeated here for clarity,

$$\mathbf{D}(\mathbf{x},\omega) = \varepsilon_0 \int d\mathbf{x}' \varepsilon(\mathbf{x},\mathbf{x}',\omega)\mathbf{E}(\mathbf{x}',\omega). \tag{8.1}$$

The assumption was made in Chap. 2 (which has been kept up until this point) that this relationship is local in space, $\varepsilon(\mathbf{x},\mathbf{x}',\omega) = \varepsilon(\omega)\delta(\mathbf{x}-\mathbf{x}')$. However, a simple argument was given which demonstrated that at very small length scales, such an approximation is not valid. This is the situation now considered.

In a homogeneous environment (which arbitrarily shaped structures are approximated as in this chapter), $\varepsilon(\mathbf{x}, \mathbf{x}', \omega)$ only spatially depends on $|\mathbf{x} - \mathbf{x}'|$. Therefore, $\varepsilon(\mathbf{x}, \mathbf{x}', \omega)$ is more simply expressed in $\mathbf{k}$-space as [3]

$$\mathbf{D}(\mathbf{k}, \omega) = \varepsilon_0 \varepsilon(\mathbf{k}, \omega) \mathbf{E}(\mathbf{k}, \omega). \tag{8.2}$$

The $\mathbf{k}$ dependence in $\varepsilon(\mathbf{k}, \omega)$ leads to a spatially nonlocal relationship between $\mathbf{D}(\mathbf{x}, \omega)$ and $\mathbf{E}(\mathbf{x}, \omega)$ when Eq. 8.2 is Fourier transformed to the spatial domain [3] (which is apparent from Eq. 8.1). Physically, this implies that since $\mathbf{D}(\mathbf{x}, \omega)$ is related to the electric polarization, or dipole moment per unit volume, the polarization at one point in space depends on both the local $\mathbf{E}(\mathbf{x}, \omega)$ and that in its neighborhood. This dependence has long been known necessary to describe optical responses of structures with features less than $\sim$10 nm. For example, anomalous absorption is experimentally observed in thin metal films [4, 5], and theoretically, inclusion of $\mathbf{k}$ dependence provides an additional absorption mechanism through the excitation of longitudinal (or volume) plasmons [6] (called such because they are longitudinal to $\mathbf{k}$ and are contained within the volume of the structure, unlike SPs which propagate along the metal–dielectric interface). More recently, such effects have also been found necessary to describe the blueshifting of LSPRs (relative to classical local predictions) [7] observed in small Au nanoparticles [8].

Since the first formulation of nonlocal electromagnetics [3], complications introduced by such nonlocal, $\mathbf{k}$-dependent dielectric functions have caused applications to remain limited to simple systems (until recently [7, 9]), such as spherical structures [10, 11] or aggregates there of [12–16] and planar surfaces [6], and mostly within the electrostatic limit (primarily due to the complexity of treating the nonlocality). Even computationally, the $\mathbf{k}$ dependence has been neglected in previous studies of arbitrarily shaped nanostructures (see, for example, Ref. [17]). However, it has been predicted that nonlocal effects are particularly important for structures with apex features and dimers [12], even for large sizes where this limit is invalid. (Recently, these predictions have been confirmed [7, 9, 12, 16]).

8.3 Methodology

Just as in local electrodynamics (Chap. 2), before Maxwell's equations can be solved, an explicit form for $\varepsilon(\mathbf{k}, \omega)$ in the constitutive relationship between $\mathbf{D}(\mathbf{k}, \omega)$ and $\mathbf{E}(\mathbf{k}, \omega)$ (Eq. 8.2) must be specified. Since the focus here continues to be on Au and Ag, $\varepsilon(\mathbf{k}, \omega)$ can again be described in the continuum limit by three separate components,

$$\varepsilon(\mathbf{k}, \omega) = \varepsilon_\infty + \varepsilon_{\text{inter}}(\omega) + \varepsilon_{\text{intra}}(\mathbf{k}, \omega), \tag{8.3}$$

where ε_∞ and $\varepsilon_{\text{inter}}(\omega)$were defined and discussed in Chap. 2 (which will not be repeated here), but $\varepsilon_{\text{intra}}(\mathbf{k},\omega)$, still responsible for the *sp*-band electron motion, now contains a $\mathbf{k}$ dependence. Note that the notation in Eq. 8.3 highlights the $\mathbf{k}$ and ω dependencies.

$\varepsilon_{\text{intra}}(\mathbf{k},\omega)$ is responsible for both the plasmonic optical response (as in Chap. 2) and nonlocal effects. Based on quantum mechanical considerations (in a DFT formulation [18]), the hydrodynamic Drude model (which reduces to the local Drude expression for electron motion, Eq. 2.25, if $\mathbf{k} \to 0$) accurately describes these effects [19],

$$\varepsilon_{\text{intra}}(\mathbf{k},\omega) = -\frac{\omega_{\text{D}}^2}{\omega(\omega + i\gamma) - \beta^2\mathbf{k}^2} \tag{8.4}$$

where ω_{D} and γ are defined as in Eq. 2.25, and β^2 will be referred to as the "nonlocal parameter", which for a free electron gas is $\beta^2 = Cv_{\text{F}}^2/D$, where C is a constant, v_{F} is the Fermi velocity (1.39×10^6 m/s for Au and Ag), and D is the dimension of the system. It is possible to show that $C = 1$ at low frequencies and $C = 3D/(D+2)$ at high frequencies [20], values which are somewhat justified by the fact that at high frequencies in 3D, in order to correlate the model with the random phase approximation (RPA), β^2 should be $(3/5)v_{\text{F}}^2$ [21]. However, even the RPA model neglects quantum mechanical exchange and correlation effects that in a local density approximation would decrease the value of β^2. See Appendix D for a related discussion, and the relation of Eq. 8.4 to quantum mechanics. Therefore, this parameter, in some respects, should be considered free to use to fit results to experimental data (which is considered below in relation to core–shell nanowires) [22]. In this chapter, the low and high-frequency forms of β^2 are used in various situations, and the usage will be made clear in the specific instances.

It should be noted in passing that other analytical forms for $\varepsilon(\mathbf{k},\omega)$ can be used within the following framework. In principle, quantum mechanical electronic structure theory can be used to provide rigorous estimates of $\varepsilon(\mathbf{k},\omega)$. See, for example, recent interesting work on carbon nanotubes based on time-dependent DFT [23]. It remains a challenge, however, to reliably apply such methods to nanostructures involving many hundreds of atoms or more.

Inserting Eqs. 8.2 and 8.3 (using Eqs. 2.24 and 8.4) into the Maxwell–Ampère law in $\mathbf{k}$-space for a time-harmonic field, $-i\omega\mathbf{D}(\mathbf{k},\omega) = i\mathbf{k} \times \mathbf{H}$, gives

$$-i\omega\varepsilon_0\varepsilon_\infty\mathbf{E}(\mathbf{k},\omega) + \sum_n \mathbf{J}_{\text{L}n}(\omega) + \mathbf{J}_{\text{HD}}(\mathbf{k},\omega) = i\mathbf{k} \times \mathbf{H}(\mathbf{k},\omega), \tag{8.5}$$

where the $\mathbf{J}_{\text{L}n}(\omega)$ are phasor polarization currents associated with Eq. 2.24,

$$\mathbf{J}_{\text{L}n}(\omega) = -i\omega\varepsilon_0 \frac{\omega_{\text{L}n}^2 \Delta\varepsilon_{\text{L}n}}{\omega(\omega + i2\delta_{\text{L}n}) - \omega_{\text{L}n}^2}\mathbf{E}(\mathbf{k},\omega), \tag{8.6}$$

and $\mathbf{J}_{\text{HD}}(\mathbf{k},\omega)$ is a nonlocal phasor polarization current associated with Eq. 8.4,

$$\mathbf{J}_{\mathrm{HD}}(\mathbf{k},\omega) = i\omega\varepsilon_0 \frac{\omega_{\mathrm{D}}^2}{\omega(\omega+i\gamma)-\beta^2\mathbf{k}^2}\mathbf{E}(\mathbf{k},\omega). \tag{8.7}$$

Equations of motion for the currents in Eqs. 8.6 and 8.7 can be obtained by multiplying through each equation by the appropriate denominator and inverse Fourier transforming ($i\mathbf{k} \rightarrow \nabla$ and $-i\omega \rightarrow \partial/\partial t$; Appendix A). This leads to the following partial differential equations

$$\frac{\partial^2}{\partial t^2}\mathbf{J}_{\mathrm{L}n}(\mathbf{x},t) + 2\delta_{\mathrm{L}n}\frac{\partial}{\partial t}\mathbf{J}_{\mathrm{L}n}(\mathbf{x},t) + \omega_{\mathrm{L}n}^2\mathbf{J}_{\mathrm{L}n}(\mathbf{x},t) = -\varepsilon_0\omega_{\mathrm{L}n}^2\Delta\varepsilon_{\mathrm{L}n}\frac{\partial}{\partial t}\mathbf{E}(\mathbf{x},t) \tag{8.8}$$

$$\frac{\partial^2}{\partial t^2}\mathbf{J}_{\mathrm{HD}}(\mathbf{x},t) + \gamma\frac{\partial}{\partial t}\mathbf{J}_{\mathrm{HD}}(\mathbf{x},t) - \beta^2\nabla^2\mathbf{J}_{\mathrm{HD}}(\mathbf{x},t) = \varepsilon_0\omega_{\mathrm{D}}^2\frac{\partial}{\partial t}\mathbf{E}(\mathbf{x},t). \tag{8.9}$$

Equations 8.8 and 8.9 form the basis of the approach in this chapter to calculate nonlocal dielectric effects, and are solved self-consistently with Eq. 2.2 and the inverse Fourier-transformed form of Eq. 8.5,

$$\varepsilon_0\varepsilon_\infty\frac{\partial}{\partial t}\mathbf{E}(\mathbf{x},t) + \sum_n \mathbf{J}_{\mathrm{L}n}(t) + \mathbf{J}_{\mathrm{HD}}(\mathbf{x},t) = \nabla\times\mathbf{H}(\mathbf{x},t) \tag{8.10}$$

(with the requirement that Eqs. 2.3 and 2.4 remain satisfied; see Appendix E).

To solve Eqs. 2.2 and 8.8–8.10, standard finite-difference techniques [24] (Appendix A) can be used, including those from FDTD [25] (see Sect. 3.2), such as CPML [26], the TF–SF technique [27–29], and methods to calculate optical cross sections. The full set of nonlocal finite-difference equations, including their derivations, can be found in Appendix E. By not updating Eqs. 8.8 and 8.9 outside of the nonlocal materials, arbitrarily shaped structures can be numerically simulated. Furthermore, the additional boundary condition (ABC) (an important aspect in nonlocal electromagnetics, but which is not particularly relevant to this discussion) of Pekar is implicitly imposed—i.e., the total nonlocal polarization current vanishes outside of the structure [30].

Before leaving this section, it should be mentioned that, at the time of this writing, instabilities have been encountered in some 3D calculations employing this method [9] (in 2D, these do not occur). For example, simulations become unstable for 1.0 nm diameter nanoparticles using grid spacings of 0.05 nm. The resolution of this issue remains to be an important aspect of future work.

8.4 Nonlocal Dielectric Function of Au

To model nanostructures and use the approach outlined in Sect. 8.3 for electrodynamics calculations, Eq. 8.3 must first be fit to empirically inferred dielectric data [31] (again using simulated annealing, for example). This is done in the limit of $\mathbf{k} \rightarrow 0$, which is valid for large structures (such as those used to obtain the empirical

data). However, unlike before (local electrodynamics), to make sure that the separate terms in Eq. 8.3 accurately capture the physics of the problem, it is necessary to fit Eqs. 2.24 and 8.4 over the appropriate energy ranges separately. For example, for Au, Eq. 8.4 (and ε_∞) can first be fit over the range 1.0–1.8 eV, where $\varepsilon(\mathbf{0},\omega)$ is dominated by *sp*-band electron motion. Then, keeping these parameters constant (except ε_∞), the entire dielectric function in Eq. 8.3 can be fit over the full optical range, 1.0–6.0 eV. Parameters from fits to Au and Ag [31] are given in Appendix B.

A plot of dielectric values from such a fit to Au, against those empirically inferred [31], is shown in Fig. 8.1. The fit is reasonably good given the simple form of Eq. 8.3. For example, features of the two interband transitions are captured [evident in $\Im(\varepsilon)$] near 3.15 and 4.30 eV (note that ω_{L1} and ω_{L2} are also close to these values; Appendix B). Although, the fit is not as good as could be achieved with a more flexible function (e.g., an unrestricted fit, as considered in previous chapters). However, the present fitting scheme leads to parameters that are more physically realistic, and this is essential given that these local dielectric parameters are used in the nonlocal hydrodynamic expression. One consequence of this fit, for example, is that the minimum value of $\Im(\varepsilon)$, near 1.85 eV, is not as small as the experimental one, which will tend to give broader LSPRs than expected. Besides such minor details, these differences will not play a significant role in the results that are presented.

It is interesting to look at the dependence of Eq. 8.3 with both k (the magnitude of $\mathbf{k}$) and ω; Fig. 8.2. (Note that the slice through $k = 0$ reduces to the local dielectric data in Fig. 8.1.) When $\beta k \ll \omega$,$\varepsilon(\mathbf{k},\omega)$ is relatively constant for a given ω (i.e., it remains close to the local value). However, as βk approaches ω from below, $\varepsilon(\mathbf{k},\omega)$ quickly becomes very negative and changes sign rapidly as it passes through $\beta k \approx \omega$ [and $\varepsilon(\mathbf{k},\omega)$ is thus no longer plasmonic]. Absorption of light by materials is related to the value of $\varepsilon(\mathbf{k},\omega)$ and the structure under consideration {e.g., for a small spherical particle in air, the maximum absorption occurs when $\Re(\varepsilon) = -2$ [32]}. Figure 8.2 therefore indicates that, in addition to the local absorption ($\mathbf{k} = 0$), additional (anomalous) absorption will occur when $\beta k \approx \omega$ [when a rapid variation in $\Re(\varepsilon)$ occurs].

Nonlocal effects are most prominent for very small structures (or those with apex features) [7], as will be demonstrated below. In these structures, it is also necessary to consider the reduced mean free path of the *sp*-band electrons due to electron–interface scattering, which was discussed in Chap. 1. In order to take this into account in Eq. 8.4, a modified collision frequency [33] can be used: $\gamma' = \gamma + Av_{\mathrm{F}}/L_{\mathrm{eff}}$, where the effective mean free electron path is $L_{\mathrm{eff}} = 4V/S$ in 3D and $\pi S/P$ in 2D, where V is the volume of the structure with surface area S and perimeter length P, and A can be considered the proportion of electron–interface collisions that are totally inelastic. For a metal–dielectric interface, $A \approx 0.1$ has been suggested [34], so this is what was used for the calculations in this chapter, unless otherwise noted. It should be mentioned that such scattering can also be considered a nonlocal effect [12, 35]. In a formal sense, A is related to the translational invariance at the surface, the full description of which depends on the dielectric constant of the material, which is ultimately nonlocal in character. However, the general magnitude of A can be arrived at in the local limit, and in a

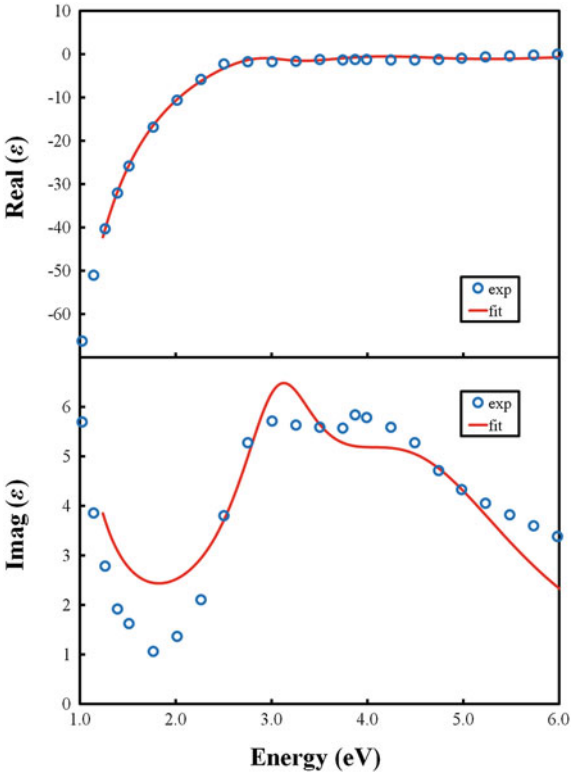

Fig. 8.1 Fitted dielectric data for Au, compared to that empirically inferred

variety of ways [36]. The physical origins of the nonlocal effects that arise from Eq. 8.4, however, are quite different in character. These arise by treating the electron density as an inhomogeneous gas through an effective pressure gradient term that describes the (quantum mechanical) kinetic, exchange, and correlation energies [19]; see Appendix D. This feature, coupled with the additional boundary condition that the polarization vector be zero outside of the structure (the Pekar ABC), leads to the possibility of longitudinal plasmon modes that do not exist in the local limit. In contrast, interfacial scattering leads to a size-dependent broadening and slight energetic shifts of existing, local spectral features.

8.5 Applications

8.5.1 Basic Geometric Shapes

Metal Films (1D Systems)

In this section, the transmission, reflection, and absorption spectra of thin Au films illuminated at normal incidence are determined. For simplicity of the presented

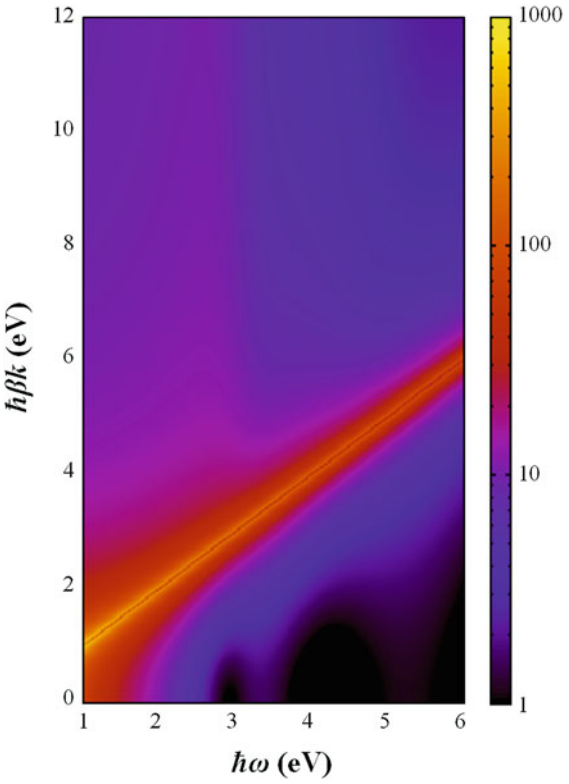

Fig. 8.2 $|\Re(\varepsilon)|$ of Au as a function of k and ω. Note that below $\beta k \approx \omega$, $\varepsilon(\mathbf{k}, \omega) < 0$, and above, $\varepsilon(\mathbf{k}, \omega) > 0$

results, the surrounding medium is taken to be to be air, although it would be straightforward to introduce other dielectric layers into the calculations (e.g., a glass substrate, which would probably be used in an experiment). These systems have an effective dimension of one, and because significant wavevector excitation can only occur for the direction normal to the surface, they are ideal for studying and qualitatively highlighting nonlocal effects. Furthermore, these systems allow some connections to be drawn with related experimental results [4, 5]. (It should be noted that it is not possible to compare directly to experiments, since the method outlined in Sect. 8.3 is limited to normal incident light, as are most finite-difference methods [25], whereas the experiments are not). For these calculations, grid spacings of 0.1 nm were used in all directions for the 2-nm film and 0.2 nm for the others, and the 2D high-frequency value of β^2 was used.

The transmission, reflection, and absorption spectra for 2, 10 and 20 nm thick Au films are shown in Figs. 8.3, 8.4 and 8.5, respectively. In the absorption spectra, narrow additional (anomalous) absorption peaks are seen in the nonlocal results relative to the local ones. The appearance of these peaks is identical to theoretical predictions [6] and experimental observations [4, 5] on other thin metal films, where they are the result of optically excited longitudinal (or volume) plasmons—vide infra. Not surprisingly, at the anomalous absorption energies there

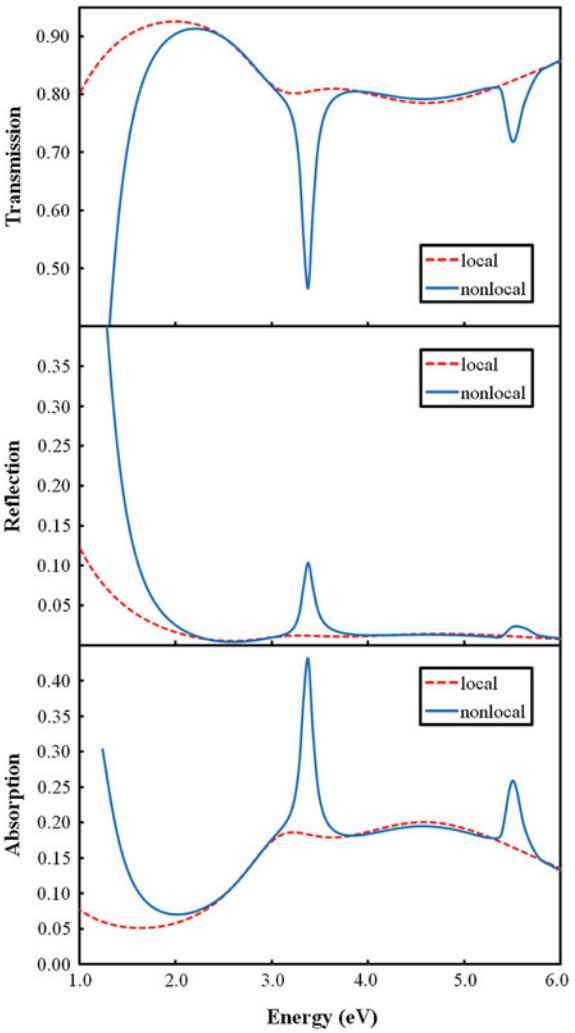

Fig. 8.3 *Top* transmission, *middle* reflection, and *bottom* absorption for a 2-nm thick Au film obtained from both local (*broken red lines*) and nonlocal (*solid blue lines*) calculations

is corresponding decrease in the transmission. However, contrary to the expectation of an analogous decrease in reflection, it is seen that there can be either an increase or a decrease depending on if it occurs well above (giving an increase) or below (giving a decrease) the main SP energy (e.g., around 2.65 eV for the 10-nm film).

Although a little hard to discern from Figs. 8.3, 8.4 and 8.5, the anomalous absorption resonances redshift as the film thickness is increased (as can be inferred from other results [7], which will be discussed below). This causes many more anomalous absorption resonances that were at higher energies to appear at (lower) optical energies, where, for example, there are three for the 2-nm film (Fig. 8.3) and twelve for the 10-nm one (Fig. 8.4). In addition, the intensity of the anomalous

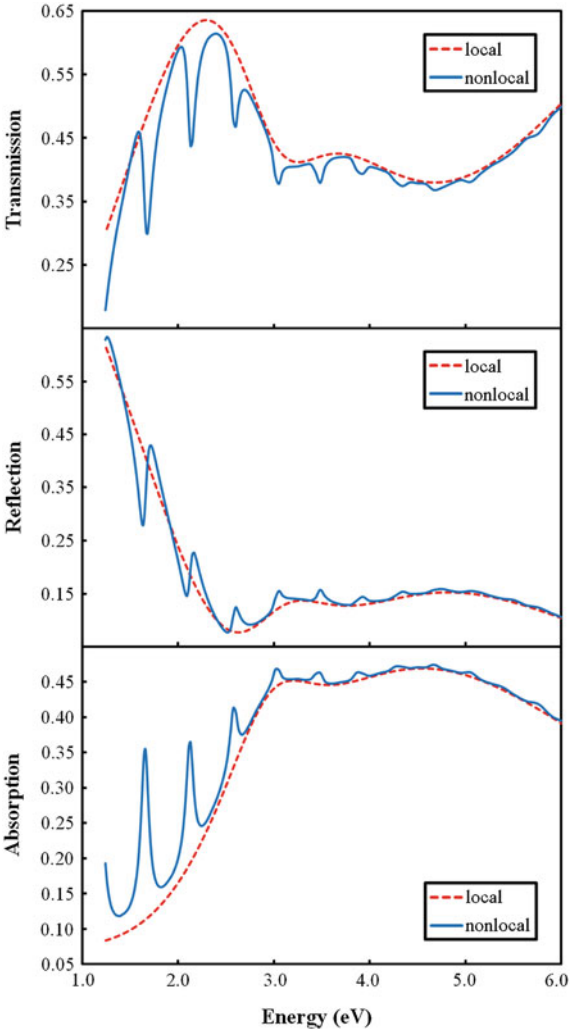

Fig. 8.4 *Top* transmission, *middle* reflection, and *bottom* absorption for a 10 nm thick Au film obtained from both local (*broken red lines*) and nonlocal (*solid blue lines*) calculations

absorption peaks drastically decrease with increasing thickness, where by 20-nm the nonlocal results are almost converged to the local ones; Fig. 8.5. These points will be revisited below.

In order to determine whether the anomalous absorption in these results is actually from the excitation of longitudinal plasmons, profiles of $|\mathbf{D}(\mathbf{x},\omega)|^2$ at the anomalous absorption energies can be examined. For example, Fig. 8.6 shows these for the 2-nm film at energies of 1.14 (not shown in Fig. 8.3), 3.36, and 5.54 eV. Well-defined standing wave patterns of $|\mathbf{D}(\mathbf{x},\omega)|^2$ longitudinal to $\mathbf{k}$ are seen with increasing nodal structure with energy, thus confirming the assumption of longitudinal plasmons. The wavelengths of these modes are found to be

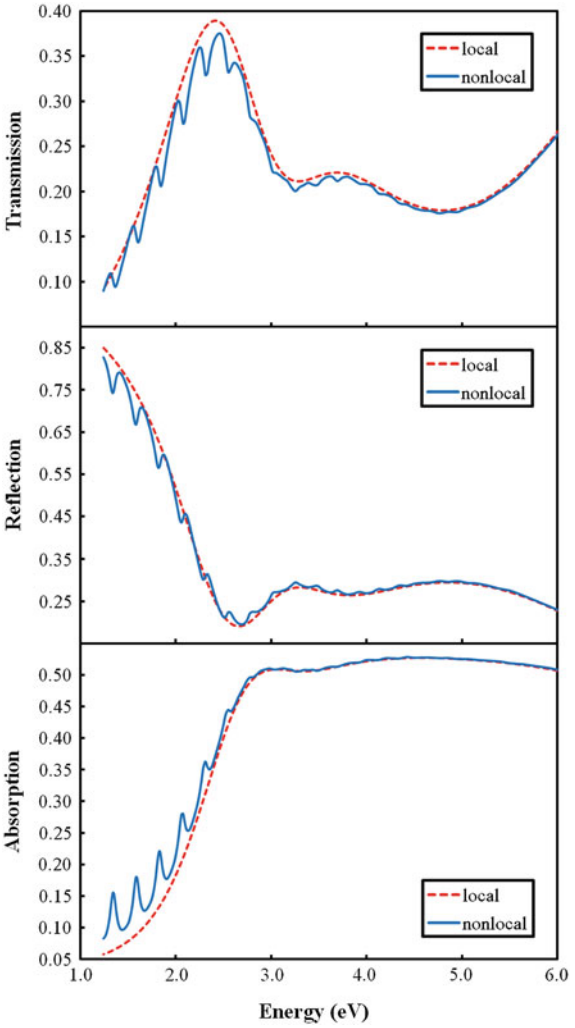

Fig. 8.5 *Top* transmission, *middle* reflection, and *bottom* absorption for a 20 nm thick Au film obtained from both local (*broken red lines*) and nonlocal (*solid blue lines*) calculations

$$\lambda_{\mathrm{L}} = 2h/m, \tag{8.11}$$

where h is the film thickness and $m = 1, 3, 5, \ldots$ (i.e., odd numbers of half-wavelengths that fit into h). (In Fig. 8.6, the $m = 1$, 3, and 5 modes are explicitly shown.) These profiles are significantly different from the local results of a relatively uniform $|\mathbf{D}(\mathbf{x}, \omega)|^2$ in the film (regardless of energy). However, the qualitative features here again agree with previous theoretical predictions [6] and experimental observations [4, 5] on analogous systems, providing further support for the validity of the method. Based on the observations in Fig. 8.6 and the analysis above, it makes sense that the longitudinal resonances redshift with increasing thickness and that the intensities of the excitations decrease with increasing m.

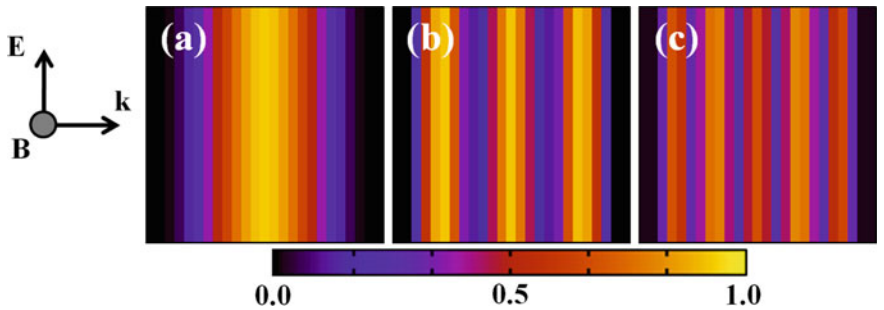

Fig. 8.6 Normalized $|\mathbf{D}(\mathbf{x},\omega)|^2$ intensity profiles inside a 2 nm thick Au film at energies of **a** 1.14, **b** 3.36, and **c** 5.54 eV

From the discussion above and that in Sect. 8.4, the approximate anomalous absorption energies for any film thickness can be predicted. From Eq. 8.4, it can be seen that rapid variations in $\varepsilon(\mathbf{k},\omega)$ will occur when $\omega \approx \beta k$, which will likely lead an absorption condition. Also, Fig. 8.2 shows that discrete longitudinal resonances with wavelength λ_L (dependent on h) are excited inside the film. These are generated by momentum states with magnitude $k = 2\pi/\lambda_L$, and everything needed to predict the (approximate) modal energies is thus known: $\hbar\omega = m\beta\pi/h$. Using the 2-nm film as an example, this analysis predicts anomalous absorption at energies of $\hbar\omega = m \cdot 1.44\,\text{eV}$. For the first three m modes, these are 1.44, 4.31, and 7.19 eV, while those actually calculated are 1.14, 3.36, and 5.54 eV. While not exact, the predictions are reasonably close. (Part of these differences can be attributed to the grid-based finite-differencing that, in this case, leads to an uncertainty in the film thickness of ± 0.2 nm.) This analysis can also be applied to related experimental results [4]. However, it is important to keep in mind that this is a simple approximation, and more accurate values can in some cases be obtained using rigorous theory [6].

Solid Nanowires (2D Systems)

In this section, the optical responses of Au nanowires of various shapes excited with TE_z polarized light are studied. Grid spacings of either 0.2 or 0.25 nm were used for the calculations, as well as the 2D low-frequency value of β^2.

The optical responses of nanowires with radii of $r = 2$–8 nm in the local and nonlocal limits can be compared by calculating extinction cross sections [32] (which for these small systems is dominated the absorption); Fig. 8.7. The appearance of anomalous absorption peaks relative to local theory in Fig. 8.7 is similar to theoretical predictions [6], experimental observations [4, 5], and nonlocal calculations on thin metal films [9] (vide supra), where they arise from the optical excitation of longitudinal plasmons that cannot be described by local electrodynamics. It is important to note that the hydrodynamic Drude model,

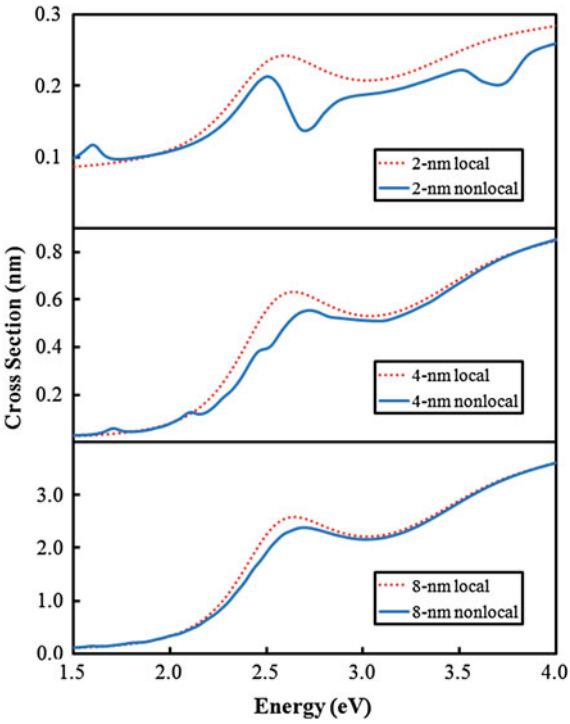

Fig. 8.7 Optical responses of Au cylindrical nanowires with radii of *top* 2, *middle* 4, and *bottom* 8 nm. *Full curve* is nonlocal theory; *broken curve* is local theory

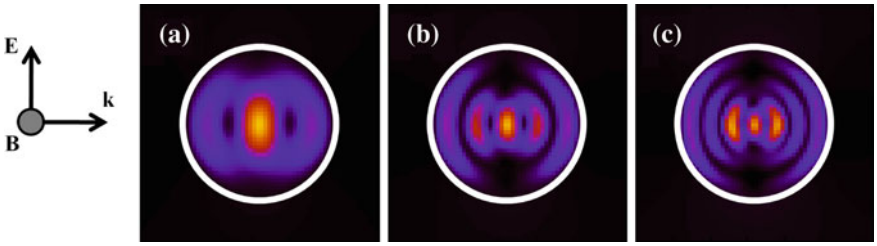

Fig. 8.8 Longitudinal plasmons inside a $r = 2$ nm Au cylindrical nanowire at energies of **a** 1.60, **b** 2.71, and **c** 3.69 eV. The polarization and direction of incident light are indicated; the nanowire is outlined in white

Eq. 8.4, can have an effect at much higher energies than the local Drude model, because of the interplay between ω and $\mathbf{k}$.

To investigate the nature of the anomalous absorption, profiles of $|\mathbf{D}(\mathbf{x}, \omega)|^2$ at the peak energies can again be looked at. Figure 8.8 shows $|\mathbf{D}(\mathbf{x}, \omega)|^2$ for the $r = 2$ nm nanowire, where discrete standing-wave longitudinal plasmon modes are again seen at wavelengths satisfied by Eq. 8.11, where in this case $h = 2r$. (Only the $m = 3, 5$, and 7 modes are explicitly shown in Fig. 8.8.) As with the metal films, this result is in sharp contrast to the local result of a relatively uniform $|\mathbf{D}(\mathbf{x}, \omega)|^2$, but is nonetheless

identical to all experimental, theoretical, and calculated results for analogous thin metal films, as mentioned above. Considering that these modes arise from confining an electron gas that is treated quantum mechanically (see Appendix D), these modes can be considered analogous to one-particle quantum states.

In addition to anomalous absorption, the nonlocal effects blueshift the main LSPR, where at $r = 4$ nm, for example, there is a 0.014 eV blueshift. This can be understood by looking at the form of Eq. 8.4. The interplay between ω and $\mathbf{k}$ causes the nonlocal LSPR to appear at a higher energy compared to the local Drude model, because for a fixed $\mathbf{k}$,ω must be higher to lead to the same absorption condition (as indicated above).

At optical energies, the discrete nature of these modes is quickly lost with increasing r (as $r \to \infty$,$n \to \infty$ and $\lambda_L \to 0$), and nonlocal effects become less important. This can be seen in Fig. 8.7, where for $r = 4$ nm there is only minor anomalous absorption, and for $r = 8$ nm it is hardly distinguishable. However, even at $r = 8$ nm there is a broadening, reduction in intensity, and blueshift of 0.0056 eV of the main LSPR due to the excitation of many closely spaced modes.

While these explicit examples correspond to 2D nanowires, the $r = 4$ nm results are remarkably similar to recent experimental observations on individual Au spherical nanoparticles with similar radii [8]. For example, these results predict a 0.014 eV blueshift, while that observed is 0.011 eV. In addition, these results predict anomalous absorption at energies below the main LSPR with peaks near 1.7 and 2.1 eV, and the experimental results show similar peaks near 1.8 and 1.9 eV (discrepancies that can be attributed to the difference in dimensionalities).

While cylindrical nanowires are useful because their simplicity allows easy understanding of the main results, nonlocal effects have been suggested [12] and recently shown (using this method [7, 9]) to be particularly strong in structures with apex features. As examples, Au (equilateral) triangular nanowires, which have been thoroughly studied within local electrodynamics because of the large $|\mathbf{E}(\mathbf{x}, \omega)|^2$ enhancements that occur at the apices [37], are considered below.

The optical responses of nanowires with side lengths of l = 5–40 nm are shown in Fig. 8.9. (Note that unlike the cylindrical nanowires studied above, when l is greater than $\sim$10 nm, both absorption and scattering are important). Strikingly, for small enough l the main plasmon resonance is hardly distinguishable from the nonlocal anomalous absorption features. In addition, for all l significant dampings and blueshifts of the LSPRs relative to the local results are seen. This effect persists for l much larger than the analogous cylindrical nanowires, where even at l = 40 nm there is a 0.1 eV blueshift.

Profiles of $|\mathbf{D}(\mathbf{x}, \omega)|^2$ again investigated at the anomalous absorption energies are shown in Fig. 8.10. Similar to the cylindrical nanowires, longitudinal plasmon modes are excited inside the structures with analogous discrete wavelengths, except that in this case h is the distance between the nanowire sides along the longitudinal direction. However, comparison of Figs. 8.8 and 8.10 reveals an interesting difference. In the triangular structures, the longitudinal plasmon modes occur at discrete vertical positions, at each point where the equation for λ_L is

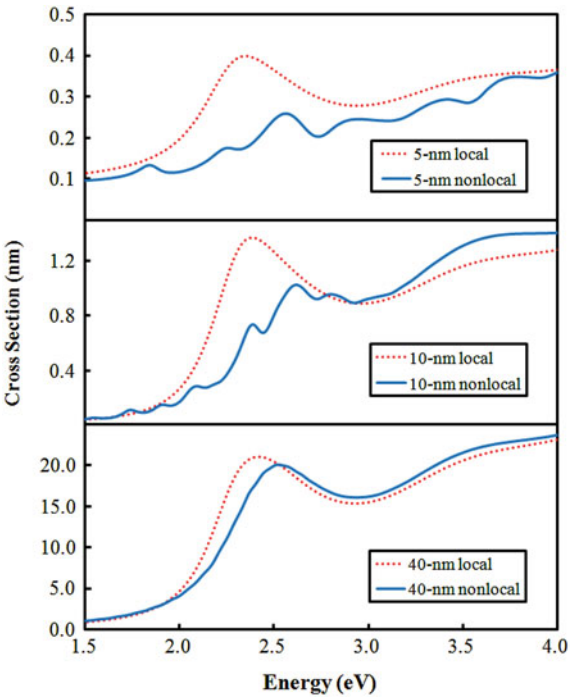

Fig. 8.9 Optical responses of Au triangular nanowires with side lengths of *top* 5, *middle* 10, and *bottom* 40 nm. *Full curve* is nonlocal theory; *broken curve* is local theory

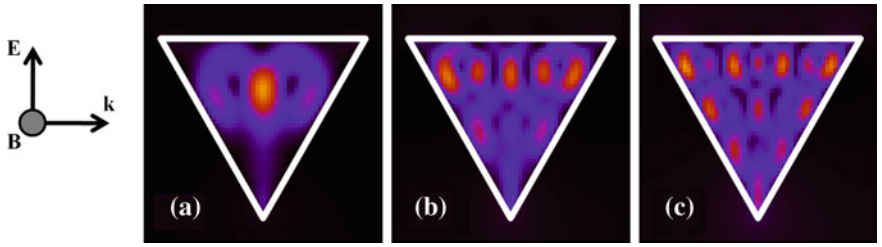

Fig. 8.10 Longitudinal plasmon modes inside a $l = 5$ nm Au triangular nanowire at energies of **a** 1.88, **b** 2.82, and **c** 3.71 eV. The polarization and direction of incident light are indicated; the nanowire is outlined in *white*

satisfied, which increases with n. The ability of a triangular nanowire to strongly sustain these resonances over the entire structure at multiple positions (particularly near the apex, where h can be arbitrarily small and low-order longitudinal plasmon modes can always be sustained) explains the strength of the calculated nonlocal effects compared to a cylindrical nanowire, where the modes are only efficiently sustained along the central axis. Generalizing this result to other apex structures suggests that longitudinal plasmon modes can always be sustained (at least near the apex), causing nonlocal effects to remain important for arbitrarily large sizes.

Spherical Nanoparticles (3D Systems)

In this section, spherical nanoparticles are discussed, utilizing the full 3D nonlocal electrodynamics method outlined in Sect. 8.3. These are also simple systems, much like the metal films and solid nanowires, and it has been theoretically shown that they too exhibit nonlocal effects [10]. For the calculations in this section, grid spacings of 0.2 nm were used in all directions for the 4 and 7-nm nanoparticles, and 0.5 nm for the 15-nm nanoparticle, as well as the 3D high-frequency value of β^2.

The optical responses of nanoparticles with diameters of 4, 7, and 15 nm, determined by again calculating the extinction cross sections, are shown in Fig. 8.11. (Just as for small nanowires, extinction in these systems is mostly determined by absorption, although scattering can be dominant for sizes greater than approximately 20 nm). Figure 8.11 shows that inclusion of nonlocal effects leads to significant anomalous absorption and LSPR blueshifting for nanoparticle sizes of less than approximately 10 nm, analogous to the cylindrical nanowires (vide supra). Both the blueshifting and anomalous absorption becomes more significant as the nanoparticle size is reduced. For example, for both the 4 and 7-nm nanoparticles, these effects are so large that the LSPR peak is hardly distinguishable.

Analogous to the metal films and cylindrical nanowires, the anomalous absorption peaks arise from the excitation of longitudinal plasmon modes. However, the anomalous absorption quickly diminishes with increasing nanoparticle size much faster than for the other systems. For example, at 15-nm the additional peaks show up only as slight indents on the main LSPR. These differences can be attributed to two effects. First, in a metal film the only **k** component is that of the incident field (normal to film), which leads to well-defined longitudinal plasmons (Fig. 8.6). However, in a spherical nanoparticle, scattering off of the surface generates many **k** components, which can interact and dephase one-another, especially for the high-order m modes containing multiple nodes. In addition, scattering of the conduction electrons off of the spherical surface can also lead to dephasing of the longitudinal plasmons. Both of these processes cause nonlocal effects to diminish at a much smaller distance than in more simple systems. Additionally, much like the nanowires discussed above, the LSPRs are blueshifted relative to the local results. Definitive LSPR blueshifting is most apparent for the 15-nm nanoparticle, because the anomalous absorption is low, which allows the LSPR peak to be clearly identified. The local LSPR peak is at 2.57 eV, while the nonlocal one is at 2.71 eV.

Based on the results in Fig. 8.11, one might wonder why such strong nonlocal effects have not been experimentally observed in such systems. Obviously nonlocal effects are important, as they have been experimentally observed in thin metal films [4, 5]. There are many possible reasons for this. The most probable one is that experimental measurements are often made on heterogeneous collections of nanoparticles. Given that the anomalous absorption is very sensitive to nanoparticle dimensions, slight heterogeneity could essentially average these effects away. Support for this claim comes from the aforementioned study of isolated Au

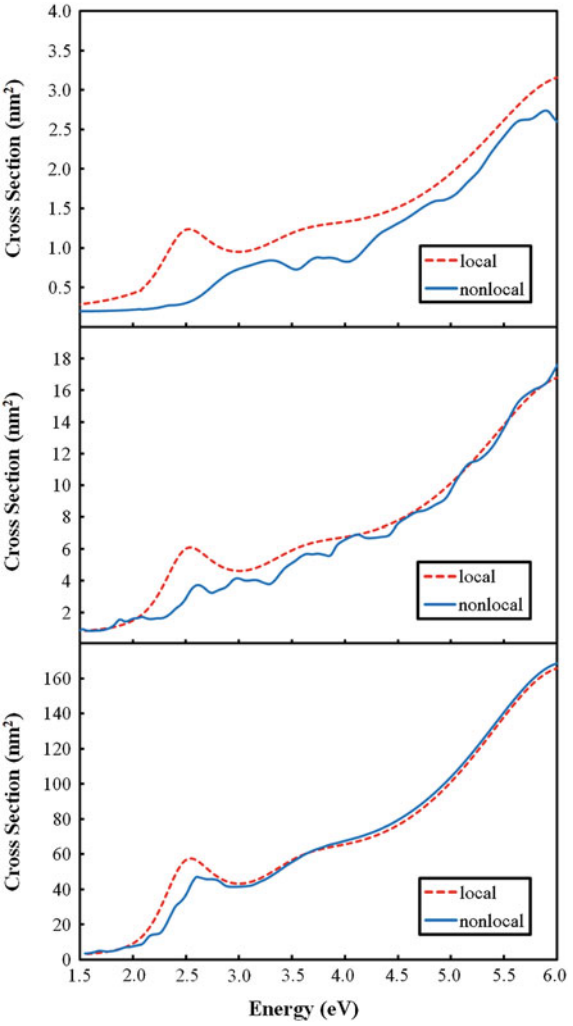

Fig. 8.11 Extinction cross sections of Au spherical nanoparticles with diameters of *top* 4, *middle* 7, and *bottom* 15 nm obtained from both local (*broken red lines*) and nonlocal (*solid blue lines*) calculations

nanoparticles, which showed the LSPR blueshift and possible anomalous absorption features [8]. Another possible explanation is that the value of β^2 is not optimal, which will be discussed in Sect. 8.5.2 in the context of Au core–shell nanowires [22]. It is also worth reiterating that the hydrodynamic Drude model neglects quantum mechanical exchange and correlation effects, which in a local density approximation would decrease β^2, and in turn, the strength of the nonlocal effects (see Sect. 8.5.2). A third possible explanation is that the damping parameter A is too low, which will also be discussed in Sect. 8.5.2. Increasing this would damp all spectral features, but give smoother spectra (i.e., the anomalous absorption would not appear as strong). Support for this comes from a combined theoretical and experimental study of metallic nanoshells, where A values greater than 1.0 are

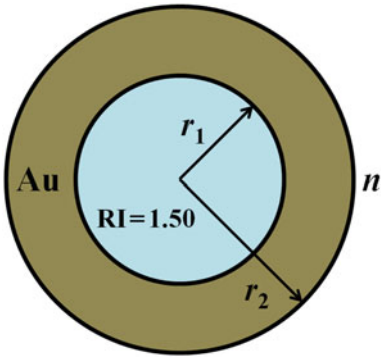

Fig. 8.12 Schematic diagram of a Au with parameters described in the text

needed (in the local limit) to describe the experimental results [38] (which corresponds to L_{eff} reduced below that based on geometric considerations alone).

8.5.2 Core–Shell Nanowires

One particular nanostructure that has generated considerable interest, while being conceptually simple, is a core–shell metallic nanoparticle, a nanoshell [38–41]. A schematic diagram of the basic nanoshell system considered in this section is shown in Fig. 8.12. The outer shell is Au, the inner core is glass with a RI of 1.50, and the surrounding medium has a RI of n. The nanoshell dimensions are denoted by (r_1, r_2)—the (inner, outer) radii. One of the exceptionally novel properties of metallic nanoshells is that simple variations in (r_1, r_2) can tune their LSPRs over a large energy range [42], and this effect is especially sensitive to n [41]. In this section, 2D nanoshells (core–shell nanowires) excited with TE_z polarized light are considered. Such systems are analogous to 3D nanoshells, and are expected to exhibit similar behavior, except for slightly blueshifted LSPRs due to different surface boundary conditions.

In the limit of very small or thin nanoshells, the question of spatial nonlocality in the dielectric response becomes important [11, 12]. However, as discussed in Sect. 8.2, because of the difficulties to describe theoretically or calculate numerically nonlocal effects, most previous studies of metallic nanoshells [38, 40, 41] (and other systems) have neglected them. Because of the ability to fabricate very thin nanoshells, these are probably the ideal systems beyond simple thin films and spherical nanoparticles where comparisons between experiment and nonlocal theory/computation can be made.

In this section, the optical properties of Au core–shell nanowires described by the hydrodynamic Drude nonlocal dielectric function, Eq. 8.4, are calculated. This section is more in-depth than Sect. 8.5.1 (basic geometric shapes), and is broken down into sections and outlined as follows. The parameters of the nonlocal model are first investigated by making comparisons with related hypothetical

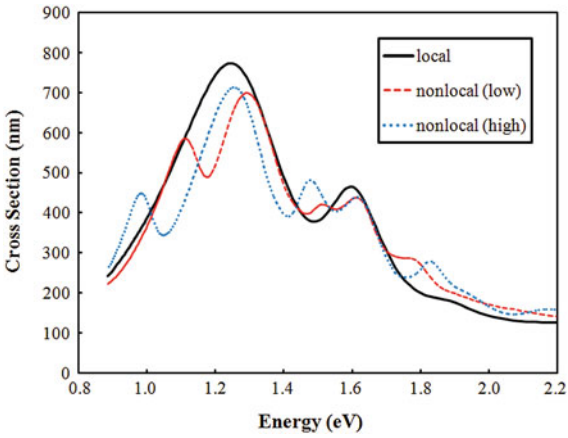

Fig. 8.13 Optical responses of (91.5 nm, 103 nm) nanoshells in $n = 1.22$ calculated using both the low and high-frequency values of β^2

"experimental data" and previous theoretical work. Then (using the appropriate parameters), the dependence of nonlocal effects on nanoshell features, such as shell thickness, overall size, and the ratio of core radius to shell radius are investigated. The optical responses of nanoshells immersed in various RI environments are also studied.

Computational Considerations

For these calculations, grid spacings of 0.5 nm were used in both directions. Based on calculations using much smaller spacings (e.g., 0.25 nm), it is found that this is sufficient to resolve all nonlocal effects for these systems up to approximately 3 eV with relative convergence (less than 0.2 eV error in spectral positions, and about 5–20% error in cross section magnitudes, although often much less). Note that in order to resolve spectral features above 3 eV (not of direct relevance to this section), grid spacings of 0.25 nm or smaller are needed.

Nonlocal Parameter and Interfacial Scattering

In this section, the parameters β^2 and γ of the hydrodynamic Drude model (Eq. 8.4) are discussed. The optical responses of (r_1, r_2) = (91.5 nm, 103 nm) nanoshells immersed in a $n = 1.22$ RI environment (which corresponds to sol–gel silica) were first calculated in the low and high-frequency limits of β^2, and with no size-dependent surface scattering corrections; Fig. 8.13. Note that this RI is high enough such that high-order multipole resonances are seen, but also low enough so that the main LSPRs all fall within the energy range of interest (optical energies). In the local result, two peaks are observed near 1.25 and 1.6 eV. The 1.25 eV peak can be attributed to the dipolar LSPR of the nanoshell, while that at 1.60 eV can be

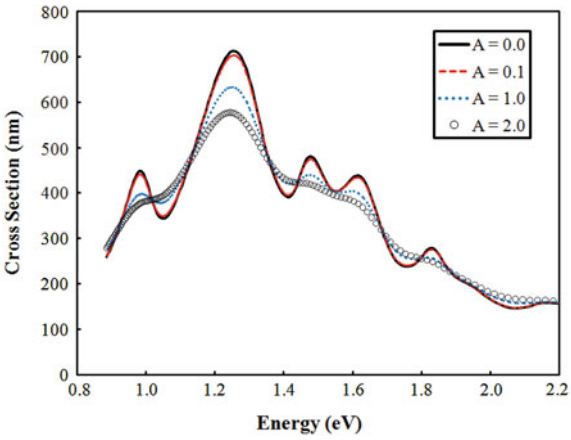

Fig. 8.14 Effect of interfacial scattering on the optical responses of (nonlocal) nanoshells

attributed to a multipolar (higher-order) LSPR [38]. In the nonlocal results, both of these resonances continue to stand out as prominent features, and the relative overall spectral shapes are similar to the local result. However, significant anomalous absorption is also observed, similar to the other applications discussed up to this point. Furthermore, while not obvious from the form of Eq. 8.4, the intensity of the anomalous absorption is also found to depend on β^2.

A related experimental study of analogous (91.5 nm, 103 nm) 3D nanoshells [38] found that local calculations accurately describe the measurements. It is therefore immediately questionable why such strong nonlocal effects were not observed (in this, or other related experiments). As discussed in relation to spherical nanoparticles, the most likely explanation is that bulk nanoshell measurements involve an averaging over a nonuniform distribution of nanoshells, and their surfaces might also be rough. These factors could easily hide nonlocal effects, since such optical properties are very sensitive to minor structural details—vide infra. This is further supported by electronic structure calculations for small isolated nanoshells [43], where similar additional absorption and discrepancies with experiment have been found.

Another possible effect that addresses the "experimental discrepancies" that has not yet been included in the current discussion is interfacial scattering, as discussed above. In other studies, taking this into account has been found necessary to accurately describe some aspects of the experimental results [38], such as linewidths.

Using the high-frequency value of β^2 (because of the increased nonlocal effects), the optical responses of (91.5 nm, 103 nm) nanoshells in $n = 1.22$ for values of $A = 0.0, 0.1, 1.0$, and 2.0 were calculated; Fig. 8.14. For these nanoshells, $A = 0.1$ (used in the applications discussed in Sect. 8.5.1) is found to have relatively little effect. Even when $A = 1.0$, all of the peaks are still visible, except that they are broadened and damped. When A increases beyond 1.0, the peaks become significantly damped and the major anomalous ones (e.g., near 1.0 eV)

appear only as shoulders. Such values of A are consistent with previous studies that have considered interfacial scattering in nanoshells [38], and it is thus likely that this effect combined with bulk averaging explains why such strong nonlocal effects as in Fig. 8.13 have not previously appeared prominently in the descriptions of experimental results. Nonetheless, it is shown below that these effects do have significant implications. Since other studies have shown that for some metal–dielectric interfaces $A \approx 0.1$ [34], it can be inferred that fabrication/synthesis details likely strongly affect this parameter. Regardless of the choice of A, the positions of both the LSPRs and anomalous absorption resonances remain relatively unchanged. Thus, while taking interfacial scattering into account is probably necessary to describe experimental results (especially linewidths)—although, likely as a free parameter—this will hereon be neglected to highlight the nonlocal effects (i.e., *A will be taken to be* 0.0).

Returning to the appropriate choice of β^2, the results of Figs. 8.13 and 8.14 can be compared to the local result, which should be a good representation of related "hypothetical" experimental measurements made on bulk core–shell nanowires. Comparing the results indicates that the low-frequency value of β^2 is probably the most accurate. It is likely that even bulk measurements of nanoshells would be able to observe the strong anomalous absorption predicted by the high-frequency value, even after taking into account interfacial scattering. Although, it is possible that even lower values of β^2 would be better. However, without experimental results for isolated nanoshells it is difficult to make such claims with certainty. Therefore, the low-frequency value of β^2 is used in the remainder of this section.

Nanoshell Geometry

In this section, the dependence of nonlocal effects on nanoshell geometry is explored. First, the effect of shell thickness (i.e., the thickness of the structure along the longitudinal direction of the incident light) on $r_2 = 100$ nm nanoshells in carbon disulfide ($n = 1.64$) with $r_1 = 80$, 90, and 95 nm (shell thicknesses of 20, 10, and 5 nm, respectively), is determined. The calculated optical responses of these nanoshells in the local and nonlocal limits are shown in Fig. 8.15.

For all thicknesses, the nonlocal spectra qualitatively follow the local ones, with resonances redshifting as shell thickness is reduced. The most significant nonlocal effects in these results are blueshifts of the LSPRs relative to the local ones, which increase dramatically with decreasing thickness. Figure 8.15 thus suggests that shell thickness is a strong controlling factor of nonlocal effects. For $r_1 = 80$ nm, there is relatively little blueshift of the dipolar LSPR $<$(0.01 eV), and minor anomalous absorption features only appear as a collection of many shoulders to the red. Increasing r_1 to 90 nm more significantly blueshifts the dipolar LSPR relative to the local result $\approx$(0.02 eV). In addition, there is an approximately equal blueshift in the quadrupolar LSPR near 1.45 eV. However, the octupolar resonance near 1.70 eV does not blueshift much, if at all. The most severe differences

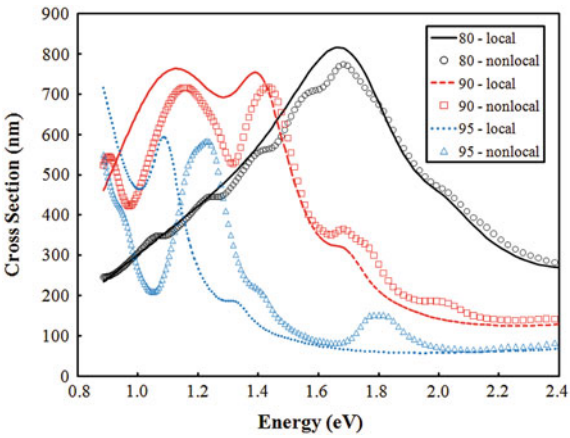

Fig. 8.15 Effect of shell thickness on nonlocal effects in nanoshells in $n = 1.64$. The results correspond to various r_1 values (shown in nm) for a fixed $r_2 = 100$ nm

between the local and nonlocal results occurs for $r_1 = 95$ nm. The dipolar LSPR occurs at too low of an energy to be observable on the scale of the figure, however the quadrupolar LSPR is seen to blueshift by 0.14 eV, and even the octupolar resonance blueshifts by 0.08 eV. These results are consistent with the recent analogous work on Au core–shell spheres using a specular reflection model [12], where the LSPRs blueshift with decreasing shell thickness, with very little occurring for thicknesses greater than ~ 10 nm.

Based on the above results, all LSPRs (dipolar, quadrupolar, octupolar, etc.) are blueshifted by nonlocal effects. The dipolar LSPR is blueshifted most significantly, followed by the quadrupolar octupolar, and so on. Issues that can influence this are the coupling strength between the LSPRs and longitudinal plasmons, and the spatial properties of the resonance fields. Below it is shown that the longitudinal plasmons extend around the entire nanoshell, so in this case the dominant effect is the coupling strength, which is directly related to the overlap of the fields associated with the two types of resonances. Since the LSPR field amplitudes show a rapid decrease in radial intensity with increasing order, the coupling should be strongest for the dipolar LSPR followed by the quadrupolar and so on.

In addition to shell thickness, another geometric consideration is the impact of the overall size on nonlocal effects. For a fixed shell thickness of 5 nm, the optical responses of nanoshells with $r_2 = 25, 50,$ and 100 nm in air ($n = 1.00$) were calculated and are shown in Fig. 8.16. For all r_2, nonlocal effects are seen to be significant, with blueshifts of the dipolar LSPRs by 0.15, 0.08, and 0.23 eV for r_2 values of 25, 50, and 100 nm, respectively. Comparing the results, it is reasonable to assume, based on the amount of blueshift of the dipolar LSPR and the anomalous absorption features, that there is no (clear) direct relationship between r_2 and the strength of nonlocal effects.

As a further and final measure of the effect of nanoshell geometry on the nonlocal optical response, nanoshells with the same r_1/r_2 ratio can be looked at. For example, optical responses of nanoshells in water ($n = 1.33$) with the same r_1/r_2 ratio of 0.8 but with varying r_2 values of 100, 50, and 25 nm are shown in Fig. 8.17.

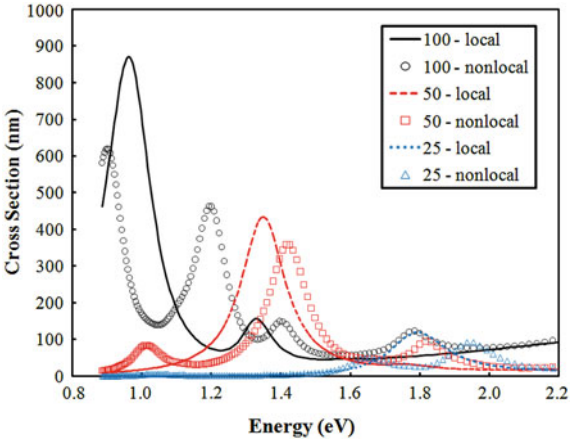

Fig. 8.16 Optical responses of nanoshells in $n = 1.00$ with 5 nm thick shells for various r_2 values (shown in nm)

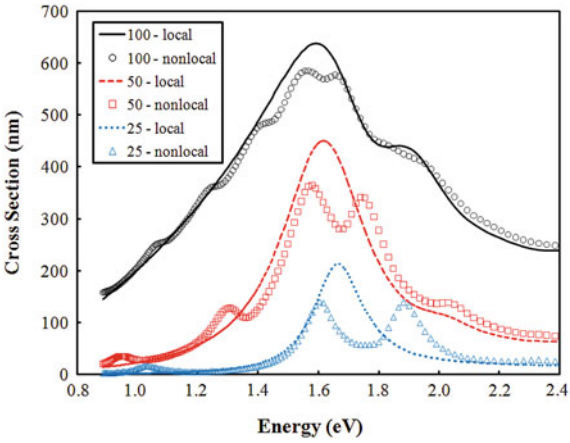

Fig. 8.17 Optical responses of nanoshells with a fixed r_1/r_2 ratio of 0.8 in $n = 1.33$ for various r_2 values (shown in nm)

As r_2 decreases, the nonlocal effects significantly increase in intensity. This is not that surprising, considering that as r_2 decreases so does the shell thickness (for a fixed r_1/r_2 ratio). Comparing the results directly, it is not possible to draw any conclusive assumptions, demonstrating little (if any) dependence of nonlocal effects on the ratio r_1/r_2. However, this result combined with the others suggests (in addition to those in Sect. 8.5.1) that the primary controlling factor of nonlocal effects is the thickness of the structure along the longitudinal direction of the incident light.

Refractive Index Sensitivity

The RI dependence of nonlocal effects is now discussed. This would correspond to the situation of immersing the nanoshells in various solvents, for example. The optical responses of (45 nm, 50 nm) nanoshells in RI environments of n = 1.00,

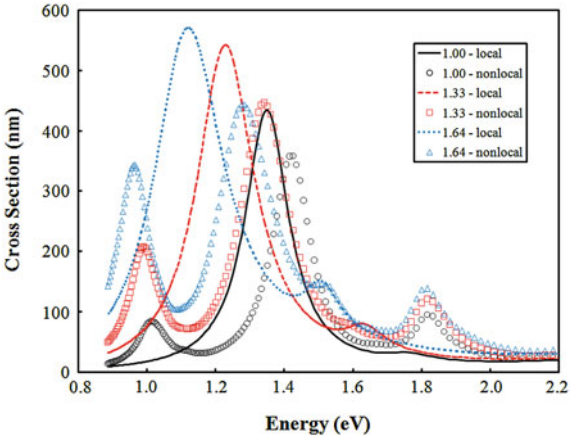

Fig. 8.18 Effect of RI on the optical response of (45 nm, 50 nm) nanoshells

1.33, and 1.64 (corresponding to air, water, and carbon disulfide, respectively) are shown in Fig. 8.18. The local results are found to be in qualitative agreement with previous studies [41]. The dipolar LSPRs (i.e., the ones with the greatest intensities and occurring at the lowest energies in the local results) redshift approximately linearly with increasing RI [41]. In addition, for $n = 1.33$ and 1.64, multipolar (higher-order) LSPRs become visible at higher energies.

When nonlocal effects are included, the results are quite different. For example, strong anomalous absorption is observed near 0.95 and 1.85 eV, independent of the RI. In order to determine if the anomalous absorption at each energy is identical for all RIs, profiles of $|\mathbf{D}(\mathbf{x}, \omega)|^2$ can be examined; Fig. 8.19. Standing wave patterns of $|\mathbf{D}(\mathbf{x}, \omega)|^2$ are seen inside the nanoshells with intensity variation along the longitudinal direction of the incident light. The wavelength of these again follows Eq. 8.11, where h is now the shell thickness, and thus can be attributed to nonlocal longitudinal plasmons [7] (see Sect. 8.5.1). For each energy (0.95 or 1.85 eV), the intensity patterns of $|\mathbf{D}(\mathbf{x}, \omega)|^2$ are qualitatively identical—i.e., they correspond to the same m. The energies of each m mode are therefore found to be independent of RI. At first this is surprising, considering that LSPRs are affected by the RI [2]. However, it is important to keep in mind that LSPRs exist on a metal–dielectric interface, and are thus influenced by both materials, whereas longitudinal plasmons exist only inside the metal; and because in the presented method to treat nonlocal effects [7] (Sect. 8.3) the same boundary condition (ABC) is imposed at all metal–dielectric interfaces (the nonlocal polarization current vanishes) [9], it is understandable that there is no RI dependence. In reality, however, nonlocal effects should have a weak RI dependence due to addition quantum mechanical surface effects, such as surface diffuseness [36]. There is an analogous picture that emerges when it is considered that the anomalous resonances represent single electron excitations within the metal particle that are similar to the RI dependence of the excitation energy in molecular chromophores. These points represent possible directions for future investigation.

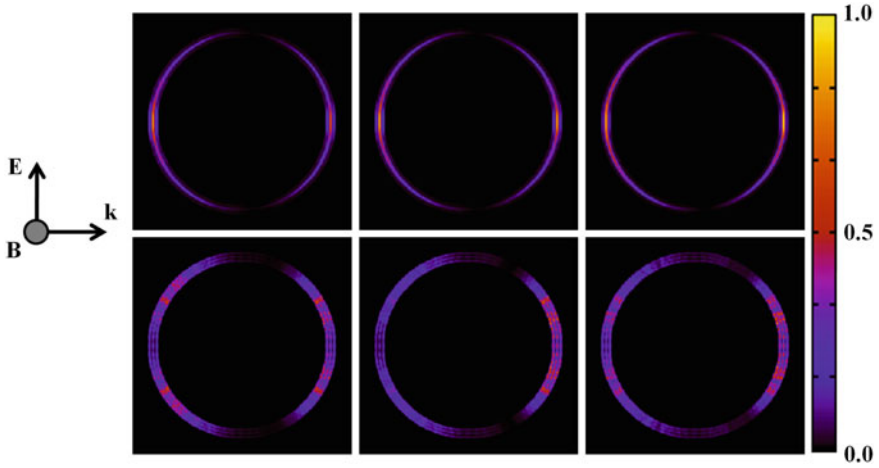

Fig. 8.19 Normalized $|\mathbf{D}(\mathbf{x},\omega)|^2$ intensity profiles for (45 nm, 50 nm) nanoshells at the anomalous absorption energies of *top* 0.95 and *bottom* 1.85 eV for RIs of $n =$ *left* 1.00, *middle* 1.33, and *right* 1.64

While the anomalous absorption modes are qualitatively the same regardless of the RI, they are not identical. Specifically, the intensities of the internal modes decrease with increasing RI (which cannot be inferred from the normalized scale in Fig. 8.19) by approximately $1/3$ and $2/3$ when going from $n = 1.00$ to 1.64 for the $m = 3$ and 5 modes, respectively. However, there are increases in $|\mathbf{D}(\mathbf{x},\omega)|^2$ (or $|\mathbf{E}(\mathbf{x},\omega)|^2$) outside of the nanoshell, giving the stronger calculated optical response. This can be understood in terms of local quasistatic theory, where the surface $|\mathbf{E}(\mathbf{x},\omega)|^2$ resulting from LSPRs is expected to increase with RI [2].

In addition to anomalous absorption, the dipolar LSPRs are blueshifted relative to the local results. Unlike the anomalous absorption, the relative blueshift is found to increase strongly with RI. Figure 8.18 shows that the $n = 1.00, 1.33$, and 1.64 dipolar LSPRs blueshift by 0.07, 0.12, and 0.17 eV, respectively. Therefore, when nonlocal effects are included, the RI sensitivity of the LSPRs is not linear as predicted by local theory and experiments [41]. However, the differences are again most likely the result of experimental measurements made on collections of heterogeneous nanoshells. Based on this discussion, it would be interesting to experimentally study isolated nanoshells, where the nonlinear RI dependence could be observed.

8.5.3 Nonlocal Electric Field Enhancements

$|\mathbf{E}(\mathbf{x},\omega)|^2$ enhancements, a quantity important for many physical processes [e.g., SERS, which is dependent on $|\mathbf{E}(\mathbf{x},\omega)|^4$], were discussed in Chap. 5. There it was

mentioned that $|\mathbf{E}(\mathbf{x},\omega)|^2$ enhancements in nanostructures (including nanowires) have been thoroughly studied in the past, from isolated nanoparticles [37, 44] and dimers [44–47] to other structures. From these studies, values as large as 10^5 have been found for isolated nanoparticles (specifically triangular nanowires) [37] and 10^7 for junction structures (e.g., cylindrical and spherical dimers) [45, 47]. However, these studied have all been performed within the framework of classical local electrodynamics. Within nonlocal electrodynamics, it has been found that $|\mathbf{E}(\mathbf{x},\omega)|^2$ enhancements are greatly diminished relative to local predictions because such effects damp LSPRs [7, 9, 12, 16]. The quantitative accuracy of the large body of work concerning $|\mathbf{E}(\mathbf{x},\omega)|^2$ enhancements, as well as the interpretation of effects that rely on them (e.g., SERS), are thus questionable. It is the purpose of this section to address EM enhancements using the nonlocal electrodynamics method outlined in Sect. 8.3.

Computational Considerations

For the calculations in this section, grid spacings of 0.2 nm were used in both directions for the isolated Au nanowires and 0.25 nm for the Ag dimers. Unless otherwise stated, the 2D high-frequency value of β^2 was used. Note that Ag was modeled analogously to Au (as outlined in Sects. 8.3 and 8.4), and parameters for the dielectric model are given in Appendix B.

Convergence of Nonlocal Near-Field Properties to Local Results

As mentioned in Sect. 8.5.1 in relation to triangular nanowires, much of the interest in apex structures is due to their high surface $|\mathbf{E}(\mathbf{x},\omega)|^2$ enhancements. It was suggested that there could possibly be no convergence of nonlocal properties to local ones in such structures, especially near their apices, where the longitudinal distance can be arbitrarily small. In this section, these structures are revisited with particular emphasis on their maximum $|\mathbf{E}(\mathbf{x},\omega)|^2$ enhancements and the convergence of nonlocal results to local ones.

$|\mathbf{E}(\mathbf{x},\omega)|^2$ enhancements at the bottom apices of triangular nanowires (where for the incident light considered these are maximized) in the local and nonlocal limits are compared in Fig. 8.20 for l values up to 80 nm. (Note that these enhancements were calculated at the dipolar LSPR energies, obtained from the extinction spectra, and using the 2D low-frequency value of β^2). Over the entire l range, local electrodynamics predicts enhancements greater than twice the nonlocal results, significant differences. Furthermore, as suggested in Sect. 8.5.1, there seems to be no convergence of the nonlocal and local results. Even though there appears to be no convergence of the near-field properties such as $|\mathbf{E}(\mathbf{x},\omega)|^2$, relative convergence of those in the far-field does occur (e.g., anomalous absorption and LSPR blueshifting); see Fig. 8.9.

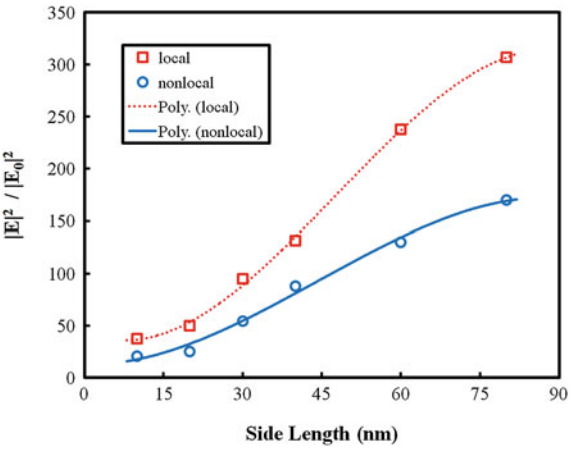

Fig. 8.20 $|\mathbf{E}(\mathbf{x},\omega)|^2$ enhancements at the apex of a Au triangular nanowire. *Symbols* denote the calculated points, and *curves* are polynomial fits to the data. The *full curve* with *open circles* represents nonlocal calculations; the *broken curve* with *open squares* represents local ones

Geometry Effect on Electric Field Enhancements

In this section, the maximum and average $|\mathbf{E}(\mathbf{x},\omega)|^2$ enhancements around nanowires of various shapes are investigated.

$|\mathbf{E}(\mathbf{x},\omega)|^2$ enhancements are expected to be high at or near the LSPR energies [48]. Therefore, the optical responses of cylindrical, square, and triangular nanowires with dimensions of 50 nm (either the diameter or side-length), a common size used in experimental and theoretical studies (and based on the discussion above, as good of size as any), were calculated; Fig. 8.21. There is no significant anomalous absorption that was seen for the thin metal films, solid or core–shell nanowires, or nanoparticles (see Sects. 8.5.1 and 8.5.2). This is because the dimensions are large enough such that the discrete anomalous absorption resonances are not apparent (see Figs. 8.5 and 8.11, as well as the relevant discussions). However, many closely spaced longitudinal plasmon modes do exist, leading to the LSPR blueshift and very minor closely spaced "bumps" (as well as affecting other properties—vide infra). This can be confirmed by again looking at intensity profiles of $|\mathbf{D}(\mathbf{x},\omega)|^2$ (as in all other cases thusfar discussed); Fig. 8.22.

At the LSPR energies (which are slightly different in the local and nonlocal results, due to blueshifting), $|\mathbf{E}(\mathbf{x},\omega)|^2$ profiles were calculated; Fig. 8.23. Note that normalized $|\mathbf{E}(\mathbf{x},\omega)|^2$ values are shown in Fig. 8.23, and thus only relative intensity comparisons of the shapes in the local and nonlocal results should be made—e.g., the local cylinder to the nonlocal one. Qualitatively, the $|\mathbf{E}(\mathbf{x},\omega)|^2$ values are very similar (both inside and around the structures) in both the local and nonlocal results. Quantitatively, however, it is seen that the nonlocal fields are of lower intensity. This is especially true for the triangular nanowires, and to a lesser extent the square ones. (It is hard to discern a difference in the cylindrical nanowires.)

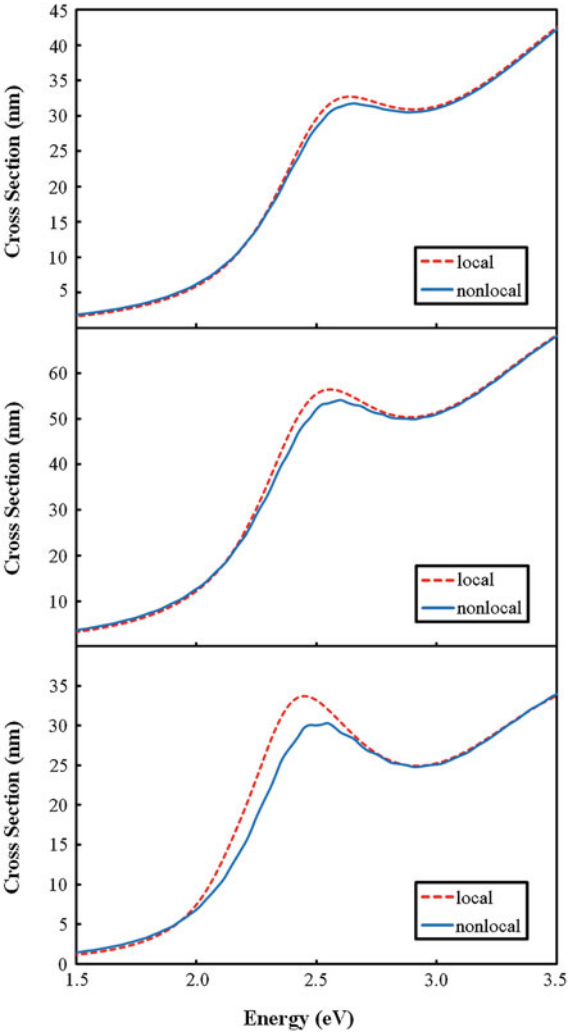

Fig. 8.21 Extinction cross sections of *top* cylindrical, *middle* square, and *bottom* triangular Au nanowires from both local (*broken red lines*) and nonlocal (*solid blue lines*) calculations

In order to quantitatively assess the $|\mathbf{E}(\mathbf{x},\omega)|^2$ enhancements in Fig. 8.23, the maximum and average values around the nanowires were calculated, which are shown in Table 8.1.

(The average values refer to fields averaged only over certain distances from the nanowire surfaces.) In all cases, significant decreases in both the maximum and average $|\mathbf{E}(\mathbf{x},\omega)|^2$ enhancements are found outside of the structures. For the cylindrical nanowire, a negligible difference exists between the local and nonlocal enhancements. (It is also interesting to note that the average enhancements are higher 1.0 nm away from the surface than they are at 0.5 nm.) For the square nanowire, the difference is larger. There is approximately a 10% difference in the

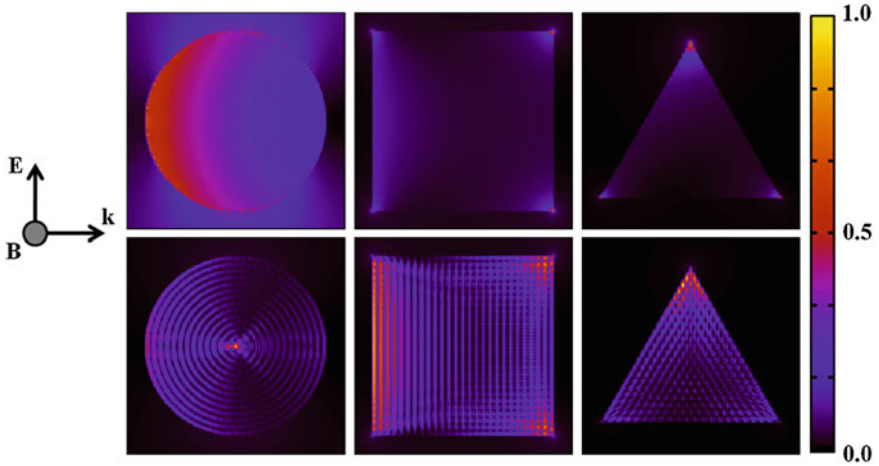

Fig. 8.22 Normalized $|\mathbf{D}(\mathbf{x},\omega)|^2$ intensity profiles in and around *left* cylindrical, *middle* square, and *right* triangular Au nanowires obtained from both *top* local and *bottom* nonlocal calculations at the LSPR energies

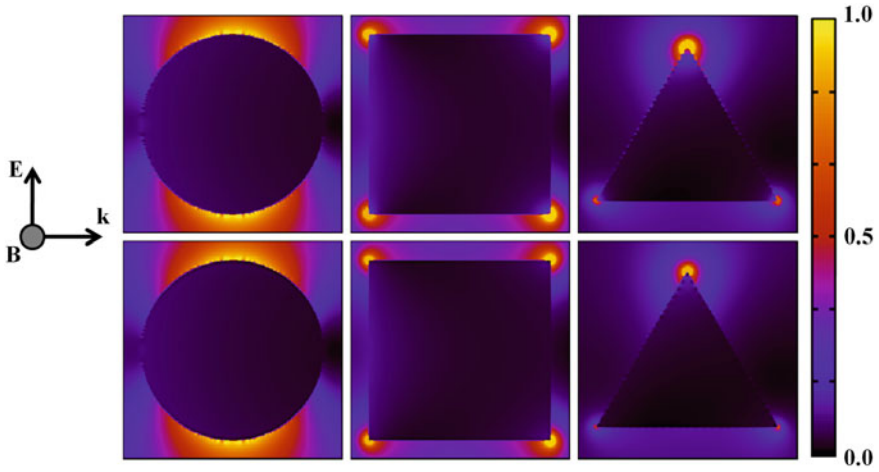

Fig. 8.23 Normalized $|\mathbf{E}(\mathbf{x},\omega)|^2$ intensity profiles in and around *left* cylindrical, *middle* square, and *right* triangular Au nanowires obtained from both *top* local and *bottom* nonlocal calculations at the LSPR energies

maximum and average $|\mathbf{E}(\mathbf{x},\omega)|^2$ enhancements at 1.0 nm, and a 6% difference in the average values at 2.0 nm. It is expected that the difference in average enhancements will decrease further away from the surfaces, as the near-fields exponentially decay. The differences for the triangular nanowire are strikingly larger. A 104% difference in the maximum enhancement and 61% difference in the

Table 8.1 Maximum and average $|\mathbf{E}(\mathbf{x},\omega)|^2$ enhancements for cylindrical, square, and triangular nanowires at the LSPR energies

Nanowire shape	Max	0.5 nm	1.0 nm	2.0 nm
Cylindrical (local)	8.64	2.42	2.47	2.40
Cylindrical (nonlocal)	7.85	2.32	2.39	2.34
Square (local)	60.58	3.54	3.33	3.01
Square (nonlocal)	39.79	3.02	2.91	2.69
Triangular (local)	145.77	5.49	4.90	4.18
Triangular (nonlocal)	71.40	3.42	3.30	3.01

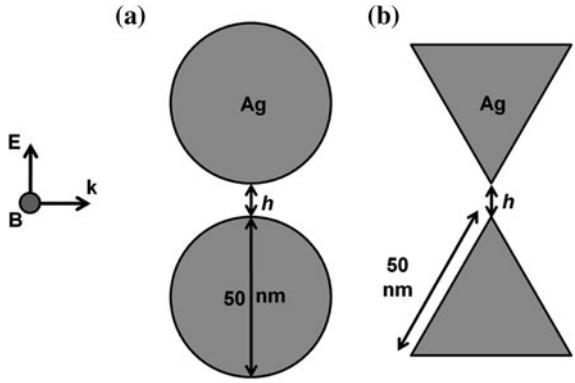

Fig. 8.24 Schematic diagrams of **a** cylindrical and **b** triangular nanowire dimers considered in this section

average enhancement at 0.5 nm are seen. These are significant differences, and it is remarkable that they are only for an isolated nanostructure, which generates relatively low $|\mathbf{E}(\mathbf{x},\omega)|^2$ enhancements in comparison to a junction structure [44]; see both Chap. 5 and the section below.

Cylindrical and Triangular Nanowire Dimers

In this section, systems known to give high $|\mathbf{E}(\mathbf{x},\omega)|^2$ enhancements (likely, the most promising systems; see Chap. 5) are considered, Ag cylindrical and triangular nanowire dimers [46–47]. Schematic diagrams of these systems are shown in Fig. 8.24. The Ag cylindrical nanowire dimer, Fig. 8.24a, consists of two nanowires, each with a 50 nm diameter, separated by a distance h. The other system is analogous, and consists of two equilateral triangular nanowires with side lengths of 50 nm; Fig. 8.24b. These sizes were chosen as they are representative of those often used in experiments, and are also sufficiently large to generate very high $|\mathbf{E}(\mathbf{x},\omega)|^2$ enhancements; see the above section. The dimers are illuminated by an incident field with the $\mathbf{E}(\mathbf{x},\omega)$ components in-plane and polarized along their long axes (the incident $\mathbf{k}$ is obviously perpendicular to this, giving normal incident

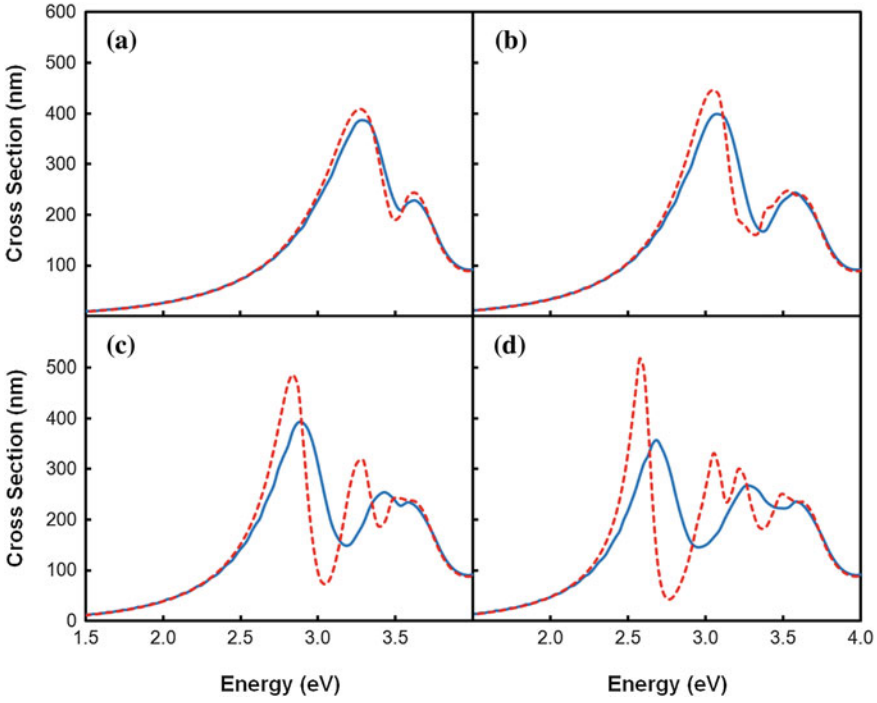

Fig. 8.25 Extinction cross sections of 50 nm diameter cylindrical nanowires separated by **a** 5, **b** 2, **c** 1, and **d** 0.5 nm

light). Based on the discussion in Chap. 5, $|\mathbf{E}(\mathbf{x}, \omega)|^2$ enhancements are very high for small junction sizes. Therefore, h values of 5, 2, 1, and 0.5 nm are considered in this section. Although smaller separations would likely lead to even larger $|\mathbf{E}(\mathbf{x}, \omega)|^2$ enhancements than are obtained below [45], these are not considered. This is because surface boundaries are not infinitely sharp. Therefore, electron spill-out would likely "blur" boundaries of smaller size [49]. Even if sharp boundaries were realistic, it is unlikely that such small separations are experimentally achievable due to fabrication techniques and surface imperfections.

The optical responses of the dimers were determined by calculating extinction cross sections; Figs. 8.25 and 8.26. For the cylindrical nanowires, the optical responses are nearly identical in both the local and nonlocal results when the separation is 5 nm. There are, however, some minor differences, in that there is both a slight reduction in the magnitude and the LSPR is slightly blueshifted in the nonlocal results (not surprising, based on the discussion in Sects. 8.5.1 and 8.5.2). As the nanowire separation is reduced, for example to 2 nm, there is an overall redshift of the LSPRs. This is understandable, as the LSPR dispersion relation in such structures redshifts as the junction distance is decreased [50]. Comparing the local and nonlocal results, the relative LSPR blueshift is seen to increase. For

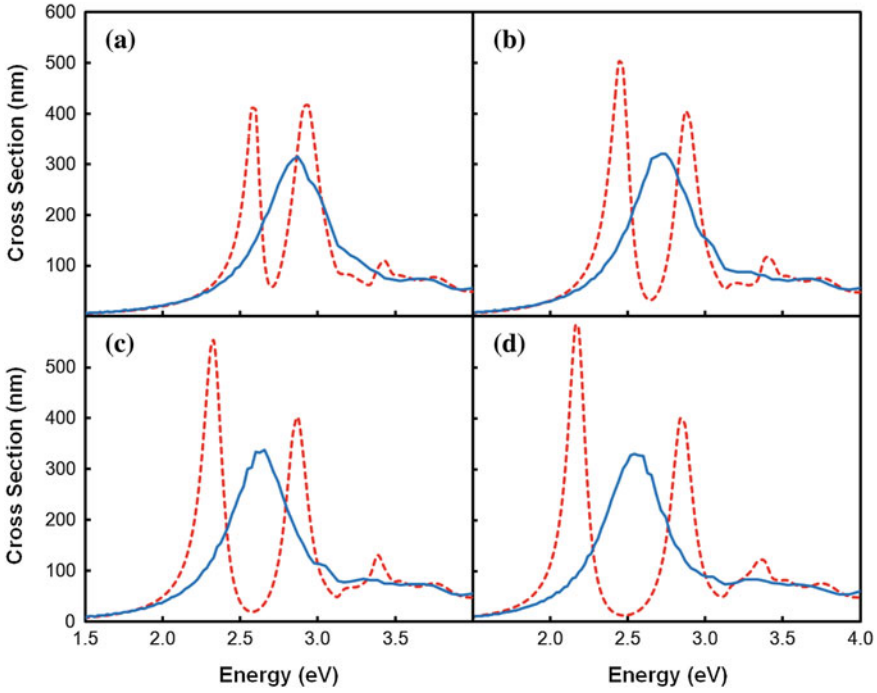

Fig. 8.26 Extinction cross sections of 50 nm side-length triangular nanowires separated by **a** 5, **b** 2, **c** 1, and **d** 0.5 nm

example, the dipolar LSPR (the lowest energy peak) blueshifts by 0.11 eV at 0.5 nm separation, whereas it is only 0.05 eV at 5 nm. The increase in strength of the nonlocal effects can be understood by examination of Eq. 8.2. As the junction gap is reduced, higher magnitude $\mathbf{k}$ components are generated, which, in turn, cause LSPRs to occur at higher frequencies relative to $\mathbf{k} = \mathbf{0}$. In addition to blueshifting, the nonlocal peaks are much broader compared to the local ones. Presumably this occurs because the lifetime of the LSPR modes is decreased through coupling to the internal (volume) plasmon modes that only occurs when nonlocal effects are included. These points will be revisited below.

Additional peak structures also appears with decreasing separation, which can be attributed to higher-order LSPRs (quadrupolar, octupolar, etc.). Because of the increase in relative LSPR blueshift with decreasing nanowire separation, these resonances are less apparent (not as easily excited) in the nonlocal results. Therefore, much smaller junctions than previously demonstrated [45] are realistically needed to excite them. Nonetheless, they are still apparent, and are also blueshifted relative to the local results, much like the dipolar LSPR. Focusing on the 1-nm results, for example, the relative blueshift of the quadrupolar LSPR (the second lowest energy peak) is 0.18 eV. This suggests that higher-order LSPRs are more blueshifted than those of lower-order, which is opposite to what was found

for the core–shell nanowires discussed in Sect. 8.5.2, and thus represents a point for possible future investigation. It is likely that this trend is system dependent, as is further discussed below. Also similar to the dipolar LSPR, the nonlocal higher-order LSPR peaks are broadened relative to the local results.

Qualitatively similar trends are found in the optical responses of the triangular nanowires; Fig. 8.26. Quantitatively, however, much greater differences between the local and nonlocal results occur. For example, the relative blueshift of the dipolar LSPRs are 0.27 and 0.35 eV at 5 and 0.5 nm separations, respectively, compared to 0.05 and 0.11 eV for the cylindrical nanowires. In addition, the nonlocal peaks are even more (relatively) broadened. The differences between the cylindrical and triangular nanowires can be attributed to the fact that larger magnitude **k**-components are generated by the sharp tips of the triangular structures, and thus the nonlocal effects are stronger (as discussed in Sect. 8.5.1). This is also part of the reason why the $|\mathbf{E}(\mathbf{x},\omega)|^2$ enhancements in such structures are often high relative to other shapes [37]. This also leads to easier excitation of high-order LSPRs, where even at 5 nm such resonances are excited in the local results. Due to such strong nonlocal effects, it is unclear if high-order LSPRs are excited in the nonlocal results at all.

The most important differences are seen by comparing the junction $|\mathbf{E}(\mathbf{x},\omega)|^2$ enhancements (the position of maximum EM enhancement; see Chap. 5); Figs. 8.27 and 8.28. In the local results, the $|\mathbf{E}(\mathbf{x},\omega)|^2$ enhancements, shown as *dashed red curves* in Figs. 8.27 and 8.28, are qualitatively similar to the extinction cross sections (the peaks and valleys are similar), a trend that is often [45], but not always [51] the case. This often occurs because the LSPRs increase multiple scattering events at the junction, which in turn lead to large $|\mathbf{E}(\mathbf{x},\omega)|^2$ enhancements. The nonlocal results (*solid blue curves* in Figs. 8.27 and 8.28), on the other hand, show that while both dipolar and higher-order LSPRs are clearly distinguishable in the extinction cross sections (see the 0.5-nm cylindrical results, for example), only the dipolar LSPR shows a significant $|\mathbf{E}(\mathbf{x},\omega)|^2$ enhancement. However, it is possible that systems with more prominent high-order LSPRs (likely not junction structures, but possibly core–shell nanostructures [22], for example) will show higher $|\mathbf{E}(\mathbf{x},\omega)|^2$ enhancements at these resonances. Nonetheless, enhancements for higher energies than those of the dipolar LSPRs are still relatively large, and are slowly decreasing functions of energy. This is in contrast to the local results, where distinct peaks and valleys are seen. By inspection of the broadened spectral shapes in Figs. 8.25 and 8.27, it can be inferred that the two effects are related. However, the effects are not identical, as can be seen by comparison of the relative $|\mathbf{E}(\mathbf{x},\omega)|^2$ enhancements between the dipolar and higher-order LSPRs in relation to the relative cross section magnitudes in both the local and nonlocal results. These points will be returned to below.

It is also seen in Figs. 8.27 and 8.28, much like for the cross sections, that the nonlocal $|\mathbf{E}(\mathbf{x},\omega)|^2$ enhancements are blueshifted relative to the local results, and this effect also becomes more prominent with decreasing gap distance. For

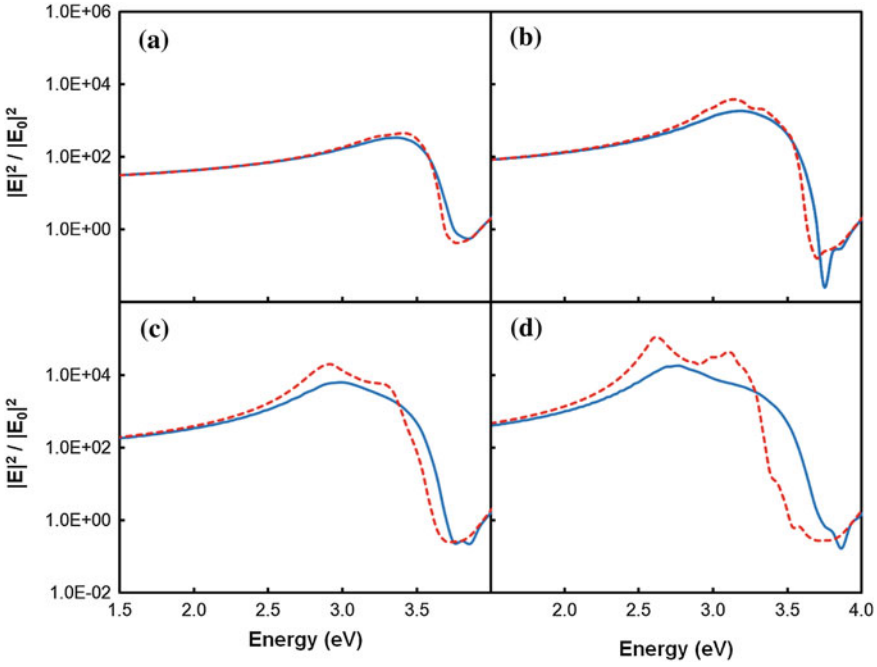

Fig. 8.27 $|\mathbf{E}(\mathbf{x},\omega)|^2$ enhancements at the junction of 50 nm diameter cylindrical nanowires separated by **a** 5, **b** 2, **c** 1, and **d** 0.5 nm

example, while the nonlocal and local results are similar at 5 nm for the cylindrical nanowires, there are significant differences for separations of less than approximately 2 nm, where at 0.5 nm there is a 0.14 eV relative blueshift. It is interesting to note that these blueshifts are different than those of the cross sections, but not unreasonable considering that $|\mathbf{E}(\mathbf{x},\omega)|^2$ enhancements are not necessarily correlated with the optical cross sections, contrary to popular belief [51].

Perhaps the biggest and most important difference between the local and nonlocal results is that the $|\mathbf{E}(\mathbf{x},\omega)|^2$ enhancements are significantly different when nonlocal effects are included [7, 12]. The triangular nanowires separated by 0.5 nm represent possibly the most extreme example of this; Fig. 8.28d. The maximum $|\mathbf{E}(\mathbf{x},\omega)|^2$ enhancements are 2.3×10^5 in the local results, but only 1.4×10^4 when nonlocal effects are included. Considering that the nonlocal results are more rigorous than the local ones (in principle), it is possible that the maximum achievable $|\mathbf{E}(\mathbf{x},\omega)|^2$ enhancements are over an order of magnitude less than previously thought. Also considering that some physical processes, such as SERS, are dependent on $|\mathbf{E}(\mathbf{x},\omega)|^4$ enhancements [2], these differences could have significant implications to the interpretation of results. For example, if the actual electromagnetic contribution (including nonlocal effects) to SERS is smaller than

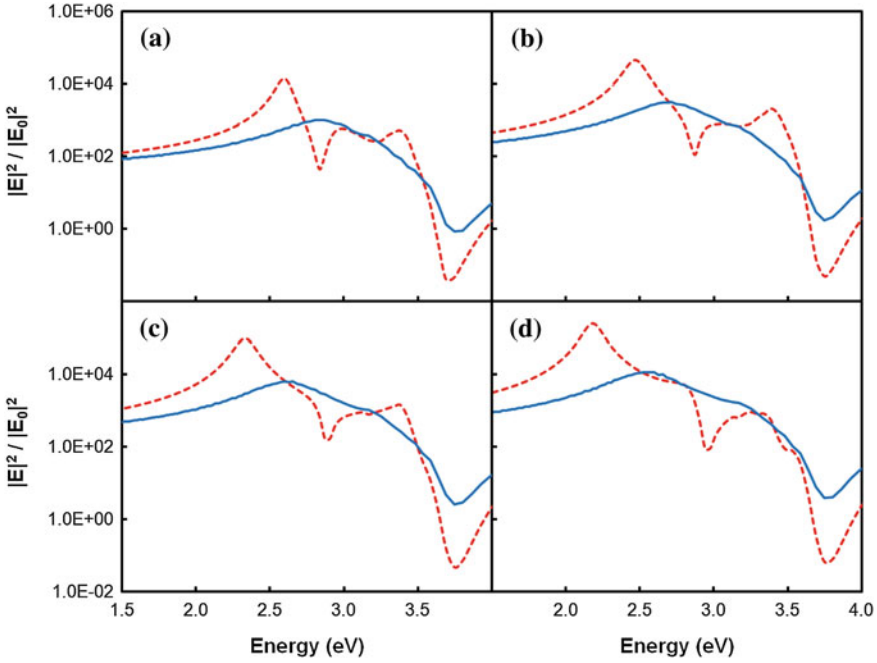

Fig. 8.28 $|\mathbf{E}(\mathbf{x},\omega)|^2$ enhancements at the junction of 50 nm side-length triangular nanowires separated by **a** 5, **b** 2, **c** 1, and **d** 0.5 nm

expected on the basis of local theory (which, based on this discussion, could be up to three orders of magnitude less than previously thought), it is possible that chemical effects play a more important role than has been considered in the past [52]. These results are also important to the interpretation of electron energy loss measurements for anisotropic nanoparticle structures [53].

In addition to the quantitative difference in maximum enhancements, their qualitative behavior is also different, as can be seen from intensity profiles of $|\mathbf{E}(\mathbf{x},\omega)|^2$; Figs. 8.29 and 8.30. In the nonlocal results, besides noticeable decreases in maximum intensities, the field enhancements are found to be distributed around the nanowire surfaces. For example, there are noticeable enhancements at the poles of the dimers, whereas in the local results the primary enhancement occurs at the junction.

The differences that occur in the nonlocal results can be understood by looking at intensity profiles of the electric displacement field, $|\mathbf{D}(\mathbf{x},\omega)|^2$. Figures 8.31 and 8.32 show such profiles for $h = 0.5$ nm separations of the cylindrical and triangular nanowires, respectively, at the energies of maximum $|\mathbf{E}(\mathbf{x},\omega)|^2$ enhancements. The nonlocal results show discrete longitudinal (volume) plasmons inside the structures. Although difficult to discern from these complex profiles, these

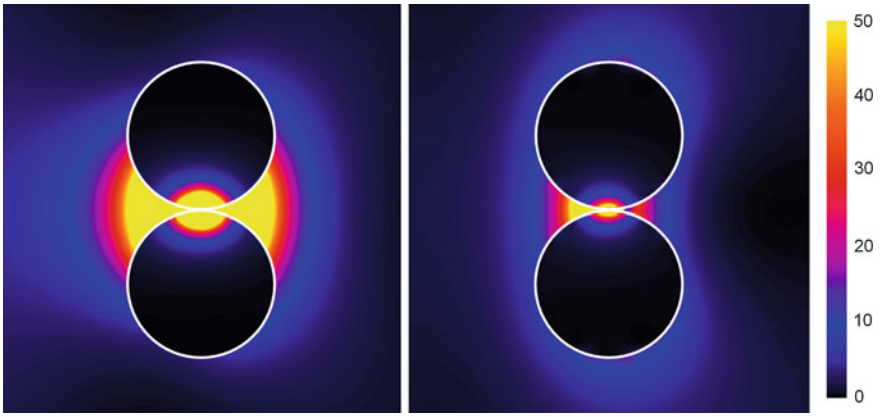

Fig. 8.29 Intensity profiles of $|\mathbf{E}(\mathbf{x},\omega)|^2$ for 0.5 nm spaced cylindrical nanowires. Local and nonlocal calculations are shown on the *left* and *right*, respectively; the nanowires are outlined in *bold white*

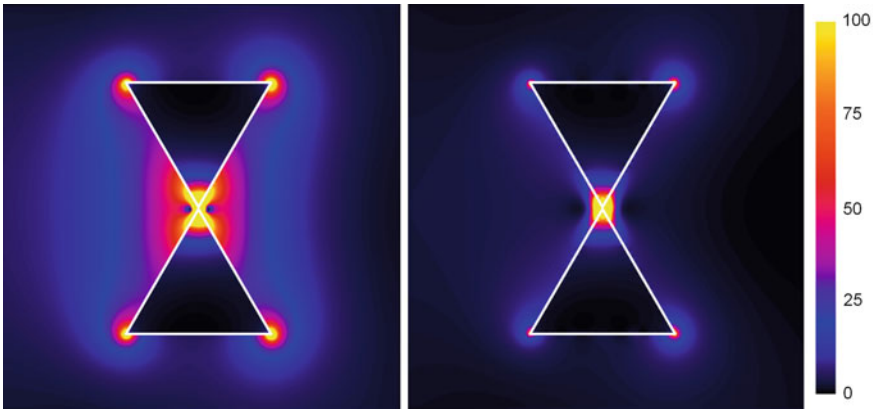

Fig. 8.30 Intensity profiles of $|\mathbf{E}(\mathbf{x},\omega)|^2$ for 0.5 nm spaced triangular nanowires. Local and nonlocal calculations are shown on the *left* and *right*, respectively; the nanowires are outlined in *bold white*

modes can also be considered analogous to one-particle quantum states, just as in the more simple isolated nanostructures [7] (Sect. 8.5.1). As for all other examples considered, these profiles are in sharp contrast to the local results, where $|\mathbf{D}(\mathbf{x},\omega)|^2$ is a smooth function. In both cases (local and nonlocal), however, $|\mathbf{D}(\mathbf{x},\omega)|^2$ is concentrated near the junction. This is expected, since the junction is where most of the scattering events occur, leading to a high localization of both $|\mathbf{E}(\mathbf{x},\omega)|^2$ and $|\mathbf{D}(\mathbf{x},\omega)|^2$. In comparison to the longitudinal plasmon modes in isolated

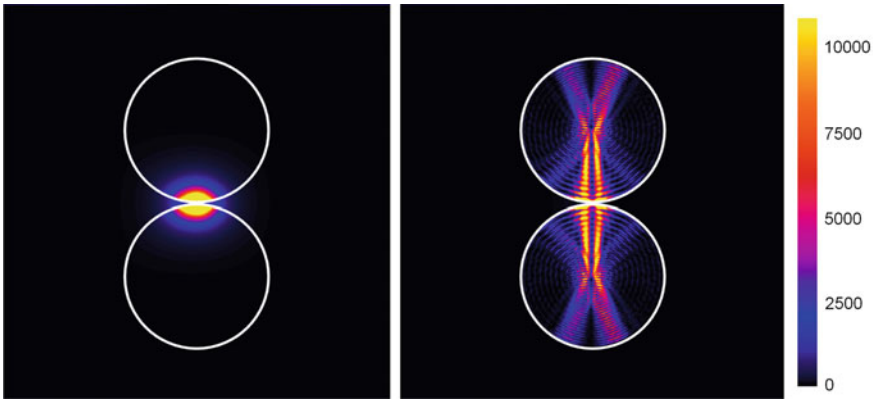

Fig. 8.31 Intensity profiles of $|\mathbf{D}(\mathbf{x},\omega)|^2$ for 0.5 nm spaced cylindrical nanowires. Local and nonlocal calculations are shown on the *left* and *right*, respectively; the nanowires are outlined in bold white

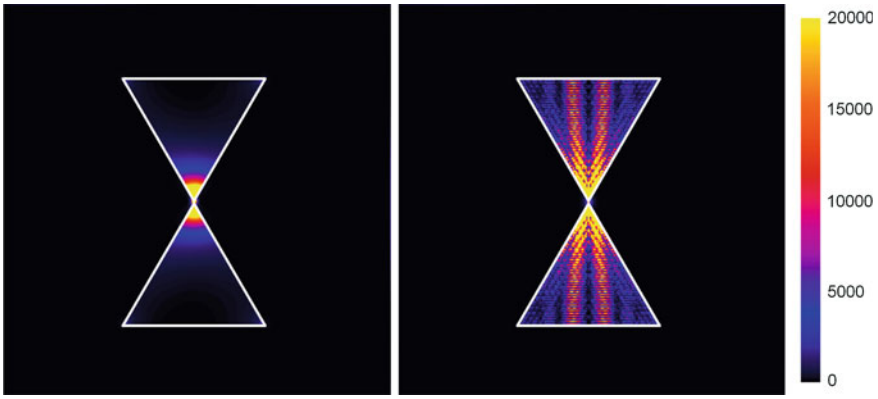

Fig. 8.32 Intensity profiles of $|\mathbf{D}(\mathbf{x},\omega)|^2$ for 0.5 nm spaced triangular nanowires. Local and nonlocal calculations are shown on the *left* and *right*, respectively; the nanowires are outlined in bold white

nanostructures [7, 9], which are longitudinal to the incident **k**, the modes in this case show wave structure along both the incident **k**-axis and the (perpendicular) long-axis of the dimer structure. This can be seen in the (slight) cylindrical symmetry of the volume plasmons in the cylindrical nanowires, as well as the orthogonal directions of maxima and minima in the triangular nanowires. Furthermore, the direction along the long axes shows the greatest intensities. This indicates that in such junction structures, while the **k** from the incident field excites longitudinal plasmons, the dominant **k**-components are generated by scattering at the junction. These results highlight an essential difference between isolated and

dimer structures, and also help explain why nonlocal effects are more dramatic in the latter.

By considering the LSPRs and volume plasmons as distinct "modes", the qualitative differences between the nonlocal optical responses and $|\mathbf{E}(\mathbf{x},\omega)|^2$ enhancements relative to the local results can be further understood. The overlap of these modes will cause the SPs to be damped. Since SPs are responsible for the scattering that results in the high $|\mathbf{E}(\mathbf{x},\omega)|^2$ enhancements, they are likely to be lower when coupled to volume plasmons. Furthermore, since the concentration of the volume modes is in the junction region, it makes sense that the $|\mathbf{E}(\mathbf{x},\omega)|^2$ enhancements related to the higher-order LSPRs (which are oriented along other directions than that of the polarization) are more significantly damped than the dipolar one. In addition, the SPs will have decreased lifetimes due to this damping, and thus the spectral broadening can also be understood.

8.6 Surface Effects

Before concluding this chapter, it is worthwhile mentioning that other effects not explicitely discussed (and also indirectly related to quantum mechanical effects, such as electron spill-out) also become important for small particles. In this section, surface effects at the sub-nanometer-scale are discussed, which have recently been found to cause LSPRs to redshift with decreasing particle size, but only for very small particles [1], contrary to the expectation of a blueshift [36, 54]. Conflicting results have been presented previously regarding this, showing a blueshift in some cases and a redshift in others; for a complete discussion, see Ref. [55] and references therein.

The aim of this section is to provide a discussion of the resolution of this conflict, by presenting results from a combined theoretical and experimental study of small Ag nanoparticles. An important feature of the presented results is that the experimental systems have a high uniformity in size ($\sim$10% distribution), shape (icosahedral), and crystallinity (information known from HRTEM measurements) [1]. Furthermore, the nanoparticles all have identical surface chemistry (which was confirmed using Fourier-transformed infrared spectroscopy). The actual details are irrelevant, but such uniformities rule out other possible effects (e.g., shape effects) that could possibly provide alternative explanations to the following.

Experimental absorption cross sections per nanoparticle for diameters of $d \approx 2$ to 18 nm in hexane (RI of $n = 1.375$) are shown in Fig. 8.33. It is seen that the LSPR blueshifts with increasing diameter for nanoparticles with $d < 12.5$ nm, contrary to the expected redshift [36]. For example, the LSPR peak significantly blueshifts from 442.3 to 425.6 nm when the nanoparticle size increases from $d = 2.2$ to 3.9 nm. The peak position continuously blueshifts to 402.3 nm for nanoparticles with $d = 12.5$ nm. The blueshift then stops, and a redshift takes over as the particle size increases further, consistent with the expected behavior [36]

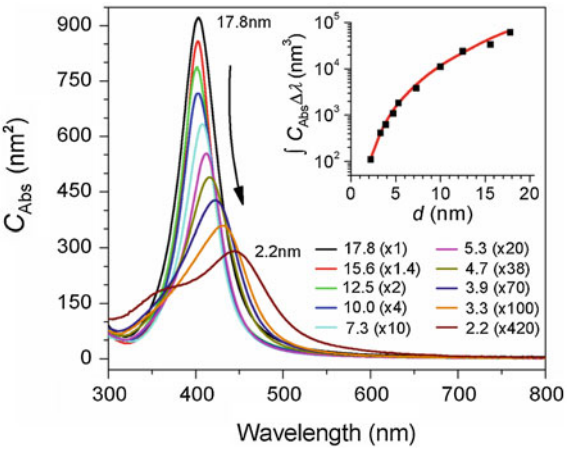

Fig. 8.33 Absorption cross section per nanoparticle for various d values in hexane. For clarity, each spectrum has been multiplied by an arbitrary factor listed in the parentheses. The *inset* plots the experimental (*black squares*) and theoretically calculated (*red line*) integrated absorption from 320 to 600 nm

(due to radiative depolarization effects when the particle size is not negligible compared to the size of the wavelength [54]). For instance, the LSPR positions are $\lambda = 402.4$ and 403.3 nm for nanoparticles with $d = 15.6$ and 17.8 nm, respectively.

In order to explain these trends, a model that contains precise system details at the sub-nanometer-scale must be taken into account, such as surface effects and chemical interactions of each nanoparticle with the surrounding medium (e.g., surfactant molecules). It is possible to construct a simple model containing all of these details. In this model, the Ag nanoparticles (assumed to be spheres with diameter d) are composed of a core with radius $r_c = d/2 - t$ (where t will be defined in a moment) that is treated with bulk dielectric data (modified to take into account the interfacial scattering correction with $A = 1.0$, determined by comparisons to experiment [1]). A thin shell of thickness t that extends from r_c to $r_c + t = d/2$ is then assumed on the surface of the nanoparticles, in which the electron conductivity (carrier density) is lowered compared to the inner core because of the partial participation of these electrons in chemical interactions (e.g., bonding) with the surfactant molecules (note that there is no interfacial scattering correction in this layer). It should be noted that an analogous picture of lowered free electron density emerges if quantum mechanical electron spill-out is considered [49]. However, such an effect is not able to accurately account for the results presented here. Considering that it is the outermost Ag atoms that participate in bonding, t should be taken to be roughly the thickness of a single Ag atomic layer, so $t = 0.25$ nm is considered. Additionally, a shell corresponding to the surfactant layer is assumed to exist from radii $d/2$ to $d/2 + s$, where $s = 2$ nm is the thickness of the shell with a RI $n = 1.4595$ (consistent with the experimental surfactant). The precise molecular details are irrelevant for this discussion, as it has been found that the model predictably describes situations of different surface chemistry [1]. Solvent is then assumed to exist for radii greater than $d/2 + s$, and

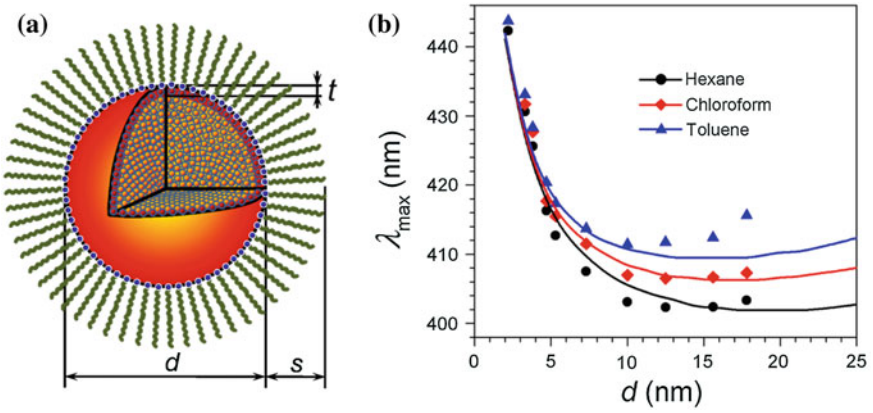

Fig. 8.34 **a** Schematic diagram of the theoretical model developed: d represents the diameter of a nanoparticle, t is the thickness of the outermost layer with lowered conductivity, and s is the thickness of the surfactant layer. *Blue dots* represent atoms bonded to the nanoparticle surface. **b** Experimental (*symbols*) and calculated (*lines*) LSPR peak positions for various nanoparticle sizes dispersed in hexane (*black*), chloroform (*red*), and toluene (*blue*)

is either hexane ($n = 1.375$), chloroform ($n = 1.445$), or toluene ($n = 1.496$). A schematic diagram of the model is shown in Fig. 8.34a. While seemingly complicated, the optical response of such a system can be found using analytical multilayer Mie theory [56].

However, before the optical response can be determined, the reduced conductivity of the layer t must be taken into account. Such a proceduce is illustrated here using the Drude model. First, a Drude model for the permittivity, $\varepsilon_{\mathrm{D}}(\omega) = \varepsilon_{\infty} + \varepsilon_{\mathrm{intra}}(\omega)$ (Eqs. 2.23 and 2.25), is fit to the empirically inferred dielectric data [31]; Appendix B. Then, the full dielectric function, $\varepsilon(\omega)$, is assumed to be given by Eq. 2.23, where $\varepsilon_{\mathrm{intra}}(\omega)$ is the difference between the empirical data and $\varepsilon_{\mathrm{D}}(\omega)$. Thus, at this point, $\varepsilon(\omega)$ in Eq. 2.25 describes the empirical data exactly, but the Drude portion captures the physics of electron motion. To lower the conductivity, $\varepsilon_{\mathrm{intra}}(\omega)$ is kept constant and ω_{D} [in $\varepsilon_{\mathrm{D}}(\omega)$] is lowered. This lowers the conductivity, because the carrier density (and thus conductivity) is proportional to ω_{D}. Specifically, the Drude dielectric function is related to the (alternating current, AC) conductivity, $\sigma(\omega)$, via

$$\varepsilon_0 \varepsilon_{\mathrm{D}}(\omega) = \varepsilon_0 \varepsilon_{\infty} + i\frac{\sigma(\omega)}{\omega}, \tag{8.12}$$

where

$$\sigma(\omega) = \frac{\varepsilon_0 \omega_{\mathrm{D}}^2/\gamma_{\mathrm{D}}}{1 + i\omega/\gamma_{\mathrm{D}}}. \tag{8.13}$$

[Notice the multiplicative factor of ε_0 because $\varepsilon_{\mathrm{D}}(\omega)$ is a relative dielectric function]. Obviously, decreasing ω_{D} lowers both $\Re[\varepsilon_{\mathrm{D}}(\omega)]$ and $\Im[\varepsilon_{\mathrm{D}}(\omega)]$. It is the

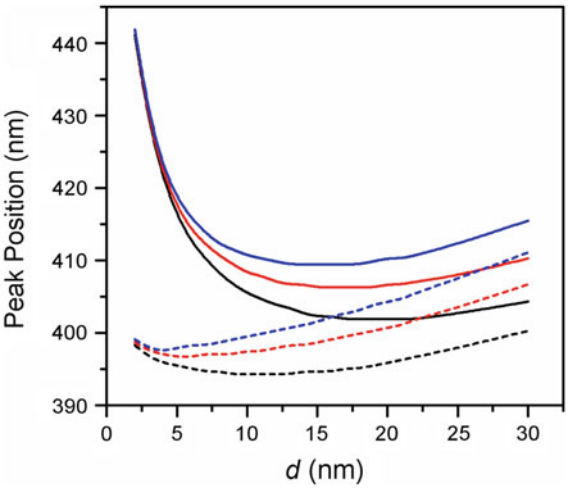

Fig. 8.35 Comparison of calculated LSPR peak positions for Ag nanoparticles of various sizes dispersed in hexane (*black*), chloroform (*red*), and toluene (*blue*). Calculations performed both including (*solid lines*) and excluding (*dotted lines*) the reduced surface conductivity are shown

effect on the former which leads to the redshifting with decreasing nanoparticle size. (The latter effect is not as significant, nor relevant to this discussion.) For the remainder of this section, a lowering of ω_D by 15% is used, determined by comparisons between theory and experiment.

Figure 8.34b compares theoretical and experimental size-dependent LSPR wavelengths for nanoparticles in the three solvents under consideration (hexane, chloroform, and toluene). Comparison of the spectra shows that, regardless of the solvent, the dependence of the absorption peak on nanoparticle size exhibits a very similar relationship, a blueshift followed by strong redshift as d is decreased. Interestingly, the turnover size becomes smaller and the redshift becomes steeper for larger particles when the RI of the solvent is higher. For example, the size-dependent peak positions turn over at $\sim$10, 12.5, and 15 nm for toluene, chloroform, and hexane, respectively. Although not fitting perfectly in these cases, the level of agreement between the experimental and theoretical results, given the simplicity of the model, is outstanding. (The calculated turnovers for toluene, chloroform, and hexane are 15.5, 17, and 19.5 nm, respectively.) Additionally, the experimental integrated absorption cross sections presented in the inset of Fig. 8.33 are also found to increase with nanoparticle size in a manner perfectly consistent with the absolute values calculated according to the theoretical model.

It is informative to look at the LSPR peak positions calculated both with and without the reduced conductivity layer (also for the same three solvents); Fig. 8.35. It is remarkable that without including the layer of reduced conductivity there is no turnover until very small sizes ($d \approx 4$ nm), given that this layer is only 0.25 nm thick.

The degree of both qualitative and quantitative agreement achieved with the model presented in this section strongly suggests that the conductivity of the outer atomic layers of nanoparticles is a previously unappreciated feature that must be considered in the small-particle limit. Based on these careful and systematic

results, it is clear that previous discrepancies regarding this effect [55] are due to system differences and/or experimental uncertainties. This novel behavior could lead to the development of new techniques (e.g., sensing) or devices based on the tuning of the conductivity of single atomic layers in small metal nanoparticles.

For a further discussion of this effect, including additional theoretical and experimental details, see Ref. [1].

8.7 Summary and Outlook

An electrodynamics method to calculate the optical responses of arbitrarily shaped structures described by a spatially nonlocal dielectric function (which incorporates quantum mechanical effects) was presented. This formulation was based on converting the equation of motion of the conduction electons from the hydrodynamic Drude model into a partial differential equation for the current field that serves as an ADE to Maxwell's equations. By discretizing this equation using standard finite-difference techniques, it was shown to be easily incorporated into a self-consistent computational scheme along with the standard discretized Maxwell's equations, such as those used in FDTD.

Many applications of the method were presented. First, basic geometric nanostructures in one, two, and three dimensions were calculated (thin metal films, solid nanowires, and spherical nanoparticles, respectively). These calculations showed the basic phenomena that occur when nonlocal effects are included; specifically, anomalous absorption and blueshifting of the LSPRs in the optical responses. Intensity profiles of $|\mathbf{D}(\mathbf{x},\omega)|^2$ revealed that these effects are due to the excitation of longitudinal (or volume) plasmons.

The application to core–shell nanowires revealed more technical aspects of nonlocal effects, such as the impact of various parameters of the nonlocal model. However, this discussion also demonstrated that the most important factor of nonlocal effects (in simple systems) is the thickness of the structure along the longitudinal direction of the incident light. Different order LSPRs were shown to be affected differently by these effects, and while the anomalous absorption is insensitive to the RI, blueshifts of the LSPRs are.

Perhaps the most important results were that significant decreases in $|\mathbf{E}(\mathbf{x},\omega)|^2$ enhancements were found, similar to results found theoretically for Ag nanoparticle dimers [12], which in some cases were over an order of magnitude. Considering that the nonlocal calculations are, in principle, more rigorous than the local ones, these results have significant implications. For example, the interpretation of physical processes that rely on such effects (e.g., SERS) could be much different than previously thought.

Connections with experiment were made when possible, and reasons were suggested why these effects have not been experimentally realized for nanostructures studied in bulk. The presented discussions are a strong motivation for

future studies of isolated nanostructures, where nonlocal effects are likely to play a larger role.

In addition to nonlocal effects, a combined theoretical and experimental study of small Ag nanoparticles was discussed. It was shown that in the small-particle limit, detailed interactions at the sub-nanometer-scale (atomic-length, yet still in the continuum picture) can lead to unexpected effects. For example, redshifting LSPRs with decreasing particle size, which is contrary to expectations [36].

These results demonstrate the importance of including nonlocal effects and making sub-nanometer considerations when describing metal–light interactions at the small end of the nanoscale, especially now that experimental investigation there is becoming possible.

References

1. Peng S, McMahon JM, Schatz GC, Gray SK, Sun Y (2010) Reversing the size-dependence of surface plasmon resonances in colloidal nanoparticles (submitted)
2. Willets KA, Van Duyne RP (2007) Localized surface plasmon resonance spectroscopy and sensing. Annu Rev Phys Chem 58:267–297
3. Agarwal GS, Pattanayak DN, Wolf E (1974) Electromagnetic fields in spatially dispersive media. Phys Rev B 10:1447–1475
4. Anderegg M, Feuerbacher B, Fitton B (1971) Optically excited longitudinal plasmons in potassium. Phys Rev Lett 27:1565–1568
5. Lindau I, Nilsson PO (1970) Experimental evidence for excitation of longitudinal plasmons by photons. Phys Lett A 31:352–353
6. Jones WE, Kliewer KL, Fuchs R (1969) Nonlocal theory of the optical properties of thin metallic films. Phys Rev 178:1201–1203
7. McMahon JM, Gray SK, Schatz GC (2009) Nonlocal optical response of metal nanostructures with arbitrary shape. Phys Rev Lett 103:097403
8. Palomba S, Novotny L, Palmer RE (2008) Blue-shifted plasmon resonance of individual size-selected gold nanoparticles. Opt Commun 281:480–483
9. McMahon JM, Gray SK, Schatz GC (2009) Calculating nonlocal optical properties of structures with arbitrary shape (submitted)
10. Dasgupta BB, Fuchs R (1981) Polarizability of a small sphere including nonlocal effects. Phys Rev B 24:554–561
11. Chang R, Leung PT (2006) Nonlocal effects on optical and molecular interactions with metallic nanoshells. Phys Rev B 73:125438
12. García de Abajo FJ (2008) Nonlocal effects in the plasmons of strongly interacting nanoparticles, dimers, and waveguides. J Phys Chem C 112:17983–17987
13. Tserkezis C, Gantzounis G, Stefanou N (2008) Collective plasmonic modes in ordered assemblies of metallic nanoshells. J Phys Condens Matter 20:075232
14. Pack A, Hietschold M, Wannemacher R (2001) Failure of local Mie theory: optical spectra of colloidal aggregates. Opt Commun 194:277–287
15. Yannopapas V (2008) Non-local optical response of two-dimensional arrays of metallic nanoparticles. J Phys Condens Matter 20:325211
16. McMahon JM, Gray SK, Schatz GC (2011) Fundamental behavior of electric field enhancements in the gaps between closely spaced nanostructures. Phys Rev B 83:115428
17. Liu M, Guyot-Sionnest P, Lee T-W, Gray SK (2007) Optical properties of rodlike and bipyramidal gold nanoparticles from three-dimensional computations. Phys Rev B 76:235428

18. Hohenberg P, Kohn W (1964) Inhomogeneous electron gas. Phys Rev 136:B864–B871
19. Boardman AD (1982) Hydrodynamic theory of plasmon-polaritons on plane surfaces. In: Boardman AD (eds) Electromagnetic Surface Modes. Wiley, New York
20. Fetter AL (1973) Electrodynamics of a layered electron gas. I. Single layer. Ann Phys 81:367–393
21. Harris J (1971) Surface-plasmon dispersion: a comparison of microscopic and hydrodynamic theories. Phys Rev B 4:1022–1027
22. McMahon JM, Gray SK, Schatz GC (2010) Nonlocal dielectric effects in core–shell nanowires. J Phys Chem C (in press)
23. Marinopoulos AG, Reining L, Rubio A (2008) Ab initio study of the dielectric response of crystalline ropes of metallic single-walled carbon nanotubes: tube-diameter and helicity effects. Phys Rev B 78:235428
24. Press WH, Flannery BP, Teukolsky SA, Vetterling WT (1988) NUMERICAL RECIPES in C: The Art of Scientific Computing. 1st edn. Cambridge University Press, Cambridge
25. Taflove A, Hagness S (2005) Computational electrodynamics: the finite-difference time-domain method. 3rd edn. Artech House, Boston
26. Roden JA, Gedney SD (2000) Convolutional PML (CPML): an efficient FDTD implementation of the CFS-PML for arbitrary media. Microw Opt Tech Lett 27:334–339
27. Merewether DE, Fisher R, Smith FW (1980) On implementing a numeric Huygen's source scheme in a finite difference program to illuminate scattering bodies. IEEE T Nucl Sci 27:1829–1833
28. Mur G (1981) Absorbing boundary conditions for the finite difference approximation of the time-domain electromagnetic field equations. IEEE T Elecromagn C 23:377–382
29. Umashankar KR, Taflove A (1982) A novel method to analyze electromagnetic scattering of complex objects. IEEE Electromagn Compat 24:397–405
30. Halevi P, Fuchs R (1984) Generalised additional boundary condition for non-local dielectrics: I Reflectivity. J Phys C Solid State 17:3869–3888
31. Johnson PB, Christy RW (1972) Optical constants of the noble metals. Phys Rev B, 6:4370–4379
32. Bohren CF, Huffman DR (1983) Absorption and scattering of light by small particles. Wiley, New York
33. Coronado EA, Schatz GC (2003) Surface plasmon broadening for arbitrary shape nanoparticles: a geometrical probability approach. J Chem Phys 119:3926–3934
34. Liu M, Guyot-Sionnest P (2004) Synthesis and optical characterization of Au/Ag core/shell nanorods. J Phys Chem B 108:5882–5888
35. Apell P, Penn DR (1983) Optical properties of small metal spheres: surface effects. Phys Rev Lett 50:1316–1319
36. Kreibig U, Vollmer M (1995) Optical properties of metal clusters. Springer, Berlin
37. Kottmann JP, Martin OJF, Smith DR, Schultz S (2000) Spectral response of plasmon resonant nanoparticles with a non-regular shape. Opt Express 6:213–219
38. Westcott SL, Jackson JB, Radloff C, Halas NJ (2002) Relative contributions to the plasmon line shape of metal nanoshells. Phys Rev B 66:155431
39. Oldenburg SJ, Averitt RD, Westcott SL, Halas NJ (1998) Nanoengineering of optical resonances. Chem Phys Lett 288:243–247
40. Hao E, Li S, Bailey RC, Zou S, Schatz GC, Hupp JT (2004) Optical properties of metal nanoshells. J Phys Chem B 108:1224–1229
41. Tam F, Moran C, Halas NJ (2004) Geometrical parameters controlling sensitivity of nanoshell plasmon resonances to changes in dielectric environment. J Phys Chem B 108:17290–17294
42. Oldenburg SJ, Westcott SL, Averitt RD, Halas NJ (1999) Surface enhanced Raman scattering in the near infrared using metal nanoshell substrates. Chem Phys Lett 111:4729
43. Prodan E, Nordlander P, Halas NJ (2003) Effects of dielectric screening on the optical properties of metallic nanoshells. Chem Phys Lett 368:94–101

44. Hao E, Schatz GC (2004) Electromagnetic fields around silver nanoparticles and dimers. J Chem Phys 120:357–366
45. McMahon JM, Henry A-I, Wustholz KL, Natan MJ, Freeman RG, Van Duyne RP, Schatz GC (2009) Gold nanoparticle dimer plasmonics: finite element method calculations of the electromagnetic enhancement to surface-enhanced Raman spectroscopy. Anal Bioanal Chem 394:1819–1825
46. Kottmann JP, Martin OJF (2001) Plasmon resonant coupling in metallic nanowires. Opt Express 8:655–663
47. Xu H (2004) Theoretical study of coated spherical metallic nanoparticles for single-molecule surface enhanced spectroscopy. Appl Phys Lett 85:5980–5982
48. Camden JP, Dieringer JA, Wang Y, Masiello DJ, Marks LD, Schatz GC, Van Duyne RP (2008) Probing the structure of single-molecule surface-enhanced Raman scattering hot spots. J Am Chem Soc 130:12616–12617
49. Ruppin R (1976) Optical properties of a metal sphere with a diffuse surface. J Opt Soc Am 66:449–453
50. Schmeits M, Dambly L (1991) Fast-electron scattering by bispherical surface-plasmon modes. Phys Rev B 44:12706–12712
51. Höflich K, Gösele U, Christiansen S (2009) Near-field investigations of nanoshell cylinder dimers. J Chem Phys 131:164704
52. Qian X-M, Nie SM (2008) Single-molecule and single-nanoparticle SERS: from fundamental mechanisms to biomedical applications. Chem Soc Rev 37:912–920
53. N'Gom M, Li S, Schatz GC, Erni R, Agarwal A, Kotov N, Norris TB (2009) Electron-beam mapping of plasmon resonances in electromagnetically interacting gold nanorods. Phys Rev B 80:113411
54. Kelly KL, Coronado E, Zhao LL, Schatz GC (2003) The optical properties of metal nanoparticles: the influence of size, shape, and dielectric environment. J Phys Chem B 107:668–677
55. Jensen LL, Jensen L (2009) Atomistic electrodynamics model for optical properties of silver nanoclusters. J Phys Chem C 113:15182–15190
56. Peña O, Pal U (2009) Scattering of electromagnetic radiation by a multilayered sphere. Comput Phys Commun 180:2348–2354

Chapter 9
Conclusions and Outlook

In Chap. 1, a number of outstanding questions in nanoscience were posed, which formed the basis of this dissertation. These questions are now revisited, in light of the results that were presented and discussed.

- What are the main theoretical and computational tools needed to study systems at the nanometer length scale? How can Maxwell's equations be solved to arbitrarily high precision, while preserving dynamical invariants of the problem (e.g., the energy density)?
  In Chap. 3, two of the most generally applicable computational methods for solving Maxwell's equations were discussed, FDTD and FEM [1–3]. These methods were used heavily throughout this dissertation. Two specialized methods, RCWA and the modal analysis method, were also discussed [4], which proved useful in Chaps. 6 and 7 when discussing subwavelength hole arrays and optical corrals, respectively.
  Chapter 3 also presented a discrete action principle for electrodynamics [5]. This was used to construct explicit symplectic integrators for Maxwell's equations, to any order of accuracy, which are capable of preserving dynamical invariants of electrodynamics problems. The numerical stability was shown to be greatly increased and the numerical dispersion greatly decreased, compared to other methods, by using the high-order integrators.
- At the single nanoparticle level, how well do experiment and classical electrodynamics agree? What is the detailed relationship between optical response and nanoparticle morphology, composition, and environment?
  In Chap. 4, experimental HRTEM and LSPR measurements made on a single Ag nanocube were correlated with FDTD calculations (classical electrodynamics) using bulk dielectric data [6, 7]. It was found that at the single nanoparticle level, near perfect agreement can be obtained (at least for relatively large nanoparticles). However, care must be taken in selection of the dielectric data set to use for modeling, as the JC Ag dielectric data [8] was found to be more accurate for describing perfect crystalline nanoparticles compared to that of LH [9].

J. M. McMahon, *Topics in Theoretical and Computational Nanoscience*,
Springer Theses, DOI: 10.1007/978-1-4419-8249-0_9,

By varying structural parameters, FDTD calculations showed a strong sensitivity between a nanocube's optical response and its face-to-face width, corner and side rounding, and substrate. These results are beneficial understanding the detailed relationship between optical response, structure, and dielectric environment of single nanoparticles. The near-field contact area between particle and substrate was shown to be particularly influential on the optical response. Moreover, the results presented impose strict requirements on determination of these parameters ($\sim$1 nm resolution) if calculation and experiment are to match, and also demonstrate that there are no "free parameters" (at least, geometric) that can be used in such simulations.

- Does an optimal nanostructure exist for generating large EM field enhancements? Is there a fundamental limit to this?
  Chapter 5 showed that EM field enhancements do not correlate with aggregation state in nanoparticle junction structures [10]. This means that a single hot spot between two particles is sufficient to generate them, and additional ones do not significantly contribute. Rather, the major factor is the gap size of the hot spot, especially for spacings less than $\sim$1 nm. The most conclusive evidence for this is that for structures with more than one hot spot, the one with the smallest gap size dominates the overall enhancement.
  Additionally, for small enough gaps the EM contribution to SERS in junction structures can completely dominate the signal, where enhancements can be as high as 10^{14} [2], which enables the possibility of SMSERS.
- Can nanostructures be used to control light, such as confining it, or causing fundamentally different scattering phenomena to interact, such as electromagnetic surface modes and diffraction effects?
  Chapters 6 and 7 discussed nanostructures that are useful for controlling light, specifically nanostructured metal films [4, 11–14] and optical corrals [15, 16]. Many phenomena were shown to be associated with these systems, such as SPPs, RAs, and LSPRs. These phenomena were shown to lead to complex optical properties, including EOT. It was emphasized on numerous occasions that these effects are not isolated from one-another, and FDTD and RCWA calculations revealed that SPPs and RAs can strongly interact (the RA–SPP effect), producing especially narrow EOT features [11–13]. Even the weakly plasmonic material Pd displayed this effect.
  Other systems were also shown to exhibit interesting effects, including isolated holes, pillar arrays, superlattices (patches of nanoholes), and other periodic systems [4]. For example, superlattices demonstrated that plasmons can interact over multiple length scales (e.g., intrapatch SPPs, which act on the order of hundreds on nanometers, can interact with interpatch SPPs, which act on the order of tens of micrometers) [14].
  Optical corrals were also discussed [15, 16], which can confine light to dielectric surfaces. Circular corrals were used as the platform to elucidate the novel effects associated with these structures, such as well-defined standing-wave patterns. It was found that these effects depend heavily on corral size and material,

excitation wavelength, and the substrate. FDTD calculations of $|\mathbf{E}(\mathbf{x},\omega)|^2$ supported the experimental evidence, and also revealed that $|\mathbf{H}(\mathbf{x},\omega)|^2$ is almost completely backwards (in terms of maxima and minima). A simple waveguide model was presented to explain these effects. It was shown that light scattering by the corrals produces evanescent waveguide modes at the dielectric interface with an effective wavelength similar to that of the incident light. The superposition of these modes onto the propagating ones leads to a dephasing of $\mathbf{E}(\mathbf{x},\omega)$ and $\mathbf{H}(\mathbf{x},\omega)$. These effects were also investigated in elliptical structures, and it was shown that these offer additional tunability of such effects through both their eccentricity and the polarization of the incident light.

- Is it possible to calculate quantum effects using classical electrodynamics, and if so, how do they affect optical properties?
  In Chap. 8, an electrodynamics method to calculate the optical responses of arbitrarily shaped structures described by a spatially nonlocal dielectric function (which incorporates quantum effects) was presented [17–20]. This formulation was based on converting the equation of motion of the conduction electrons from the hydrodynamic Drude model into a partial differential equation for the current field that serves as an ADE to Maxwell's equations. By discretizing this equation using standard finite-difference techniques, it was easily incorporated into a self-consistent computational scheme along with the standard discretized Maxwell's equations used in FDTD [17, 18].
  Many applications of this method were presented. Basic geometric nanostructures in one, two, and three dimensions (thin metal films, solid nanowires, and spherical nanoparticles, respectively) showed the basic phenomena that occur due to nonlocal effects: anomalous absorption, LSPR blueshifting, and significant decreases in $|\mathbf{E}(\mathbf{x},\omega)|^2$ enhancements (in some cases over an order of magnitude). Intensity profiles of $|\mathbf{D}(\mathbf{x},\omega)|^2$ showed that all of these effects can be attributed to the excitation of longitudinal (or volume) plasmons. Considering that the nonlocal calculations are, in principle, more rigorous than the local ones, the presented results have significant implications. For example, the interpretation of physical processes that rely on such effects could be much different than previously thought [e.g., diminished $|\mathbf{E}(\mathbf{x},\omega)|^2$ enhancements in relation to SERS].

The methods and applications that were presented in this dissertation answered some of the fundamental (and practical) outstanding questions in nanoscience. However, this work only forms a small selection of the total amount that has been done, and even as of now many open questions remain. Additionally, as the experimental techniques for making structures at the nanoscale becomes more sophisticated, more complex phenomena will be demonstrated, posing even more questions to the theorist. The study of structures at this scale will remain rich for many years to come, and the theoretical and computational tools presented in Chap. 3 will continue to play a large part in modeling and describing the novel effects that they display.

References

1. Zhao J, Pinchuk AO, McMahon JM, Li S, Ausman LK, Atkinson AL, Schatz GC (2008) Methods for describing the electromagnetic properties of silver and gold nanoparticles. Acc Chem Res 41:1710–1720
2. McMahon JM, Henry A-I, Wustholz KL, Natan MJ, Freeman RG, Van Duyne RP, Schatz GC (2009) Gold nanoparticle dimer plasmonics: finite element method calculations of the electromagnetic enhancement to surface-enhanced Raman spectroscopy. Anal Bioanal Chem 394:1819–1825
3. Atkinson AL, McMahon JM, Schatz GC (2009) FDTD studies of metallic nanoparticle systems. In: Self organization of molecular systems, from molecules and clusters to nanotubes and proteins, NATO science for peace and security. Series A: Chemistry and biology. Springer, Netherlands
4. McMahon JM, Gray SK, Schatz GC (2011) Surface nanophotonics theory. In: Wiederrecht G (ed) Comprehensive nanoscience and technology. Elsevier, Amsterdam
5. McMahon JM, Gray SK, Schatz GC (2009) A discrete action principle for electrodynamics and the construction of explicit symplectic integrators for linear, non-dispersive media. J Comp Phys 228:3421–3432
6. McMahon JM, Wang Y, Sherry LJ, Van Duyne RP, Marks LD, Gray SK, Schatz GC (2009) Correlating the structure, optical spectra, and electrodynamics of single silver nanocubes. J Phys Chem C 113:2731–2735
7. Ringe E, McMahon J, Sohn K, Cobley C, Xia Y, Huang J, Schatz GC, Marks LD, Van Duyne RP (2010) Unraveling the effects of size, composition, and substrate on the localized surface plasmon resonance frequencies of gold and silver nanocubes: a systematic single-particle approach. J Phys Chem C 114:12511–12516
8. Johnson PB, Christy RW (1972) Optical constants of the noble metals. Phys Rev B 6:4370–4379
9. Lynch DW, Hunter WR (1985) Comments on the optical constants of metals and an introduction to the data for several metals. In: Palik ED (eds) Handbook of optical constants of solids. Academic Press, Orlando, pp 275–368
10. Wustholz KL, Henry A.-I, McMahon JM, Freeman RG, Valley N, Piotti ME, Natan MJ, Schatz GC, Van Duyne RP (2010) Structure–activity relationships in gold nanoparticle dimers trimers for surface-enhanced raman spectroscopy. J Am Chem Soc 132:10903–10910
11. McMahon JM, Henzie J, Odom TW, Schatz GC, Gray SK (2007) Tailoring the sensing capabilities of nanohole arrays in gold films with Rayleigh anomaly-surface plasmon polaritons. Opt Express 15:18119–18129
12. Schatz GC, McMahon JM, Gray SK (2007) Tailoring the parameters of nanohole arrays in gold films for sensing applications. In: Stockman MI (ed) Plasmonics: metallic nanostructures and their optical properties V, pp 664103/1–8
13. Gao H, McMahon JM, Lee MH, Henzie J, Gray SK, Schatz G, Odom TW (2009) Rayleigh anomaly-surface plasmon polariton resonances in palladium and gold subwavelength hole arrays. Opt Express 17:2334–2340
14. Odom TW, Gao H, McMahon JM, Henzie J, Schatz GC (2009) Plasmonic superlattices: hierarchical subwavelength hole arrays. Chem Phys Lett 483:187–192
15. Babayan Y, McMahon JM, Li S , Gray SK, Schatz GC, Odom TW (2009) Confining standing waves in optical corrals. ACS Nano 3:615–620
16. McMahon JM, Gray SK, Schatz GC (2008) Dephasing of electromagnetic fields in scattering from an isolated slit in a gold film. In: Kawata S (ed) Plasmonics: nanoimaging, nanofabrication, and their applications IV, pp 703311/1–6
17. McMahon JM, Gray SK, Schatz GC (2009) Nonlocal optical response of metal nanostructures with arbitrary shape. Phys Rev Lett 103:097403
18. McMahon JM, Gray SK, Schatz GC (2010) Calculating nonlocal optical properties of structures with arbitrary shape. Phys Rev B 82:035423

19. McMahon JM, Gray SK, Schatz GC (2010) Nonlocal dielectric effects in core–shell nanowires. J Phys Chem C 114:15903–15908
20. McMahon JM, Gray SK, Schatz GC (2011) Fundamental behavior of electric field enhancements in the gaps between closely spaced nanostructures. Phys Rev B 83:115428

Appendix A
Common Mathematical Formulas

Mathematical formulas and relationships that are commonly used in this dissertation are given in this appendix. Specifically, these include Fourier transforms and finite-difference approximations to derivatives. Other mathematical formulas, such as vector identities or theorems and functional derivatives, are also used a few times in this work. However, these are given at the positions at which they are used.

A.1 Fourier Transforms

The Fourier transform decomposes a function (or waveform) into its component sinusoids (with respective amplitude) that sum to the original function. The Fourier transform of $f(x)$ is defined as

$$F(\xi) = \int_{-\infty}^{\infty} dx f(x) e^{2\pi i x \xi}, \tag{A.1}$$

where x and ξ form a Fourier-transform pair. The inverse Fourier transform [Fourier transform of $f(\xi)$] is

$$f(x) = \int_{-\infty}^{\infty} d\xi \, F(\xi) e^{-2\pi i x \xi}. \tag{A.2}$$

From Eqs. A.1 and A.2 it is seen that the Fourier transform and its inverse are symmetric.

In electrodynamics, Fourier transforms of $\omega \leftrightarrow t$ and $x \leftrightarrow k$ are often useful. For the former, if the substitutions $x \rightarrow t$ and $\xi \rightarrow \omega/2\pi$ are made in Eqs. A.1 and A.2, then

J. M. McMahon, *Topics in Theoretical and Computational Nanoscience*,
Springer Theses, DOI: 10.1007/978-1-4419-8249-0,

$$F(\omega) = \frac{1}{(2\pi)^{1/2}} \int_{-\infty}^{\infty} dt f(t) e^{i\omega t} \tag{A.3}$$

$$f(t) = \frac{1}{(2\pi)^{1/2}} \int_{-\infty}^{\infty} d\omega\, F(\omega) e^{-i\omega t}, \tag{A.4}$$

where the factor of $1/(2\pi)$ has been split between both equations in order to retain symmetry. For $x \leftrightarrow k$, if the substitutions $x \rightarrow x$ and $\xi \rightarrow -k/2\pi$ (sign conventions chosen to be consistent with electrodynamics [1, 2]) are made in Eqs. A.1 and A.2, then

$$F(k) = \frac{1}{(2\pi)^{1/2}} \int_{-\infty}^{\infty} dx f(x) e^{-ikx} \tag{A.5}$$

$$f(x) = \frac{1}{(2\pi)^{1/2}} \int_{-\infty}^{\infty} dk\, F(k) e^{ikx}. \tag{A.6}$$

It can be seen that the (effective) result of Fourier transforming from t to ω, or vice versa, is that the substitutions $\frac{\partial}{\partial t} \rightarrow -i\omega$ and $t \rightarrow \omega$ are made; and from x to k, or vice versa, the substitutions $\frac{\partial}{\partial x} \rightarrow ik$ and $x \rightarrow k$ are made.

A.2 Finite-Difference Expressions

A finite-difference expression can be used to obtain an approximation to the derivative of a function f with respect to an independent variable x, $df/dx = f'$. Consider the Taylor expansion of the function f around the point a,

$$f(x) = \sum_{n=0}^{\infty} \frac{f^{(n)}(a)}{n!} (x-a)^n. \tag{A.7}$$

Suppose that f is discretized on a 1D domain along x with grid points separated by Δx. Then, using Eq. A.7, f can be expanded around point a in either the forward or backward direction,

$$f(a+\Delta x) = f(a) + \Delta x f'(a) + O(\Delta x) \tag{A.8}$$

$$f(a-\Delta x) = f(a) - \Delta x f'(a) - O(\Delta x), \tag{A.9}$$

respectively, where $O(\Delta x)$ is the "error", a function which contains all terms not explicitly included from the expansion of Eq. A.7. Rearranging both of these expressions gives an approximation to the derivative of f with respect to x at the point a,

$$f'(a) = \frac{f(a+\Delta x) - f(a)}{\Delta x} + O(\Delta x) \tag{A.10}$$

$$f'(a) = \frac{f(a) - f(a-\Delta x)}{\Delta x} - O(\Delta x). \tag{A.11}$$

One way to reduce the error in these expressions is to add them together, giving a central finite-difference,

$$f'(a) = \frac{f(a+\Delta x) - f(a-\Delta x)}{2\Delta x} + O(\Delta x^2), \tag{A.12}$$

where some of the errors in the forward and backward finite-difference expressions cancel, giving an error on the order of Δx^2 (which is smaller than Δx). Because of the increased accuracy of this expression, which also does not require additional time to compute relative to Eqs. A.10 and A.11, central finite-differences are often used in practice.

Other derivatives, such as those of higher order, can be computed similarly. For example, a central finite-difference expression for the second derivatives of f with respect to x (at the point a), $f''(a)$, is

$$f''(a) = \frac{f(a+\Delta x) - 2f(a) + f(a-\Delta x)}{\Delta x^2} + O(\Delta x^2). \tag{A.13}$$

Appendix B
Drude Plus Two Lorentz Pole (D2L) Dielectric Model Parameters

In this appendix, parameters for the D2L model, Eqs. 2.23–2.25, are given. The parameters are tabulated, and in the left column of both tables chapter numbers are given in which the dielectric model applies. In some chapters, a specific dielectric model may only apply to a single section (but another is used for the rest of the chapter), and so, in these cases, the section number is also given. For Ag and Au, the parameters correspond to fits to either the Johnson and Christy (JC) [3] or Lynch and Hunter (LH) [4] empirically inferred dielectric data. The empirical data for the fits to C and Pd can be found in Refs. [5] and [6], respectively.

Table B.1 Drude parameters for the D2L model. $\hbar\omega_D$ and $\hbar\gamma_D$ are in units of eV and ε_∞ is unitless

Chapter	Material	ε_∞	$\hbar\omega_D$	$\hbar\gamma_D$
4	Ag JC	1.171	9.189	0.000
	Ag LH	2.365	8.738	0.075
	C	2.544	1.415	6.237
5	Au JC	3.559	8.812	0.075
5.4	Au LH	5.398	9.200	0.068
6	Ag JC	1.172	9.189	0.000
	Au LH	5.398	9.200	0.068
	Pd	1.000	6.681	0.000
6.6	Au JC	3.559	8.812	0.075
7	Ag JC	1.172	9.189	0.000
	Au LH	5.398	9.200	0.068
8	Ag JC	3.189	9.183	0.018
	Au JC	3.559	8.812	0.075
8.6	Ag JC	1.000	8.775	0.020

J. M. McMahon, *Topics in Theoretical and Computational Nanoscience*, Springer Theses, DOI: 10.1007/978-1-4419-8249-0,

Table B.2 Lorentz oscillator parameters for the D2L model. $\hbar\omega_{Ln}$ and $\hbar\delta_{Ln}$ are in units of eV and other parameters are unitless

Chapter	Material	$\hbar\omega_{L1}$	$\hbar\omega_{L2}$	$\hbar\delta_{L1}$	$\hbar\delta_{L2}$	$\Delta\varepsilon_{L1}$	$\Delta\varepsilon_{L2}$
4	Ag JC	5.435	2.012	0.129	0.561	2.240	0.223
	Ag LH	4.489	1.865	3.159	1.202	0.315	0.868
	C	4.380	5.183	0.280	0.548	3.568	2.510
5	Au JC	4.693	3.112	1.541	0.525	2.912	1.272
5.4	Au LH	2.813	3.439	0.287	0.435	0.681	1.861
6	Ag JC	5.435	2.012	0.129	0.561	2.240	0.223
	Au LH	2.813	3.439	0.287	0.435	0.681	1.861
	Pd	6.129	0.936	3.419	1.483	2.730	118.0
6.6	Au JC	4.693	3.112	1.541	0.525	2.912	1.272
7	Au LH	2.813	3.439	0.287	0.435	0.681	1.861
8	Ag JC	4.668	4.240	0.207	0.186	0.432	0.224
	Au JC	4.693	3.112	1.541	0.525	2.912	1.272
8.6	Ag JC	–	–	–	–	–	–

Appendix C
Derivation of the FEM Functional

In this appendix, the functional given in Eq. 3.39 is derived. Note that $\mathbf{x}$ and ω dependencies are assumed in all quantities. A functional for Eq. 3.37 can be obtained by multiplying by a testing function, $\mathbf{T}$, and integrating over the entire domain,

$$F(\mathbf{T}) = \frac{1}{2}\int_V \left[\mathbf{T}\cdot\left(\nabla\times\frac{1}{\mu_r}\nabla\times\mathbf{E}\right) - k_0^2\varepsilon(\omega)\mathbf{T}\cdot\mathbf{E}\right]dV - ik_0Z_0\int_V(\mathbf{T}\cdot\mathbf{J})dV. \tag{C.1}$$

Using the first vector Green's theorem (which relates vector and scalar functions inside a volume V to those on the surface ∂V),

$$\int_V [\varphi(\nabla\times\mathbf{A})\cdot(\nabla\times\mathbf{B}) - \mathbf{A}\cdot(\nabla\times\varphi\nabla\times\mathbf{B})]dV = \int_{\partial V}[\varphi(\mathbf{A}\times\nabla\times\mathbf{B})\cdot\hat{n}]d(\partial V) \tag{C.2}$$

where φ is a scalar and $\mathbf{A}$ and $\mathbf{B}$ are vectors, Eq. C.1 can be written as

$$\begin{aligned} F(\mathbf{T}) = {} & \frac{1}{2}\int_V \left[\frac{1}{\mu_r}(\nabla\times\mathbf{T})\cdot(\nabla\times\mathbf{E}) - k_0^2\varepsilon(\omega)\mathbf{T}\cdot\mathbf{E}\right]dV \\ & -\frac{1}{2}\int_{\partial V}\left[\frac{1}{\mu_r}(\mathbf{T}\times\nabla\times\mathbf{E})\cdot\hat{n}\right]d(\partial V) - ik_0Z_0\int_V(\mathbf{T}\cdot\mathbf{J})dV. \end{aligned} \tag{C.3}$$

In FEM, it is desirable to have a symmetric functional of $\mathbf{T}$ and $\mathbf{E}$. Therefore, the surface integral term should be modified. Using the Sommerfeld radiation condition, Eq. 3.78, the scattered field at an infinite distance from the scattering object(s) satisfies the relation

J. M. McMahon, *Topics in Theoretical and Computational Nanoscience*, Springer Theses, DOI: 10.1007/978-1-4419-8249-0,

$$\hat{r} \times \nabla \times \mathbf{E}^{\mathrm{sc}} = ik_0 n_b \hat{r} \times \hat{r} \times \mathbf{E}^{\mathrm{sc}}. \tag{C.4}$$

Upon making use of the linearity of Maxwell's equations to relate the total field to the scattered and incident fields,

$$\mathbf{E} = \mathbf{E}^{\mathrm{sc}} + \mathbf{E}^{\mathrm{inc}}, \tag{C.5}$$

Eq. C.4 becomes

$$\hat{r} \times \nabla \times \mathbf{E} = ik_0 n_b \hat{r} \times \hat{r} \times \mathbf{E} + \mathbf{U}^{\mathrm{inc}}, \tag{C.6}$$

where $\mathbf{U}^{\mathrm{inc}}$ is defined in Eq. 3.80. Treating Eq. C.6 as a boundary condition, the surface integral in Eq. C.3 becomes

$$\begin{aligned} &-\frac{1}{2}\int_{\partial V}\left[\frac{1}{\mu_r}(\mathbf{T} \times \nabla \times \mathbf{E}) \cdot \hat{n}\right] d(\partial V) \\ &\quad = -\frac{1}{2}\int_{\partial V}\left[\frac{ik_0 n_b}{\mu_r}(\hat{r} \times \mathbf{T}) \cdot (\hat{r} \times \mathbf{E}) - \frac{1}{\mu_r}\mathbf{T} \cdot \mathbf{U}^{\mathrm{inc}}\right] d(\partial V), \end{aligned} \tag{C.7}$$

by also using $\hat{r} = \hat{n}$ and the vector identity

$$\mathbf{A} \cdot (\mathbf{B} \times \mathbf{C}) = -\mathbf{B} \cdot (\mathbf{A} \times \mathbf{C}). \tag{C.8}$$

Using Eq. C.7 in Eq. C.3 and taking $\mathbf{T} = \mathbf{E}$ gives the functional in Eq. 3.79.

Appendix D
Derivation of the Hydrodynamic Drude Model

In this appendix, the hydrodynamic Drude model, Eq. 8.4, is derived, and the connection with quantum mechanics is made. Additionally, it is shown how expressions with greater accuracy can be obtained. Note that $\mathbf{x}$ and t dependencies are assumed in all quantities, unless otherwise specified.

Assume that the *sp*-band (conduction band) electrons in a metal can be treated as a continuous fluid, such as an electron gas. In this case, a density n and velocity $\mathbf{v}$ can be used to describe the fluid, which together gives an electric current density

$$\mathbf{J} = -en\mathbf{v}, \tag{D.1}$$

where e is the charge of an electron. Since the charge density of the fluid is $-en$, n and $\mathbf{v}$ are related via the continuity equation

$$\frac{\partial n}{\partial t} + \nabla \cdot (n\mathbf{v}) = 0. \tag{D.2}$$

$\mathbf{v}$ obeys the acceleration equation, which can also be considered a generalized momentum equation derivable from a quantum mechanical Hamiltonian [7],

$$m_e\left(\frac{\partial}{\partial t} + \mathbf{v}\cdot\nabla\right)\mathbf{v} = -e(\mathbf{E} + \mathbf{v}\times\mathbf{B}) - m_e\gamma\mathbf{v} - \nabla\left(\frac{\delta g[n]}{\delta n}\right) \tag{D.3}$$

where m_e is the electron mass which has been included so that units work out (this will not explicitly appear in any final expressions), γ is the inverse of the collision time, and $g(n)$ is the energy functional of the fluid. (Note that a hydrodynamic total derivative is used on the left side of Eq. D.3.) The term $\mathbf{v}\cdot\nabla\mathbf{v}$ is nonlinear and typically negligible, so in what follows it will be neglected. Furthermore, assuming that the driving force of the fluid is the electric field, $\mathbf{B}$ can also be neglected.

In order for the system of equations in D.1–D.3 to be complete, an expression for $\delta g[n]/\delta n$ is needed. At the most fundamental level, $g[n]$ should include

J. M. McMahon, *Topics in Theoretical and Computational Nanoscience*, Springer Theses, DOI: 10.1007/978-1-4419-8249-0,

quantum mechanical kinetic, exchange, and correlation energies. Note that many such functionals in fact exist for DFT [8]. Herein, exchange and correlation effects are neglected, and only the kinetic energy of the fluid is considered. For a free electron gas (i.e., kinetic energy only)

$$g[n] = \frac{3}{5}\frac{[k_{\mathrm{F}}(n)]^2}{2m_e}n, \tag{D.4}$$

where $k_{\mathrm{F}}(n)$ is the Fermi momentum, $k_{\mathrm{F}}(n) = (3\pi^2 n)^{1/3} = m_e v_{\mathrm{F}}$ with v_{F} being the Fermi velocity [8] (and again the electron mass is unimportant). Therefore,

$$\frac{\delta g[n]}{\delta n} = \frac{1}{2m_e}(3\pi^2)^{2/3}n^{2/3}. \tag{D.5}$$

By assuming that the electron fluid is only slightly (linearly) perturbed from equilibrium, the density can be written $n = n_0 + n_1$, where n_0 is the equilibrium value and n_1 is the perturbation. In this case,

$$\nabla\left(\frac{\delta g[n]}{\delta n}\right) = \frac{1}{3}(3\pi^2 n_0)^{2/3}\frac{1}{n_0}\nabla n_1 = m_e\frac{1}{3}v_{\mathrm{F}}^2\frac{1}{n_0}\nabla n_1, \tag{D.6}$$

and Eqs. D.1–D.3 become complete.

In order to use Eqs. D.1–D.3 in electrodynamics, they are first rewritten in time-harmonic ($\partial/\partial t \rightarrow -i\omega$; see Appendix A) and linearized (slightly perturbed) form,

$$\mathbf{J} = -en_0\mathbf{v} \tag{D.7}$$

$$-i\omega n_1 + n_0\nabla\cdot\mathbf{v} = 0 \tag{D.8}$$

$$i\omega m_e\mathbf{v} = e\mathbf{E} + m_e\gamma\mathbf{v} + m_e\beta^2\frac{1}{n_0}\nabla n_1 \tag{D.9}$$

where $\beta^2 = v_{\mathrm{F}}^2/3$. Note that this factor will play the same role as β^2 in Chap. 8 and corresponds to the low-frequency value discussed, and at high frequencies, it should be multiplied by an additional constant factor [9]. Inserting Eq. D.8 into Eq. D.9, Fourier transforming to $\mathbf{k}$-space ($\nabla \rightarrow i\mathbf{k}$; see Appendix A), and rearranging for $\mathbf{v}$ gives

$$\mathbf{v} = \frac{e\mathbf{E}}{m_e}\frac{1}{i\omega - \gamma - i\beta^2\mathbf{k}^2/\omega}. \tag{D.10}$$

Inserting Eq. D.10 into Eq. D.7 (in **k**-space) gives an auxiliary current density that can be used directly in the Maxwell–Ampére law (also in **k**-space),

$$-i\omega\varepsilon_0\mathbf{E} + \mathbf{J} = i\mathbf{k} \times \mathbf{H}. \tag{D.11}$$

By comparing Eq. D.11 with the equivalent form

$$-i\omega\varepsilon_0\varepsilon(\mathbf{k}, \omega)\mathbf{E} = i\mathbf{k} \times \mathbf{H}, \tag{D.12}$$

$\varepsilon(\mathbf{k}, \omega)$ can be identified as

$$\varepsilon(\mathbf{k}, \omega) = 1 - \frac{\omega_{\mathrm{D}}^2}{\omega(\omega + i\gamma) - \beta^2\mathbf{k}^2}, \tag{D.13}$$

which has been written in terms of the Drude plasma frequency, $\omega_{\mathrm{D}}^2 = n_0 e^2/\varepsilon_0 m_e$. Equation D.13 is equivalent to the hydrodynamic Drude model, Eq. 8.4.

The above derivation used the most simple form for $g[n]$, that for a free electron gas, Eq. D.4. However, more accurate expressions could be used allowing modeling of additional effects with classical electrodynamics, such as those due to exchange and correlation [8]. Such a procedure, including comparisons to DFT calculations, represents a promising avenue for future research.

Appendix E
Derivation of Nonlocal Finite-Difference Equations

In this appendix, the finite-difference equations used to model nonlocal dielectric effects are derived.

First, the temporal derivatives in Eqs. 2.2 and 8.10 are discretized using a leapfrog algorithm [10],

$$\mu_0 \frac{\mathbf{H}(\mathbf{x})^{n+1/2} - \mathbf{H}(\mathbf{x})^{n-1/2}}{\Delta t} = -\nabla \times \mathbf{E}(\mathbf{x})^n \tag{E.1}$$

$$\varepsilon_0 \varepsilon_\infty \frac{\mathbf{E}(\mathbf{x})^{n+1} - \mathbf{E}(\mathbf{x})^n}{\Delta t} + \sum_n \mathbf{J}_{Ln}(\mathbf{x})^{n+1/2} + \mathbf{J}_{HD}(\mathbf{x})^{n+1/2} = \nabla \times \mathbf{H}(\mathbf{x})^{n+1/2} \tag{E.2}$$

where the superscript n denotes a discrete time step, and should not be confused with the subscript n denoting a particular Lorentz pole. Equations 8.6 and 8.9 are discretized using central finite-differences (necessary because of the second-order derivatives) centered at time-step n,

$$\frac{\mathbf{J}_{Ln}(\mathbf{x})^{n+1} - 2\mathbf{J}_{Ln}(\mathbf{x})^n + \mathbf{J}_{Ln}(\mathbf{x})^{n-1}}{\Delta t^2} + 2\delta_{Ln} \frac{\mathbf{J}_{Ln}(\mathbf{x})^{n+1} - \mathbf{J}_{Ln}(\mathbf{x})^{n-1}}{2\Delta t} + \omega_{Ln}^2 \mathbf{J}_{Ln}(\mathbf{x})^{J_{Ln}} = -\varepsilon_0 \omega_{Ln}^2 \Delta\varepsilon_{Ln} \frac{\mathbf{E}(\mathbf{x})^{n+1} - \mathbf{E}(\mathbf{x})^{n-1}}{2\Delta t} \tag{E.3}$$

$$\frac{\mathbf{J}_{HD}(\mathbf{x})^{n+1} - 2\mathbf{J}_{HD}(\mathbf{x})^n + \mathbf{J}_{HD}(\mathbf{x})^{n-1}}{\Delta t^2} + \gamma \frac{\mathbf{J}_{HD}(\mathbf{x})^{n+1} - \mathbf{J}_{HD}(\mathbf{x})^{n-1}}{2\Delta t} - \beta^2 \nabla^2 \mathbf{J}_{HD}(\mathbf{x})^n = \varepsilon_0 \omega_D^2 \frac{\mathbf{E}(\mathbf{x})^{n+1} - \mathbf{E}(\mathbf{x})^{n-1}}{2\Delta t}. \tag{E.4}$$

Next, update equations for $\mathbf{J}_{Ln}(\mathbf{x})$ and $\mathbf{J}_{HD}(\mathbf{x})$ are obtained by rearranging Eqs. E.3 and E.4,

J. M. McMahon, *Topics in Theoretical and Computational Nanoscience*, Springer Theses, DOI: 10.1007/978-1-4419-8249-0,

$$\mathbf{J}_{\mathrm{L}n}(\mathbf{x})^{n+1} = \frac{1}{\alpha_{\mathrm{L}n}}\left(\frac{-2\mathbf{J}_{\mathrm{L}n}(\mathbf{x})^{n} + \mathbf{J}_{\mathrm{L}n}(\mathbf{x})^{n-1}}{\Delta t^2} + \omega_{\mathrm{L}n}^2\mathbf{J}_{\mathrm{L}n}(\mathbf{x})^{n} - 2\delta_{\mathrm{L}n}\frac{\mathbf{J}_{\mathrm{L}n}(\mathbf{x})^{n-1}}{2\Delta t} - \varepsilon_0\omega_{\mathrm{L}n}^2\Delta\varepsilon_{\mathrm{L}n}\frac{\mathbf{E}(\mathbf{x})^{n+1} - \mathbf{E}(\mathbf{x})^{n-1}}{2\Delta t}\right) \tag{E.5}$$

$$\mathbf{J}_{\mathrm{HD}}(\mathbf{x})^{n+1} = \frac{1}{\alpha_{\mathrm{HD}}}\left(\frac{-2\mathbf{J}_{\mathrm{HD}}(\mathbf{x})^{n} + \mathbf{J}_{\mathrm{HD}}(\mathbf{x})^{n-1}}{\Delta t^2} - \beta^2\nabla^2\mathbf{J}_{\mathrm{HD}}(\mathbf{x})^{n} - \gamma\frac{\mathbf{J}_{\mathrm{HD}}(\mathbf{x})^{n-1}}{2\Delta t} + \varepsilon_0\omega_{\mathrm{D}}^2\frac{\mathbf{E}(\mathbf{x})^{n+1} - \mathbf{E}(\mathbf{x})^{n-1}}{2\Delta t}\right) \tag{E.6}$$

where

$$\alpha_{\mathrm{L}n} = -\frac{1}{\Delta t}\left(\frac{1}{\Delta t} + \delta_{\mathrm{L}n}\right) \tag{E.7}$$

$$\alpha_{\mathrm{HD}} = -\frac{1}{\Delta t}\left(\frac{1}{\Delta t} + \frac{\gamma}{2}\right). \tag{E.8}$$

To use Eqs. E.5 and E.6 in Eq. E.2, $\mathbf{J}_{\mathrm{L}n}(\mathbf{x})$ and $\mathbf{J}_{\mathrm{HD}}(\mathbf{x})$ are centered at time step $n + 1/2$ by averaging,

$$\mathbf{J}_{\mathrm{L}n}(\mathbf{x})^{n+1/2} = \frac{\mathbf{J}_{\mathrm{L}n}(\mathbf{x})^{n+1} + \mathbf{J}_{\mathrm{L}n}(\mathbf{x})^{n}}{2} \tag{E.9}$$

$$\mathbf{J}_{\mathrm{HD}}(\mathbf{x})^{n+1/2} = \frac{\mathbf{J}_{\mathrm{HD}}(\mathbf{x})^{n+1} + \mathbf{J}_{\mathrm{HD}}(\mathbf{x})^{n}}{2}. \tag{E.10}$$

Equations E.2, E.5, and E.6 all contain $\mathbf{E}(\mathbf{x})^{n+1}$. To obtain a consistent update, Eqs. E.9 and E.10 (using Eqs. E.5 and E.6) are inserted into Eq. E.2 and rearranged,

$$\mathbf{E}(\mathbf{x})^{n+1} = \frac{1}{\eta_1}\left[\eta_2\mathbf{E}(\mathbf{x})^{n} + \eta_3\mathbf{E}(\mathbf{x})^{n-1} - \mathbf{J}_{\mathrm{T}}(\mathbf{x})^{n,n-1} + \nabla\times\mathbf{H}(\mathbf{x})^{n+1/2}\right] \tag{E.11}$$

where

$$\eta_1 = \frac{\varepsilon_0}{\Delta t}\left(\varepsilon_\infty + \frac{\omega_{\mathrm{D}}^2}{4\alpha_{\mathrm{HD}}} - \sum_n \frac{\omega_{\mathrm{L}n}^2\Delta\varepsilon_{\mathrm{L}n}}{4\alpha_{\mathrm{L}_n}}\right) \tag{E.12}$$

$$\eta_2 = \frac{\varepsilon_0 \varepsilon_\infty}{\Delta t} \tag{E.13}$$

$$\eta_3 = \frac{\varepsilon_0}{4\Delta t}\left(\frac{\omega_{\mathrm{D}}^2}{\alpha_{\mathrm{HD}}} - \sum_n \frac{\omega_{\mathrm{L}n}^2 \Delta\varepsilon_{\mathrm{L}n}}{\alpha_{\mathrm{L}n}}\right) \tag{E.14}$$

and

$$\begin{aligned}\mathbf{J}_{\mathrm{T}}(\mathbf{x})^{n,n-1} = {} & \frac{1}{2\alpha_{\mathrm{HD}}}\left[\left(-\frac{2}{\Delta t^2} + \alpha_{\mathrm{HD}} - \beta^2\nabla^2\right)\mathbf{J}_{\mathrm{HD}}(\mathbf{x})^n + \left(\frac{1}{\Delta t^2} - \gamma\right)\mathbf{J}_{\mathrm{HD}}(\mathbf{x})^{n-1}\right] \\ & + \sum_n \frac{1}{2\alpha_{\mathrm{L}n}}\left[\left(-\frac{2}{\Delta t^2} + \alpha_{\mathrm{L}n} + \omega_{\mathrm{L}n}^2\right)\mathbf{J}_{\mathrm{L}n}(\mathbf{x})^n + \left(\frac{1}{\Delta t^2} - 2\delta_{\mathrm{L}n}\right)\mathbf{J}_{\mathrm{L}n}(\mathbf{x})^{n-1}\right].\end{aligned} \tag{E.15}$$

Finally, simple rearrangement of Eq. E.1 gives the appropriate update equation for $\mathbf{H}(\mathbf{x})$,

$$\mathbf{H}(\mathbf{x})^{n+1/2} = \mathbf{H}(\mathbf{x})^{n-1/2} - \frac{\Delta t}{\mu_0}\nabla \times \mathbf{E}(\mathbf{x})^n. \tag{E.16}$$

In order to satisfy Eqs. 2.3 and 2.4, a Yee spatial-discretization [11] is used for the components of $\mathbf{E}(\mathbf{x})$ and $\mathbf{H}(\mathbf{x})$ (i.e., they are offset and circulate one another); see Fig. 3.1. The $\mathbf{J}_{\mathrm{L}n}(\mathbf{x})$ and $\mathbf{J}_{\mathrm{HD}}(\mathbf{x})$ components are centered at the same spatial locations as the corresponding $\mathbf{E}(\mathbf{x})$ components. All of the spatial derivatives, including those in Eqs. E.6 and E.15, are approximated using central finite-differences (see Appendix A.2).

In order to model structures with arbitrary shape, the $\mathbf{J}_{\mathrm{L}n}(\mathbf{x})$ and $\mathbf{J}_{\mathrm{HD}}(\mathbf{x})$ components only exist at the grid positions of the nonlocal materials. By not updating the currents outside of the structures, the ABC of Pekar is imposed [12] (i.e., the total nonlocal polarization current vanishes outside of the structure; see Chap. 8).

Equations E.5, E.6, E.11, and E.16 form the complete and consistent set necessary to solve Eqs. 2.1–2.4 for materials described by the constitutive relationship in Eq. 8.2 and with dielectric function given in Eqs. 8.3 and 8.4.

References

1. Jackson JD (1998) Classical Electrodynamics, 3rd edn. Wiley, New York
2. Schwartz M (1987) Principles of Electrodynamics, 1st edn. Dover Publications, New York
3. Johnson PB, Christy RW (1972) Optical constants of the noble metals. Phys Rev B 6:4370–4379
4. Lynch DW, Hunter WR (1985) Comments on the optical constants of metals and an introduction to the data for several metals. In: Palik ED (ed) Handbook of Optical Constants of Solids. Academic Press, Orlando, FL, pp 275–368
5. Arakawa ET, Dolfini SM, Ashley JC, Williams MW (1985) Arc-evaporated carbon films: Optical properties and electron mean free paths. Phys Rev B 31:8097–8101
6. Johnson PB, Christy RW (1974) Optical constants of transition metals: Ti, V, Cr, Mn, Fe, Co, Ni, and Pd. Phys Rev B 9:5056–5070
7. Boardman AD (1982) Hydrodynamic theory of plasmon-polaritons on plane surfaces. In: Boardman AD (ed) Electromagnetic Surface Modes. Wiley, New York
8. Hohenberg P, Kohn W (1964) Inhomogeneous electron gas. Phys Rev 136:B864–B871
9. Fetter AL (1973) Electrodynamics of a layered electron gas. I. Single layer. Ann Phys 81:367–393
10. Taflove A, Hagness S (2005) Computational Electrodynamics: The Finite-Difference Time-Domain Method, 3rd edn. Artech House, Boston
11. Yee SK (1966) Numerical solution of initial boundary value problems involving Maxwell's equations in isotropic media. IEEE Trans Antennas Propagat 14:302–307
12. Halevi P, Fuchs R (1984) Generalised additional boundary condition for non-local dielectrics: I. Reflectivity. J Phys C Solid State 17:3869–3888

Biographical Sketch

Jeffrey Michael McMahon was born in Lawrence, KS in 1982. He did his undergraduate studies at Western Washington University (WWU), receiving a B.S. in chemistry with minors in physics and mathematics. While at WWU, he performed undergraduate research under the supervision of Steven R. Emory, one of the discoverers of single molecule surface-enhanced Raman scattering, publishing one peer-reviewed article. In 2005, he entered the Ph.D. program in chemistry at Northwestern University (NU), performing research under the supervision of George C. Schatz. While at NU, he also performed research at Argonne National Laboratory (ANL) under the supervision of Stephen K. Gray. While at NU, he published many more peer-reviewed manuscripts, was an author on two book chapters, and published two proceedings of SPIE. He is the recipient of numerous awards, including the ACS Graduate Student Award in Computational Chemistry and a Graduate Student Award to Attend the 59th Lindau Nobel Laureate Meeting. His full curriculum vitae, including a full list of publications, can be obtained from his personal website: http://www.thecomputationalphysicist.com.

J. M. McMahon, *Topics in Theoretical and Computational Nanoscience*, Springer Theses, DOI: 10.1007/978-1-4419-8249-0,

Glossary

Activity: (In the context herein) the optical response of, and the electromagnetic field enhancement from, a structure.

Additional boundary condition: A boundary condition at a material interface that only exists when nonlocal dielectric effects are included.

Blueshift: The shift of a spectral feature to higher energy.

Convolutional perfectly matched layers: A technique used to truncate a computational domain in the finite-difference time-domain method, which is an improvement on basic perfectly matched layers.

Continuum limit: (In the context herein) the length at which a structure can be considered continuous, where the actual atomic positions that compose the structure are irrelevant.

Density-functional theory: The theoretical basis for a computational method used to solve the Schrödinger equation.

Dielectric function: A function that describes the ability of a material to polarize in response to an electric field.

Dispersion diagram: (In the context herein) a graphic representation of the energy vs. wavevector magnitude (of a wave).

Drude model: A model that describes the *sp*-band (conduction band) electron motion in metals.

Extraordinary optical transmission: The enhanced transmission through a subwavelength structured metal film (often through an aperture or apertures) relative to the prediction of geometric optics.

Enhancement factor: Magnitude of the electric field enhancement to the fourth power (often in the context of a maximum or average), which is the electromagnetic enhancement factor for surface-enhanced Raman scattering.

J. M. McMahon, *Topics in Theoretical and Computational Nanoscience*,
Springer Theses, DOI: 10.1007/978-1-4419-8249-0,

Fano profile: A spectral profile in which there is a sharp minimum followed by an adjacent maximum.

Full width at half maximum: (In the context herein) the width of a spectral peak at the maximum position measured at half intensity.

Hole array: A periodic array of subwavelength holes in a metal film.

Hot spot: A position of significant electromagnetic field enhancement.

Hydrogen-like atom: An atom with a single electron.

Intraband electron motion: (In the context herein) the motion of *sp*-band (conduction band) electrons in a metal.

Interband electron transition: (In the context herein) an electron transition from the *d*-band to *sp*-band (conduction band) in a metal.

Localized surface plasmon resonance: A surface plasmon confined to a particular area (e.g., the surface of a particle) and in resonance with a driving field.

Longitudinal plasmon: An electromagnetic volume wave inside a metallic structure, longitudinal to the wavevector.

Lorentz oscillator: (In the context herein) a model that describes the *d*-band to *sp*-band electron transitions (interband transitions) in a metal.

Micro-: Prefix for 10^{-6}.

Micrometer: 1.0×10^{-6} m.

Microscale: Length scale of micrometers.

Nano-: Prefix for 10^{-9}.

Nanocube: A cubic particle that has nanoscale dimensions.

Nanometer: 1.0×10^{-9} m.

Nanoparticle: An isolated generic structure (often a spherical particle) that has nanoscale dimensions.

Nanoscale: Length scale of nanometers.

Nanostructure: An isolated generic structure that has nanoscale dimensions.

Noble metals: (In the context herein) silver and gold (even though many metals form the complete set of such elements).

Nonlocal dielectric effect: (In the context herein) the (spatially) nonlocal relationship between the electric displacement field and electric field. (See also "nonlocal effect".)

Nonlocal effect: (In the context herein) a (spatially) nonlocal relationship between two quantities.

Optical energies: (In the context herein) 1–6 eV, which contains the visible region and parts of the ultraviolet and infrared.

Partitioned Runge–Kutta method: A numerical multistage time-integration technique, which is often symplectic.

Perfect electric conductor: A material which cannot sustain internal fields. For such a material, the dielectric function goes to infinity, and the tangential component of the (external) electric field goes to 0 on the surface of the structure.

Perfectly matched layers: A technique to truncate a computational domain in the finite-difference time-domain method.

Plasmonic crystal: A periodically structured system made from the noble metals, particularly silver or gold, where the overall properties are controlled by the particular material and periodic lattice arrangement.

Rayleigh anomaly: A diffraction grating anomaly, where light is diffracted at an angle parallel to the surface.

Rayleigh anomaly—surface plasmon polariton: The effect in a hole array where the conditions for a Rayleigh anomaly and a surface plasmon polariton (on opposite interfaces of the metal film) coexist, which leads to enhanced extraordinary optical transmission over a narrow wavelength range.

Redshift: The shift of a spectral feature to lower energy.

Refractive index unit: The change in a quantity with respect to the refractive index.

Surface-enhanced Raman scattering: Enhancement of Raman scattering by a surface (often a noble metal), such as that of a nanoparticle.

Surface plasmon: A collective oscillation of charge density at a metal–dielectric interface.

Surface plasmon polariton: The coupling of light with a surface plasmon.

Surface plasmon polariton—Bloch-wave: A periodic (often standing) surface plasmon polariton wave.

Symplectic integrator: A numerical integrator capable of preserving the dynamical invariants of a problem (e.g., the energy density) up to a desired order of accuracy.

Transverse electric to z: A polarization of light where the electric field is transverse to the z-axis.

Transverse magnetic to z: A polarization of light where the magnetic field is transverse to the z-axis.

Total-field–scattered-field technique: A technique to introduce incident electromagnetic fields into a computational domain in the finite-difference time-domain method.

Waveguide: (In the context herein) a structure that guides electromagnetic waves.

Weakly plasmonic: The lack of ability of a material to (strongly) support surface plasmon polaritons, often due to a strong attenuation of them.

Index

J. M. McMahon, *Topics in Theoretical and Computational Nanoscience*, Springer Theses, DOI: 10.1007/978-1-4419-8249-0,